Manufacturing of a polymeric membrane with integrated porous electrode

P.A. Kapel

Technische Universiteit Delft

TU Delft

Department of Precision and Microsystems Engineering

Manufacturing of polymeric membrane with integrated porous electrode

P.A. Kapel

Report no : 2018.004
Coach : Dr. L. Sasso & Dr. P. Fanzio
Professor : Dr. Ir. M. Tichem
Specialisation : Micro and Nano Engineering
Type of report : Master Thesis
Date : 14 February 2018

Manufacturing of a polymeric membrane with integrated porous electrode

by

P.A. Kapel

to obtain the degree of Master of Science
at the Delft University of Technology,
to be defended publicly on Wednesday February 28, 2018

Student number:	4234502	
Supervisors:	Dr. L. Sasso,	TU Delft, 3ME - PME
	Dr. P. Fanzio,	TU Delft, 3ME - PME
Thesis committee:	Dr. Ir. M. Tichem,	TU Delft, 3ME - PME
	Dr. M. Mastrangeli,	TU Delft, EWI - ECTM

An electronic version of this thesis is available at `http://repository.tudelft.nl/`.

TU Delft

Preface

First of all, it was a wonderfull experience to work with state of the art technology to develop a new manufacturing method to push the state of the art to manufacture membranes even further. This one year research is performed to partially fulfill the requirements to obtain the degree Master of Science at Delft University of Technology.

A lot of set backs were encountered during this research. But instead of accepting the set backs and giving up, I pushed even harder during this period to get to these high quality results. We aim to publish those after my graduation as a paper in the journal of Microelectronic Engineering.

I would like to thank my supervisors Luigi Sasso and Paola Fanzio for guiding me during this research by, giving useful advice, helping me out in the lab, enabling the possibility to present the results at the international MicroNanoConference 2017, and giving me all this freedom within this research. Furthermore, I would like to thank the lab support team, Rob Luttjeboer, Spiridon van Veldhoven, Patrick van Holst, and Harry Jansen, for helping me with the experiments of this research. Last, but not least, I would like to thank fellow students, friends, and family for their support and fruitful discussion.

P.A. Kapel

Delft,
February 14, 2018

Abstract

Organ-on-a-chip systems enable the possibility to experimentally model physiological micro-environmental conditions in order to develop new medicines in a cheaper, more efficient way, eventually eliminating the need for animal models and opening up the possibility of personalized medicine. One of the current challenges of organ-on-a-chip systems is the real-time monitoring of cellular behavior and biological processes. This issue is tackled by proposing a manufacturing technology to manufacture polymeric membranes for culturing of cells, tissues, and organoids with integrated sensor capabilities and fluidic functionalities.

Aside from exploiting the well characterized, simple, and low cost techniques that can be employed in polymer manufacturing, the use of solely polymeric materials increases the opportunities for functional integration, while at the same time allowing for the translation of complex cleanroom fabrication processes into mold-based replication techniques. A multilayer substrate consists out of four layers, a conductive layer for the electrodes, an underlying substrate layer, a sacrificial layer, and a support layer. The soft mold, which contains pillars with sharp tips, is manufactured by a two-photon polymerization process. This additive manufacturing method allows to manufacture soft molds with freedom in dimensions of the pillars, the number of pillars, and the location of the pillars. Soft mold nano imprint lithography is performed to manufacture this polymeric membrane with integrated porous electrode in one manufacturing step. Pillars with sharp tips puncture through the first two layers into the sacrificial layer to create the pores. A post treatment is done by submerging the imprinted substrate in ethylene glycol to simultaneously dissolve the sacrificial layer which helps with the demolding of the mold, increase the conductivity of the conductive layer, and decreases the solubility of the conductive layer in water.

With this developed manufacturing technology, polymeric membrane with integrated porous electrode up to 1 mm by 1 mm in effective surface area, with a thickness of 10 µm, are manufactured with control over the pore diameter (as small as 400 nm), the porosity, and the location of the pores. The morphological characterization is done by scanning electron microscopy. The integrated porous electrode's performance is characterized electrically by a 4-point probe and electrochemically by cyclic voltammetry and electrochemical impedance spectroscopy. Showing the possibility to use the conductive layer to give cells electrical stimuli and for the use as a biosensor.

Contents

1 Introduction

The costs of developing and gaining market approval for a new drug is estimated to be around $2.6 billion,[1] takes at least 10 years,[2, 3] and fails more often than it succeeds.[4] The overall likelihood of FDA approval for a compound from the first phase of the clinical trials is only 9.6%.[5] Each year, over 100 million animals are used in laboratory experiments worldwide.[6]

1.1. Drug testing platforms

Currently, new drugs are tested in 3D cellular microenvironments and animal models. These kinds of 3D cellular microenvironments use human cells but are not a complete system. Also, the electrical and mechanical interactions, which significantly influence the cell behaviors, are not included. Animal models are also used to test the compounds on a complete system. But animals are not humans, which could result in different results. Additionally, testing on animals often causes ethical problems, are expensive, time-consuming, and have negative environmental impacts.[4, 6–8]

A new way of validating compounds in the preclinical phase is currently being developed, the organ-on-a-chip. Organ-on-a-chip systems enable the possibility to experimentally model physiological microenvironmental conditions in order to develop new medicines in a cheaper, more efficient way, and eventually eliminating the need for animal models. These systems are microfluidic chips which often contains a membrane, with living cells grown onto it, which separates the microfluidic channel in two. These kinds of systems are able to include the influence of chemical, electrical, and mechanical interactions on the cells.[4, 7–10]

If multiple organ-on-a-chip systems are connected to each other, a human-on-a-chip system can be created. The human-on-a-chip system will be a platform to evaluate new compounds in a more complex system, which can mimic organ to organ and tissue to tissue interactions, within a complete system based on human cells instead of an animal model.[4, 8–10]

1.2. Applications

A straightforward application of the organ-on-a-chip systems, and eventually the human-on-a-chip systems, would be in the pharmaceutical industry. It can be used in the preclinical trials to have better predictions for what will happen when a certain compound is tested on humans. These kinds of systems can also be used in the cosmetic industry. By implementing a skin-on-a-chip within the human-on-a-chip system, it could be validated whether it is safe to put the new cosmetics on your skin without the need for animal testing. Likewise it could also be used to test the safety of common household chemical products. It could be exploited to learn more about the effect of radiation on the human body. At last, it could be used for personalized medicine. Every person is unique, and this results in different reactions per person to the same medicine. By placing the cells of a specific patient in such a system, it could be used to determine which medicine is the most effective for that person and also check if that person would not have an adverse reaction to a certain medicine. This will make treatment for diseases more effective without discovering new medicines.[4, 6–9]

1.3. Current challenges

The organ-on-a-chip system still has some challenges like verification of the design, reliability issues, the need for high throughput, automation of the system, a flexible/modular design, interactions between the compound and the system, size, structural, biochemical and mechanical cues, up scaling of the manufacturing, and usability. But one of the main challenges is the real-time monitoring of cells.[7–11]

1.4. State of the art

It has been proposed to integrate electrodes on the membrane for real-time monitoring of the cells status. Commonly, this issue is tackled by integrating electrodes to perform TEER measurements,[12–14] manufacturing microelectrodes to monitor oxygen concentration and pH level,[15] manufacturing microelectrodes to monitor glucose consumption and lactate production,[15] using multi electrode arrays to measure the field potentials of cardiomyocytes,[12] and applying commercial available electrodes like tungsten microelectrodes in the device[16] or by making a modular platform to use commercial available sensors to measure microenvironmental parameters (e.g., pH, O2, temperature), electrochemical immunobiosensors for measuring soluble biomarkers, and miniature microscopes for observation of the organoid morphologies.[17] A fully 3D printed heart-on-a-chip system with integrated sensors has already been developed. With the stress sensors they are able to measure the contractile strength of the heart cells. They developed six functional inks which can be printed with micrometer resolution. This organ-on-a-chip system does not have a membrane as discussed previously.[18]

1.5. Research question and project overview

This research can be formulated in one question. How is it possible to manufacture membrane scaffolds with integrated sensing functionality and with precise control over the pore diameter, pore location, and porosity with a suitable technology for mass manufacturing? The aim of this research is to design and manufacture a membrane scaffolds with integrated sensors, which could be applied in an organ-on-a-chip system. The conductive layer is integrated on top of the membrane, therefore, it will be located directly underneath the cell layer within the organ-on-a-chip system as graphically presented in the figure 1.1. This will make it possible to locally and real-time monitor the cellular behavior. The sensor will have an increased sensitivity due to the local sensing. This could be the solution for solving the current observability challenge. Aditionally, the integrated conductive layer can be used to provide electricial stimuli to the cell layer. To proof the concept, it has been decided to manufacture one integrated porous electrode which is electrical and electrochemical characterized to show its capability to give the cell layer electrical stimuli and for the application as biosensor.

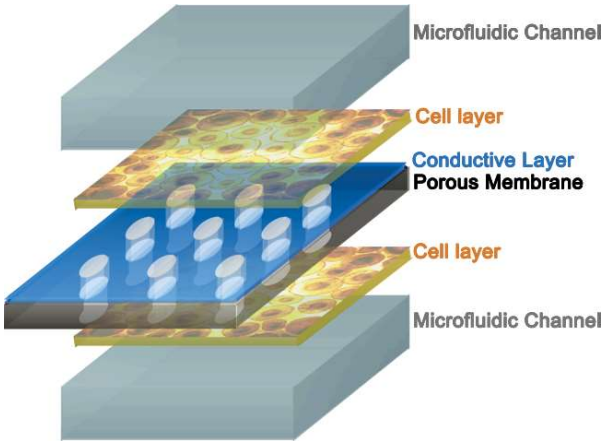

Figure 1.1: Schematic exploded view of a cross section of an organ-on-a-chip system containing a membrane scaffold with integrated conductive layer.

The main focus of this research is on the manufacturing part. There will be aimed to use as few as possible manufacturing steps to keep the production costs low, which makes it more appealing from a commercial standpoint. However, manufacturing sensing elements on the membrane with a manufacturing process which is scalable for mass production remains a challenge. In order to overcome this challenge,

solely polymeric materials are used to increase the opportunities for functional integration, while at the same time allowing for the translation of complex cleanroom manufacturing processes into mold-based replication techniques.[19]

1.6. Thesis Organization

The first part of the literature study consists of identifying the current challenges of organ-on-a-chip systems which leads to the project aim, presented in chapter 1. In the second part of the literature study, the requirements of the membrane and the kind of sensor is selected, which is discussed in chapter 2. The last part of the literature review leads to a manufacturing strategy to manufacture the organ-on-a-chip membrane scaffold with integrated conducting polymeric sensors. This is described in chapter 3. A roadmap with milestones was formulated as a checklist of tasks to complete for reaching the desired milestones. This is presented in chapter 4. The manufacturing of a membrane with integrated conducting porous electrode is presented as a paper in chapter 5. Because of the high quality of results, it is aimed to publish these results as a paper, from a manufacturing point of view, in the journal Microelectronic Engineering after graduation. The last part of this report contains a reflection about the work performed in terms of a line of thought, timeline comparison, contributions, and personal points of improved. This is discussed in chapter 6. The manufacturing methods are evaluated with a risk assessment and potential plans b are defined, which is discussed in appendix A. An additional literature review is done for selecting a material and manufacturing technique to create a soft working mold by replicating the master soft mold, described in appendix B. From the roadmap, it becomes clear that protocols had to be established of the individual manufacturing steps to be able to manufacture the membrane with integrated porous electrode. This work is described in appendix C and appendix D. The written algorithm used to characterize the morphology of the membrane is explained in appendix E. The developed permeability experiment to validate the fluidic functionality of the manufactured membranes is presented in appendix F.

2

Membranes requirements and sensor selection

2.1. Membrane requirements

Permeable supports, which have a microporous membrane to resemble the in vivo state for the growth of specialized cell types, have become a standard method for culturing cells. These membranes are a good reference for the membranes used in organ-on-a-chip systems, because organ-on-a-chip systems are an improved version of the in vivo cell culturing platform. That is why, the aim is to create a membrane which has the same pore diameters, pore densities, and thickness as commercial permeable supports. The pore diameter of commercially available permeable supports ranges from 0.4 µm to 8 µm. It depends on the application which pore size is desired. The commercial culture inserts are available in two thicknesses, 10 µm and 50 µm, which differs per pore size. The nominal pore density ranges from 6×10^4 pores/cm^2 to 1×10^8 pores/cm^2, which also differs for different pore sizes. This is summarized in table 2.1.[20–22]

Pore size [µm]	Membrane thickness [µm]	Pore density [pores/cm^2]	Applications
0.4	10, 50	2×10^6, 4×10^6, 1×10^8	Transport and Permeability Studies, Cell Polarity, Endocytosis, Drug Transport, Co-culture, Microfobial Pathogenesis, Tissue Remodelling, In Vitro Fertillization, Toxicity testing
1.0	10	2×10^6	Transport and Permeability Studies, Cell Polarity, Endocytosis, Drug Transport, Co-culture, Microfobial Pathogenesis, Tissue Remodelling, In Vitro Fertillization, Migration
3.0	10, 50	6×10^5, 2×10^6	Transport and Permeability Studies, Cell Polarity, Endocytosis, Drug Transport, Chemotaxis/Motility Studies, Co-culture, Microfobial, Pathogenesis, Tissue Remodelling, In Vitro Fertillization, Angiogenesis, Migration, Invasion, Toxicity Testing
5.0	10	4×10^5	Metastatic Potential and Invasion, Chemotaxis/Motility Studies, Migration
8.0	10	6×10^4, 1×10^5	Metastatic Potential and Invasion, Chemotaxis/Motility Studies, Migration

Table 2.1: Overview specifications of commercially available permeable supports

2.2. Biosensor selection

A biosensor is an analytical device which consists of a biological element and a transducer which are connected to a detector which processes the signal. The biological element is immobilized on the transducer and with the usage of a detector, the device can identify one or more specific analytes and their concentration. Different kind of biological elements can be used, like enzymes, antibodies, aptamers, nucleic acids, whole cells, and receptors. For transducers there are multiple techniques like, optical, colorimetric, mass/mechanical, magnetic, and electrochemical.[23, 24] First, a tranducer technique is selected. Followed by the selection of sensor type. Finally, a design is selected for the sensor.

2.2.1. Selecting a transducer technique

Optical The working principle of an optical transducer is quite simple. The color indicates for example, the pH level, the amount of oxygen or carbon dioxide.[25]

Colorimetric With a colorimetric transducer, the formed colored products are measured. These products are formed due to a reaction between the analyte and the biological recognition element.[24]

Mass/mechanical A mass/mechanical transducer measures the eigenfrequency of a crystal. The mass of the crystal increases when a reaction or binding of an analyte to the biological layer on the crystal happens. This causes the eigenfrequency to change and this can be used to identify the concentration.[24]

Magnetic The magnetic tranducer uses the magnetic properties of the element which is being measured.[24]

Electrochemical Electrochemical transducers have a high sensitivity, low power requirements, low costs, and uses quite simple detector instrumentation.[24]

For the application of this research, the optical transducer has its drawbacks. Because the sensors will have micrometer dimensions, you will need an optical sensing instrument to see the color of the optical transducer. Therefore the organ-on-a-chip system has to be removed from the incubator to have a look with an optical sensing instrument, which affects the ongoing experiment and is not user-friendly. The colored product formed by the colorimetric transducers can be seen with the naked eye but it cannot be used to measure something at different locations of the organ-on-a-chip system at the same time. The big drawback of the mass/mechanical transducer is that they are extremely complicated. The magnetic transducer has complications as well. While biomolecules have almost no magnetic properties, to use a magnetic transducer, magnetic micro/nanobeads have to bonded to the bio-molecules. Therefore, the best transducer for the application as biosensor within an organ-on-a-chip system is electrochemical, which can be used at multiple locations within this system at the same time.

2.2.2. Sensor type

The aim is to be able measure exocytosis and cell growth. This will verify if the cells are alive and if they are developing. The design of an exocytosis sensor and cell growth sensor is also less complicated than the design of an environmental sensor (like oxygen, pH, and temperature) because it does not need an additional layer to make it sensitive for what it needs to measure. Therefore, only bare electrodes are needed. This will reduce the number of manufacturing steps, and therefore, reduces the risks. Exocytosis can be measured using amperometric sensing. A constant potential is applied to the working electrode. And the current is measured over time. The trace can be related to the redox reactions, like exocytosis, which is happening at the electrode and electrolyte solution interface.[26–28] Cell growth can be measured by using electrochemical impedance spectroscopy. The resistance and reactance of a surface are monitored with electrochemical impedance spectroscopy (EIS). This is done by applying a small amplitude AC signal with a variable frequency and measuring the resulting current. The resistance and reactance are plotted in Nyquist plot, with plotted on the real and imaganary axis as a function of the frequency. The growth of the biofilm will decrease the charge transfer between the electrodes, which will result in an increased impedance. This can clearly be seen in a Nyquist plot as a curve shift on both axis.[26, 27, 29]

2.2.3. Design

Commonly, an electrochemical sensor consists of a working electrode (WE), a reference electrode (RE) and a counter electrode (CE). The WE is the location of the measurement. The RE electrode is used to maintain a constant reference signal which should be placed as close a possible to the WE because of the IR drop. The

CE supplies the needed current. It should be as big as possible to stop the CE reaction from limiting your cell current.[30] In a conventional sensor design, the area of the counter electrode, which is located around the working electrode, is relatively large. Miniturising such a design will result in a very small working electrode which only has space for a couple of cells. This will cause fluctuations among the experiment when measuring the impedance. A much higher sensitivity to impedance is demonstrated by using interdigitated electrodes.[31] A three electrode system can be used to measure the cell growth, while this setup measures the potential independant of changes that happen at the counter electrode. This is also the most common setup in electrochemistry. Excocytosis can be measured with a four electrode setup because this setup makes it possible to measure the solution itself instead of the reactions which are taking place at WE and CE.[32] In previous studies, disk-shaped electrodes were used to measure exocytosis. But the shape of these electrodes is limited to primarily address the cell-growth and not the axon-like outgrowths. Even when the radius was increased of the disk-shaped electrodes, it still cannot accommodate the long outgrowths of the cells. Therefore an interdigitated working electrode will be optimal and will be aimed for in this research.[33] To conclude, the same sensor, containing four electrodes, can be used to measure and monitor exocytosis using amperometric sensing and cell growth using electrochemical impedance spectroscopy. And by using interdigitated electrodes as working electrodes will lead to an increased sensitivity and will better accommodate the axon-like outgrowths of the cells than disk shaped electrodes.

3

Methods and materials selection

In this chapter, the manufacturing methods and the materials are selected to manufacture polymeric membranes with an integrated porous electrode.

3.1. Material electrodes

There are a couple of requirements which influence the material choice. The material has to be biocompatible because cells are going to be grown onto the membrane with the integrated porous electrode. This membrane with integrated porous electrode should not be soluble in water, which is important for its application. Finally, it is desired that the material has the highest conductivity possible. Because this will create a more sensitive electrode and reduce the losses of the electrical stimuli. There is decided to use a polymer, aside from exploiting the well characterized, simple and low cost techniques that can be employed in polymer manufacturing, the use of solely polymeric materials increases the opportunities for functional integration, while at the same time allowing for the translation of complex cleanroom manufacturing processes into mold-based replication techniques.[19] Common conjugated conducting polymer for biomedical applications are polypyrrole (PPy), polyaniline (PAni), polythiophene (PTh), and poly(3,4-ethylene dioxthiophene) (PEDOT). PPy and PTh have both a high electrical conductivity (up to 10×10^3 S/cm). But to make the conducting polymer non soluble in water, a composite has to be created. The best conductivity was reached with a composite of PEDOT and glycol (1486 S/cm).[34] This is in the range of metallic conducters, which have a conductivity in the range from 1 S/cm to 1×10^6 S/cm.[35] Treating PEDOT:PSS with ethylene glycol also reduced the water solubility drastically.[19]

Conductive polymers are gaining interest from acedemics and industry, in particular PEDOT:PSS.[36] Conductive polymers are increasingly used for sensing applications, drug delivery systems, biomedical implants, and tissue engineering.[34] PEDOT:PSS has already been reported to be able to use as a material to manufacture sensors to detect glucose,[37, 38] air humidity,[39], exocytosis,[40] and strain.[41] Additionally, it has been reported that it is possible to decouple a PEDOT:PSS layer with an additional polyaniline layer on top of it with a single soft embossing step to manufacture a wearable pH sensor.[42]

PSS is added to the PEDOT to make it soluble. Charge is conducted by the PEDOT molecules, ordered from the highest conductivity to the lowest conductivity, along the backbone by delocalized electrons, along the π - π stacking described by the hopping transport and along the side chains. The conductivity is improved with a the treatment with ethylene glycol because it makes the PEDOT domains smaller, more densely packed, it partially removes the non conductive PSS molecules, and reorientates the PEDOT molecules. This reorientation enhances the edge-on orientation, for which the backbone as well as the π - π stacking is oriented in the lateral direction of the PEDOT:PSS film. This results in enhanced conductivity in the lateral direction of the film, which is desired in our application.[43]

3.2. Membrane manufacturing techniques

The choice of a manufacturing method of the membrane depends on the material and the structure desired of the membrane. The electrode has to be manufactured as well which influences the selection of the manufacturing method. There will also be aimed to minimalize the number of manufacturing steps to keep the

production costs low, which makes it more also appealing from a commercial standpoint. Aditionally, a manufacturing method will be selected which is also possible to use on a large scale. First, an overview of the most common techniques for membrane obtaining will be given. And second, a suitable choice for the manufacturing method of the membrane with integrated sensors will be given.

Phase inversion In a controlled manner, the polymer transits from a liquid to a solid state thanks to a demixing process. This can be done in several ways: immersion precipitation, thermally induced phase separation, evaporation-induced phase separation and vapor-induced phase separation.[44, 45]

Sol-Gel process This process uses the hydrolysis-condensation reaction indirectly to obtain a network of oxide from molecular precursors. The sol-gel process makes it possible to obtain inorganic structures with a controlled porosity.[45]

Directional freezing Commonly within this process, a solution of polymer and water is frozen to create oriented crystallization. These crystals will create the pores within the polymer.[36]

Anadization Membranes have been manufactured by anodizing an aluminum substrate with a chemical which eventually etches channels straight down through the substrate.[46]

Immersion precipitation A polymer solution is cast on a support. Subsequently, it is immersed in a coagulating bath containing a non-solvent. In this bath, an exchange of solvent and non-solvent happens which forms the membrane.[44]

Interface reaction Interface reactions are mostly used commercially for obtaing thin-film membranes. It consists out of interfacial polymerization and polycondensation reactions.[45]

Stretching A polymer is heated above the melting point and extruded in thin sheet forms. Subsequently, it is stretched to create a porous membrane.[44, 45]

Track-etching The emission of an ion beam on the surface of a polymer film will create tracks. After it is placed in an acid bath, uniform cylindrical pores which are famous for its precise control of the pore size and pore density are created.[44, 45]

Electrospinning Between the polymer solution and the grounded collector a high voltage is supplied, this will cause the polymer solution droplets to overcome their surface tension and polymer fibers will be formed, which will form the membrane.[44]

Microfabrication Membranes can also be obtained by common microfabrication techniques like injection molding, pressure molding, hot embossing, and spin-coating.[45, 47]

Additive manufacturing With additive manufacturing, the membrane is created by building layers on top of each other. This enables the possibility to create membranes with different shapes, types, and designs. The highest possible resolution is 100nm, which is done by two-photon polymerization.[48]

If a pore is created on the location of a small part of an electrode (in the case of a decoupled interdigitated electrodes for example), the electrode will be decoupled from itself, and therefore the sensor will fail. Therefore all membrane obtaining methods can be rejected except microfabrication and additive manufacturing. Because those are the only techniques which makes it able to determine where the pores will be located. Both techniques make it possible to manufacture the membrane and the sensors in one manufacturing step. Additive manufacturing does not support the earlier selected material for the electrodes, and is not suitable for mass volume productions compared to microfabrication processes.[48] Of the four listed microfabrication processes, the most appealing one is hot embossing. While injection moulding and pressure moulding have higher fixed costs which could makes them cheaper when more than 1000-20000 pieces will be manufactured. The exact number depends on multiple factors like materials used and overall design. With the spin coating process there are some technical difficulties regarding removing the manufactured membrane from the substrate due to the pillars which are needed to create the pores. Hot embossing will be used to be able to manufacture the membrane and electrode in one manufacturing step. This improves the manufacturing throughput and the eliminates the risk of alignment problems.[19, 42, 44, 45, 47, 49, 50]

3.3. Techniques for through-hole hot embossing

There are multiple techniques for the molding of through-holes. Reactive ion etching and controlled fracture of the residual layer are post-processing methods, which means that first are molding step is done and after that, a second (post-processing) step is performed which removes the residual layer to create through-holes. All the other techniques listed in this section, the through-holes are created during the imprinting step.[51]

Reactive ion etching Ions are used to etch away the residual layer. This can be done from the top with an etching mask or from the bottom. This is a time-consuming method.[51]

Controlled fracture of the residual layer The microstructures which will create the holes have an extra circular ring on top of it. This will create a groove in the residual layer during the molding step. In the post-processing step, the residual layer can be removed by controlled fracture due to the groove.[51]

Molding on a stack of foils This technique creates a complete displacement of the residual layer by embossing freestanding structures of mold inserts into modified substrates. A relative high load is needed to accomplish this. Therefore the risk of damaging the structures increases and a proper selection of materials is needed.[51]

Molding onto soft metal substrates A soft metal substrate is created by adding a flexible layer on top of the regular metal substrate plate. This makes it possible to completely displace the residual layer. It has the advantage that no graded structures are needed in the mold, and therefore the mold can be manufactured by lithographic processes. This technique has two main problems. The metal foils cannot be used twice because the mold leaves imprints on it. And the other problem is that the replicated part has to be demolded manually due to the lack of the adhesion between the metal foil and the residual layer.[51]

Multilayer molding Instead of using a substrate which contains one layer of polymer, a second layer of polymer is placed underneath it. The microstructures which create the through-holes are pressed down through the first layer of the polymer into the second layer. The advantage of this technique is the maintenance of the adhesion on the substrate plate, therefore it can be demolded in the vertical direction. Because of the needed adhesion between the two layers of polymer, only selected material combinations can be used. Because of the strong adhesion between the two polymers, the first layer has to be peeled off.[51, 52]

Hot punching Hot punching is a two-step molding process. First, a polymer with a high melting temperature is molded with an one-sided embossing process. Subsequently, a thin film of polymer with a low melting temperature is placed on top of the molded layer of polymer. The thin film polymer is then punched between the one-sided mold and the polymer with the high melting temperature. The residual layer is punched into this polymer.[51]

To have a minimal number of manufacturing steps, a method which requires a post-processing step to create through-holes will not be used. The mold for the molding onto soft metal substrates cannot be used twice due to the damage. So, for each embossing step, a new mold is needed which is not commercially appealing. Molding on a stack of foils is a sensitive process and that will introduce a lot of risks. The hot punching process has a lot more steps than the multilayer molding method. Therefore the multilayer molding method is selected. Because of the selected method, the imprinting step is called nano imprint lithography.

3.4. Techniques for peeling off the membrane

There are two main techniques for peeling of the membrane, manually and chemically. Two layers of polymer can be peeled off manually with the help of some tools like a scalpel[47] or with the help of tape.[53] Or, the second layer of polymer can be completely dissolved with a chemical solvent.[54, 55]

It is prefered to dissolve the complete second layer of polymer because, in comparison with manually peeling it off, it reduces the risk of fracture and it is easier due to its small dimensions. Also, it is easier to be scaled to be used for mass production.

3.5. Material substrate

While the membrane is going to be used in a microfluidic device, it is useful to look at commonly used substrates for polymeric microfluidic devices. This will give a decent overview of possible polymeric substrate materials which could be used for the membrane with integrated porous electrode. These can be divided into the following categories: UV-curable, paper-based, foil-based, shrink film-based, and lithography-based. First, these will be discussed. And subsequently, a material will be selected within one of these categories.

UV-curable A resin is cured using ultraviolet light (UV light), which only takes few seconds to a few minutes. This makes it interesting for fast prototyping. But it is important to use the right amount of UV dosage. If the resin is not cured enough, it will result in a poor replication of the features. And if the resin is over-cured, it will be hard to demold or subsequent bond. Aspect ratios of 3.5:1 can be obtained using this method. UV-curable materials are Norland 63, Polyacrylate (PC), thermoset polyester substrate (TPE), polydimethylsiloxane (PDMS), polyurethanemethacrylate (PUMA), Ormocomp, and SU-8. Where PUMA is the only USP VI graded material.[56]

Paper-based Paper is patterned with hydrophobic walls or hydrophilic channels to create a microfluidic device. By stacking different layers of paper on top of each other, 3D structures can be obtained. Materials used for these kinds of paper-based devices are Whatman #1, Kimwipe, paper towels, coffee filters, and TechniCloth. None of these are USP VI graded.[56]

Foil-based Foils are less than 500 µm thick and flexible. Materials that can be used for foils are: polyethylene (PE), polystyrene (PS), polyethylene terephthalate (PET), polypropylene (PP), polycarbonate (PC), polymethylmethacrylate (PMMA), polydimethylsiloxane (PDMS), cyclic olefin polymers and co-polymers (COP and COC), and thermoset polyimide (PI). Some of the COC/COP materials that are manufactured by TOPAS and ZEONEX are USP VI graded.[56]

Shrink film-based First, multiple heat-shrink films are patterned on the millimeter scale. Subsequently, these films are stacked on top of each other. And finally, they are shrunk with a controlled temperature ramp, which makes the films shrink up to 95%. Channels of 95 µm were successfully manufactured using this method. Materials which can be used as a heat-shrink film are polyvinyl chloride (PVC), polystyrene (PS), and polyolefins. Heat-shrink films are commonly used for packing instead of microfluidic devices. [56]

Lithography-based Parylene is a transparent polymer commonly used as a biocompatible coating. It is USP VI graded and successfully implemented in rabbits for more than six months. Parylene can also be used as a barrier against dye absorption or oxygen permeation. It is not used to construct a monolithic device. Lithography processes are used to pattern parylene onto a device or a part of the device.[56]

Paper-based, shrink film-based, and lithography based materials are not suited for the application of the membrane with integrated porous electrode while it cannot be used with the selected imprinting step. And UV-curable materials are really sensitive to the UV dosage which is a big drawback. So for creating the membrane, a foil-based material is selected.

Subsequently, a material has to be selected. PDMS is one of the most popular materials used for soft lithography. It has higher oxygen and carbon dioxide permeability than any other polymer, and it is optically transparent. But it does not resist pressure above a few bars, swells in organic solvents and surface treatments are often unstable over time. Rigid polymers like PMMA and PC can be used to make less flexible structures but have a low stability against organic solvents. Cyclic olefin polymers and Co-polymers (COP and COC) have become more common materials for microfluidic chips. COCs/COPs are hydrophobic, absorb < 0.01 % water which is four times less than PC and ten times less than PMMA. COCs/COPs are highly resistant to chemicals including polar solvents but it is attacked by non-polar organic solvents like toluene and hexane. The high chemical resistance makes them suitable for organic electrochemical applications. And they are highly transparent in the visible and near UV regions of the spectrum. COCs/COPs also have great electrical properties, they have good insulating properties (a volume resistivity of more than 1×10^{16} Ω cm), a high dielectric breakdown voltage (30 $kV\,mm^{-1}$), a dissipation factor below those of PS and PP, and it is less depended on temperature than the dielectric constants of PP and other olefinic materials. Also, they have high biological inertness that makes them suitable for biomedical applications. To eliminate risks it is useful to use a material which is already certified by the USP's biocompatible guidelines to use for medical devices. And this keeps it also more appealing to be commercialized. This leaves the choice between TOPAS and ZEONEX,

which both have COCs/COPs with almost the same general physical (including impact strength) and optical properties. They have both a high electric volume resistivity (>1×10^{17} Ω cm). The only difference is that the COCs from TOPAS have a higher tensile strength, that is why a COC of TOPAS will be used. Because it can handle more stress which can occur in an organ-on-a-chip device.[57–60]

3.6. Material sacraficial layer

A lot of materials are possible to use as a sacrificial layer. For example, hydrofluoric acid (HF) is used to etch silica, metal oxides, and organic polymers. Due to its poor selectivity, it limits its use as a solvent for a sacrificial layer. Aluminum can be etched with an HF-free solvent and porous silicon is etched with KOH. Reactive ion etching (RIE) can be used to etch away organic polymers but has a poor selectivity like HF. Photoresists (like polymethylmethacrylate (PMMA), diazonapthoquinonenovolac (DNQ-novolac), and epoxies (e.g., SU-8)) can be dissolved by developers (like acetone, aqueous tetramethyl ammonium hydroxide (TMAH), and propylene glycol methyl ether acetate (PGMEA)) or by thermal degration. But these removal steps are incompatible with many organic polymers.

All the described solvents, used to dissolve the sacrificial layer, have some disadvantages. There are, for example, problems with using acetone while it also dissolves PEDOT:PSS. The PEDOT is going to be treated with glycol to ensure that it does not dissolve in water. To eliminate the risk of also dissolving the PEDOT, a polymer which dissolves in water will be used as a sacrificial layer. This developer is also the cheapest one in comparison with the earlier mentioned ones, has good selectivity due to its mild environment, avoids the use of toxic developers which can cause serious health hazards, and does not require a cleaning step after dissolving the sacrificial layer. Poly(acrylic acid) (PAA), Dextran, poly(methacrylic acid), poly(acrylamide), poly(ethylene imine), poly(vinyl alcohol), poly(ethylene oxide) 2 kDa, poly(ethylene oxide) 100 kDa, Chitosan, and Sucrose are all water-soluble polymers. But PAA and Dextran are the only two polymers which have a homogeneous film after spin-coating, still only soluble in water before photolithography, and after photolithography.[53, 61, 62]

PAA has the advantages over Dextran that it is more stable in a wide range of solvents, and has a faster etching rate (750 µm min^{-1}).[53, 61] Therefore, PAA is selected as material for the sacrificial layer.

3.7. Substrate preparation

Techniques for thin polymer films fabrication, which will be used to manufacture the multilayer substrate, are briefly discussed in this chapter. From which a final thin film fabrication technique is selected.

Casting This is the easiest process. A solution is cast on a horizontal substrate and dried. But there is a lack of control of the thickness of the layer.[63]

Spin coating A coating solution is applied on a substrate, which, by rotating the substrate, spreads the liquid over the substrate due to the centrifugal forces. It can also be applied while the disk is already spinning. A lot of material is lost because it is ejected during the spinning of the substrate. But it has the advantages that it creates highly reproducible formations of films which are very homogeneous over a large area.[63, 64]

Doctor blading A blade is placed close to the surface of the substrate that has to be coated (typically 10 µm to 500 µm). The coating solution is placed in front of the blade. Subsequently, the blade moves over the substrate and nicely spreads the coating solution over the substrate. This process has good controllability of the thickness of the film and less material is lost in comparison with the spin coating process if it is done by an experienced user. However, in practice, a lot of material is lost and it takes some time to find the right parameters. In comparison with spin coating, it is a relatively slow process and it is harder to create a homogeneous film with high concentration solutions.[63]

Knife-over-edge coating This process is similar to doctor blading. But instead of moving the blade, the substrate is placed on a roller which moves.[63]

Meniscus coating The difference between meniscus coating and knife-over-edge coating is that the metering of the ink is done by a separate roller.[63]

Slot die coating The substrate is placed on a roller. And a nozzle dispenses the coating solution in a line onto the substrate, which makes it well suited for creating stripes of different materials onto a substrate.[63]

Gravure coating This process uses two rollers. One contains the substrate and the other is the coating roller. The coating roller is engraved with the desired pattern for creating patterned coatings. The roller is partly immersed into the coating solution so that no ink has to be deposited separately onto the substrate.[63]

Curtain, multilayer slot and slide coating This is the most complex and expensive coating technique. It has the ability to create 18 different layers on top of each other simultaneously. The ink is pushed through a holder from which the different layers will flow on top of eachother. This curtain of liquid ink then falls on top of a web (curtain coating), is pressed on a roller (multiple slot coating), or slides against a roller (slide coating).[63]

Screen printing This complicated process needs a flexible screen, which contains the negative pattern of where the coating should be deposited, which is mounted under tension in a frame on top of the substrate. The coating solution is placed on the screen and the squeegee presses into the screen. At the locations of the holes in the screen, the coating solution will be pressed onto the substrate, forming a film.[63]

Inkjet printing Inkjet printing is depositing a specially formulated ink onto a substrate. This is an additive process which has some interesting printable materials like conductive materials, polymers, silicon nanoparticles, and isolating materials. The diameter of one drop of the printable material is typically less than 40 µm.[65] State of the art inkjet printers, for the creating of micro parts, have a resolution of 20 µm. A wide range of materials can be used for this process. But there is a need for support structures for creating 3D micro parts and it is a sensitive process.[66] A minimum feature size of 20 µm to 50 µm can be obtained. Using an aerosol printing system, feature sizes as small as 5 µm can be obtained.[63, 67, 68]

Pad printing A silicone rubber stamp is used to transfer the motif from a gravure to the substrate. This technique is only suited for small areas to create full 2D printed patterns.[63]

Chemical vapour deposition Chemical vapor deposition (CVD) is normally not possible for polymers due to the high temperatures which damage the functional groups of the polymer. But by modifying the process, polymers can be deposited at low temperatures. Some of these modified processes are plasma-enhanced CVD, photoinitiated CVD, hot-filament CVD, initiated CVD, vapor deposition polymerization, molecular layer deposition, and oxidative CVD. It has the advantage that it does not use any solvents to deposit the polymer onto the substrate, and can be scaled-up to be used for mass production. [69]

Spray coating The coating solution is pushed through a nozzle by compressed air, creating a flow of coating solution droplets mixed with air. The nozzle is moved around above the substrate surface to cover the complete surface. The temperature of the substrate surface is controlled by a hot plate.[64]

Bar-coating In this process a coating solution is placed on the substrate. A bar, with a certain load, on one side of the substrate is swiped to the other side. Which creates a thin film on top of the substrate. It shows good application prospects because it does not waste as much coating solution as spin coating. But further investigation is still needed of the coating conditions.[70]

Dip-coating A substrate is submersed for a certain time in a coating solution. Subsequently, it is pulled out and cured to create a thin film onto the substrate.[71]

It is important to create a substrate with a polymer film which has an uniform thickness to not make the embossing step even more complicated than choosing a substrate fabrication method which also can be used for mass-production. A precise control of the thickness of the polymer layer is also more important than mass-production to be able to experiment and find an optimal thickness of the polymer layer for the membrane with the integrated sensor which can be reproduced without to much variation. That is why a spin coating process is selected to manufacture the substrate, it has precise control over the thickness, and because of its highly reproducible formations of film which is very homogeneous over a large area.

3.8. Master mold manufacturing

There is looked into techniques for to manufacture the master mold to be able to select the best suiting one for this research.

Photolithography A light-sensitive chemical, called photoresist, is placed on a substrate. Subsequently, the photoresist is illuminated through a photomask. The photomask contains the design which is desired onto the substrate. The commonly used lightning is ultraviolet light with wavelengths ranging from 193 nm to 436 nm. The exposure chemically modifies the photoresist at certain areas due to the photomask. These parts will be soluble or insoluble in the developing stage. This depends on if a positive photoresist or a negative photoresist is used. It can create micro parts with a layer thickness of 1 µm to 10 µm. It has a high repeatability but limited materials can be used. The minimum feature size is in the order of a 15 nm.[65, 66, 72]

Depth lithography Depth lithography started in the early 80's to create high aspect ratio structures by using the same kind of process as photolithography but instead of ultraviolet light, X-rays were used instead. This technology is called LIGA. A special photoresist was developed, SU-8, which enabled the fabrication of high-aspect-ratio structures with ultraviolet light. Structures with details in the submicron range can be manufactured using LIGA due to the use of X-rays.[65, 67]

Etching Etching is the process of chemically removing material. Two main parameters characterize the etching process, selectivity and anisotropy. The selectivity determines which materials will be etched at which rate. By choosing the right material for the mask layer and the layer which will be etched, just the desired material will be etched at the desired location. The anisotropy determines if the etched layer is only etched in the direction away from the mask layer (anisotropic etching) or in all directions (isotropic), which means also under the mask layer. The feature size that can be obtained is in the nanometer range.[65, 73]

Selective laser sintering process A layer of powder is placed on a substrate, and a high-temperature laser will locally heat up the powder to sinter the layer of powder. When the layer is produced, a roller spreads new layer of powder on top of it to create the second layer. State of the art selective laser sintering machines can produce microcomponents with a resolution less than 30 µm and can create microparts with metal features of above 100 µm. For this high-temperature process, you need fine powders to get to this kind of resolution.[66, 74]

Selective laser melting process This process is very similar to the selective laser sintering process. Selective laser melting uses a higher energy density laser to fully melt the powder to create much denser microparts. A state of the art machine can create micro parts with a size of 40 µm and a thickness of 20 µm.[66]

Laser micromachining A laser is focused on the substrate, consisting out of a bulk material, and it sends out short laser pulses. The substrate will heat up so much locally, due to the absorption of the laser photons, that the material will melt, evaporate, or sublimate. Different kind of lasers are used for this kind of process, like microsecond carbon dioxide lasers, nanosecond solid-state lasers, and femtosecond solid-state lasers. Feature sizes down to 10 µm can be obtained.[65, 67]

Inkjet printing This process is explained in section 3.7.

Three-dimensional printing process This process is based on inkjet printing. A layer of powder is placed on a powder bed. Drops of binder material are deposited onto this layer. Multiple layers will create the final micro part. No support structures are needed. With state of the art machinery, a resolution of 20 µm can be obtained but the minimum feature size is 200 µm for this low-temperature process.[66]

Two-photon polymerization process/multi-photon polymerization In this process, two lasers are used to locally polymerize the photoinitiator which needs two photons, within a timewindow of 1 femtosecond, to initiate polymerization. Therefore, this will propably only happen at the focal point of the laser which enables a high resolution and a relative small minimum feature size. A feature size of 30 nm was reported for SU-8 photoresist. And a minimum feature size down to 120 nm was obtained with photopolymers. Using multi-photon polymerization minimum feature sizes of submicron dimension can be obtained.[66, 75–77]

Micromaching techniques Another way to manufacture the master mold is to process a piece of substrate material by downscaled macro processes like micro grinding, micro drilling, and micro milling. This kind of techniques have a minimum feature size of 25 µm.[65, 67]

Microelectrical discharge machining The electrical discharge machining uses a tool electrode which is in the negative shape of the desired structure (die-sinking EDM), a microwire (micro WEDM), a rod (micro EDM-drilling which is further developed into micro EDM-milling), or a grinding disc (micro-electrical discharge grinding). It is placed in a bath filled with a dielectric fluid together with the substrate. The tool electrode and the substrate are separated by a small gap. An electric discharge from the tool to the substrate will cause the substrate to locally evaporate or melt in the shape of the tool electrode. With micro-wire EDM, 2.5D structures of 1 µm with high-aspect-ratios can be obtained. Micro-diesinking can vary in width from 20 µm to 40 µm, have channels of 20 µm, and corner radii of 10 µm. The deviations of contouring are ~1 µm. With EDM micro-electrical discharge drilling minimal diamter of 2.9 µm is achieved. And for micro-electrical milling an electrode of 100 µm can be used. With micro-electrical discharge grinding, 2.5D structures with a minimum structure width of 70 µm can be created.[65, 67]

Fused deposition modeling and extrusion-based techniques A nozzle deposits material in a continuous flow onto a printing bed or onto the micro part itself. This can be done by melting the material or without melting the material. Precision extrusion deposition, 3D fiber deposition, precise extrusion manufacturing, and multiphase jet solidification are additive manufacturing techniques which melt the material. Pressure-assisted microsyringe, low-temperature deposition manufacturing, 3D bioplotting, robocasting, direct-write assembly, and solvent-based extrusion freeform are the most common additive manufacturing techniques which do not melt the material. The fused deposition modeling process is a relatively easy process with high operating temperatures. And a minimum feature size of 45 µm can be obtained.[66, 76]

Laminated object manufacturing process A laser beam cuts out a profile from a sheet which will be one layer of the final micropart. The different layers are glued to each other by a heat-activated plastic which is plated on one surface of the sheet. The best resolution which can be obtained for this kind of process is 50 µm and the minimum feature size is limited to 80 µm with a layer thickness of 30 µm to 1.3 mm or even more. This process can create fully dense microstructures with high mechanical strength but post-processing is required.[66]

Laser chemical vapor deposition process The substrate is heated selectively by a laser beam to locally convert gaseous reacts into thin solid layers. It has a resolution of 1 µm with a low deposition rate. A controlled atmosphere chamber is required for this process. And a minimum feature size down to 40 µm can be realized with this technique.[66, 76]

Focused ion beam direct writing This process is similar to the laser chemical vapor deposition process, but instead of a laser beam, it uses a focused ion beam. The microparts manufactured by this process can have features as small as 80 nm and a thickness of 10 nm. It is a slow, high resolution, and sensitive process which is commonly used for repair work and low volume production.[66]

Electrochemical fabrication process The electrochemical fabrication process is based on multilayer electrodeposition and planarization of at least two metals, one structural material, and one sacrificial material. The structutural material will be the final micropart. First, the sacrificial layer is electrodeposited using instant masking. Subsequently, the mask is chemically removed and the structural layer is deposited into the area where the mask is removed. The structural material fills the gaps between the sacrificial layer. Subsequently, both layers are planarized to the same level. Multiple layers will form together the micro part. The thickness of one layer can range from 2 µm to 25 µm. And the smallest feature size possible is 20 µm. The maximum height is 1.25 mm. Afterwards, the sacrificial layers have to be removed completely which is difficult in some cases.[66]

First, there is the requirement of creating pores with a diameter of maximum 8 µm. The techniques that are left which are able to do this are photolithography, depth lithography, etching, laser micromachining, inkjet printing, two-photon polymerization, multi-photon polymerization and, micro-wire EDM and micro-EDM drilling. To be able to integrate multiple sensors onto the membrane, much smaller features sizes are needed to create the small finger-like structures of the working electrode. Also the smallest diameter of pores

which are aimed for in this research is 0.4 µm. The techniques that are able to produce features with a minimum size of 0.4 µm are etching, two-photon polymerization and multi-photon polymerization. Keeping the research in mind, multiple master molds have to be manufactured to investigate the influence of different design parameters like the dimensions of the pin to create a thorugh hole for example. So, a fast process would be favored to perform an iterative process to determine the design parameters of the master mold. This expels cleanroom processes like etching. Left are two-photon polymerization and multi-photon polymerization. The Photonic Professional GT from Nanoscribe is a state of the art machine which uses two-photon polymerization which offers the highest resolution commercially available and with the fastest printing speed.[78]

3.9. Material master mold

In this chapter there is looked into different materials which can be used to manufacture the master mold with the Photonic Professional GT. A final material is selected afterwards.

IP Photoresists These are Nanoscribe's own developed photoresists. They have developed a total of 4 photoresists, IP-Dip, IP-L 780, IP-G 780, and IP-S. IP-Dip is index-matched resist formula to serve as immersion and photosensitive material with high resolution and medium shrinkage. It has a Young's Modulus ranging from ~0.8 GPa to ~3.6 GPa for ranging laser powers from ~5 mW to ~13 mW. The IP-L 780 is the highest-resolution resist formula and has low shrinkage. The Young's Modulus ranges from ~1.25 GPa to ~2 GPa for ranging laser power from ~8.5 mW to ~16 mW. A high-viscosity resist for complex 3D writing trajectories is the IP-G 780, which has a high resolution and low shrinkage. IP-G 780 has a Young's Modulus in the range of ~2.1 GPa to ~3.5 GPa for a laser power ranging from ~6 mW to ~13 mW. The IP-S is an index-matched resist for smooth surfaces and fast structuring of large 3D parts. It has a medium resolution and low shrinkage. Feature sizes down to 100 nm are possible with the IP photoresists. Also, it has the advantage of low proximity effect, low stress, little shrinkage, good adhesion to the glass substrates, easy handling because of the possibility of drop-casting of the photoresist, requires no pre-bake (IP-L 780, IP-G and IP-S), and requires no post-exposure bake.[79–81]

SU-8 The SU-8 photoresist is a serie of commonly used negative-tone resists. The different available by MicroChem are the 25, 50, 100, 2100, and 3000-series, which all have different viscosities. For the SU-8 2100, the Youngs Modulus ranges from ~2.3 GPa to ~3.1 GPa for a laser power ranging from ~2.2 mW to ~4.8 mW. Feature sizes down to 30 nm were reported for a two-photon polymerization process, but it was not manufactured with the Nanoscribe Photonic Professional GT. In combination with the Photonic Professional GT, it should have around double the feature size of the IP photoresists. This will be around 200 nm.[77, 79, 81, 82]

Chalcogenide Glass The biggest advantage of this material is its high refractive index of 2.45. This makes it possible to manufacture photonic waveguides, couplers, splitters, resonators and 3D photonic crystals. Feature sizes down to 200 nm are possible. And others features of the material that it has low stress and little shrinkage.[79]

Ormocere This is an organically modified ceramic. It has a Young's Modulus in the range of ~0.85 GPa to ~1.2 GPa in the laser power range of ~8.5 mW to ~15 mW.[79, 81]

PEG-DA with PETA This material combination is used as scaffolds for cell studies.[79]

AZ MiR 701, AR-P-3120, AZ 9260 These positive-tone resists are used for 2D structuring and electrodeposition in air voids.[79]

AZ 5214 And this a negative-tone resist is used for 2D structuring.[79]

AZ MiR 701, AR-P-3120, AZ 9260, AZ 5214, PEG-DA with PETA and Chalcogenide Glass are non-suitable or badly-suitable materials for the required application of a master mold. That is why they are also not used for these kind of applications. The IP photoresists and SU-8 both can create feature sizes which are small enough for the master mold to create a membrane with integrated porous electrode. Pillars which have to be pressed through the first two layers are going to experience a lot of force for their size. To minimalize the risk of fracture of those beams a material has to be selected with a high Young's Modulus. But the resolution is even more important while this will limit the sharpness of the tips of the printed pillars, which will increase the required puncturing force.[83] IP-L 780 is selected while it has a high Young's Modulus, the smallest possible features, the highest resolution, and there is in-house experience of creating structures with IP-L 780. This has the big advantange it reduces the risk because structures are already printed sucessfully with this material.

3.10. Electrical connections

To be able to characterize the integrated porous electrode, it has to be connected to detector instrumentation. There is a need for temporary electrical connection because during the prototyping process, different membranes with different integrated porous electrodes will be connected to different machines. This eliminates permanent electrical connections like wire bonding, flip-chip bonding, through-silicon-vias (TSVs) and soldering as possibilities for electrical connections. An overview of different kind of temporary electrical connections which are used for Lab-on-Chip devices in the past are edge connectors and sockets, spring-loaded contacts/pogo pins, flexible interconnections, wireless connection, and liquid metals. Lab-on-Chip devices are also microfluidic devices with electrical components. Because of the same environment, the overview can also be applied for the connection of the integrated porous electrode of the membrane.[84]

Edge connectors and sockets A well-known example of edge connectors and sockets is the USB port. The chip is slide into the socket and the mechanical alignment is reached by the sides of the chip. The contact pads of the socket and the chip are connected in this manner. Because all the electrical contacts have to be aligned next to each other it is limited how many electrical connections can be used, without getting extremely wide sockets and edge connectors. Which can be a porblem when you have a lot of interconnections.[84]

Spring-loaded contacts/Pogo pins Small pins are pressed vertically against the contact pad onto the chip, creating a temporary connection.[84]

Flexible interconnections A disposable layer with contact pads on top of it are created and placed on top of the electronics. The wires are connected to the disposable layer, and when new connections are required only the disposable layer has to be replaced.[84]

Wireless The power and signals could also be transmitted wirelessly using antennas placed onto the chip.[84]

Liquid metals A liquid metal alloy is injected through steel tubes to the microfluidic channels which aligned the contact pads of the CMOS chips. The tubes were left in the holes to function as electrical connections. [84]

Edge connectors and sockets are for this stage of prototyping unnecessary complicated while these also have to be manufactured as a (extra) part of the membrane with the integrated porous electrode. The same holds for wireless connections and flexible interconnections. This introduces unnecessary risks which are not desired. There is no need for allignment so there is no advantage of using the liquid metal model. So, spring-loaded contacts/pogo pins will be used while this is a straight-forward and simple electrical connection. Because a metal pin can be pressed easy against or even through the contact pad to create an electrical connection.

3.11. Overview of the manufacturing process

To conclude the literature review, an overview of the manufacturing process is given in figure 3.1. The overall manufacturing process consists out of four parts. The manufacturing of the soft mold which is manufactured out of IP-L 780 and by the Photonic Professional GT, figure 3.1A. The preparation of the substrate is done by spin coating a layer of TOPAS on a glass Petri dish. Subsequently, one one side a thick layer of PAA is spin coated and on the other side a layer of PEDOT:PSS is spin coated, figure 3.1D. The final multilayer substrate is shown in figure 3.1E. The multilayer substrate is imprinted with the manufactured soft mold, figure 3.1B. The pillars will puncture through the conductive layer and the substrate layer to create the through-holes. The smaller parts of the mold is used to decouple the conductive layer in the same step. After imprinting the mold is removed. The multilayer substrate is immersed in ethylene glycol to increase the conductivity and to decrease the water solubilty of the conductive layer. Finally, it is immersed in DI water to dissolve the sacrificial layer. The final product will be the membrane with integrated sensor, 3.1C. This process will be explained in chapter 5 section 5.4.

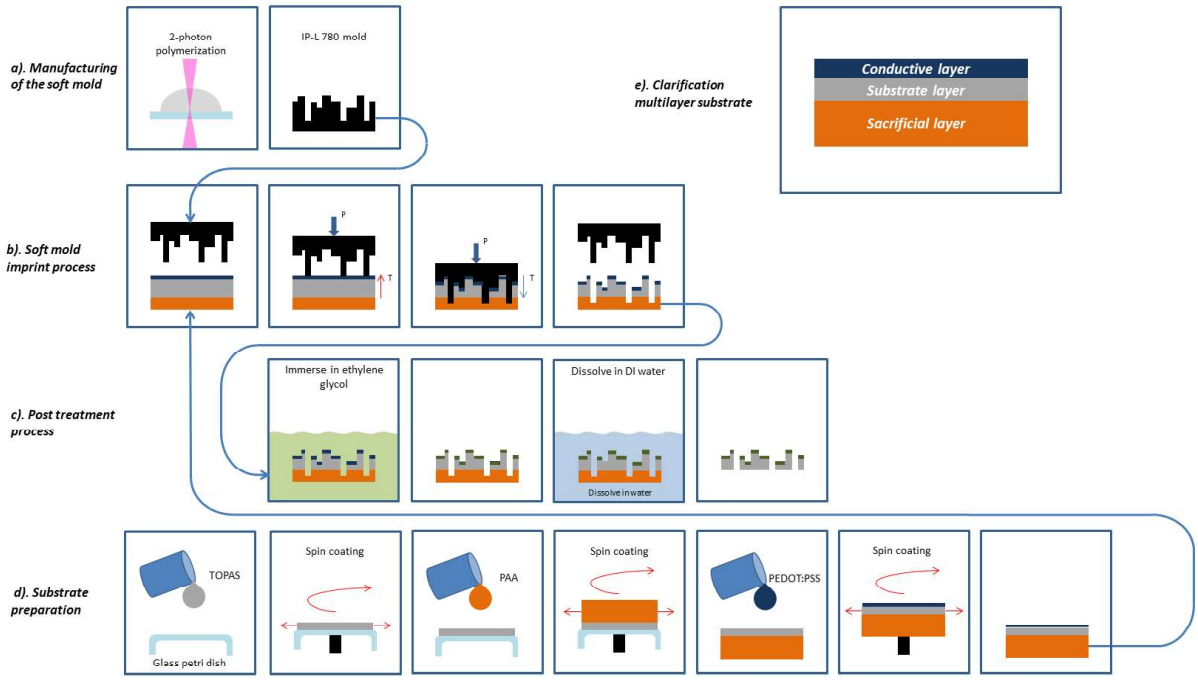

Figure 3.1: Schematic overview of the manufacturing process divided into four steps. A: The master mold is manufactured with a two-photon polymerization process. D: The substrate consists out of four polymeric layers, a conductive layer (PEDOT:PSS), a substrate layer (TOPAS), a sacrificial layers (PAA) and a support layer (TOPAS), which are spin coated (conductive layer and substrate layer) or casted (sacrificial layer) and placed on top of each other. B: The multilayer substrate is imprinted (soft NIL) to create the sensor and the through holes. C: A post treatment step is performed to enhance the conductivity of the conductive layer, to decrease the water solubilty of the conductive layer and to dissolve the sacrificial layer which helps the demolding of the soft mold.

4

Outline research

In this chapter, the outline of this research is discussed. In appendix A a risk assesment is done which can be used to create a roadmap to success which includes all the required tasks which have to be completed, milestones, and deliverables of this research. This is presented in figure 4.1. From the roadmap to succes two main topics can be identified. The first one is the determination of all required manufacturing and design parameters which are covered by milestones. The second is the characterization of the membrane and the integrated porous electrode/sensor. This is covered by deliverables.

4.1. Manufacturing and design parameters

First, the two milestones have to be accomplished to be able to successfully manufacture membranes with integrated porous electrode, as presented in figure 4.1. Therefore, multiple tasks have to be accomplished by experimentally determining these unknown parameters. Milestone one is accomplished when all manufacturing parameters are identified. The optimal printing parameters have to be determined to be able to print the soft mold. Protocols for spin coating TOPAS onto glass Petri dish and PAA onto TOPAS have to be established as well. A protocol for spin coating PEDOT:PSS is already available. All the layer thicknesses depended on the spin speed have to be evaluated. An imprinting protocol of the soft mold into the multilayer substrate has to be formulated. It has to be verified whether the adhession between the different layers is strong enough for the imprinting process. The influence of the ethylene glycol treatment onto the PAA layer has to be identified.

Subsequently, the influence of the shape and the minimal dimensions possible of the pillars for imprinting through-holes has to be identified. And, there has to be found what the minimum size of the electrodes which is possible. This is covered by milestone two.

4.2. Characterization of the membrane with the integrated porous electrode/sensors

With the identified optimal manufacturing parameters and optimal design parameters, a design of the membrane with integrated porous electrode can be made. SEM images of the membrane with integrated porous electrode can be made from the bottom to check if the membrane is indeed perforated. 4-point probe measurements of the conductive sheet have to be done. Finally, cyclic voltammatry and electrochemical impedance spectroscopy has to be performed to verify the electrochemical functionality of the conductive layer. This leads to deliverable one, figure 4.1.

If the membrane with integrated porous electrode is functioning correctly, more complicated tests can be done. The design of the electrodes can be imprinted into the multilayer substrate to check if this will result in working decoupled electrodes. The sensor functionality can be validated by testing it in different test solutions to see the response of the sensors. And finally, the membrane with the integrated sensors can be manufactured. Even more complicated experiments could be done like testing the membrane with integrated sensors with actual cells to test the biocompatibility and/or testing it in a dynamic environment, like an organ-on-a-chip system, because this may cause new complications.

Figure 4.1: Roadmap to success which contains all the required experiments, milestones, and deliverables

5

Manufacturing of a polymeric membrane with integrated porous electrode

5.1. Abstract

A manufacturing technology is proposed to manufacture polymeric membrane scaffolds for culturing of cells, tissues, and organoids with integrated sensor capabilities and fluidic functionalities. A multilayer substrate is imprinted with a soft mold to manufacture polymeric membrane scaffolds for culturing of cells, tissues, and organoids with integrated sensor capabilities and fluidic functionalities. Aside from exploiting the well characterized, simple and low cost techniques that can be employed in polymer manufacturing, the use of solely polymeric materials increases the opportunities for functional integration, while at the same time allowing for the translation of complex cleanroom fabrication processes into mold-based replication techniques. With this developed manufacturing technology, polymeric membranes with integrated porous electrode up to 1 mm by 1 mm in effective surface area, with a thickness of 10 µm, are manufactured with control over the pore diameter (as small as 400 nm), the porosity, and the location of the pores. The morphological characterization is done by scanning electron microscopy. The integrated porous electrode's performance is characterized electrically by a 4-point probe and electrochemically by cyclic voltammetry and electrochemical impedance spectroscopy. Showing the possibility to use the conductive layer to give cells electrical stimuli and for the use as a biosensor.

5.2. Keywords

Organ-on-Chip, porous membrane, micro-manufacturing, two-photon polymerization, conductive polymer, nano imprint lithography, electrode integration, characterization

5.3. Introduction

In 2015, the costs of developing and gaining market approval for a new drug is around $2.6 billion which is estimated to increase every year,[1] the development of a new drug takes at least 10 years,[2] and the overall likelihood of FDA approval for a compound from the first phase of the clinical trials is only 9.6%.[5] Organ-on-a-chip systems enable the possibility to experimentally model physiological micro-environmental conditions in order to develop new medicines in a cheaper, more efficient way, and eventually eliminating the need for animal models and opening up the possibility of personalized medicine. Applications of organ-on-a-chip systems are in the pharmaceutical industry, in the cosmetic industry, to test the safety of common household chemical products, and to learn more about the effect of radiation on the human body. An organ-on-chip system is a microfluidic chip which often contains a membrane, with living cells grown onto it, which separates the microfluidic channel in two. These kinds of systems are able to include the influence of chemical, electrical and mechanical interactions. [6–10]

There are two challenges in the design of organ-on-chip systems: the control of the membrane porosity[36, 85–87] and the real-time monitoring of cellular behavior and biological processes.[7–11]

Regarding the design there are several techniques to manufacture porous membranes based on phase inversion, Sol-Gel process, directional freezing, anadization, immersion precipation, interface raction, stretch-

ing, track-etching, electrospinning, microfabrication, and additive manufacturing.[36, 44, 45, 47, 48, 87] However, those techniques have several drawbacks such as high costs, complexity, or poor control over density and pore shape.

Regarding the real-time monitoring it has been proposed to integrate an electrode onto the membrane for real-time monitoring of the cell behavior. Commonly, this issue is tackled by integrating electrodes to perform TEER measurements,[12–14] manufacturing microelectrodes to monitor oxygen concentration and pH level,[15] manufacturing microelectrodes to monitor glucose consumption and lactate production,[15] using multi electrode arrays to measure the field potentials of cardiomyocytes,[12] and applying commercial available electrodes like tungsten microelectrodes in the device[16] or by making a modular platform to use commercial available sensors to microenvironmental parameters (e.g., pH, O2, temperature), electrochemical immunobiosensors for measuring soluble biomarkers, and miniature microscopes for observation of the organoid morphologies.[17]

However, manufacturing sensing elements on the membrane with a manufacturing process which is scalable for mass production remains a challenge. In order to overcome these challenges the use of solely polymeric materials increases the opportunities for functional integration, while at the same time allowing for the translation of complex cleanroom fabrication processes into mold-based replication techniques.[19]

Conductive polymers are gaining interest from acedemics and industry, in particular poly(3,4ethylenedioxythiophene)-poly(styrenesulfonate) (PEDOT:PSS).[36] Conductive polymers are increasingly used for sensing applications, drug delivery systems, biomedical implants, and tissue engineering.[34] PEDOT:PSS has already been reported to be able to be used as a material to manufacture sensors to detect glucose,[37, 38] air humidity,[39] strain,[41] and exocytosis.[40] Additionally, it has been reported that it is possible to decouple a PEDOT:PSS layer with an additional polyaniline layer on top of it with a single soft embossing step to manufacture a wearable pH sensor.[42]

Moreover, a single step-manufacturing technique is really appealing to reduce the manufacturing costs because it keeps the manufacturing steps to a minimum. Nano imprint lithography (NIL) is a high resolution and high throughput tool for micro- and nano-fabrication. The working principle is based on the transfer of a pattern from a mold to a thermoplastic substrate by increasing the temperature and applying a pressure. The mold is typically a silicon substrate patterned by standard lithography. However, the use of a soft mold, made of polymers, is emerging as an interesting alternative in order to reduce the manufacturing costs, to increase the process efficiency, and to reduce the probability of breaking the mold during the NIL process. This is called soft mold nano imprint lithography (soft mold NIL). The polymeric mold is manufactured by two-photon polymerization. This technique is a high-resolution additive manufacturing technique which allows to manufacture 3D custom design out of photopolymers with feature sizes down to 120 nm.[66] The light-curable polymer is locally polymerized on a glass coverslip in order to create the pattern by using a femto-second IR laser. Due to the freedom of the manufacturing method of the mold, it eventually results precise control over the pore diameter, porosity, and the location of the pores. This improves the selectivity of the membrane which is interesting for multiple applications like, precise separation, organic electronics, microfluidics, and tissue engineering.[36]

In this work, a high-resolution manufacturing technology based on 2-photon polymerization and soft mold nano imprint lithography is reported. The two-photon polymerization has been used for the realization of custom designed polymeric molds containing pillars with sharp tips. Those molds have been used in the soft mold NIL process to manufacture a polymeric membrane with integrated porous electrode made of a bilayer of PEDOT:PSS and thermoplastic cyclic olefin copolymers (COC, TOPAS). While the polymeric onductive layer is integrated on top of the membrane, it will be located directly underneath the cell layer within an organ-on-chip system. This will make it possible to locally and real-time monitor the cell behavior. The integrated porous electrode will have a higher sensitivity due to the local sensing. And the integrated porous electrode can also be used to provide electrical stimulus to the cell layer. The manufacturing of polymeric membranes with integrated porous electrodes are reported with an effective surface area up to 1 mm by 1 mm, a thickness of 10 µm, and circular pores of different diameters, in the range between 6.6 µm and 400 nm in diameter. The membranes are morphological characterized by imaging them by scanning electron microscopy from the non conductive side to simultaneously verify that the imprinted pores are indeed thorugh-holes. The electrode performance is characterized by 4-point probe measurements and electrochemically by cyclic voltammetry and electrochemical impedance spectroscopy to demonstrate its sensor functionality.

5.4. Materials and methods

5.4.1. Membrane manufacturing

Figure C.73 contains an overview of the manufacturing process which is divided into four steps:
a). Manufacturing of the soft mold
b). Substrate preparation
c). Soft mold imprint process
d). Post treatment process.

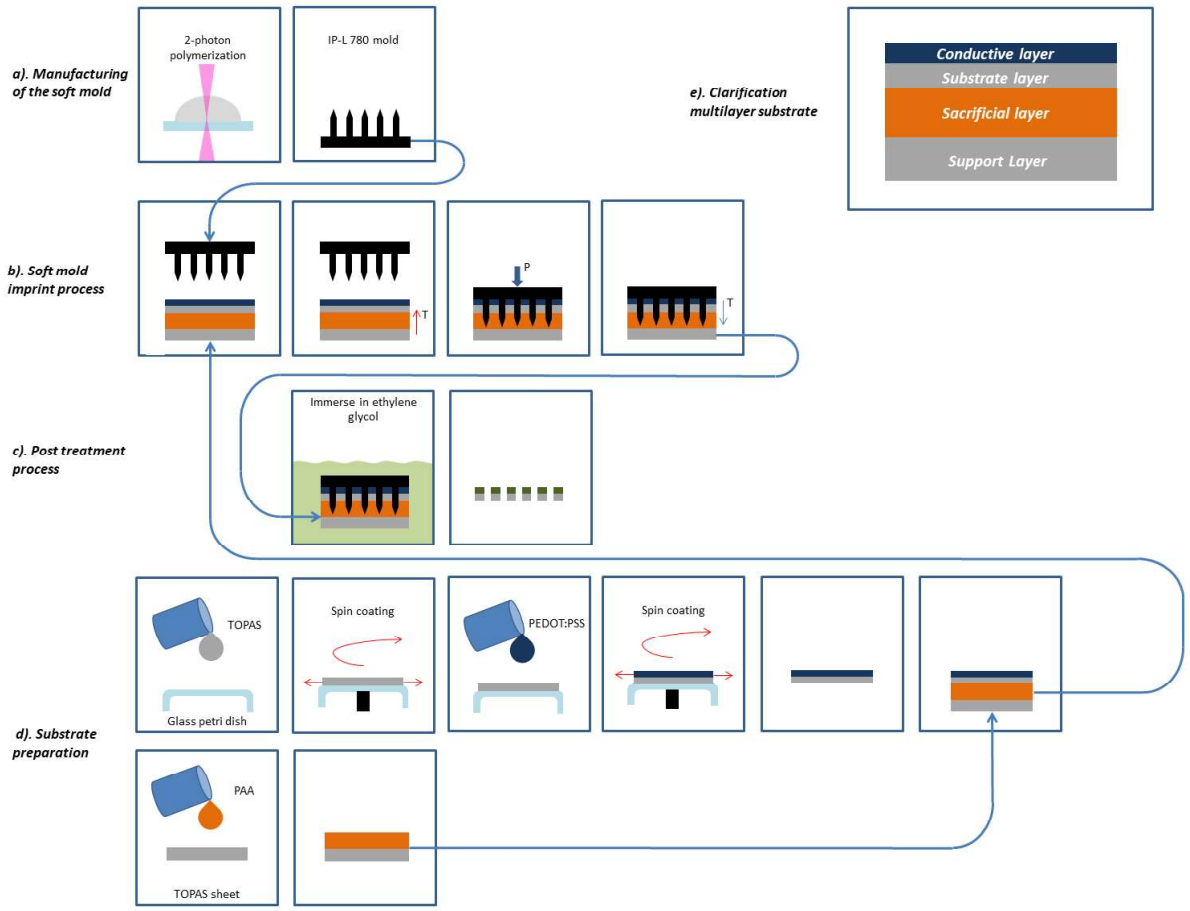

Figure 5.1: Schematic overview of the final manufacturing process divided into four steps. A: The soft mold is manufactured with a two-photon polymerization process. D: The substrate consists out of four polymeric layers, a conductive layer (PEDOT:PSS), a substrate layer (TOPAS), a sacrificial layers (PAA) and a support layer (TOPAS), which are spin coated (conductive layer and substrate layer) or casted (sacrificial layer) and placed on top of each other. B: The multilayer substrate is imprinted (soft NIL) to create the porous electrode and the through holes. C: A post treatment step is performed to enhance the conductivity of the conductive layer, to decrease the water solubilty of the conductive layer and to dissolve the sacrificial layer which helps the demolding of the soft mold.

Manufacturing of the soft mold. (Figure 5.1a)
A glass coverslip (Menzel Gläser) of 30 mm in diameter with a thickness of 0.17 mm +/- 0.01 mm from Thermo Scientific, is cleaned with acetone (EMSURE®, Sigma-Aldrich) and 2-propanol (Honeywell, Riedel-de Haën). A drop of immersion oil (Immersol^{TM} 518F, Zeiss) is placed on the bottom of the coverslip and a drop of IPL-780 (Nanoscribe) is placed on top of it. The coverslip is placed on a holder and placed in the Photonic Professional GT (Nanoscribe). A STL-file is created with Solidworks 2016 x64 edition (Dassault Systèmes SolidWorks Corp), converted into a job-file with Describe 2.2.4 (Nanoscribe), and printed with the Photonic Professional GT. Adaptive slicing is used for all models. It is printed in the conventional mode, and the following parameters are fixed: a hatching angle of 45°, a maximum slicing distance of 0.5 µm, a minimum slicing distance of 0.2 µm. The soft mold used to manufacture the membrane with 400 nm pores is printed with the 63x objective, a hatching distance of 2 µm, with a laser power of 22.5 mW, and a scan speed of 2500 µm s^{-1}. The

soft mold used to manufacture the membrane of 1 mm by 1 mm is printed with the 25x objective, a hatching distance of 0.5 µm, with a laser power of 22.5 mW and a scan speed of 10 000 µm s^{-1}. Afterwards, the coverslip with the printed structure on top of it is immersed for 25 min in propylene glycol monomethyl ether acetate, PGMEA, (≥ 99.5%, ReagentPlus®, Sigma-Aldrich), followed by 5 min in 2-propanol to remove the uncured resist.

Substrate preparation. (Figure 5.1d)
A glass bottle is cleaned with ethanol absolute (≥ 99.95%, EMPARTA®, Merck) and placed in the fumehood (Vinitex) to evaporate it for 1 h. Cyclic olefin copolymer granules (TOPAS 8007X-10, TOPAS) and toluene (Honeywell, Riedel-de Haën) are mixed in the bottle to create a 20wt% solution. The solution is placed in an ultrasonic cleaner (SHESTO SHE-UT8031-EUK) with full sinus waves for 15 min. Subsequently, the bottle is placed on an orbital shaker (IKA® VXR basic Vibrax®) at 2200 RPM for 10 min. This is repeated until the granules are dissolved, which can be observed by tilting the bottle and inspecting if there is any TOPAS left on the bottom. A glass Petri dishes (Ø60, DURAN Group) is cleaned with acetone and 2-propanol. The Petri dish are placed in the oven (Memmert UN30) at 150 °C for 15 min to dehydrate. It is placed in the fumehood to cool down to room temperature. The spin coating process consists out of two steps to get a TOPAS film of 10 µm. The first step has a spin time of 50 s at 3900 RPM. Subsequently, the sample is spin coated for 30 s seconds at 100 RPM. The accelaration for both steps is 250 RPM/s. 1 mL of the TOPAS solution is spin coated (Polos 150i), on the outside of the Petri dish, with a static dispense spin coating technique. The sample dried overnight in the fumehood.

The glass Petri dish with the 10 µm thick layer of TOPAS is treated for 5 min with oxygen plasma at 60 W (Diener Femto). 2 mL of poly(3,4-ethylenedioxythiophene)-poly(styrenesulfonate), PEDOT:PSS, (1.3 wt% dispersion in H_2O, Sigma-Aldrich) is dynamically dispensed on top of the TOPAS film during the spin coating process (750 RPM for the membrane with 400 nm pores is diameter and 1500 RPM for the manufacturing of a membrane with an effective surface area of 1 mm by 1 mm, 60 s, 1000 RPM/s). The sample dried overnight in the fumehood. This results in a PEDOT:PSS film of 0.07 µm and 0.2 µm.

A 30 wv% solutions of poly(acrylic acid), PAA, (average M_w 1800, Sigma-Aldrich) and DI water is prepared by mixing it on an orbital shaker at 2200 RPM until the PAA is completely dissolved. 1 mL of the solution, is dispensed on top of a TOPAS sheet (Thickness of 300 µm, glass transition temperature of 70 °C, microfluidic ChipShop). The thick layer of PAA is left to dry overnight in the fumehood.

The PEDOT:PSS and TOPAS films are placed, manually, on top of the PAA film and TOPAS sheet.

Soft mold Nano Imprint Lithography process. (Figure 5.1b)
The soft mold nano imprint lithography process is performed with a wafer bonder system (EVG 510, EV Group). The mold and the multilayer substrate were placed between kapton foil with on top two graphene sheets. A holding time of 10 min is used. A force of 4000 N and temperature of 120 °C is applied for the manufacturing of the membrane with 400 nm pores. To manufacture the membrane with a surface of 1 mm by 1 mm, a force of 3000 N and temperature of 140 °C is applied. Also, an anti-stiction layer (EVG) was spin coated at 2000 RPM for 60 s, rinsed afterwards with HFE7100 (HG Chemicals) and baked for 10 min at 120 °C.

Post treatment process. (Figure 5.1c)
The multilayer substrate is immersed in ethylene glycol, EG, (anhydrous, 99.8%, Sigma-Aldrich) until the sacrificial layer is completely dissolved and the soft mold is demolded from the multilayer substrate. The resulting membrane is dried overnight in the fumehood.

5.4.2. Membrane characterization

Morphological
The printed molds and the TOPAS side of the manufactured membranes are sputter coated (Quorum Technologies SC7620) with a 6.5 nm layer of gold/palladium (Au/Pd) which is imaged with a scanning electron microscope, SEM, (Jeol JSM-6010LA). A Matlab (R2016b) algorithm is written to find the number of pores, mean pore diameter, smallest pore diameter, largest pore diameter, standard deviation of the pore diameter, pore density, porosity, mean center to center distance, and standard deviation of the center to center distance. The RGB values below [45.5, 45.5, 45.5] of the SEM image are set to [10, 10, 10] and all the other RGB values are set to [200, 200, 200] to get a clear edges of the realized pores. The centers of the pores and their corresponding diameters are detected by circulair Hough transform. Delaunay triangulation is used to determine the average center to center distance of the pores. The scalebar at the bottom of the SEM images is converted

into coordinates in the matlab algorithm to be able to scale all the distances in pixels to the corresponding length by image segmentation. This algorithm is discussed in more detail in appendix E.

Electrical characterization
In the range from −0.3 µA to 0.3 µA in steps of 0.05 µA is the corresponding voltage measured of one of the manufactured membranes with an effective surface area of 1 mm by 1 mm by a 4-point probe (Signatone couple with a Keithley Sourcemeter 2400 and Nanovoltmeter 2182) after the post treatment of the membrane.

Cyclic voltammetry
A solution of 0.1 M KCl is prepared by mixing DI water with potassiom chloride, KCl, (minimum 99.0%, Sigma-Aldrich) on an orbital shaker at 2200 RPM for 10 min. Cyclic voltammetry is performed of one of the manufactured membranes with an effective surface area of 1 mm by 1 mm in the prepared 0.1 M KCl solution at different scan rates using a gold counter electrode (DropSens DRP-C223AT) and a Potentiostat (Metrohm Autolab B.V., Netherlands).

Electrical impedance spectroscopy
A solution of 10mM ferrocyanide/ferricyanide in 0.1M KCl is prepared by mixing DI water with potassiom chloride, KCl, ferricyanide (potassium hexacyanoferrate(II) trihydrate, Sigma-Alrich) and ferrocyanide (potassium hexacyanoferrate(III), Sigma-Aldrich) on an orbital shake at 2200 RPM for 10 min. Electrical impedance spectroscopy is performed of one of the manufactured membranes with an effective surface area of 1 mm by 1 mm in the prepared solution at 10 mV/s using a gold counter electrode (DropSens DRP-C223AT) and a potentiostat (Metrohm Autolab B.V., Netherlands). The equivalent circuit is fitted by the supplied Nova software of the potentiostat (version 1.10.1.9).

5.5. Results and discussion

As illustrated in figure 5.1E, the multilayer substrate consists of four layers, a conductive layer for the integrated porous electrode (PEDOT:PSS), an underlying substrate layer which will be part of the membrane (cyclic olefin copolymer, TOPAS). Underneath, there is a sacrificial layer (poly(acrylic acid), PAA) and a support layer (cyclic olefin copolymer, TOPAS). The multilayer substrate is manufactured by casting the sacrificial layer and by spin coating the conductive layer and substrate layer, schematically shown in figure 5.1D. The polymeric mold (photoresist, IP-L 780) is manufactured by a two-photon polymerization process, which enables precise control of the diameter, location, and density of the pores, figure 5.1A. With a soft mold NIL process, pillars with sharp tips puncture through the first two layers into the sacrificial layer to create the pores shown in figure 5.1B. Finally, illustrated in figure 5.1D, a post treatment is done by submerging the imprinted substrate in ethylene glycol (EG) to increase the conductivity of the conductive layer and to decrease solubility in water of the conductive layer.[19] It will simultaneously dissolve the sacrificial layer which helps the demolding of the soft mold.

Optimization of the soft mold printing parameters via two-photon polymerization
First, the optimal printing parameters to print the desired pillars have to be found. This is done by printing 400 nm pillars with varying base angles from 0° to 4° in steps of 1° and varying tip angles from 0° to 80° in steps of 10°. This can be seen in figure 5.2B. This matrix of pillars is printed with varying laser power from 17.5 mW to 30.0 mW in steps of 2.5 mW and varying scan speeds from 10 000 µm s^{-1} to 2500 µm s^{-1} in steps of 2500 µm s^{-1}. The overview of this is given in figure 5.2A. When too much dose is applied, a combination of a laser power which is too high and scan speed which is too low, the photoresist will start to boil which leads to partly or no printed pillars. This can be seen in the top of the SEM image in figure 5.2A. Therefore, the pillars printed with the heighest dose are printed last. The set of pillars which looks the closest to the modeled ones are presented in figure 5.2B. These are printed with a laser power of 22.5 mW and a scan speed of 2500 µm s^{-1}. Some of the pillars tipped over due to the capillary forces experienced between the pillars during the development process of the soft mold. The same approach is done to determine the optimal printing parameters of the pillars with a diameter of 8 µm. All the used parameters are the same as for the optimization of the 400 nm pillars except for the base angle which is varied from 0° to 40° in steps of 10° and the laser power which is varied from 17.5 mW to 30.0 mW in steps of 2.5 mW. An overview of all printed pillars with a diameter is shown in figure 5.2C. And the set of pillars which looks the most like the modeled ones is presented on the right of figure 5.2D. These are printed with a laser power of 25.0 mW and a scan speed of 2500 µm s^{-1}.

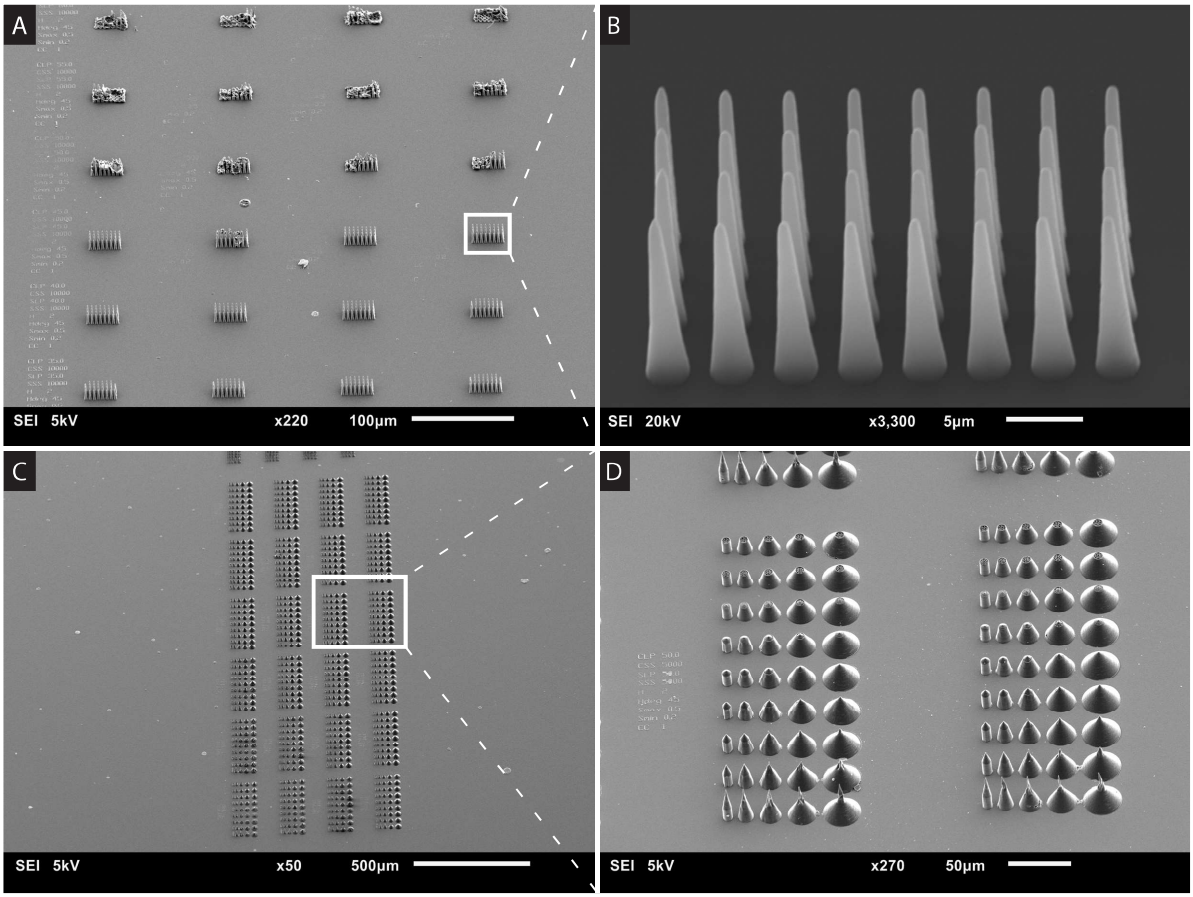

Figure 5.2: Results of the optimization of the soft mold printing parameters via two-photon polymerization. From left to right, the scan speed is varied, and from top to bottom, the laser power is varied. A: Overview of the printed pillars with a diameter of 400 nm with varying base angle and tip angle. B: Zoomed in on the set of pillars which looks the most like the modeled ones, printed with a laser power of 22.5 mW and a scan speed of 2500 µm s^{-1}. C: Overview of the printed pillars with a diameter of 8 µm with varying base angle and tip angle. D: Zoomed in on the set of pillars which looks the most like the modeled ones, printed with a laser power of 25.0 mW and a scan speed of 2500 µm s^{-1}.

Optimization of the soft mold Nano Imprint Lithography process

During the imprinting step, some pillars have the tendency to transfer from the soft mold to the multilayer substrate. This is not desired and, therefore, different imprinting protocols are tried to minimize the number of transferred pillars of which the results is presented are figure 5.3. The imprinting temperature, imprinting force, and holding time are varied while these have the biggest effect on the quality of the imprint.[88]

Regarding the imprinting of a membrane with a pore diameter of 400 nm, the used imprinting parameters are presented in figure 5.3A. The optimal imprinting parameters found are an imprinting force of 4000 N, an imprinting temperature of 120 °C, and a holding time of 10 min. This combination of imprinting parameters led to a low number of transferred pillars of which the experiments are presented in Appendix C. In the described experiments, it was also found that a minimal tip angle of 80° is required to puncture through the conductive layer and the substrate layer. All the pillars transferred with a holding time of 20 min, and therefore, the holding time is not altered for optimizing the imprinting parameters to imprint a membrane of 1 mm by 1 mm. The different combinations of imprinting parameters used to optimize the imprinting protocol to manufacture the scaled-up membrane is shown in figure 5.3B. An optimal imprinting temperature of 130 °C is found. An imprinting force of 3000 N results in a low number of transferred pillars. While the puncturing of the conductive layer also depends on the force applied,[83] the higher imprinting force of 3000 N is selected as the optimal imprinting force. The experiments performed to obtain figure 5.3B are presented in Appendix D.

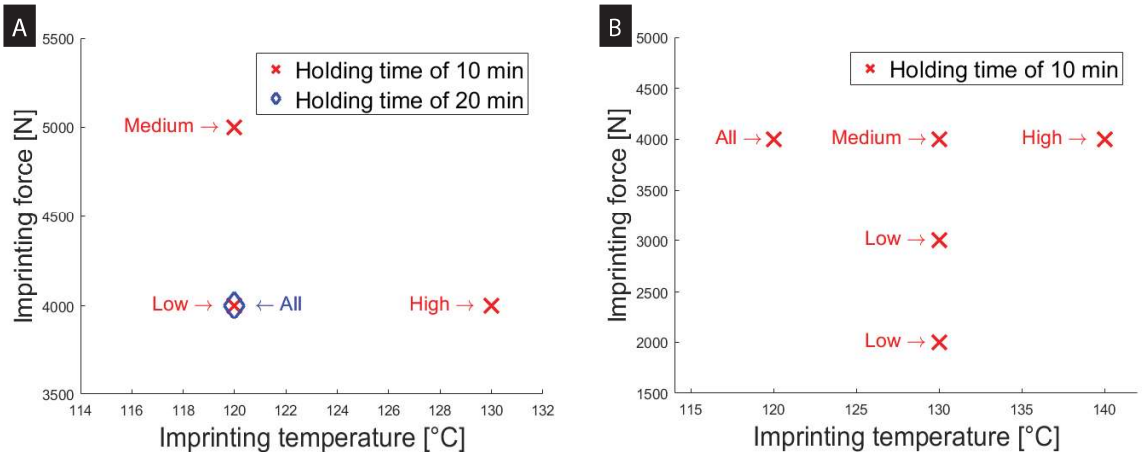

Figure 5.3: Two figures containing the imprinting parameters (imprinting temperature, imprinting force, and holding time) used to optimize the imprinting parameters per kind of manufactured membrane. Each point, which is a combination of the three imprinting parameters, in the figures contains a comment regarding the number of pillars that transferred. A: Figure regarding the optimization of the imprinting parameters used to manufacture a membrane with 400 nm pores. B: Figure regarding the optimization of the imprinting parameters used to manufacture a membrane of 1 mm by 1 mm.

Membrane manufacturing: Soft mold Nano Imprint Lithography

The first soft mold contains 8 rows of pillars of 400 nm in diameter, 16 µm in height, a tip angle of 10° and varying base angles from 1° to 4° in steps of 1°. A bigger base angle has two main advantages, it results in increased stiffness of the pillar due to the added material and increases adhesion between the pillar and the substrate because the surface of the pillar increases at the base. But it limits how close the pillars can be placed next to each other due to their larger diameter at the base of the pillar. The center to center spacing between the rows of pillars is designed to be 14 µm and the center to center spacing between the pillars in one row is designed to be, from the smallest base angle to the largest base angle, 13 µm, 14 µm, and 14 µm to keep the distance between the edges of the pillars at their base constant. The mold and the resulting membrane are presented in figure 5.4A and 5.4B. Because the membranes are imaged from the TOPAS side of the conductive membrane, it can been seen that the pillars punctured through the first two layers of the multilayer substrate. The pillars with the smallest base angle were able to successfully be demolded since there are no pillars to be seen in figure 5.4B.

Scaling up of the process

The process can be scaled up easily. Therefore, the second mold contains 32 by 32 pillars of 8 µm in diameter, 35 µm in height, center to center distance of 31 µm, covering an area of 1 mm by 1 mm, a tip angle of 10° and a base angle of 40°. The mold and the resulting membrane are presented in figure 5.4C and 5.4D. Because the membranes are imaged from the TOPAS side of the conductive membrane, confirming that the pillars went all the way through the first two layers of the multilayer substrate. A total of 173 through holes were found by the Matlab code of the 1024 pillars. This results in a pore density of 1.73×10^4 pores/cm^2 and a 16.9% success rate to manufacture through holes of the intended pores. This success rate can be explained by a couple of reasons. The tip is not a sharp tip because the top part shranked resulting in the small mini tip on top of the actual tip, as presented in figure 5.4E. During the imprinting step, the adhesion force of the pillars to the substrate just is not large enough to withstand the experienced forces. This causes the pillars to transfer from the mold to the substrate. Figure 5.4E shows that the edges of the cone are lifted from the substrate. This is due to the fact that the upward force of the structure due to shrinkage is larger than the adhesion force of the material to the glass coverslip. Because of this edge, some of the polymer during the imprinting process can get between the printed pillars and the glass coverslip. During the post treatment step, the pillars will get separated from the glass coverslip causing them to get stuck in the membrane, which can be seen in figure 5.4F. Futhermore, it shows that a lot of pillars just were not able to go through the the conductive layer and substrate layer of the substrate. Instead of puncturing those layers, they got pressed down. While these pillars pressed the layers downwards, the pillars were not able to fully puncture the layers which causes the pores not to be the aimed diameter of 8 µm. Therefore, the resulting mean pore diameter is 2.74 µm (standard deviation = 0.55 µm, smallest pore diameter = 2.35 µm, largest pore diameter = 6.63 µm), the porosity is 0.1%, the mean center to center distance of the pores is 70.83 µm, and the standard deviation of the center to center distance

is 51.98 µm.

Electrical and electrochemical characterization
Cyclic voltammetry (CV) was performed to analyze the redox reaction between the porous electrode and the solution. Figure 5.5A shows the redox activity of PEDOT:PSS films created with the described manufacturing technology. This shows that the conductive film is electrochemical active which is required to use this layer as part of a biosensor. The electrochemical characterization displays a quasi-reversible electrode behavior, illustrated by a shift in peak potential in an otherwise linear correlation between peak current and the square root of the potential sweep rate (as shown in the insert of figure 5.5A).

Electrochemical impedance spectroscopy (EIS) was used to investigate the electrochemical properties of the conductive membrane. The nyquist plot of the electrical impedance spectroscopy (EIS) of the conductive membrane which was preformed at 10mV/s in 10mM ferrocyanide/ferricyanide in 0.1M KCl is presented in figure 5.5B. The insert contains the fitted equivalent circuit. Normally, a Randels circuit is used, when the charge transfer is influenced by diffusion to and from the electrode, to decouple the various effects influencing the impedance of the cell. It consists out of a resistor in series which models the resistance of the electrolyte. The capacitor models the double-layer capacitance. In the parallel part of the circuit, the resistor models the charge transfer resistance and the Warburg element models the diffusion process of species into the electrode. This gives the well known shape of a semi circle at the higher frequencies and the linear part at the lower frequencies.[89] While the conductive layer contains pores, it effects the interface where the diffusion process takes place. This alters the slope at the lower frequencies, which will be a second semi circle instead which won't necessarily follows the 45 degree slope anymore.[90] To fit the data more accurately, a constant phase element is introduced in parallel to the Warburg element to be able to approximate the second semi circle at a different degree slope by a linear line. It is placed parallel, instead of replacing the Warburg element, to prevent the software from finding a local minimum during the fitting of the circuit. Preventing this will result in more accurate values of the resistors and the capacitor in the circuit. In the fitted circuit, the effect of the Warburg element can be neglected due to the small value of the Warburg constant (Y0 = 900 fMho) in comparison with the constant of the constant phase element (Y0 = 4.54 µ Mho).

A membrane with an effective surface area of 1 mm by 1 mm is evaluated by measuring the voltage/current curve with a 4-point probe after the post treatment step. The voltage/current curve is fitted by a linear line, with a coefficient of determination of 1.00, presented in figure 5.5C. The slope indicates a resistance of 80.0 kΩ which can be converted, by multiplying the resistance with $\pi/ln(2)$, in a sheet resistance of 363 kΩ/ sq.[91] This is more than the sheet resistance found in literature. This can be explained by the fact that the PEDOT:PSS film is thinner. The post treatment of the substrate after imprinting with EG increases again the conductivity.[19] The US cleaner has also a negative effect on the conductivity of the PEDOT:PSS layer, and therefore, decreasing the conductivity.

5.6. Conclusions

In conclusion, a high resolution manufacturing technology based on 2-photon polymerization and soft mold nano imprint lithography process is presented. These are well characterized, simple and low cost techniques that can be employed in polymer manufacturing, which makes it possible to translate complex cleanroom fabrication processes into mold-based replication techniques. Furthermore, the use of solely polymeric materials increases the opportunities for functional integration, like the integration of electrical functionality.

This technology is applied to manufacture polymeric membranes with an integrated porous electrode. It is demonstrated that there is control over the pore diameter (as small as 400 nm), the porosity, and location of the pores. This is due to the large freedom of the 2-photon polymerization process. Which has the ability to manufacture soft molds with freedom in the dimensions of the pillars, the number of pillars and location of the pillars. It is possible to scale this technology to large area manufacturing. This is presented in this paper by manufacturing membranes with an effective surface area of 1 mm by 1 mm. Finally, the manufactured polymeric membranes with integrated porous electrodes with demonstrated sensor functionalities. Becuase the porous electrode is conductive, it is possible to give cells electrical stimuli. The integrated porous electrode is electrochemically active as well. Which makes it possible to use an electrochemical biosensor, as already shown in literature. By exploiting the existing techniques to decouple the conductive layer, it opens up the possibility to manufacture arrays of integrated biosensors on top of a membrane.

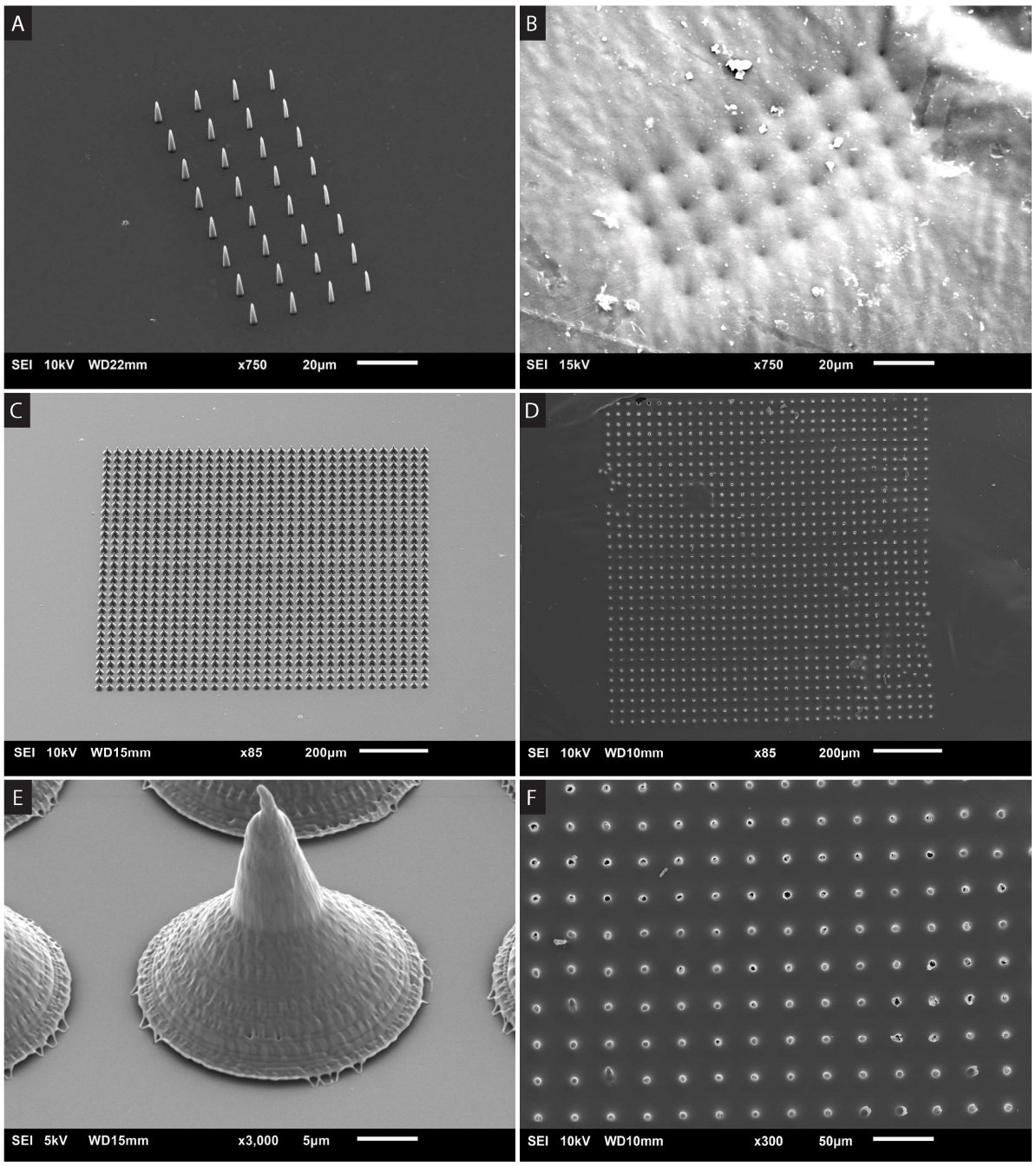

Figure 5.4: SEM Images of the soft molds and the resulting polymeric membranes with integrated porous electrode after post treatment. A: Soft mold with 32 pillars with a diameter of 400 nm, a tip angle of 80°, and varying base angles. B: Resulting polymeric membrane with integrated porous electrode imaged from the TOPAS side. C: Soft mold with a field of 32 by 32 pillars covering an effective surface area of 1 mm by 1 mm, with a diameter of 8 µm, a tip angle of 80°, and a base angle of 40°. D: Resulting polymeric membrane with integrated porous electrode imaged from the TOPAS side. E: Close up of one of the pillars of the soft mold presented in C. F: Close up of the membrane presented in D.

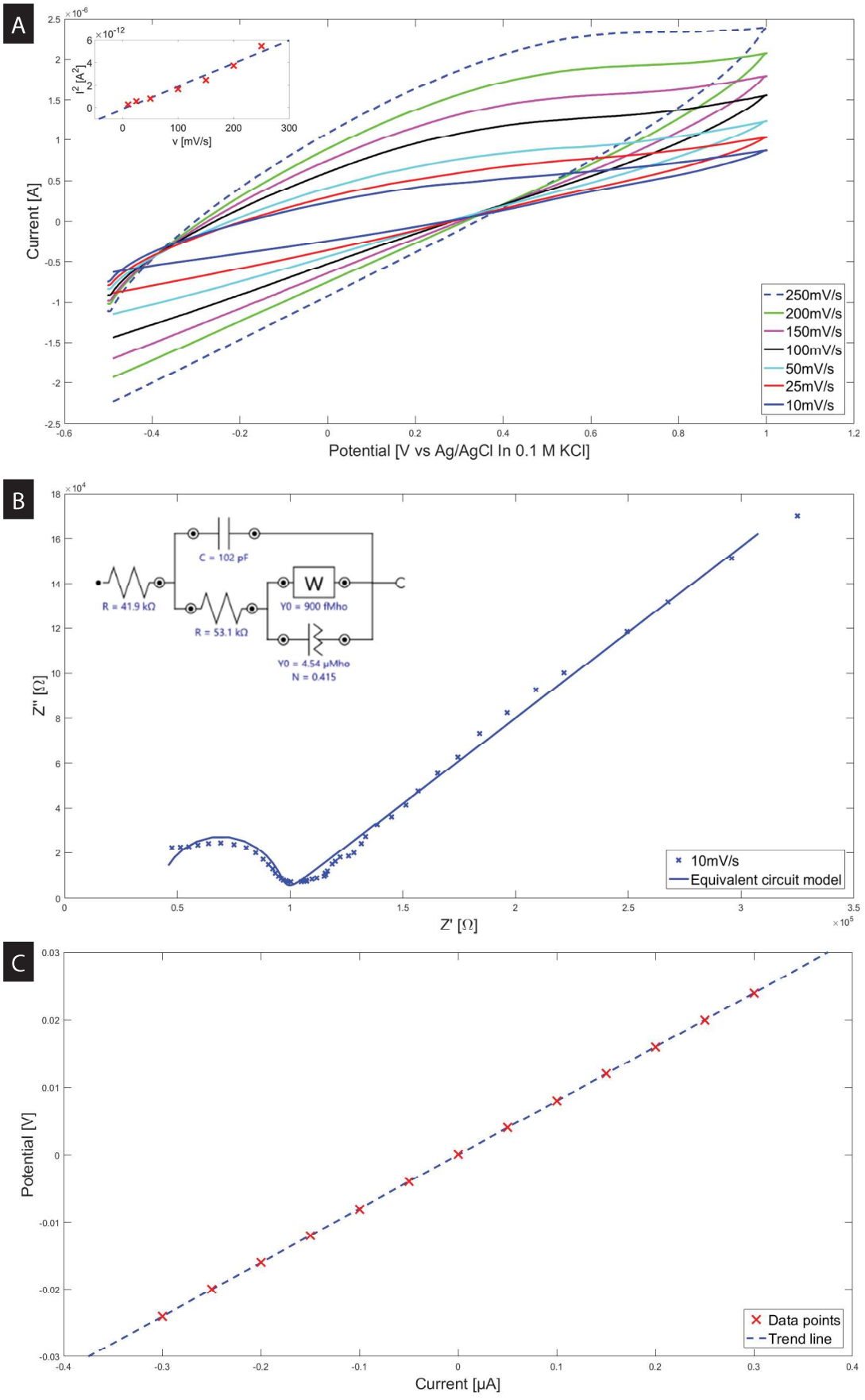

Figure 5.5: Characterization of the 1 mm by 1 mm membrane. A: Cyclic voltammogram containing the CV curves at different scan rates of a membrane with an effective surface area of 1 mm by 1 mm in 0.1M KCl. The inset contains the graph of the square of the oxidation peak height versus the scan rate. B: Electrochemical impedance spectroscopy spectra of a membrane with an effective surface area of 1 mm by 1 mm at 10mV/s in 10mM ferrocyanide/ferricyanide in 0.1M KCl. In the inset, a schematic representation of the fitted equivalent circuit with their corresponding values. The pores of the membrane will lower the slope of the linear part of the EIS data. The circuit is a Randells equivalent with constant of the constant phase element (Y0 = 4.54 µ Mho), to correct the lowering of linear part of the EIS data, in parallel with a negligible Warburg constant (Y0 = 900 fMho) which is added to prevent the fitting software from finding a local minimum. C: Voltage/current curve of a membrane with an effective surface area of 1 mm by 1 mm after the post treatment step.

6

Reflection

This chapter contains the self-reflection. First, the line of thought is discussed. Subsequently, a timeline comparison is done. Followed by a brief discussion of the contributions of this research. At last, personal points of improvement are discussed.

6.1. Line of thought

The first part of the literature study consists of identifying the current challenges of organ-on-a-chip systems which leads to the project aim, presented in chapter 1. From the second part of the literature study, the requirements of the membrane and the kind of sensor was selected, which is discussed in chapter 2. The last part of the literature review leads to a manufacturing technology to manufacture a polymeric membrane with integrated porous electrode. This is described in chapter 3 and an additional literature review for selecting a material and manufacturing technique to create a second soft working mold is described in Appendix B. The manufacturing methods are evaluated with a risk assessment and potential plan b's are defined, discussed in Appendix A. A roadmap with milestones and deliverables is formulated as a checklist of tasks to complete for reaching the desired milestones and deliverables. This is presented in chapter 4. From the roadmap, it became clear that most of the work would be to establish the required protocols of the individual manufacturing steps. This work is described in appendix C and D. The manufacturing of a polymeric membrane with integrated porous electrode is presented as a paper in chapter 5. Because of the high quality of the results, it is aimed to get it published in the journal Microelectronic Engineering after graduation. The algorithm written to characterize the used to characterize the morphology of the membrane is explained in appendix E. The performed permeability experiment to validate the fluidic functionality of the manufactured membranes is presented in appendix F.

6.2. Timeline comparison

In figure 6.1 the planned timeline and actual timeline is presented in a Gantt chart. While the tasks were already defined in chapter 4, this could easily be converted into the different activities of this research to be used in this timeline.

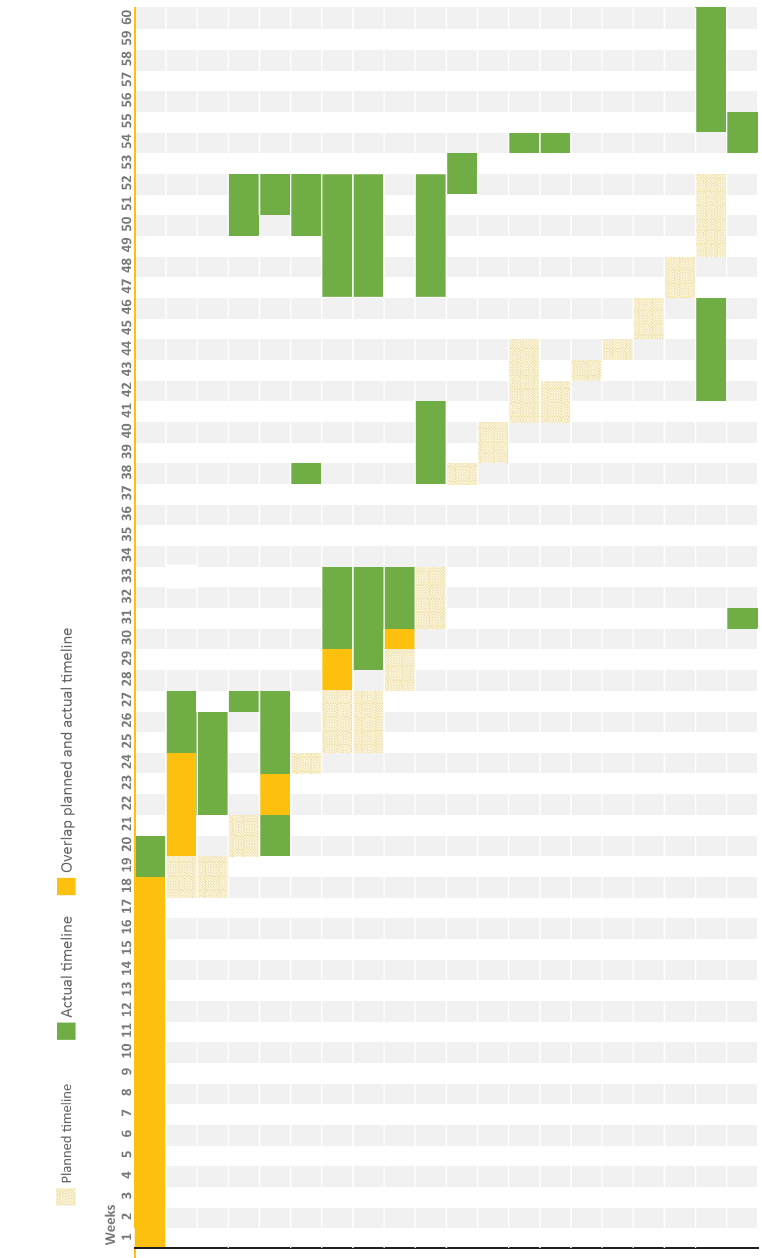

Figure 6.1: Gantt chart which contains the planned timeline and the actual timeline of this research

Looking at figure 6.1, just a small delay was encountered when the planned timeline is compared with the actual timeline of the first 41 weeks. This happened because the literature study was planned to take more than three months while some exams had to be done in the mean time. Eventually, it took even a bit longer to finish the literature because I underestimated the actual writing of the literature review itself. Also, I underestimated the time it takes to get trained for the needed equipment. But I had a headstart while Sam Smit took the time to walk me through his protocol of manufacturing TOPAS films and training/explaining to me how to use all the relevant equipment to do this on my own. Also, I underestimated the number of setbacks I would encounter during the labwork. For example, stacking of the different layers to create the multilayer substrate was not as easy as expected at the start of this research. So, no time was schaduled to find the best way to do this. The gap in the weeks 34 till 37 was time spend on holidays. After holidays I picked up the research where I left it. But week 42 till 46, I spend most of this time writing my report. I did this while we were out of glass coverslips which are used in the Nanoscribe Photonic Professional GT. These took some weeks to get delivered while the manufacturer of those coverslips had problems with their manufacturing process and was not able to deliver the glass coverslips any sooner. At this point of the research, I was depended on the Nanoscribe while I had to print a soft mold each time I imprinted a multilayer substrate because it would destroy the soft mold each time. After two weeks, a new package of coverslips arrived and I could continue with this research. But in the same week we, the users of the Nanoscribe (Paola Fanzio, Lili Maxime Hauzer, and myself), noticed a shift in the quality of the printed structures. This was confirmed by performing the same experiment which did work in week 41. Comparing pillars with sharp tips which were printed before and after this sudden shift, it looked like less of the photoresist polymerized during the printing process. In week 44 till 46 we tried multiple things in consultation with the customer support of Nanoscribe to determine the cause of this sudden shift in quality. After weeks of experiments, we could rule out the actuators, the laser, and the resist, which could all influence the observed phenomena. As this is written, we still don't know what caused this shift in quality. But I decided to continue with my research while the Photonic Professional GT was still able to print structures. I redefined the soft mold manufacturing protocol, nevertheless, the imprinting protocol still did not result in succesfull imprints. It is safe to say, it was not going to be an easy fix and the deadline for the upcoming conference was getting closer.

Therefore, I took a step back and identified the three main problems were observed after this shift, the collapsing of the pillars (figure D.3), the bending of the pillars (figure D.4), and the sticking of the pillars (figure D.5). Of each of those problems, I started visualizing what happens during the imprinting step which results in one of these three problems. Subsequently, I started drawing these visualizations and adding all the decomposed forces which the pillar would experience. After understanding which and how the forces effected this, I started brainstorming solutions. These are written around the visualization of the main problem like a mindmap. This resulted in a list of potential solutions to these three main problems. During this set-back, Luigi Sasso, Paola Fanzio, and I decided to have a supervisor meeting every week instead of every two weeks. Because of the upcoming deadline for the conference, I did not have the time to try all the solutions I came up with, Therefore, I wanted their opinion as well regarding the potential solutions and which ones to try. In the end, they have a lot more experience and knowledge about polymer micro and nano manufacturing, and they helped with ruling out potential solutions and determining which of the potential solutions to try first each week. While I had already experience with the equipment and which experiments to perform, it was not an easy fix and took weeks 47 till 52. During those weeks I was able to manufacture conductive membranes of 1 mm by 1 mm.

6.3. Contributions

To be able to manufacture the conductive membrane, multiple manufacturing protocols were established. Some as easy as spin coating a layer of PAA with it corresponding thickness at different spinning speeds and protocols to print pillars/cones with the Photonic Professional GT. These will be useful for the polymer micro and nano manufacturing group while people will also need to manufacture thin layers of the materials which were used in the multilayer substrate of this research. Multiple people are going to work with the Nanoscribe of which even some are going to print pillars/cones. But even for the people who are not going to print cones/pillars, the used job-files are a nice example which I used to verify 4 to 5 parameters at once. The established protocols during this research will save them time and eliminate risks whether it is possible or not. But it could also be useful for people outside of the polymer micro and nano group to have in-house protocols.

But the developed high resolution and high throughput technology to manufacture conductive membranes is much bigger than some spin coating protocols. Due to the freedom of the manufacturing method of the mold, it eventually results in precise control over the pore dimensions, location, and porosity. This improves the selectivity of the membrane which is interesting for multiple applications like precise separation, organic electronics, microfluidics, and tissue engineering. And the porous electrode which is integrated on top of the membrane opens up the possibility to manufacture membranes with integrated biosensors on top of it while this is the missing link. Because patterning of a PEDOT:PSS layer to manufacture a wearable pH sensor was already demonstrated within the polymer micro and nano manufacturing group.[42] And in literature multiple biosensors based on PEDOT:PSS are already reported.

6.4. Personal points of improvement

First of all, I learned a lot during this thesis. Especially how to properly do an experiment/research. This can be seen by the amount of work I was able to do in the weeks 47 till 52, which is mainly reported in chapter5 and appendix D, in comparison with the amount of work I did in weeks 20 till 41, which is mainly described in appendix C.

Except for the last couple of weeks of this research, we did supervisor meetings once every two weeks. During the first couple of supervisor meetings, I noticed that it helps me a lot to prepare a powerpoint presentation with the results of the last two weeks. Because in this way, I forced myself to structure the results, to process the results, and to write it down. And, I prefer to explain things with images instead of a lot of words. Therefore, showing and explaining the experiments I performed, and their results during the supervisor meetings, were much more clear. This made it possible for Luigi and Paola to give better and more useful feedback. During the first couple of months, I started to write down more and more in the slides which were eventually the notes which were the most helpful during the writing of this report. I always started the supervisor meetings with an overview of my task list, and which of thewere already completed, to give an overview of where we were with the research in the overall timeline. During the last couple of weeks of this research, I did not make a powerpoint presentation anymore due to lack of time. I needed this time to get all the results just in time for the conference, but it backfired during the writing of this report because those results were poorly documented. So, it took a lot of time to figure out which results were from which experiment. I learned from this experience that preparing such powerpoint presentation for a supervisor meeting, or just for myself as notes, helps me a lot to structure everything from experimental set-ups to thoughts how to continue with the overall research.

Also, writing all the parameters on the Petri dish which contained one sample helped me a lot, in the end, to figure out which one was which. In the beginning of the research, I did not do this as much. That was probably because I did not have that many samples at that point of the research yet. I learned from it, that you can never take enough notes of the experiments you performed at which parameters and so on. But it is exactly the same for the theoretical work I did beside the lab work, writing down what information I found in which papers would have saved me a lot of time as well.

Looking back, it would have benefitted me if I took more time to think about the experimental set-ups. This would have reduced the number of experiments I had to perform to get to the same results. Every time I 'just tried' something like some randomly selected imprinting parameters it resulted (mostly) in useless results. Currently, I identify these kind of decisions as a red flags. I realize now that at such a moment, I need to think more about the experiment or read some literature about it. Not just to be able to defend the research, but also to prevent that the experiment result in results which were not that useful, or that I was able to combine some experiments in one to be more efficient, or that I just skipped a step to determine certain parameters. This especially is true for the imprinting experiments. In contrast, the printing experiments were really well designed because I was able to verify 4 or 5 parameters at once.

Appendix C and Appendix D contain a lot of images which I have taken with my cell phone through the lens of the microscope. I did it in this manner, while the camera of my phone has a higher resolution than the one installed in the microscope. I did not image every sample with the SEM to save time. In the end, it was really efficient for the lab work but it pictures are not that clear and nice for the report. Looking back at this decision, I should have looked into other options to document the results in a nicer way which would still be efficient.

In an earlier stage of the research (weeks 22 till 27) the sputter coater was out of order. So, I could not image samples printed by the Photonic Professional GT. Luckily, I also had to establish the multilayer substrates protocols, at this point of the research, which kept me busy during those weeks. The integration of multiple

sensors onto the membrane was within the time given for this research not possible anymore. Because I lost a lot of time when the Photonic Professional GT could not be used due to the lack of glass coverslips and the shift in the quality of the printed structures. Instead, I had to work on writing my report which I always used as an activity in case I could not do anything else in the lab. But I think it is important to try to plan as much as possible parallel in the timeline, so that you never have to wait until a piece of equipment gets fixed or new materials get delivered. A Gantt chart is very useful for this while it visually illustrates the critical path. In the Gantt chart of figure 6.1, I planned the establishing of the multilayer substrate protocols and the soft mold manufacturing protocols after each other and writing the report in the end. But these could all be planned as parallel activities. Using a Gantt chart in an earlier stage of the research could have helped me to better identify which experiments could be done parallel to each other, to minimalize the length of the critical path, instead of just keeping some tasks as a plan b activity. Halfway through the research, I also started using it to determine which experiments I could do parallel to each other in a single day. This way I could do a lot more in one day, like printing a soft mold, imprinting a multilayer substrate, and preparing slides for the supervisor meeting all at the same time.

At last, English is not my strong suit. Therefore, writing the report took a lot of time. I made the decision to not to focus too much on work on the level of English of this report. Because the experimental work I could do in a month is, in my opinion, a lot more valuable. But that is no excuse for not improving my writing and speaking skills. This would benefit me a lot to speed up the writing of a high-quality report/paper, it will make some of my explanations more clear, and would help me to speak more freely during a presentation.

A

Risk assesment and plan B

In this appendix, a risk assessment is done. This will identify which experiments have to be done and for every risk there is a potential plan b introduced.

A.1. Identifiying optimal manufacturing parameters

Before the optimal design of the polymeric membrane with the integrated porous electrode and corresponding design of the soft mold can be made, some unknown parameters have to be identified. Also, creating decoupled electrodes is considered in this appendix while in the beginning of this research it was aimed for manufacturing decoupled electrodes as well. This chapter is divided into the same main manufacturing steps as used in the overview, figure 3.1. For each separate manufacturing step, there will be stated what is already known and unknown. From this information, the risks are identified and a potential plan b is discussed for the identified risks.

A.1.1. Manufacturing of the soft mold

Determine the optimal printing parameters and the limits of the dimensions of the desired structures.

Known: There is in-house experience of fabricating structures with the Photonic Professional GT and the photoresist. Features sizes down to 100 nm should be possible according to literature.[79]
Unknown: The optimal process parameters for the manufacturing of the soft mold and the limits of the specific structures of this research like pillars and contours of the sensor.
Risks: Because there is in-house experience, the risks are limited while structures were already printed successfully with the Photonic Professional GT.
Plan B: It will not be a problem to determine the optimal printing parameters. But it could be that a structure collapses due to its design. In that case, the design of the structures have to be altered.

A.1.2. Substrate preparation

The different spin coating parameters determine what the minimum layer thickness of the different materials is to obtain a good coverage. Also, the layer should be uniform.

Spin coating TOPAS

A layer of TOPAS has to be spin coated on top of a glass Petri dish with a desired thickness of 10 µm.

Known: An in-house protocol was already developed by Sam Smit to spin coat thin layers of TOPAS.[92]
Unknown: The spin coating settings needed to manufacture a film of TOPAS of the required thickness. Because the in-house protocol was not used to manufacture the required thickness of the TOPAS layer of this research.
Risks: Because there is an in-house protocol, the risk of creating a thin film is limited. The protocol just has to be tweaked a bit. This can be done with the spin coating parameters or the concentration of TOPAS in toluene.
Plan B: If TOPAS cannot be spin coated uniform and thin enough, a different material has to be selected. Or a different thin film manufacturing technique has to be selected.

Spin coating PEDOT:PSS
A layer of PEDOT:PSS has to be spin coated on top of the TOPAS film to eventually be used as an electrode.

Known: An in-house spin coating protocol is already developed forspin coating the PEDOT:PSS layer. 2-propanol is added to increase the wettability which increases the adhesion and results into a better surface quality. The size of the substrate does not influence the needed parameters for deposition the PEDOT:PSS layer.[93] Antoher in-house protocol was developed which did not add 2-propanol to the PEDOT:PSS solution but a surface treatment with oxygen plasma was done to increase the wettability of the substrate.[19]
Unknown: The relation between spin speed and film thickness has to be found for this specific substrate and the corresponding sheet resistance.
Risks: Because there is an in-house protocol, the risk of creating a thin film of PEDOT is low.
Plan B: Because there are two in-house protocols, there is no need for a plan b.

Spin coating PAA
The layer of PAA is used for the multilayer molding and it is used a sacrificial layer to lift off the membrane with integrated porous electrode.

Known: From literature, it is known that spin coating a solution of 6 wt% PAA in 18 wt% water and 76 wt% IPA at a speed of 2000 rpm (500 rpm s^{-1} ramp) for 60 s will result in a 400 nm thick PAA layer on glass.[53] Spin coating aqueous solutions of 2.5% to 19% (w/v) PAA at different speeds (1000 RPM to 4000 RPM) resulted into a film thickness of 40 nm to 9 µm on PET disks and ITO coated silicon wafers.[61]
Unknown: No literature was found regarding spin coating PAA onto Topas.
Risks: There are not a lot of protocols known for spin coating PAA, and none were found for spin coating PAA onto TOPAS. Some difficulties could be there like adhesion or wettability problems between TOPAS and PAA. Experiments have to be done to find suiting parameters to create an uniform thin film of PAA onto a TOPAS film. The relative thick layer which has to be spin coated could make it even more difficult.
Plan B: If there is a wettability problem, it could be solved by adding IPA or to do a surface treatment with oxygen plasma.[93] If it is not possible to manufacture the required uniform layer of PAA, a different material could be selected as sacrificial layer or a different manufacturing method could be selected like casting.

A.1.3. Soft imprinting process

Imprinting step
The soft mold must also be able to pattern and the dimensions of the features onto the substrate.

Known: There is in-house experience of soft embossing TOPAS with a PEDOT layer on top of it to create a microfluidic device with electrodes in one step.[93]
Unknown: The difference is that there is an additional layer underneath the substrate. And the TOPAS layer with a PEDOT layer on top of it has to be perforated to eventually create the pores of the membrane. Also, the in-house protocol does not use IP-L 780 as soft mold.
Risks: Good guidelines were already created for a soft embossing step but they probably have to be tweaked to find the optimal parameters for creating through-holes with a soft IP-L 780 mold.
Plan B: The risks are limited and imprinting with IP-L 780 should be possible. But if it introduces problems, a different material could be selected for the soft mold for which there is in-house experience. Or a soft working mold can be manufactured of the soft IP-L 780 mold, possible materials and manufacturing methods are discussed in Appendix B. Or other materials can be selected for the substrate which should make the soft mold imprinting step easier.

Adhesion between the different layers
The adhesion between the different layer should be high enough to prevent the splitting of them during the demolding step.
Known: Imprinting a PEDOT:PSS and TOPAS substrate is possible.[93]
*Unknown:*As earlier described, the adhesion between the different layers is not known.
Risks: A good adhesion is critical for the imprinting step of the through-holes while the multilayer polymers have to stick together to prevent that it separates. And that the PEDOT:PSS and TOPAS layer sticks to the mold instead of the substrate. This has to be verified.
Plan B: If the adhesion is not strong enough, a different method for embossing through-holes has to be selected. Or the mold has be treated with an anti stiction layer to lower the friction between the multilayer

substrate and the mold which will lower the required adhesion between the different layers of the multilayer substrate.

A.1.4. Post treatment

Enhancement of PEDOT:PSS layer

The ethylene glycol treatment has to positively influence the conducting and water repelling properties of PEDOT:PSS.

Known: The conductivity of the PEDOT:PSS layer is increased by an ethylene glycol treatment and the solubilty of the PEDOT:PSS layer is much lower in water.[93] At least 10 min treatment for max conductivity for a PEDOT:PSS layer of 137 $\pm$ 7 nm in thickness.[19]
Unknown: It is expected that the time of the ethylene glycol enhancement depends on the thickness of the PEDOT layer.
Risks: Successful ethylene glycol enhancements of PEDOT:PSS were done in-house. It was found that doing an immersion longer than needed will not influence the conductivity of the PEDOT:PSS negatively.[19] If another layer thickness of PEDOT:PSS is going to be used, the minimal time needed for maximal enhancement of the PEDOT:PSS has to be determined.
Plan B: Immerse the PEDOT:PSS layer long enough to increase the conductivity and to decrease the water solubility. If it cannot be done successfully for another thickness, the same thickness used in the previous research has to be used.

Disolving sacrificial layer

The PAA layer has to be dissolved successfully to release the membrane with integrated sensors.

Known: For a film thickness of $\sim$ 400 nm, the diffusion of water into the water-soluble layer was increased by performing ultrasonication in a water bath. The ultrasonication in a water bath for at least 10 min was generally required. The remaining water soluble layer was subsequently removed by rinsing with water.[53] In another paper, an etching rate of 750 $\mu m\,min^{-1}$ was determined for PAA. But the geometry was not taken into account, so it was advised to use as a guideline.[61]
Unknown: The influence of the ethylene glycol treatment on the solubility of PAA.
Risks: The effects of the immersion of PAA in ethylene glycol are not found in literature. So, the influence of this on the solubility of the sacrificial layer can not be determined. Experiments have to be conducted to find out if it still can be dissolved in water. And if that is possible, the etching rate has to be determined. But it could also be that the ethylene glycol will dissolve the PAA layer.
Plan B: If the PAA layer will not completely dissolve in water anymore, ultrasonication in a water bath could be tried. If that also does not work, a different solution could be selected which would dissolve the modified PAA layer. A solution has to be selected which does not influence the membrane with the integrated porous electrode. Or a different material for the sacrificial layer can be selected which can successfully be dissolved after a ethylene glycol treatment. Another possibility is to do the ethylene glycol enhancement before the PAA layer is spin coated. In this way, the layer cannot be affected by the threatment. Or the layer dissolves in ehtylene glycol which would be a plus while it decreases the number of manufacturing steps.

A.2. Identifying optimal design parameters

There are two main parts of the design. The part which is responsible for creating the pores and the part which creates the decoupled electrodes for the sensor.

A.2.1. Parameters membrane

The optimal dimensions and the optimal shape of the pillars has to be found. A cone shape will be probably the best shape for perforating the two layers. The needed tip angle and base angle have to be determined.

Known: A formula is known which describes the collapse of the pillars which has the following parameters: surface energy, Young's Modulus, and the Poisson's ratio.[94] Also the important parameters to insert microneedles into skin is known.[83]
Unknown: The influence of the shape of the pillar for collapsing is not taken into account. And there is not a lot known about creating through-holes with multilayer molding.
Risks: The biggest risk is the high-aspect-ratio that is needed to create the through-holes. Because of these high-aspect-ratios, sticking and collapsing of the pillars is an issue. Also, the chance increases of fracture of

the pillars when the aspect-ratio is increased.[94] Experiments have to determine what the maximum aspect-ratio is what can be obtained with a cone-shaped pillar. And also, it has to be verified if that can successfully be imprinted through the PEDOT:PSS layer and through the TOPAS layer. Because of the cone shape of the pillar, the base diameter of the cone has to be bigger than the diameter of the required hole to obtain the desired pore diameter. The material could deform a bit after removing the stamp, which will result in smaller pores. This has to be taken into account as well. Also, the required tip angle and base angle have to be determined.
Plan B: If the aspect-ratio cannot be high enough, the thickness of the total substrated has to be lowered. This can be done by creating a thinner layer of PEDOT:PSS, but this will result in thinner electrodes and, therefore, a higher resistance which will make the sensor less sensitive. The thickness of the TOPAS layer could also be lowered. The thinnest membrane used for cell culturing is 10 µm, but if necessary, a thinner membrane could be manufactured. Collapsing of the pillars themselves will not be a problem, but during the imprinting step fracture or deformations can still cause problems.[94]

A.2.2. Parameters electrodes

The parameters to decouple the PEDOT:PSS layer successfully have to be determined. It is expected to be influenced by the aspect ratio of the contour of the sensor the sharpness of the edge of the contour.

Known: A rectuangular beam with a width of $\pm$ 34 µm and 50 µm are high decoupled 100% of the electrodes, and adding angle will decrease the decoupling.[93]
Unknown: Smaller dimensions have not been looked into.
Risks: It is possible to decouple electrodes with the imprinting step and the influences of different shapes have been already looked into. But the smallest aspect ratios and the sharpness of the contour which will successfully decouple the electrodes have to be determined by experiments.
Plan B: If the dimensions cannot go small enough to create at least one sensor onto the membrane, the design has to be altered to fit a sensor (which does not have the optimal design to suit the cells) on top of the membrane. Worst case, a porous electrode could be manufactured instead of decoupled electrodes.

B

Additional literature review

There is an additional literature study done to determine a suitable material and manufacturing method to create a soft working mold from a master mold manufactured by the Photonic Professional GT.

B.1. Material soft working mold

A lot of thermoplastic polymers are used for micro molding: cyclo-olefine copolymer (COC), polymethylmethacrylate (PMMA), polycarbonate (PC), polystyrene (PS), polyoxymethylene (POM), perfluoralkoxy copolymer (PFA), polyvinlchloride (PVC), polypropylene (PP), polyethylene terephtalate (PET), polyetheretherketone (PEEK), polydimethylsiloxane (PDMS), polyamide (PA), Polysulfone (PSU), polyvinylidenefluoride (PVDF), polyetherimide (PEI), polymercaptopropylmethylsiloxane (PMMS) and perfluoropolyethers (PFPEs). Due to the large choice of polymers, a closer look into polymers which are used for soft lithography will be given. Because using a polymer which has never been used before as soft mold introduces extra risks. The used polymers for soft lithography are PDMS, PMMA, PMMS, PS, PFPEs, Ethylenetetrafluoroethylene (ETFE), Teflon, polyurethaneacrylate) (PUA), Ormostamp, COC, PC, and PEI.[50, 95–97]

PDMS PDMS is a thermally curable, elastomeric polymer, transparent down to wavelengths of 280 nm, commercially available is bulk for 100 \$ kg^{-1}. Thanks to these properties it is the most common material for soft lithography molds. Features bigger than 100 nm can be patterned using Sylgard 184. But it also has some cons, it is not the best material for high-aspect-ratio structures. Because mechanical stress, electrostatic attraction, and capillary forces may cause the features of the soft mold to self-adhere. This limits the usable aspect ratio to 10:1. Also, it swells in organic solvents and could leave cyclic silicon derivatives on the surface. A new kind of PDMS, "hard-PDMS", was developed with a higher Young's Modulus. It increases from ~0.6 MPa to ~10 MPa. This enables a higher resolution but also introduces new problems. Releasing it from the master mold could crack the hard-PDMS. And external pressure is required to create conformal contact with a substrate. X-PDMS can have a Young's Modulus up to 80 MPA and can replicates sub-10 nm features with conformal contact. Photocurable PDMS (hv-PDMS) was developed to overcome the long, thermal cure under pressure of soft PDMS molds. hv-PDMS has a higher tensile modulus than s-PDMS and the elongation at break is much higher than h-PDMS which will make it easier to handle but it has a Young's Modulus of ~3 MPa to ~4 MPa. With hv-PDMS researchers were able to replicate 300 nm features. h-PDMS and hv-PDMS have the lowest surface energy of the PDMS-based materials with of 20 mN m^{-1}.[96–100]

PMMA To overcome the problem of the low possible aspect ratio of PDMS, polymethylmethacrylate (PMMA) can be used as well. This is also a high transparent polymer. And features with an aspect ratio up to 300:1 can be created. But is has the drawback that nonconformal contact occurs due to the rigidity of the soft PMMA mold. It has a glass transition temperature starting at 80°C. [95, 99]

PMMS With PMMS features of 15 nm has been manufactured using nanoimprint technique. But a big con is that soft PMMS molds needs a fluorine functionalization for nondestructive release.[100]

PS PS is a transparent polymer with a glass transition temperature of 80°C. Surface features of 250 nm in diameter and height were successfully manufactured.[95, 101]

PFPEs PFPEs have a low Young's Modulus, low surface energy, high gas permeability, chemical resistance, solvent resistant, and swell minimally. Feature sizes of 2 nm have been fabricated with a soft PFPE mold. Variants of PFPE are hyperbranched PFPE (HPFPE), acryloxy PFPE (a-PFPE), and a-,w-methacryloxy functionalized PFPE (PFPE-DMA). a-PFPE has the highest Young's Modulus of the PFPEs with 10.5 MPa. And regular PFPE has the lowest surface energy of 12 $mN\,m^{-1}$. PFPE-DMA can replicate sub-100 nm features with no indication of limits to going even smaller and has a Young's Modulus of 4 MPa. It has a glass transition temperature in the range of 117°C to 130°C, and costs €8 per kg to €16 per kg. [96–98, 102]

ETFE ETFE has an exceptional toughness, an exceptional flexibility, low surface energy (15.6 $mN\,m^{-1}$), relative high stiffness, and high thermal stability. It can imprint features with a lateral dimension of 10 nm, has a Young's Modulus of ~1.2 GPa and a glass transition temperature in the range of 78°C to 93°C, and costs €20 per kg to €30 per kg.[97, 102]

Teflon Teflon AF 2400 has a tensile modulus of almost a thousand times higher than PDMS, a low surface energy (~16 $mN\,m^{-1}$), a Young's Modulus of ~1.6 GPa, has a high gas permeability, is inert to all chemicals and solvents except for perfluorinated solvents. So there is no swelling problem. It is sold for $2750 per 25 g, has a glass transition temperature of 340°C, and may be may be hazardous if it is inhaled.[97, 103, 104]

PUA PUA is almost impermeable to gasses, inert to chemicals and solvents (no swelling problems). A hardness of 0.15 GPa, surface energy of 23 $mN\,m^{-1}$, a glass transition temperature of 52.97°C and an elastic modulus of 2.7 GPa can be obtained. Feature sizes of 350 nm are reported with the use of a PUA mold.[97, 105]

Ormostamp It has a high UV-transparency even after thermal exposure. Due to its good Young's Modulus (650 MPa) and hardness, it can pattern nanostructures (reported feature size of 100 nm) without any cracks and fractures or deformations.[97]

COC COC is a transparent polymer, has high rigidity, excellent heat resistance and a very good dimension stability. It has a glass transition temperature possible as high as 140°C and it has a high transparency. It was used to successfully fabricate 200 µm long, 75 µm wide and 35 µm in height microchannels.[50, 95]

PC PC has a glass transition temperature of 140°C and it has a high transparency. Microchannels of 10 mm in length, with an average of 89 µm width, and an average 44 µm in depth were successfully fabricated within a difference of dimension of maximum 5%.[95, 106]

PEI PEI s a transparent polymer with high rigidity, excellent heat resistance, comparatively great dimensional stability and has a high glass transition temperature of 210°C. Channels of 308 µm to 318 µm with a depth of 40 µm to 48 µm have successfully been created into amorphous polyethylene terephthalate (APET).[107]

B.1.1. Selected material for the soft mold

The selected manufacturing method for creating membranes with an integrated porous electro can create features in the sub-micrometer range. To keep the ability to create that kind of feature size, a material has to be selected which is able to transfer that. The selected material for the membrane (TOPAS) has a glass transition temperature of about 70°C,[108] so a material is needed which has a glass transition temperature above that to be able to use it for imprinting. A lower surface energy will lower the adhesion and the friction between the polymer and the mold, which makes demolding easier. When a material is selected with a high Young's Modulus and a low surface energy, it can have structures with high-aspect-ratios without them being deformed or being destroyed during imprint. For the worst-case scenario of a membrane with the smallest pore size (0.4 µm) and a with the biggest thickness (50 µm), an aspect ratio of at least 125:1 is required. For a membrane with the smallest pore size and the smallest thickness (10 µm), an aspects-ratio of at least 25:1 is required. This is still really difficult to accomplish. The surface energy between the different materials do not range that much, and can always be influenced by adding an anti-stiction layer. The Young's Modulus does range a lot. There is aimed for a material with a Young's Modulus in the Giga Pascal range. Teflon AF 2400 does fits the requirements the best, but it costs a lot and is potentially hazardous. That is why ETFE is selected. It has a Young's modulus which is 25% lower but it has a bit lower surface energy and its price

is also > 3000% lower which makes it a lot more appealing for a commercial application. ETFE is a thermal curable.[19, 94, 97]

B.2. Soft working mold manufacturing

For the manufacturing of the soft working mold, the pattern of the master mold has to be replicated onto the soft mold. Therefore, there will be looked into replication techniques which are able to transfer micro and nano patterns onto a substrate, which is in this case is the soft working mold. Replication techniques which are used for this kind of applications are: Thermal NIL, UV-NIL, combined NIL and photolithography, roll-to-roll, step and repeat, reverse NIL, thermoforming, injection moulding, and casting. Roll-to-roll and step and repeat are techniques which are based on thermal NIL and UV-NIL but used for large scale productions. Because only a couple of soft molds have to be manufactured during this research, these will not be discussed in detail.[49, 109]

Thermal NIL This technique is also known as hot embossing. In this process a thermoplast is heated above its glass transition temperature. When it is above its glass transition temperature, the thermoplast becomes similair to liquid with a high viscosity. A master mold is pressed into this liquid and it is cooled down below the glass transition temperature of the thermoplast. The master mold is removed and the structure is replicated into the thermoplast.[109]

UV-NIL This technique uses a photosensitive polymer as substrate which is soft when it is uncured. First, the master mold is placed in the photosensitive material. Subsequently, the photosensitive polymer is cured with UV-radiation. And at last, the master mold is removed which leaves an imprint into the cured polymer.[109]

Combined NIL and photolithography This process is mainly used for imprinting large structures in combination with small structures. Normal lithograpy is used to create the large structures while the small structures are patterned by NIL.[109]

Reverse NIL The only difference between regular NIL and reverse NIL is that the master mold is coated with the material before imprinting. And subsequently, it is pressed against a substrate. Therefore, an imprint can be performed on a prepatterned substrate.[109]

Thermoforming A thermoplastic sheet is pulled over a structure to pattern it before heating.[109]

Injection pressure moulding A hot polymer is injected into a cold mold under high pressure. Subsequently, it is cooled down in the mold. And when the mold is opened a successfull patterned polymer can be collected. It can also been down without the high pressure, but a higher process temperature is required. [109]

Casting A melted polymer is casted on top of the master mold. Subsequently, it is cooled down and removed from the mold.[49, 109].

B.2.1. Choosen technique for soft mold fabrication

The most simple replication technique is casting. But the melting temperature of the EFTE is above the glass transition temperature of the master IP photoresist mold. This will cause the master mold to become a liquid with a high viscosity. Therefore, it will not be able to succesfuly pattern the structures from the master mold to the soft mold with a casting process. ETFE is not UV curable, so UV-NIL is not a possibility. Combined NIL and photolithography is way to complicated for what there have to be replicated. Injection moulding is more expensive than thermal NIL. The system required for thermoforming is cheaper than for hot embossing. But there is already in-house experience with hot embossing. That is why there thermal NIL is selected as technique to manufacture the soft working mold.[49]

C

Experiments performed for establishing manufacturing protocols

C.1. Introduction

To be able to manufacture a polymeric membrane with integrated porous electrode according to the presented manufacturing overview (figure 3.1), multiple manufacturing protocols have to be established. In this appendix, the performed experiments will be described in section C.2. Subsequently, the results of these experiments are presented and discussed in section C.3. Finally, the conclusions consisting of the final protocols which are developed to manufacture a polymeric membrane with integrated porous electrode are presented in section C.4. Per section, there will be subsections regarding the different manufacturing steps. These have the similair names as the names used for the manufacturing steps in figure 3.1, namely soft mold manufacturing protocol, imprinting protocol, substrate protocols, and post-treatment. Also, the optimal printing parameters for printing the contours of the sensor are determined within this appendix. The aim is to use such contours to decouple the conductive layer of the membrane. The work performed in this appendix is reflected on the roadmap to success, which is presented in figure C.1.

Figure C.1: Roadmap to success with symbols indicating which experiments are performed in this appendix.

C.2. Experimental

C.2.1. Soft mold manufacturing protocol

The goal of these experiments is to find the optimal values for the laser power and the scan speed to print pillars with sharp tips, electrodes, and electrodes with sharp edges. A glass coverslip (Menzel Gläser) of 30 mm in diameter with a thickness of 0.17 mm +/- 0.01 mm from Thermo Scientific, is cleaned with acetone (EMSURE®, Sigma-Aldrich) and 2-propanol (Honeywell, Riedel-de Haën). A drop of immersion oil (Immersol^{TM} 518F, Zeiss) is placed on the bottom of the coverslip and a drop of IPL-780 (Nanoscribe) is placed on top of it. The coverslip is placed in a holder and placed in the Nanoscribe Photonic Professional GT. Different models are created with Solidworks (2016 x64 edition) and converted into job-files with Describe 2.2.4. Most of the times the rendered 3D previews of the different print jobs consists of blocks because there is not enough memory to build the structure. To prevent the graphics card from crashing, the rendering mode is changed to bounding box by the software. This is, for example, the case in figure C.3. Adaptive slicing will be used for all models. With this feature, the software looks at the slope of the object to determine where to slice the following layer. The steeper the slope, the bigger the slicing distance. There is printed in the conventional mode with the 63x objective, and the following parameters are fixed: a hatching distance of 2 µm (The lateral distance between two lines in one layer.), a hatching angle of 45° (The angle between two lines in the two layers which are on top of eachother.), a maximum slicing distance of 0.5 µm (The maximum distances between two planes in the z-direction.), a minimum slicing distance of 0.2 µm (The minimum distances between two planes in the z-direction.), and a contour count of 1 (The number of contour lines around an object), unless it explicitly stated else. After the polymerization, the coverslip with the printed structure on top of it is developed for 25 min in propylene glycol monomethyl ether acetate, PGMEA, (≥ 99.5%, ReagentPlus®, Sigma-Aldrich), followed by 5 min in 2-propanol. The printed structure will be sputter coated (Quorum Technologies SC7620) with a 6.5 nm layer of Au/Pd which is imaged with a scanning electron microscope, SEM, (Jeol JSM-6010LA). The pillars will be imaged at a 45° angle to be able to inspect the tips of the pillars. The definition of the tip angle and the base angle of a pillar is explained in figure C.2.

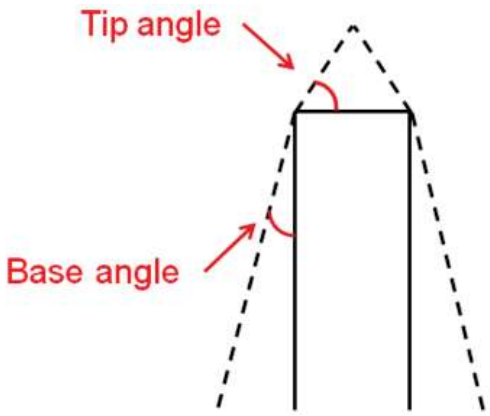

Figure C.2: Graphical explanation of tip angle and base angle of a pillar.

Pillars with different diameters and tip angles

While there are commercial membranes available with different pore diameters, as presented in table 2.1, pillars with different diameters have to be manufactured. Pillars with diameter of 0.4 µm, 1 µm, 3 µm, 5 µm and 8 µm will be manufactured. The angle of the tip will be varied while it is expected that this parameter will have an influence on the imprinting of the pores, just like the insertion of a microneedle into the skin.[83] The diameter is varied in the x-direction and the tip angle from 0° to 80° in steps of 10° in the y-direction. This is illustrated in figure C.3A. Next to this square of pillars, a text is written with information regarding the printing parameters of that square. Out of this square, a matrix of squares is created. In the x-direction the scan speed varies from 20 000 µm s^{-1} to 2500 µm s^{-1} in steps of 2500 µm s^{-1} and in the y-direction the laser power varies from 2.5 mW to 20 mW in steps of 2.5 mW. This graphically represented in figure C.3B. A hatching distance of 0.2 µm is used for this particular print job. The laser power and scan speed are varied while these are the most influencial parameters to print structures successfully.[110] Using a dose which is too high, combination of a high laser power and a low scan speed, will cause the photoresist to boil. Using a dose which is too low will not be able to polymerize the photoresist. The scan speed is lowered in the x-direction to have the boiling of the resist happen in the top right corner of the print job to minimalize the number of pillars effected by it. A 3D preview of the print job is given in figure C.3B.

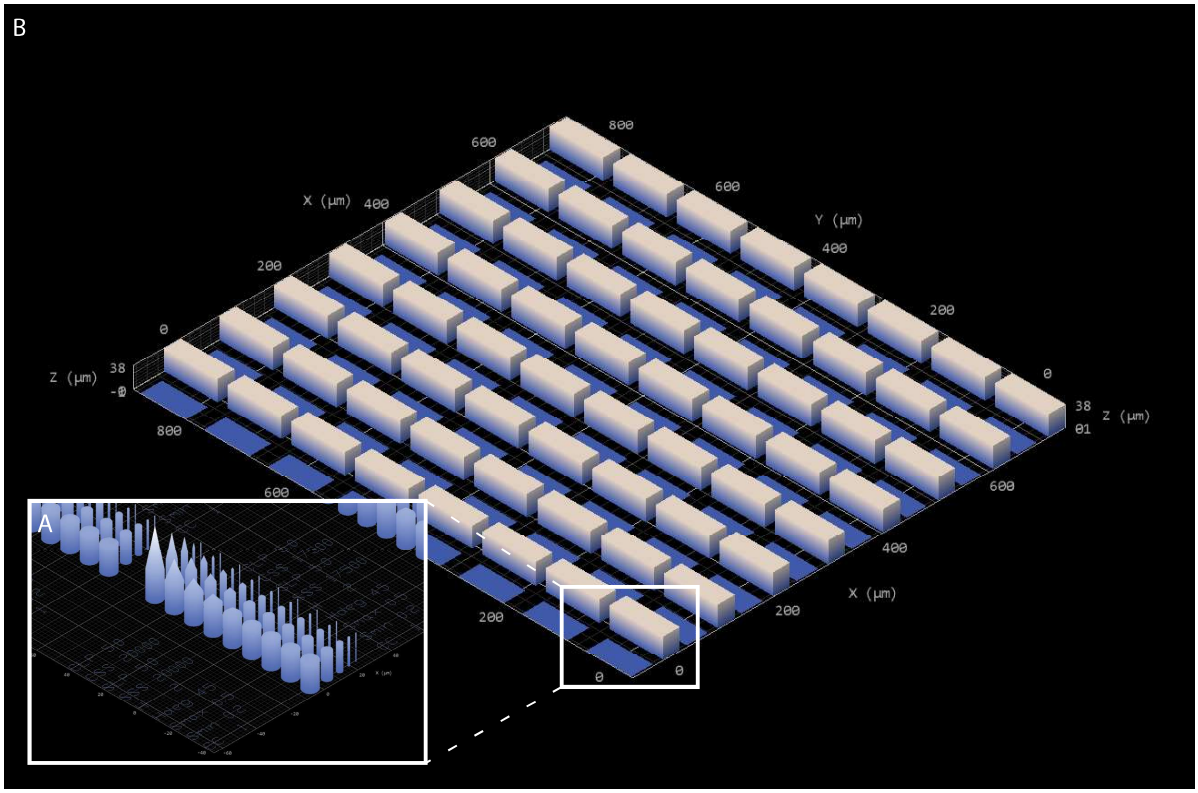

Figure C.3: 3D preview of the print job to determine the optimal dose for printing pillars with different diameters, base angles, and tip angles. A: Close up of one square of pillars in which the diameter is varied in the x-direction and the tip angle is varied in the y-direction. B: Overview of the complete print job in which the scan speed is varied in the x-direction and the laser power is varied in the y-direction.

Falling over of 0.4 µm pillars by the pillars with a base angle of 0°

Pillars for creating 0.4 µm pores have the tendency to fall over. Therefore, these pillars are printed with different base angles to determine whether a certain base would prevent the pillars from falling over. Pillars with a varying tip angle from 0° to 80° in steps of 10° were manufactured in the x-direction, while the base angle is varied from 0° to 4° in steps of 1° in the y-direction. Next to this square of pillars, a text is written with information regarding the printing parameters of that square. This is presented in figure C.4A. Out of this square, a matrix of squares is created. In the x-direction the scan speed varies from 20 000 µm s^{-1} to 2500 µm s^{-1} in steps of 2500 µm s^{-1} and in the y-direction the laser power varies from 2.5 mW to 25 mW in steps of 2.5 mW. A hatching distance of 0.2 µm is used for this particular print job. A 3D preview is given in figure C.4B.

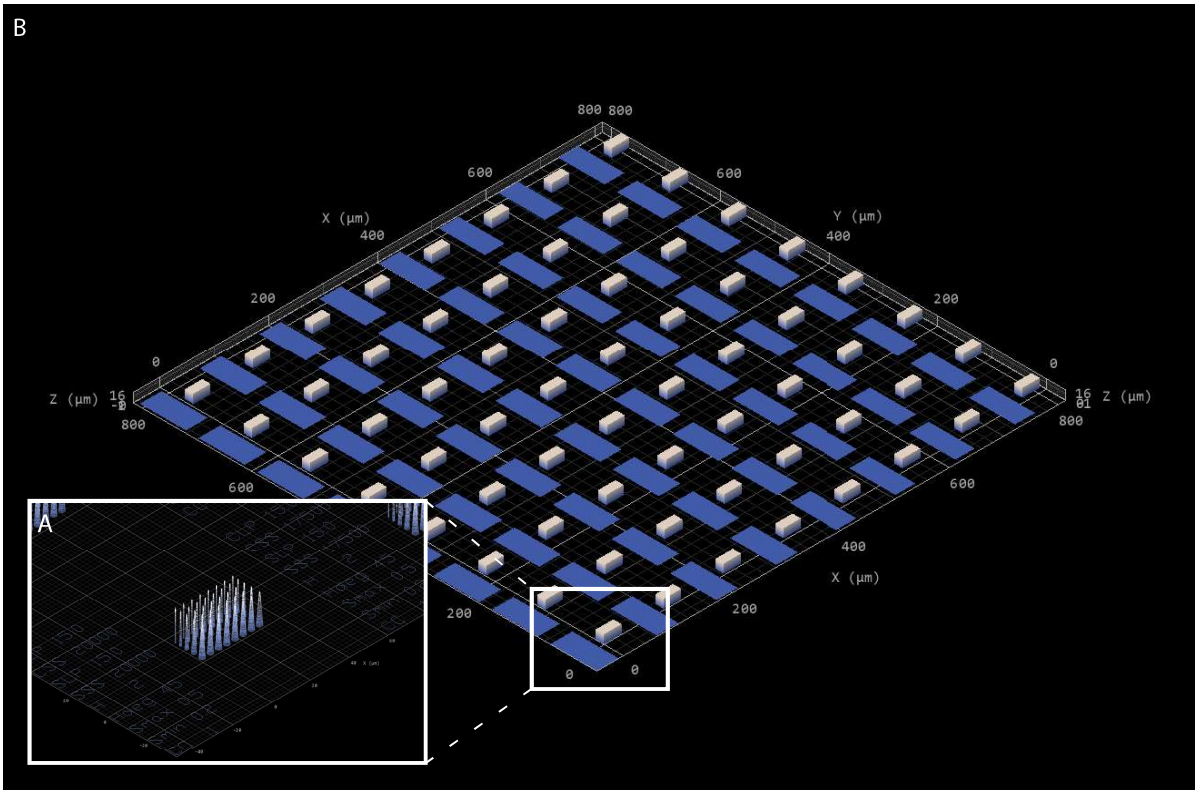

Figure C.4: 3D preview of the print job to determine the base angles needed to prevent the 0.4 µm from falling over. A: Close up of one square of pillars in which the tip angle is varied in the x-direction and the base angle is varied in the y-direction. B: Overview of the complete print job in which the scan speed is varied in the x-direction and the laser power is varied in the y-direction.

Printing pillars with different diameters, tip angles, and base angles

For each pore size, the variation of base angle is introduced to create a larger surface at the glass substrate. The larger surface will result in a larger adhesion force, which may be needed during the imprinting step to prevent the pillars from transferring from the mold to the substrate. But will increase the minimal required center to center spacing of the pillars. For each pore size, the maximum area per pore is calculated for which it is still possible to create the highest number of pores/cm^2, which are commercially available. Subsequently, the maximum diameter of a circle is calculated which would fit in the area, which can be used to determine the maximum base angle which can be used to still be able to fit the number of pillars next to each other to still create the highest number of pores/cm^2 which are commercially available. There is decided to use 5 pillars with different base angles per pore size. In the case of a pore size of 0.4 µm, it is decided to vary the base angle from 0° to 4° in steps of 1° while the maximum base angle is only 1.14°. The used base angles are all rounded, and this, including the selected base angles, is summarized in table C.1.

Table C.1: Overview of the values used to determine the maximum base angle per pore size.

Pore size [µm]	Max pore density [pores/cm^2]	Max area per pore [µm]	Max diameter [µm]	Max base angle [◦]	Base angles used [◦]
0.4	1×10^8	1.0	1.0	1.1	0, 1, 2, 3, 4
1.0	2×10^6	50	7.1	11.4	0, 3, 6, 9, 12
3.0	2×10^6	50	7.1	7.7	0, 2, 4, 6, 8
5.0	4×10^5	250	15.8	19.8	0, 5, 10, 15, 20
8.0	1×10^5	1000	31.6	38.2	0, 10, 20, 30, 40

For the 0.4 µm pores, the pillars with a base angle of 0° are removed from the print job to investigate if these pillars cause the other pillars to collapse which has been noticed in figure C.16. The tip angle varies also for each pore size from 0° to 80° in steps of 10°. The tip angle will influence whether the pillar is able to create through-holes.[83] Looking at one square of pillars, in the x-direction, the base angle varies and in

the y-direction, the tip angle varies, shown in figure C.5A. Next to this square of pillars, a text is written with information regarding the printing parameters of that square. Out of this square, a matrix of squares is created. This is shown in figure C.5A. In the x-direction, the scan speed varies from 10 000 µm s^{-1} to 2500 µm s^{-1} in steps of 2500 µm s^{-1} and, in the y-direction, the laser power varies from 12.5 mW to 22.5 mW in steps of 2.5 mW. Multiple of these matrices are placed behind each other, in the y-direction, varying the diameter of the pillar for the different pore diameters, as shown in figure C.5B.

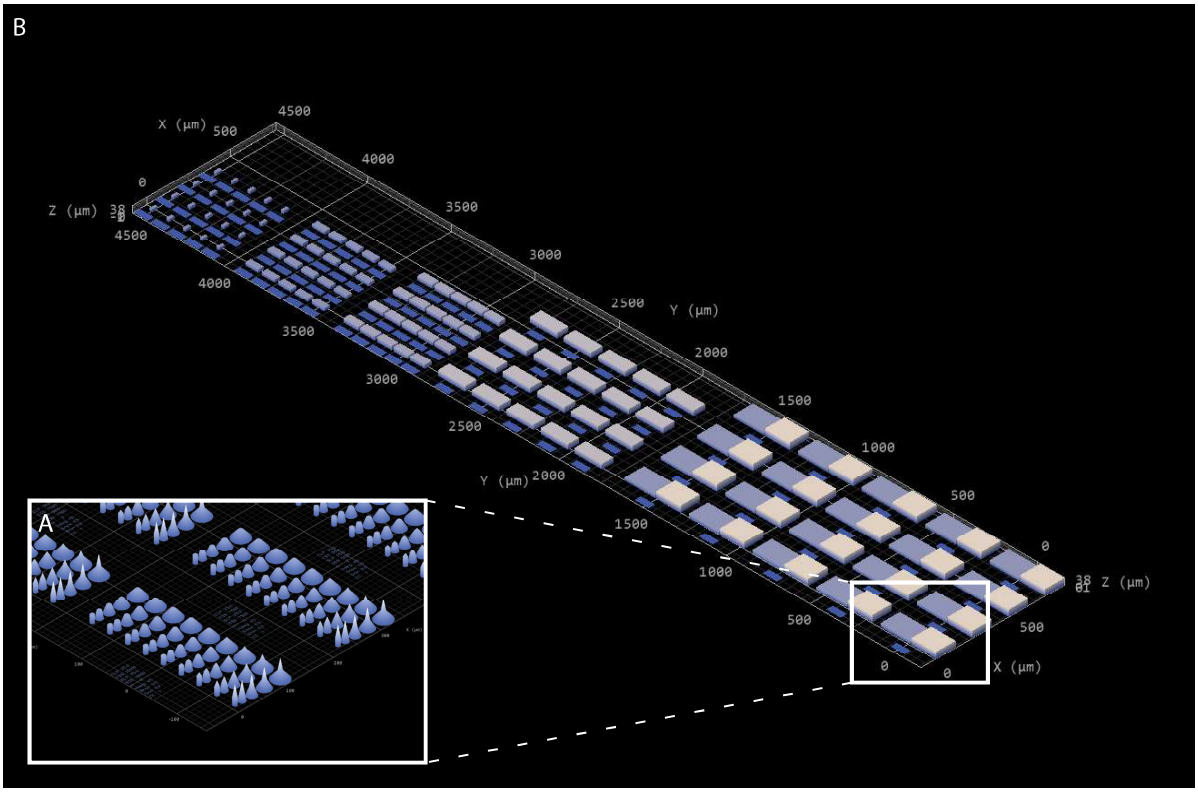

Figure C.5: 3D preview of the print job to determine the optimal dose for printing pillars with different diameters, base angles, and tip angles. A: Close up of one square of pillars in which the base angle is varied in the x-direction and the tip angle is varied in the y-direction. B: Overview of the complete print job in which the scan speed is varied in the x-direction and the laser power is varied in the y-direction. This is done per diameter pillar which is varied in the y-direction.

Influence of slicing distance

Decreasing the slicing distance could result in a better resemblance of the modelled pillars. A minimum slicing distance of 0.1 µm and a maximum slicing distance of 0.2 µm is used in this experiment instead of a minimum slicing distance of 0.2 µm and a maximum slicing distance of 0.5 µm. Only the pillars of 3 µm, 5 µm and 8 µm are printed in this experiment because those differed a bit more than the pillars with a diameter of 0.4 µm and with a diameter of 1 µm.

Again, the base angle is varied in the x-direction as stated in table D.1, and the tip angle from 0° to 80° in steps of 10° in the y-direction. Next to this square of pillars, text is written with information regarding the printing parameters of that square. Out of this square a matrix of squares is created. This is presented in figure C.6A. In the x-direction the scan speed varies from 10 000 µm s^{-1} to 2500 µm s^{-1} in steps of 2500 µm s^{-1} and in the y-direction the laser power varies from 12.5 mW to 22.5 mW in steps of 2.5 mW. This graphically represented in figure C.6B.

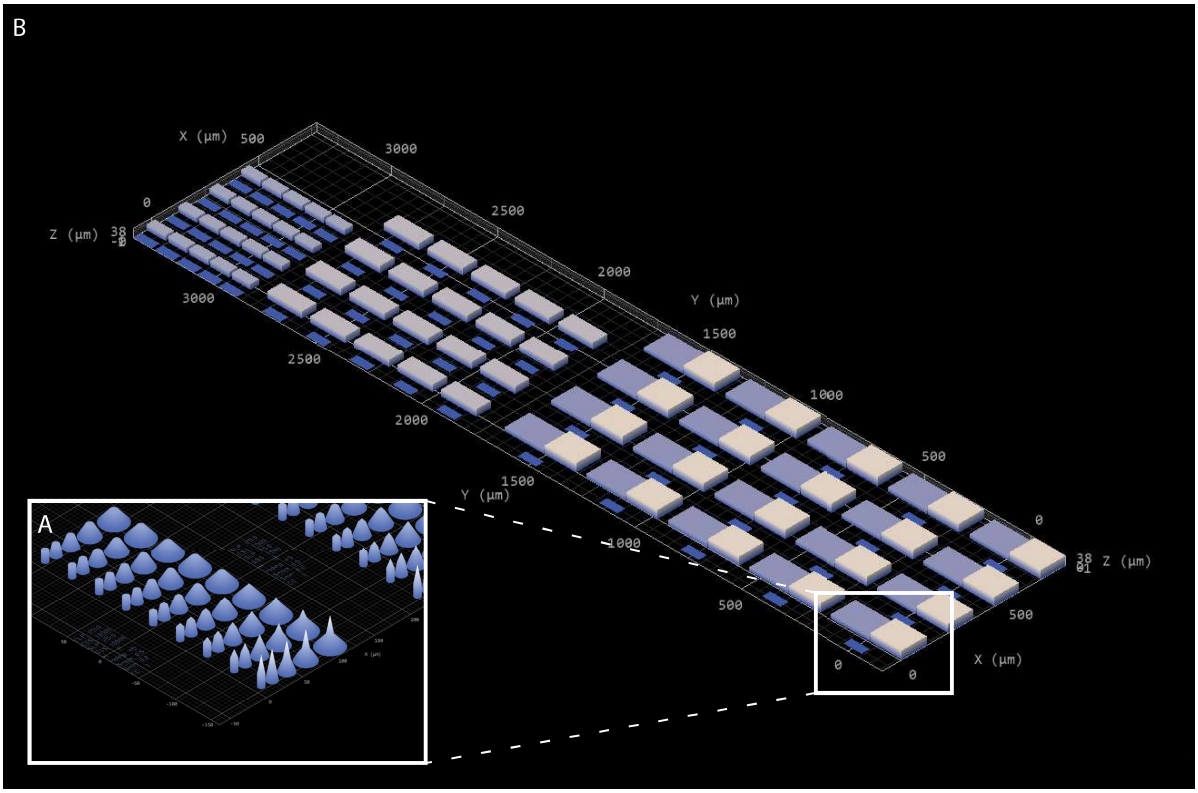

Figure C.6: 3D preview of the print job to determine the influence of the slicing distance. A: Close up of one square of pillars in which the base angle is varied in the x-direction and the tip angle is varied in the y-direction. B: Overview of the complete print job in which the scan speed is varied in the x-direction and the laser power is varied in the y-direction. This is done per diameter pillar.

Influence of the 25x objective in comparison with the 63x objective

Five STL files are created which could also be used to imprint 1 mm by 1 mm membranes. A 3D preview of the final job file in Describe is given in figure C.7A. Following the y-axis, the first field of pillars consists of 0.4 µm pillars in diameter with a center to center spacing of 7 µm between them. This is also shown in figure C.7A. Subsequently, pillars which are 1um in diameter are placed with a spacing of 7.04 µm center to center. The field in the middle consists of pillars which are 3 µm in diameter and with a center to center spacing of 7.04 µm. The next field has pillars of 5 µm in diameter which are placed 15.63 µm, center to center apart from each other. The last field consists of pillars which are 8 µm in diameter and have a center to center spacing of 31.25 µm. These STL files are converted to job files and placed in such a manner to create the 5 fields of pillars placed behind each other of which each field is 1 mm by 1 mm. A 3D preview is presented in figure C.7B. All the pillars are compiled and printed according to the optimal parameters which are presented in table C.3. For the 3 µm pillars a laser power of 20 mW is selected.

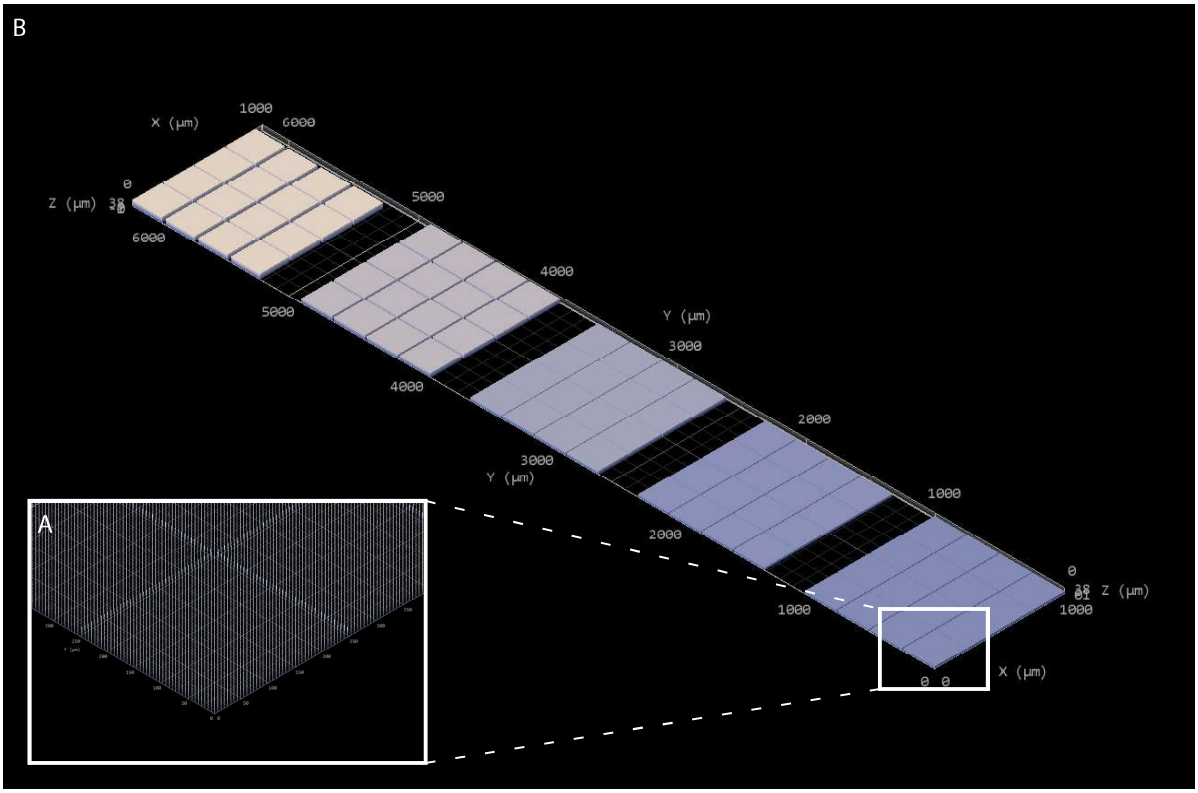

Figure C.7: 3D preview of the print job for printing 1 mm by 1 mm fields of pillars with different diameters with the 25x objective. A: Close up of the field of pillars with a diameter of 0.4 µm. B: Overview of the print job with the varying laser power in the x-direction and the different diameters of pillars in the y-direction.

Electrodes 5 µm in height

A contour of the selected sensor design is printed to be used to decouple to conductive layer. A contour is made of the design of the sensor which is scaled down until the fingers are 1 µm in thickness and have a spacing between the fingers of 1 µm. The same contour is also scaled down until the fingers are 0.5 µm in thickness and have a spacing between the finger of 0.5 µm.[33] Both sensors are 5 µm in height. Next to the contour of one sensor, text is written with information regarding the printing parameters of that contour. Out of the contour of the sensor of 1 µm in finger spacing a matrix is made with varying the scan speed from 20 000 µm s^{-1} to 5000 µm s^{-1} in steps of 5000 µm s^{-1} in the x-direction and varying the laser power from 5 mW to 20 mW in steps of 5 mW the y-direction. The same is done for the sensor contour with a finger spacing of 0.5 µm and is placed next to the matrix of the contours of the sensor which have a finger spacing of 1 µm. This is visualized in figure C.8.

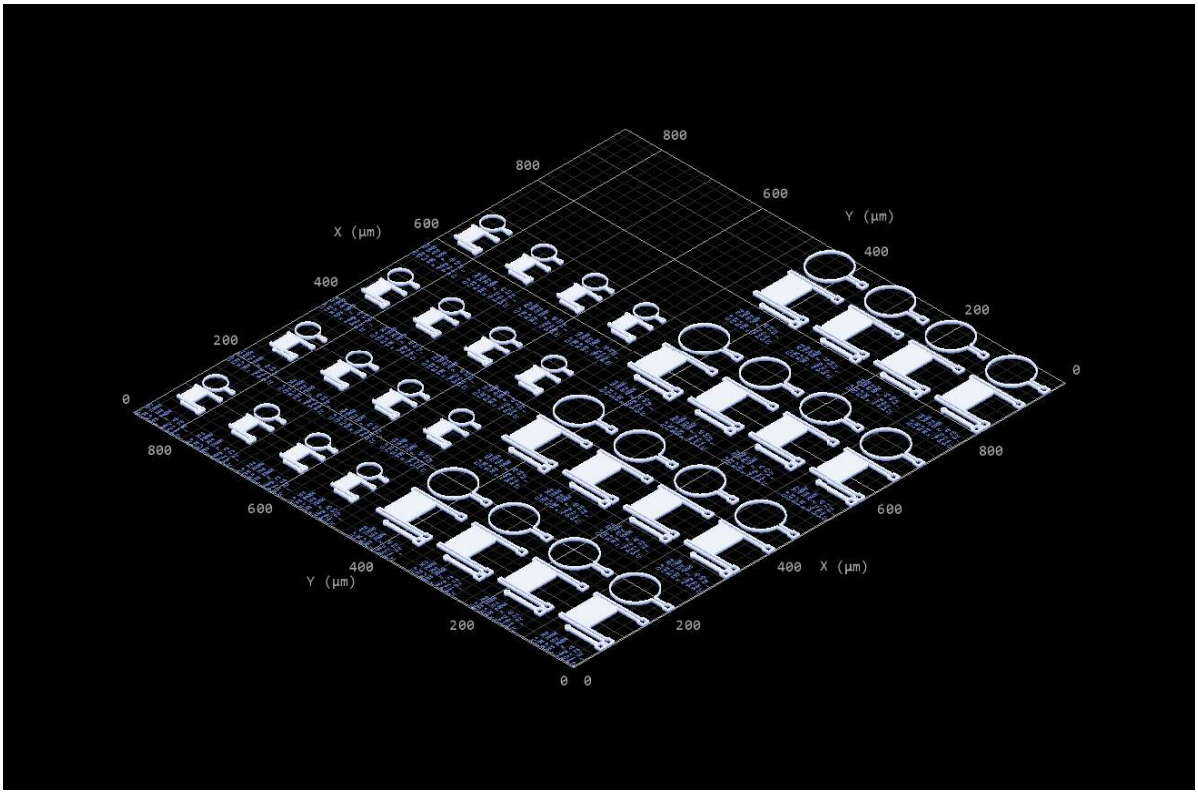

Figure C.8: 3D Preview of the print job for printing electrodes which are 5 µm in height with the varying scan speed in the x-direction and varying laser power in the y-direction.

Electrodes 1 µm, 2 µm, 3 µm and 4 µm in height

The same print job as presented in figure C.8 is used. The difference is the laser power which is varied in from 5 mW to 30 mW in steps of 5 mW in the y-direction. The print job is lowered in height. A close up of the new print job is given in figure C.9A. The print job is printed four times, varying the height of the contour of the sensor from 1 µm to 4 µm in steps of 1 µm, shown in figure C.9B.

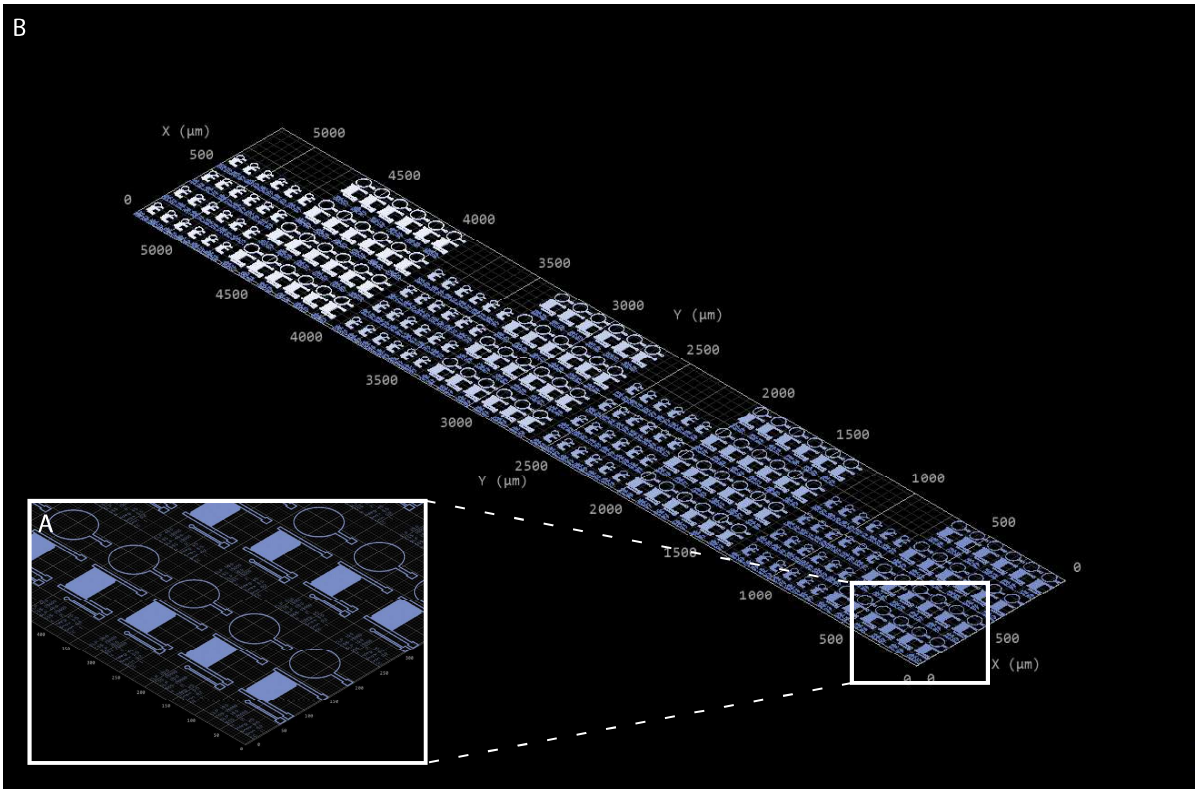

Figure C.9: 3D Preview of the print job for printing contours of the sensor of different sizes and of different heights. A: Close up of the contour of the sensor of 1 µm in height and 1 µm in finger spacing. B: Overview of the print job with the varying scan speed in the x-direction and varying laser power in the y-direction. The different sizes and heights of the contour of the sensor are placed behind each other in the y-direction.

Electrodes with sharp edges

The same print job as presented in figure C.9 is used, but sharp edges are added with an angle of 80°. The height of the contours is lowered with 1 µm. So, the first set of contours just consists of the added sharp edge, which is shown in figure C.10A. A 3D preview of the new print job is given in figure C.10B.

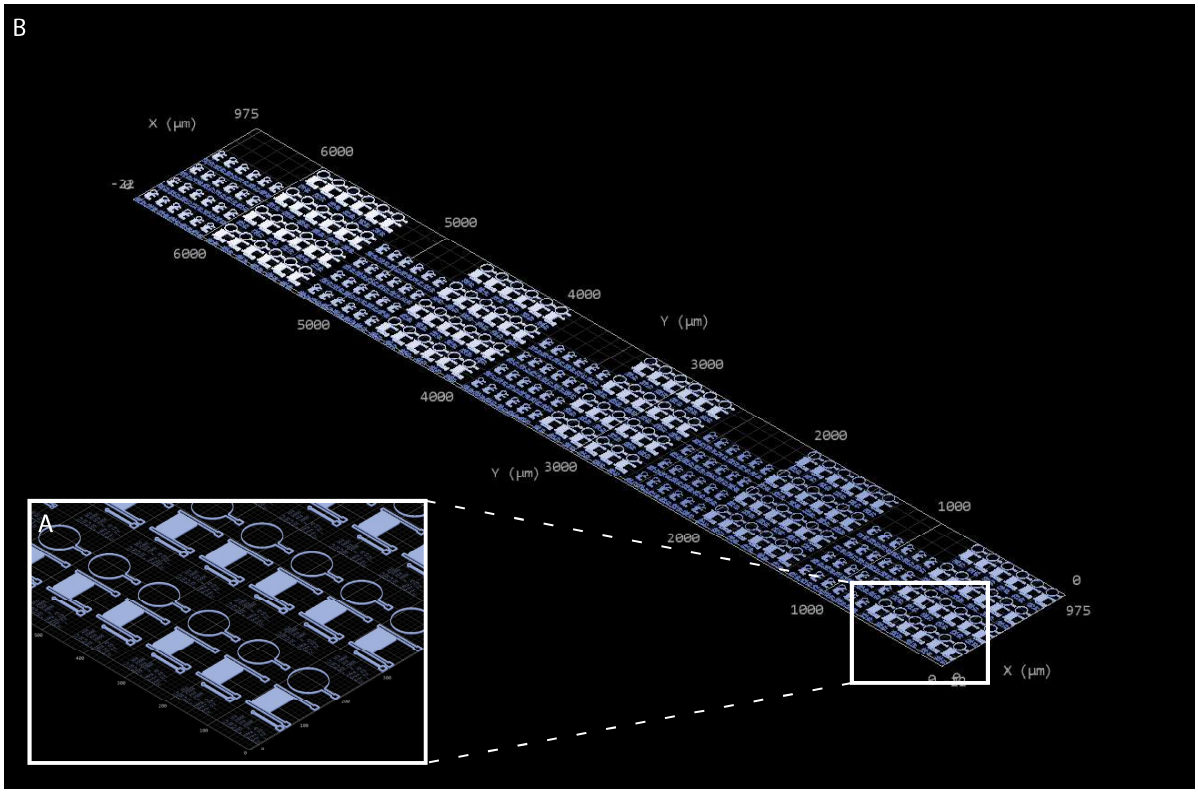

Figure C.10: 3D Preview of the print job for printing contours of the sensor of different sizes and of different heights. A: Close up of the contour of the sensor of which only contains the sharp edge. B: Overview of the print job with the varying scan speed in the x-direction and varying laser power in the y-direction. The different sizes and heights of the contour of sensor are placed behind each other in the y-direction.

C.2.2. Substrate protocols

Experiments are performed to establish protocols for spin coating the different layers. Also, there is looked into the best way of stacking the different layers on top of each other.

Protocol for spin coating uniform layers of TOPAS

The goal of this experiment is to find a protocol for dissolving TOPAS granules into toluene and to find a spin coating protocol to create uniform layers of TOPAS for different spin speeds.

A glass bottle is cleaned with ethanol absolute and placed in the fume hood (Vinitex) to let it evaporate for one hour. Cyclic olefin copolymer granules (TOPAS 8007X-10, TOPAS) and toluene (Honeywell, Riedel-de Haën) are added to the bottle to create a 20wt% solution. The bottle is placed in an ultrasonic cleaner (SHESTO SHE-UT8031-EUK) with full sinus waves until, when you tilt the bottle, the solution is viscous and fluidic. It will be investigated if shaking the solution with an orbital shaker speeds up the process. Glass Petri dishes (Ø60, DURAN Group) are cleaned with acetone and 2-propanol, and placed in the oven (Memmert UN30) at 150 °C for 15 min to dehydrate. The glass Petri dishes are placed in the fume hood to cool down to room temperature. The influence of the amount of solution dispensed, dispense spin coating techniques, the spin coating speeds, number of spin coating steps, spin coating durations, and spin accelerations is investigated. The layers will be spin coated (Polos 150i) on the outside of the glass Petri dish which will it makes it easier to peel them off afterwards. The samples are left to dry overnight in the fume hood. The spin coated TOPAS films will be inspected visually to judge whether they covered the complete Petri dish.

TOPAS film thickness

The goal of this experiment is to find the influence of different spin speeds. This will be examined in this experiment to determine the preferred spin speed.

From the results regarding spin coating an uniform film of TOPAS, in figure C.43, the following protocol is formulated to manufacture an uniform film of TOPAS. A glass bottle is cleaned with ethanol absolute and placed in the fumehood to let it evaporate for 1 h. Cyclic olefin copolymer granules and toluene are added to the bottle to create a 20wt% solution. The bottle is placed in an ultrasonic cleaner with full sinus waves for

15 min. Subsequently, the bottle is placed on top of an orbital shaker at 2200 RPM for 10 min. This is repeated until, when you tilt the bottle, the solution is viscous and fluidic. Glass Petri dishes are cleaned with acetone and 2-propanol, and placed in the oven at 150 °C for 15 min to dehydrate. The Petri dishes are placed in the fume hood to cool down to room temperature. The spin coating process consists of two steps. The first step has a spin time of 50 s, and the spin speed will be varied from 500 RPM to 5000 RPM in steps of 500 RPM. At the second step, the sample is spin coated for 30 s seconds at 100 RPM. The acceleration for both steps is 250 RPM/s. 1 mL of the TOPAS solution is spin coated, on the outside of the Petri dish, with a static dispense spin coating technique. The samples are left to dry overnight in the fume hood.

The spin coated TOPAS films, which cover the complete surface of the Petri dish, will be cut in half with a knife, and one half is removed from the Petri dish. With the interferometer (Bruker GT-K1), the difference in height between the top of the TOPAS film and surface of the Petri dish will be measured at eleven different locations, 5 mm apart, which are evenly distributed along the cutted edge of the TOPAS layer.

PAA film thickness

The goal of this experiment is to find the influence of different spin speeds on the thickness of the layer. To find the maximal required spin speed.

A glass Petri dish is treated for 30 s with oxygen plasma at 60 W (Diener Femto). A 30 wv% solutions of poly(acrylic acid), PAA, (average M_w 1800, Sigma-Aldrich) and DI water is prepared by adding the correct amounts into a Falcon tube, and place it on an orbital shaker at 2200 RPM until the PAA is completely dissolved. 1.5 mL of the solution, is dynamically dispended on the outside of the Petri dish during the spin coating process. The spin speed are varied from 500 RPM to 1250 RPM in steps of 250 RPM, the spin time is 45 s and the accelaration is 500 RPM/s. The samples are baked at 60 °C for 20 min in the oven.

The thickness of the resulting PAA layers, which cover the complete surface of the Petri dish, will be measured by making a scratch, from edge to edge of the Petri dish, through the PAA layer in the middle of the Petri dish. The height difference between the surface of the Petri dish and the PAA layer will be measured with the interferometer at eleven different locations, 5 mm apart, evenly distributed over the length of the scratch.

Additional spin coating and casting experiments PAA

Additional experiments are performed to investigate whether layers of PAA could be spin coated which are more in the range of the desired thickness. Four different spin coat setting will be used, spin coating a PAA film at 500 RPM with a spin coat time of 15 s, spin coating a PAA film at 1000 RPM with a spin coat time of 5 s, spin coating a PAA film at 1000 RPM with a spin coat time of only 15 s, and spin coating a PAA film at 1000 RPM with a spin coat time of only 15 s, but this time, a solution of 70 wv% is used instead of the 30 wv%. Also, a casting method will be used. A sidewall is made out of adhesive tape in the first experiment, and in the second experiment, a sidewall is made out of aluminum foil and duct tape. The aluminum foil is added to prevent the PAA layer to be stuck to the duct tape.

PEDOT:PSS film thickness

The goal of the experiment is to find the influence of different spin speeds on the thickness of the layer and the corresponding sheet resistance will be examined in this experiment to determine the preferred spin speed. The used protocol is based on an in-house protocol and it is known that it will result in uniform layers.[19]

A glass Petri dish is treated for 5 min with oxygen plasma at 60 W. 2 mL of poly(3,4-ethylene- dioxythiophene)-poly(styrenesulfonate), PEDOT:PSS, (1.3 wt% dispersion in H_2O, Sigma-Aldrich), is dynamically dispended on the outside of a glass Petri dish during the spin coating process. The spin speed will be varied from 500 RPM to 1500 RPM in steps of 250 RPM, the spin time is 60 s with an spin accelaration of 1000 RPM/s. The samples are left to dry overnight in the fumehood.

The thickness of the resulting PEDOT:PSS layers, which cover the complete surface of the Petri dish, will be measured by making a scratch, from edge to edge of the Petri dish, through the PEDOT:PSS layer in the middle of the Petri dish. The height difference between the surface of the Petri dish and the PEDOT:PSS layer will be measured with the interferometer at eleven different locations, 5 mm apart, evenly distributed over the length of the scratch. The sheet resistance is determined by measuring the corresponding voltage after applying a current ranging from -1.0mA to 1.0mA in steps of 0.2mA with a 4-point probe (Signatone couple with a Keithley Sourcemeter 2400 and Nanovoltmeter 2182) at the middle of the sample and at the edge of the sample.

Multilayer substrate manufacturing protocol

Three different orders of spin coating the different layers on top of each other is examined to find the optimal order. First, spin coating the PAA 30w/v% solution on the TOPAS layer, flipping it, and spin coating the

PEDOT:PSS layer on the other side. And this is placed on a different TOPAS sheet (Thickness of 300 µm, glass transition temperature of 70 °C, microfluidic ChipShop). Second, the PEDOT:PSS is spin coated on top of the TOPAS layer, flipped over, and a layer of PAA is spin coated on the other side. And placed on a different TOPAS sheet. At last, PEDOT:PSS is spin coated on top of the TOPAS layer and the PAA layer is spin coated on a different TOPAS sheet which are added together manually.

By placing the layers on top of each other, air bubbles are trapped between the layers. Four ways of removing air bubbles is looked into. Removing them by pushing them away by hand, pushing the air away with a tweezer, sliding away the air bubbles with a red stirring stick, and by placing it in a vacuum in the desiccator (Space-Saver, Bel-Art Products). The results will be visually inspected to select the best method.

C.2.3. Imprinting protocol

The multilayer substrate will be imprinted with a soft mold which is manufactured by a 2-photon polymerization process. This manufacturing process of the soft mold results in a polymeric imprinting tool. Imprinting force, imprinting temperature, and holding time are the most influential parameters.[88] Further, it is expected that the tip angle will influence the ability to create through-holes, just like the insertion of a microneedle into the skin.[83] The required base angle of the pillars will be investigated as well. A larger base angle results in a larger surface at the glass coverslip which results in a bigger adhesion force between the glass coverslip and the pillar but the minimal center to center spacing of the pillars increases.

The soft mold nano imprint lithography process was performed with a wafer bonder system (EVG 510, EV Group). The mold and the multilayer substrate were placed between Kapton foil with on top a small graphene sheet and a big graphene sheet. Within the software of the wafer bonder, a program had to be written to be able to perform all the steps of the imprinting process. This is already written within the software, and is presented in table C.2.

Table C.2: Program used for imprinting.

Command	Parameter 1	Parameter 2	Parameter 3	Parameter 4
Set Temperature	Heat Target: Both	Setpoint: 40 °C	Gradient: 20 °C/min	Allow active cooling: no
Wait Temperature	Heat Target: Both	Mode: higher	Temperature: 38 °C	
Evacuate	Mode: low			
Timer	Timer: 0:00:03.0 hh:mm:ss.s			
Wait Pressure	Mode: lower	Pressure: 1.000 mbar		
Flags	Left Flag: pull out	Center Flag: pull out	Right Flag: pull out	
Timer	Timer: 0:00:10.0 hh:mm:ss.s			
Evacuate	Mode: off			
Set Temperature	Heat Target: Both	Setpoint: 120 °C	Gradient: 20 °C/min	Allow active cooling: no
Wait Temperature	Heat Target: Both	Mode: higher	Temperature: 108 °C	
Piston Down	Setpoint: 4000 N	Gradient: max N/min		
Timer	Timer: 0:10:00.0 hh:mm:ss.s			
Purge	Mode: vent			
Wait Pressure	Mode: higher	Pressure: 800.0 mbar		
Purge	Mode: Off			
Set Temperature	Heat Target: Both	Setpoint: 30 °C	Gradient: 20 °C/min	Allow active cooling: no
Wait Temperature	Heat Target: Both	Mode: lower	Temperature: 55 °C	
Piston Up				

Imprinting force

The goal of this experiment is to determine which imprinting force is optimal. Therefore, a soft mold has to be printed with the Photonic Professional GT to imprint into the substrate which consists of 4 layers which is presented in the figure 3.1. A 3D preview of the print job is presented in figure C.11. The print job consists of some pillars and electrodes which are shown in figure C.11A. And placing two of those next two each other in each direction results in four times the same pillars and electrodes, which can be seen in figure C.11B. One of the small squares presents a field of pillars of which in the x-direction the base angles varies and in

the y-direction, the tip angle varies like the print job in figure C.5. In the x-direction, the different squares of a certain diameter of pillars are placed next to each other. And in the y-direction, the same diameters, base angles, and tip angles are used but the center to center spacing is larger. For the pillars of 8 µm in diameter, the center to center spacing between the same rows of pillars is 47.53 µm. And the center to center spacing from the biggest base angle to the smallest base angle is 43.60 µm, 36.48 µm, 30.46 µm, and 25.00 µm. For the pillars of 5 µm in diameter, the center to center spacing between the same rows of pillars is 28.48 µm. And the center to center spacing from the biggest base angle to the smallest base angle is 28.48 µm, 25.66 µm, 22.96 µm, and 20.31 µm. For the pillars of 3 µm in diameter, the center to center spacing between the same rows of pillars is 20.16 µm. And the center to center spacing from the biggest base angle to the smallest base angle is 20.16 µm, 19.10 µm, 18.05 µm, and 17.00 µm. For the pillars of 1 µm in diameter, the center to center spacing between the same rows of pillars is 18.71 µm. And the center to center spacing from the biggest base angle to the smallest base angle is 18.71 µm, 17.64 µm, 16.58 µm, and 15.53 µm. For the pillars of 0.4 µm in diameter, the center to center spacing between the same rows of pillars is 14.24 µm. And the center to center spacing from the biggest base angle to the smallest base angle is 14.24 µm, 13.71 µm, and 13.19 µm. The 0.4 µm pillars with a base angle of 0° are not modelled. At the top of figure C.11B, contours of the sensor are shown. The first row are contours of the sensor with a spacing between the fingers of 1 µm and in the x-direction the height varies from 1 µm to 4 µm in steps of 1 µm just like the print job in figure C.9. In the row above electrodes with a spacing between the fingers of 0.5 µm are printed with a height of 1 µm and 2 µm. An imprinting temperature of 120 °C is used, which is 50 °C above the glass transition temperature.[108] And a holding time of 10 min is used. These parameters are found to be optimal.[88] A force of 4000 N and 5000 N is used to see the influence of the imprinting force.

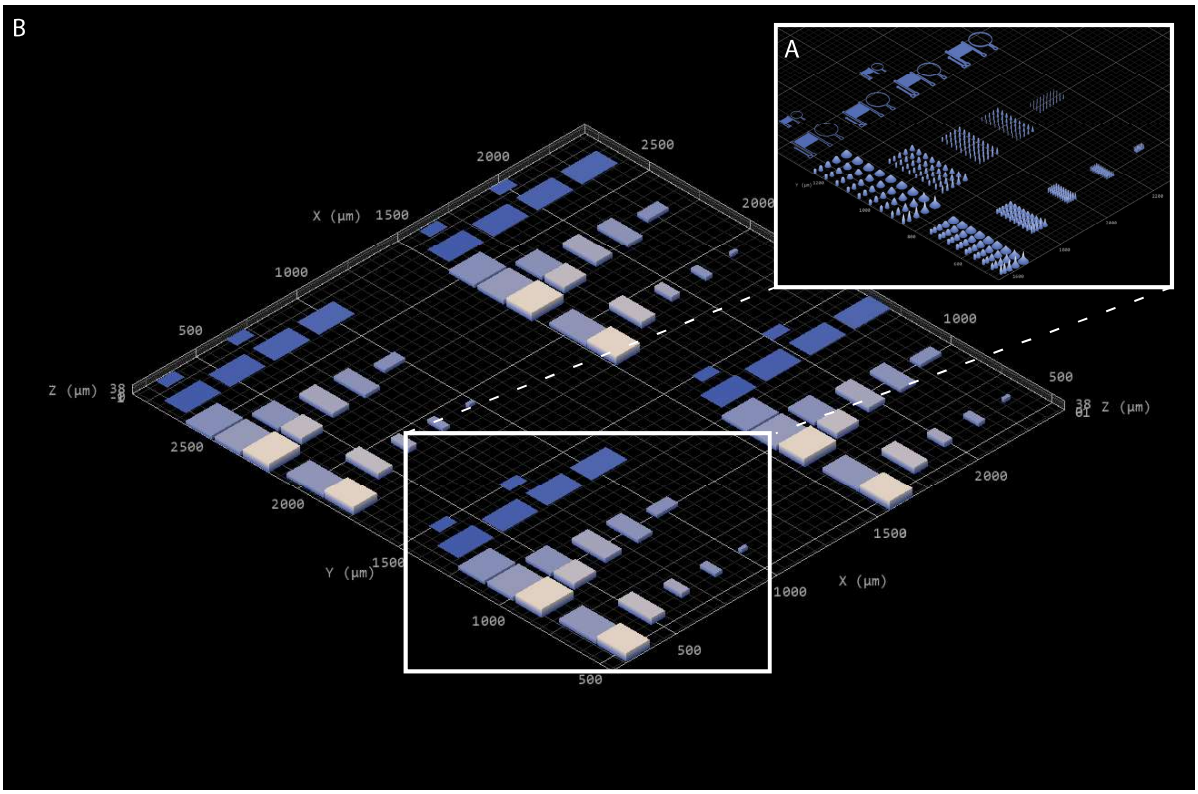

Figure C.11: 3D Preview of the print job used for imprinting pillars with different diameters, base angles, center to center spacing, and tip angles. And for imprinting contours of the sensor of different heights and sizes. A: One matrix with the contours of the sensor of different heights in the x-direction and different sizes in the y-direction on top. The two rows below contain pillars with different center to center spacings, with the smaller center to center spacing on the bottom. In one row the diameter of the pillars is varied per small field of pillars in the x-direction. Within such a field of pillars, the base angle is varied in the x-direction and the tip angle is varied in the y-direction. B: Overview of the print job which contains four times the matrix with all the structures to test all the variables.

Imprinting influence of the tip angle of the pillars with sharp tips

The same kind of print job is used to manufacture the soft mold as presented in figure C.11. But some small variations in the tip angles are introduced, to be able to test the influence of the tip angle. Three new versions

of this print job are created. The first one consists of 3 rows of pillars with a tip angle of 60°, 3 rows of pillars with a tip angle of 70°, and 3 rows of pillars with a tip angle of 80°. The 3D preview of this print job is shown in figure C.12. This version will give an indication if a relatively sharp tip angle is needed or not. The second version of the print job consists of pillars which all have a tip angle of 80°, figure C.13. And the third version has pillars all with a tip angle of 70°, presented in figure C.14. These two versions will verify if one of these tip angles is necessary for creating through-holes. The first two version will be immersed in ethylene glycol, EG, (anhydrous, 99.8%, Sigma-Aldrich) for 15 min, and the last version for 2 h after imprinting.

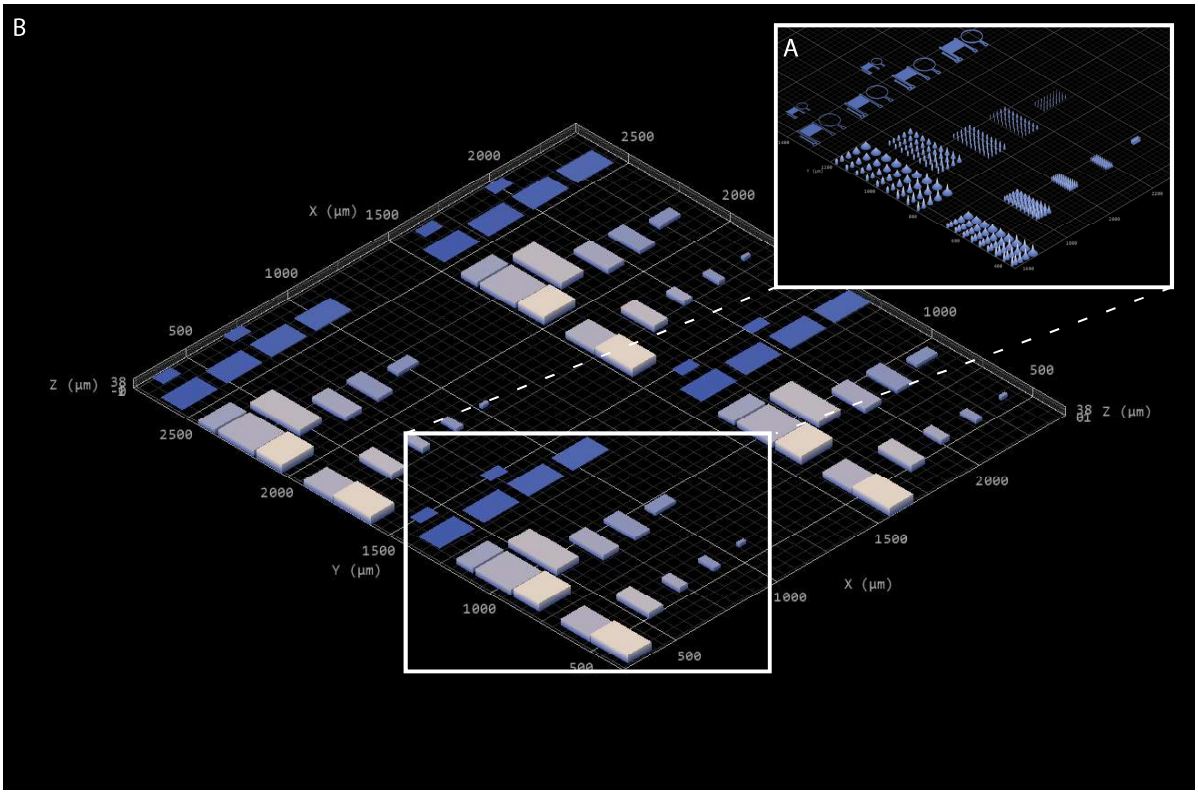

Figure C.12: 3D Preview of the print job used for imprinting pillars with different diameters, base angles, center to center spacing, and tip angles. And for imprinting contours of the sensor of different heights and sizes. A: One matrix with the contours of the sensor of different heights in the x-direction and different sizes in the y-direction on top. The two rows below contain pillars with different center to center spacings, with the smaller center to center spacing on the bottom. In one row the diameter of the pillars is varied per small field of pillars in the x-direction. Within such a field of pillars, the base angle is varied in the x-direction and the tip angle is varied in the y-direction. B: Overview of the print job which contains four times the matrix with all the structures to test all the variables.

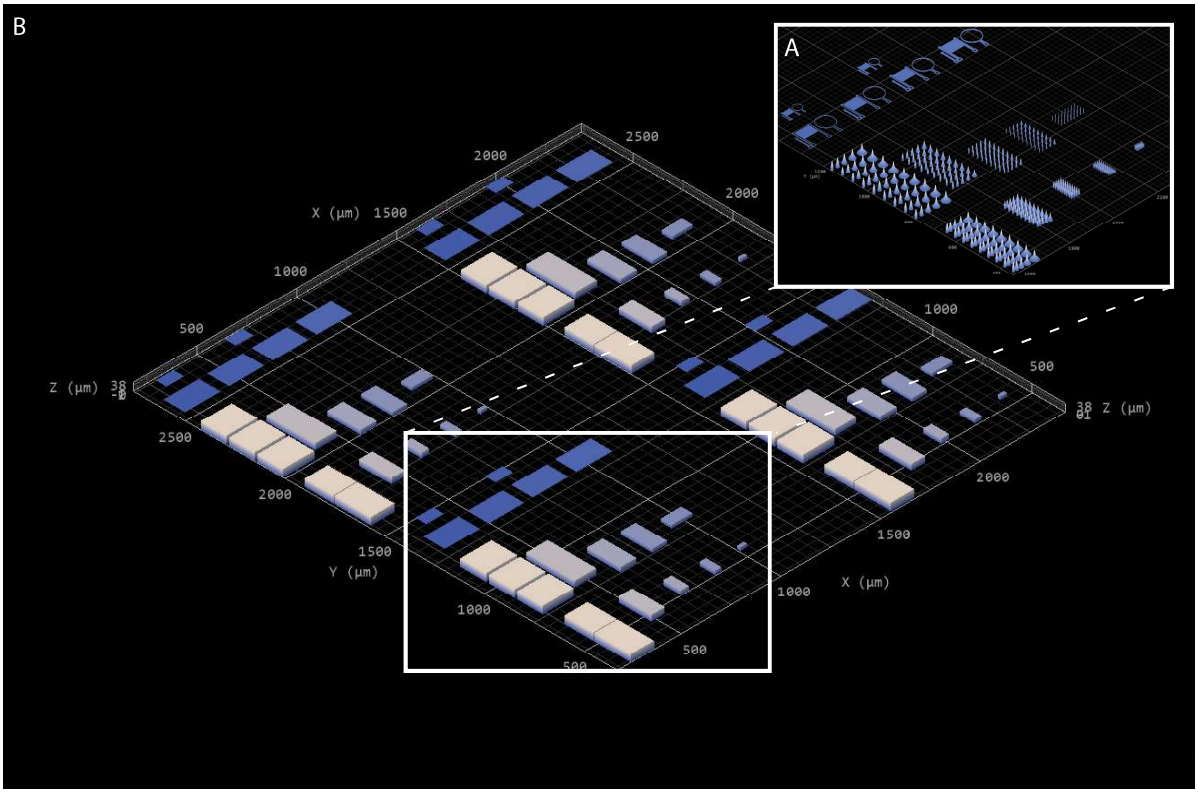

Figure C.13: 3D Preview of the print job used for imprinting pillars with different diameters, base angles, center to center spacing, and tip angles. And for imprinting contours of the sensor of different heights and sizes. A: One matrix with the contours of the sensor of different heights in the x-direction and different sizes in the y-direction on top. The two rows below contain pillars with different center to center spacings, with the smaller center to center spacing on the bottom. In one row the diameter of the pillars is varied per small field of pillars in the x-direction. Within such a field of pillars, the base angle is varied in the x-direction and a constant tip angle of 80° in the y-direction. B: Overview of the print job which contains four times the matrix with all the structures to test all the variables.

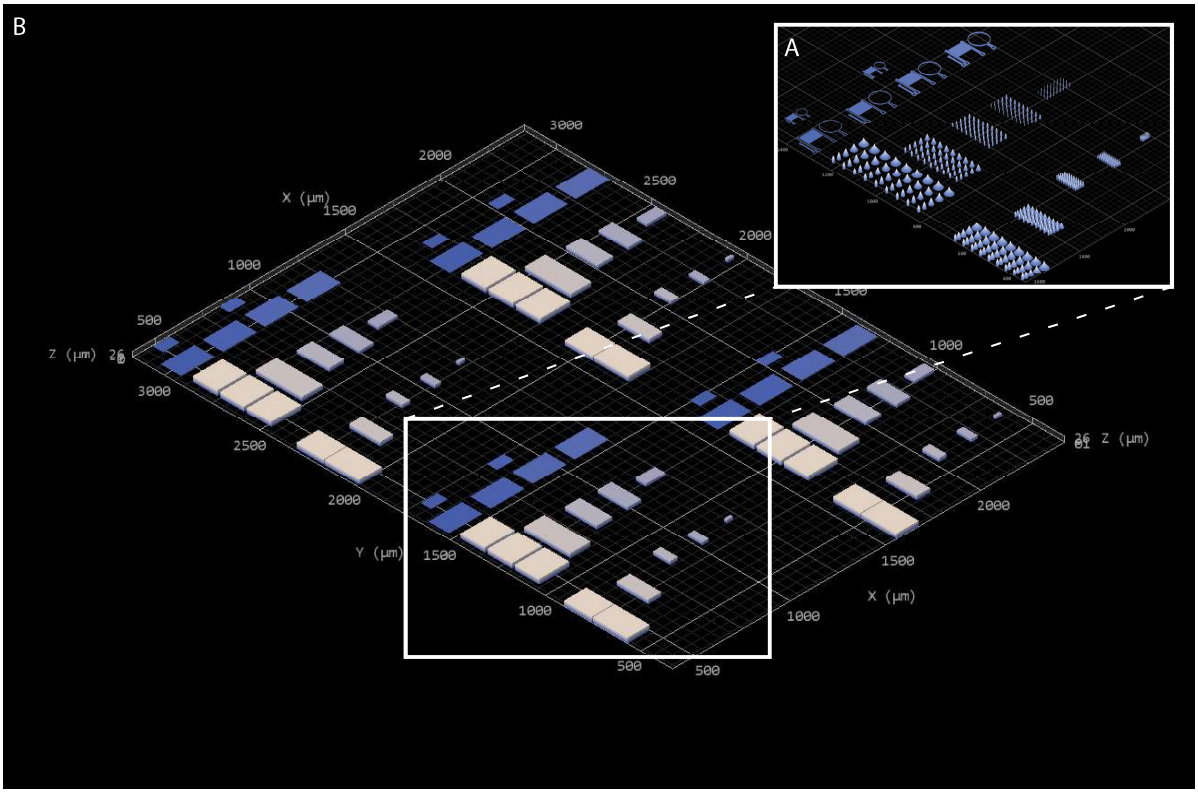

Figure C.14: 3D Preview of the print job used for imprinting pillars with different diameters, base angles, center to center spacing, and tip angles. And for imprinting contours of the sensor of different heights and sizes. A: One matrix with the contours of the sensor of different heights in the x-direction and different sizes in the y-direction on top. The two rows below contain pillars with different center to center spacings, with the smaller center to center spacing on the bottom. In one row the diameter of the pillars is varied per small field of pillars in the x-direction. Within such a field of pillars, the base angle is varied in the x-direction and a constant tip angle of 70° in the y-direction. B: Overview of the print job which contains four times the matrix with all the structures to test all the variables.

Imprinting temperature

The print job shown in figure C.13 is used to find the optimal temperature which can be used. By increasing the temperature, the polymer chains of the TOPAS increase in mobility which results in smaller replication errors of the mold.[88] The imprinting temperature will be increased by 10 °C to 130 °C. The other parameters like holding time (10 min) and imprinting force (4000 N) will remain the same.

Holding time

To find the influence of the holding time, The print job shown in figure C.13 is used. It is expected that longer holding times results in smaller replication errors.[88] A holding time of 20 min is used to investigate this. To be able to state the influence of the holding time, an imprinting temperature of 120 °C is used and an imprinting force of 4000 N is used.

C.2.4. Post treatment

Dissolving the PAA layer

The goal of this experiment is to find a suiting protocol for the post treatment step to dissolve the PAA layer. From literature, it is known that immersing the PEDOT:PSS layer for 10 min will result in the maximum increase of conductivity. And that it lowers the water solubility of the layer.[19] Three different protocols are tested. The first one is immersing the multilayer substrate for 15 min in EG. The second protocol is to immerse it for 2 h in EG. The last protocol is to place the substrate in EG in an ultrasonic cleaner for 14 min, followed letting it rest while immersed in EG for 2 h. The results will be compared to see whether it changes shape and/or size of the non-conductive PSS parts on the layer and to verify whether it improves the peeling of of the membrane. The PEDOT:PSS layer, which is on top of the multilayer substrate, will be imaged with a SEM before and after the EG treatment. After dissolving the PAA layer, the TOPAS layer will be sputter coated with a 6.5 nm layer of Au/Pd and imaged by the SEM.

C.3. Results and discussion

This chapter contains the results and discussion of the described experiments.

C.3.1. Soft mold manufacturing protocol

Pillars with a different sharp tips

An overview of the printed pillars is presented in figure C.15. The best set of pillars is shown in figure C.16A. These are printed with a laser power of 17.5 mW and a scan speed of 17 500 µm s^{-1}. Unfortunately, the pillars of 0.4 µm in diameter fell over. This has to be investigated why it is happening and how to prevent it from happening. Further, the designed tips of the pillars have some severe shrinkage phenomena, this has to be investigated as well.

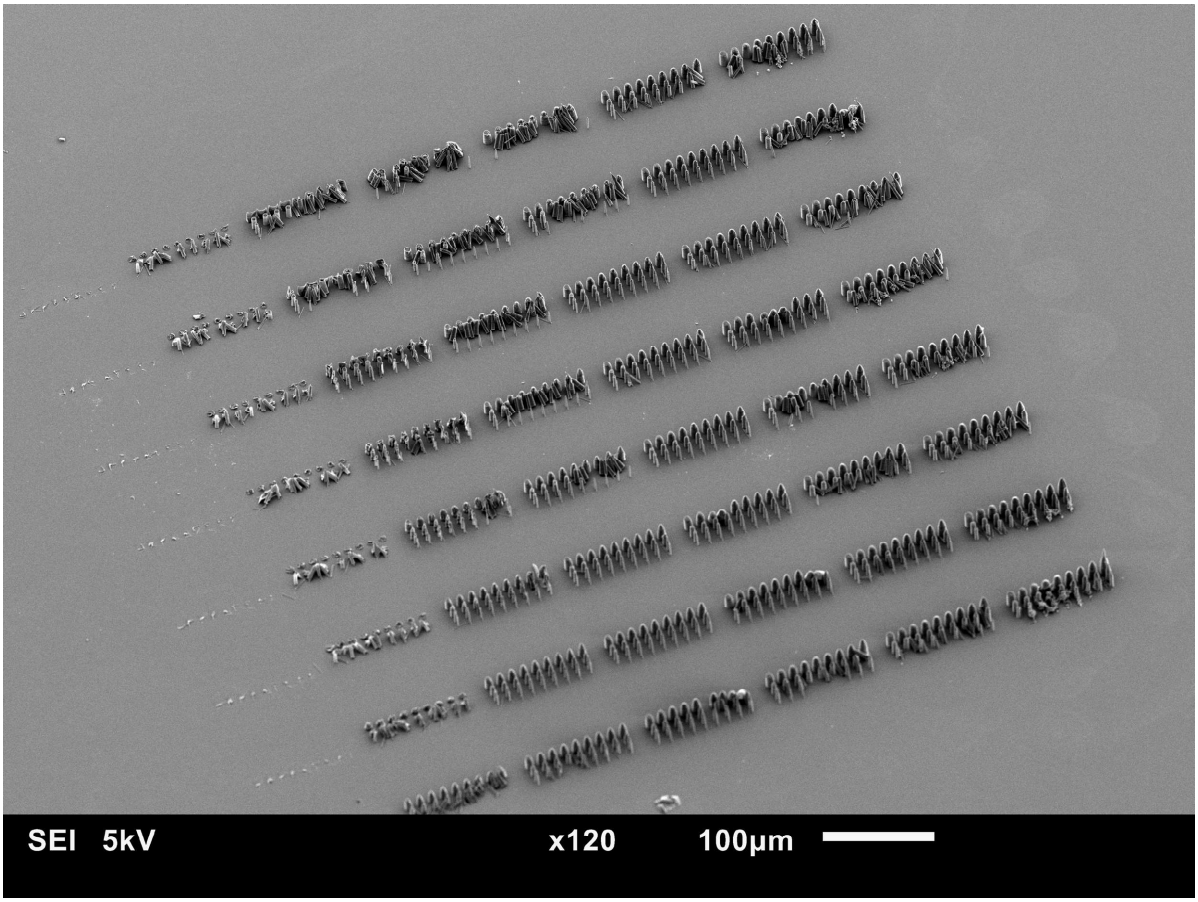

Figure C.15: Overview of the printed pillars with sharp tips and varying diameters.

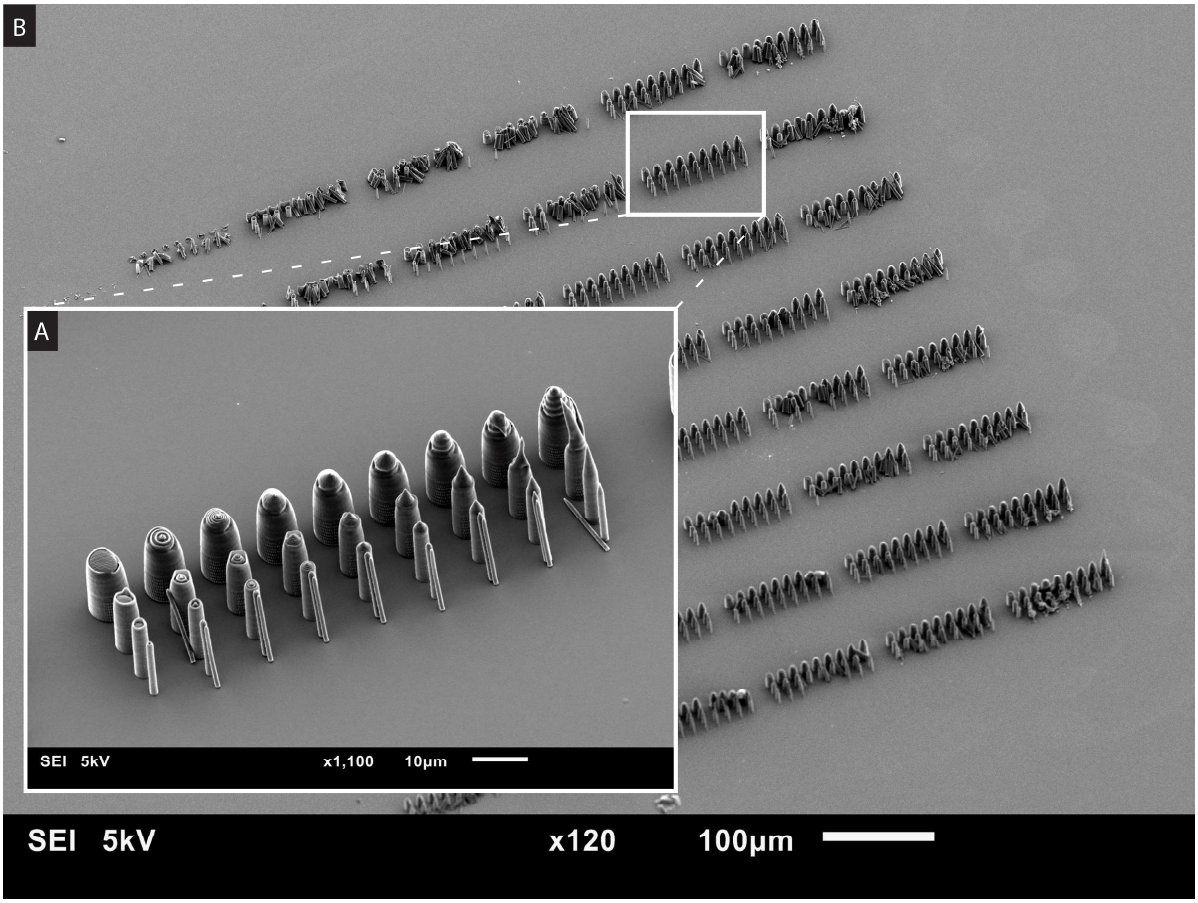

Figure C.16: Results of the printing pillars with sharp tips and varying diameters. A: Zoomed in on the set of pillars which looks the most like the modeled ones, printed with a laser power of 17.5 mW and a scan speed of 17 500 µm s^{-1}. B: Overview of the printed pillars with sharp tips and varying diameters.

Falling over of 0.4 µm pillars with sharp tips by the pillars with a base angle of 0°

The printed pillars of 0.4 µm in diameter with different base angles printed at different laser powers and scan speeds are presented in figure C.17.

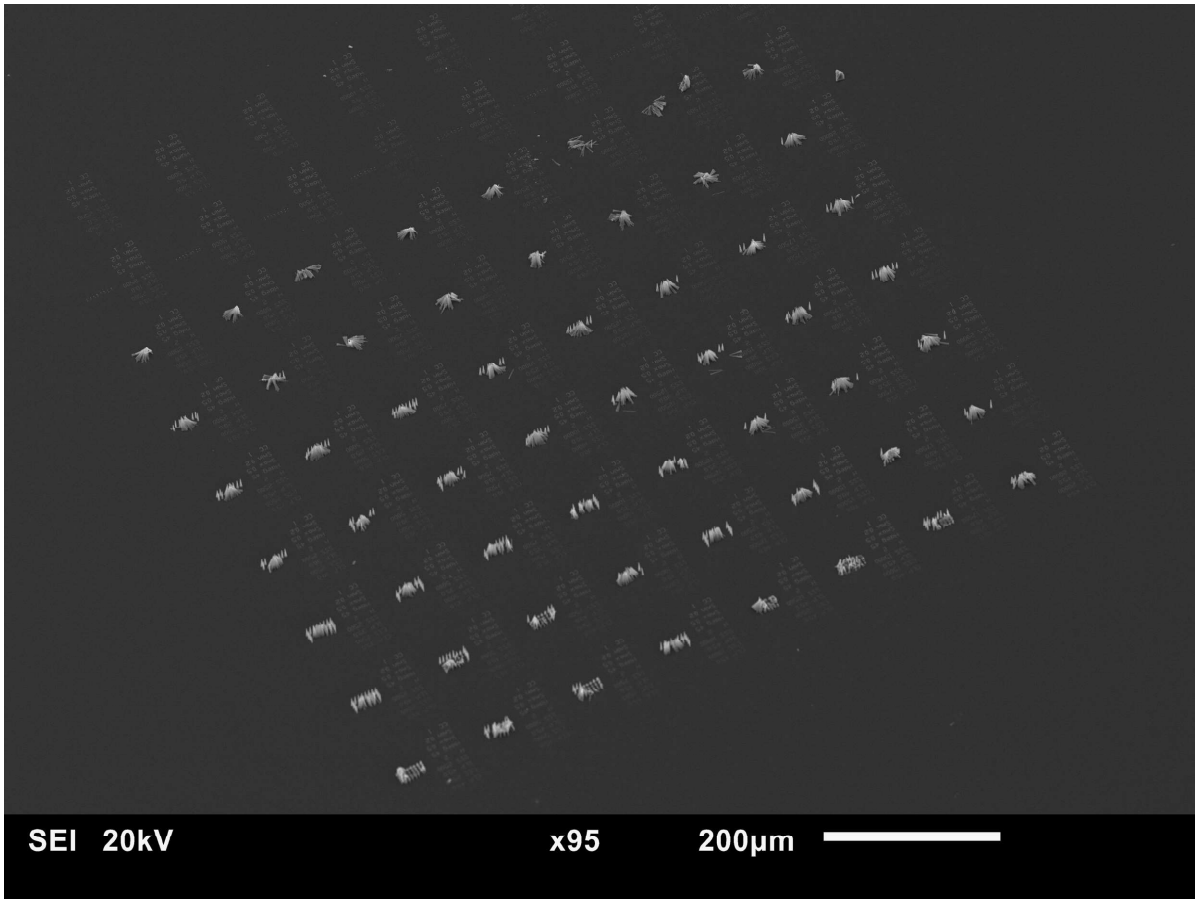

Figure C.17: Overview of the printed pillars regarding the influence of the base angle of 0.4 µm pillars to prevent them from falling over.

In figure C.18B, the same overview is presented as in figure C.17. But in figure C.18A, a close up of the printed pillars which looks the most like the modeled ones are presented, printed with a laser power of 22.5 mW and a scan speed of 2500 µm s^{-1}. The pillars with a base angle of 0° all tipped over. The pillars with a base angle of 4° are all still standing. Some of the pillars with a base angle of 1° to 3° fell over and some did not. From this, it can be concluded that a bigger base angle indeed prevents the pillars from falling over. But some more research has to be done to further understand why they are falling over.

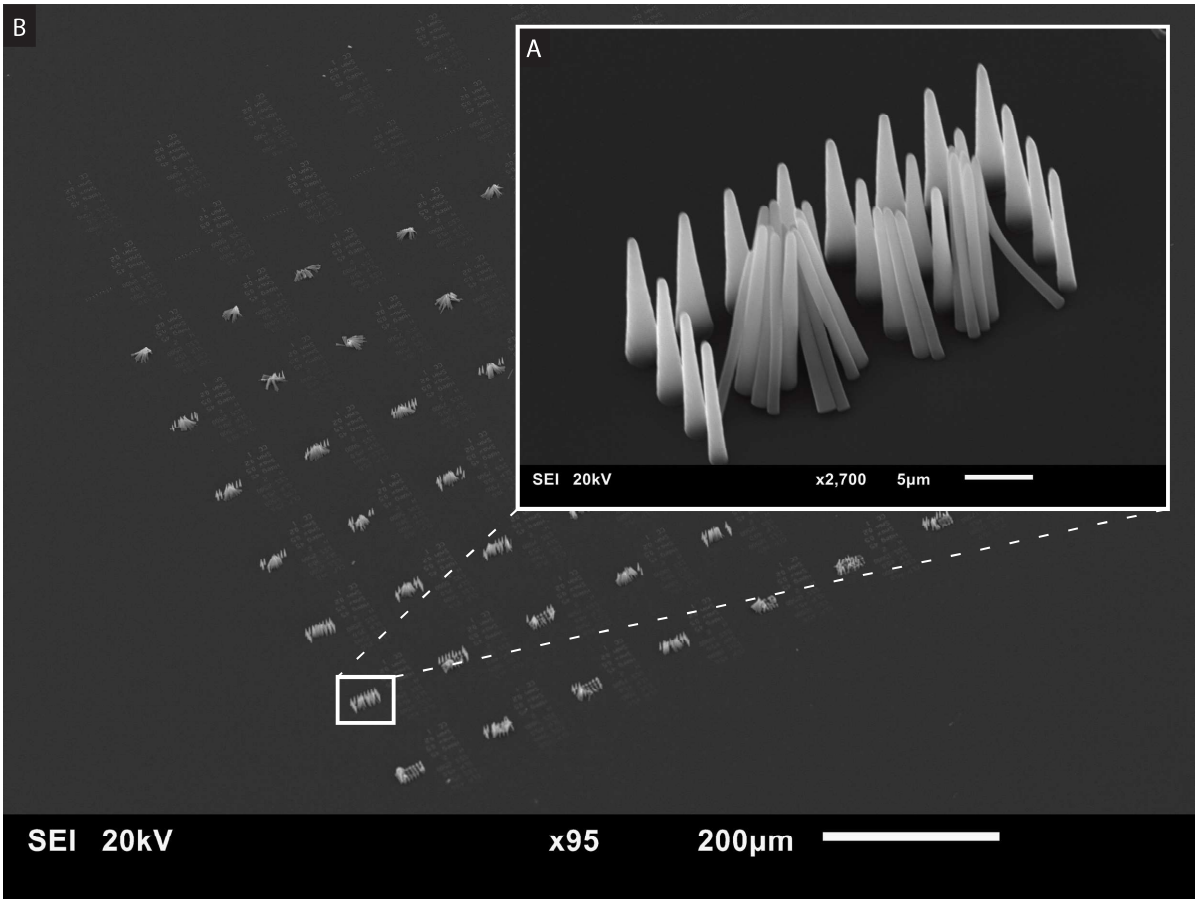

Figure C.18: Results of the printed pillars regarding the influence of the base angle of 0.4 µm pillars to prevent them from falling over. A: Zoomed in on the set of pillars which looks the most like the modeled ones, printed with a laser power of 22.5 mW and a scan speed of 2500 µm s^{-1}. B: Overview of the printed pillars.

Printing pillars with sharp tips

By visualy inspecting the SEM images of the printed pillars with sharp tips, presented in figure C.19, the optimal printing parameters are determined. These are presented in table C.3. The pins with 3 µm diameter has no clear optimal laser power. For all the pillars a scan speed of 2500 µm s^{-1} was found to be optimal. It can be concluded that a laser power of 22.5 mW is optimal for pillars with a larger diameter than 3 µm. And for pillars with a smaller diameter than 3 µm a laser power of 20.0 mW is optimal. Zoomed in SEM images of the pillars which are printed with the optimal parameters are presented in the figures C.20 to C.25. Comparing these SEM images with the SEM images of the results in figure C.16A, the designed tips are mostly printed successfully due to the increase of hatching distance from 0.2 µm to 2 µm. It can be concluded by comparing figure C.20 and figure C.18 that the 0.4 µm pillars with a 0° base angle did not cause the collapse of the other 0.4 µm pillars.

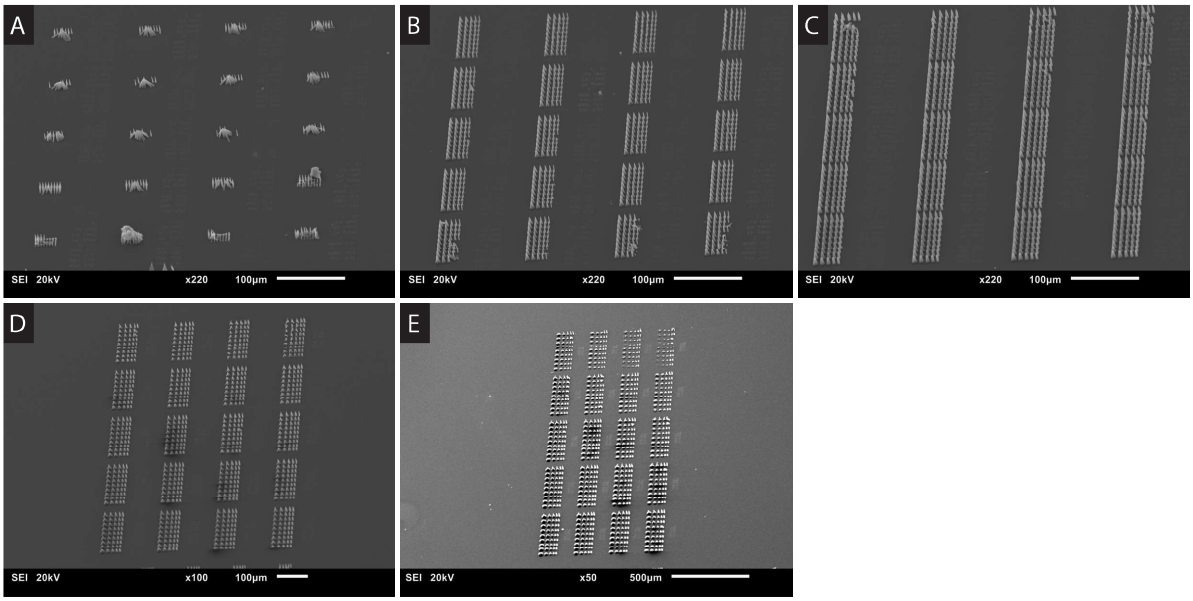

Figure C.19: Results of the printing pillars with sharp tips of different diameters. A: Overview of the printed pillars with a diameter of 0.4 µm. B: Overview of the printed pillars with a diameter of 1 µm. C: Overview of the printed pillars with a diameter of 3 µm. D: Overview of the printed pillars with a diameter of 5 µm. E: Overview of the printed pillars with a diameter of 8 µm.

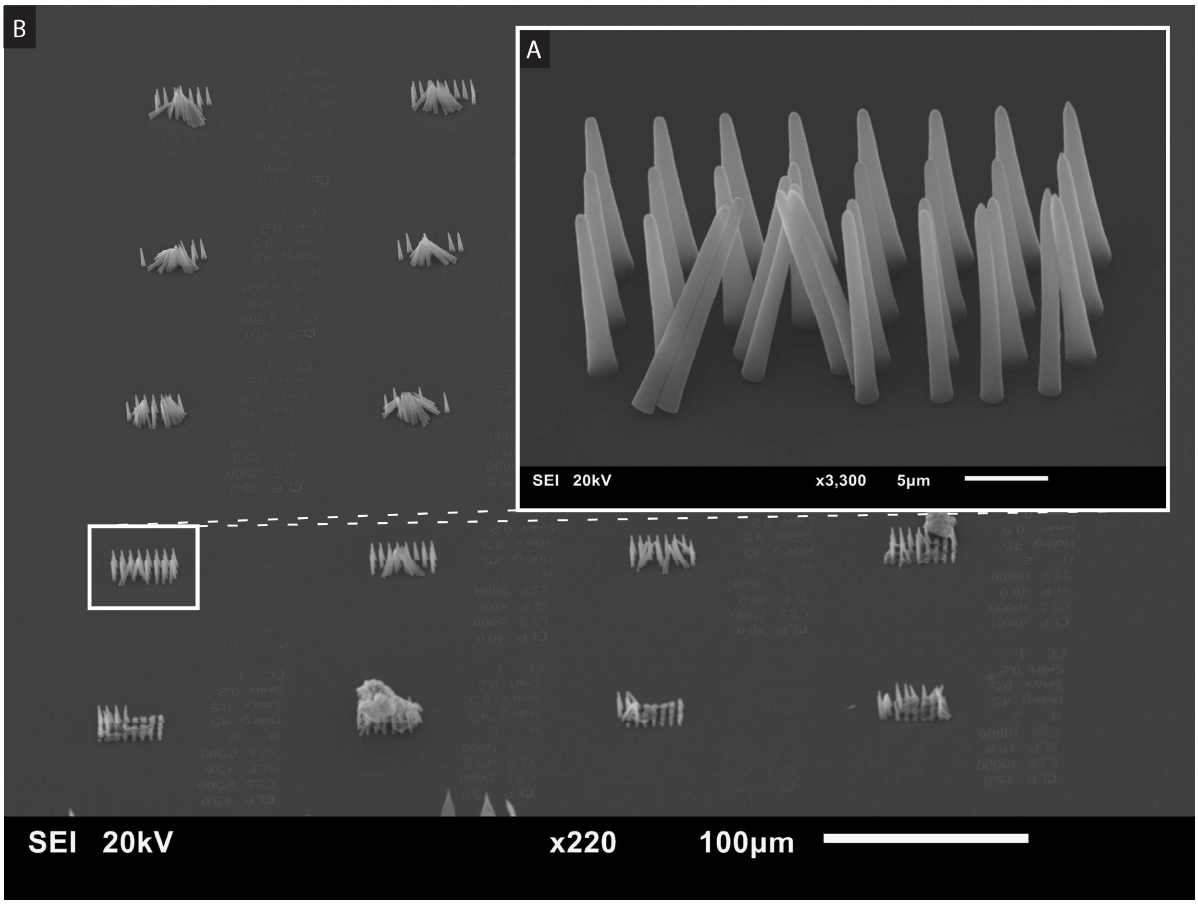

Figure C.20: Results of the printing pillars with sharp tips regarding the pillars with a diameter of 0.4 µm, printed with a laser power of 20.0 mW and a scan speed of 2500 µm s^{-1}. A: Zoomed in on the set of pillars which looks the most like the modeled ones. B: Overview of the printed pillars with a diameter of 0.4 µm.

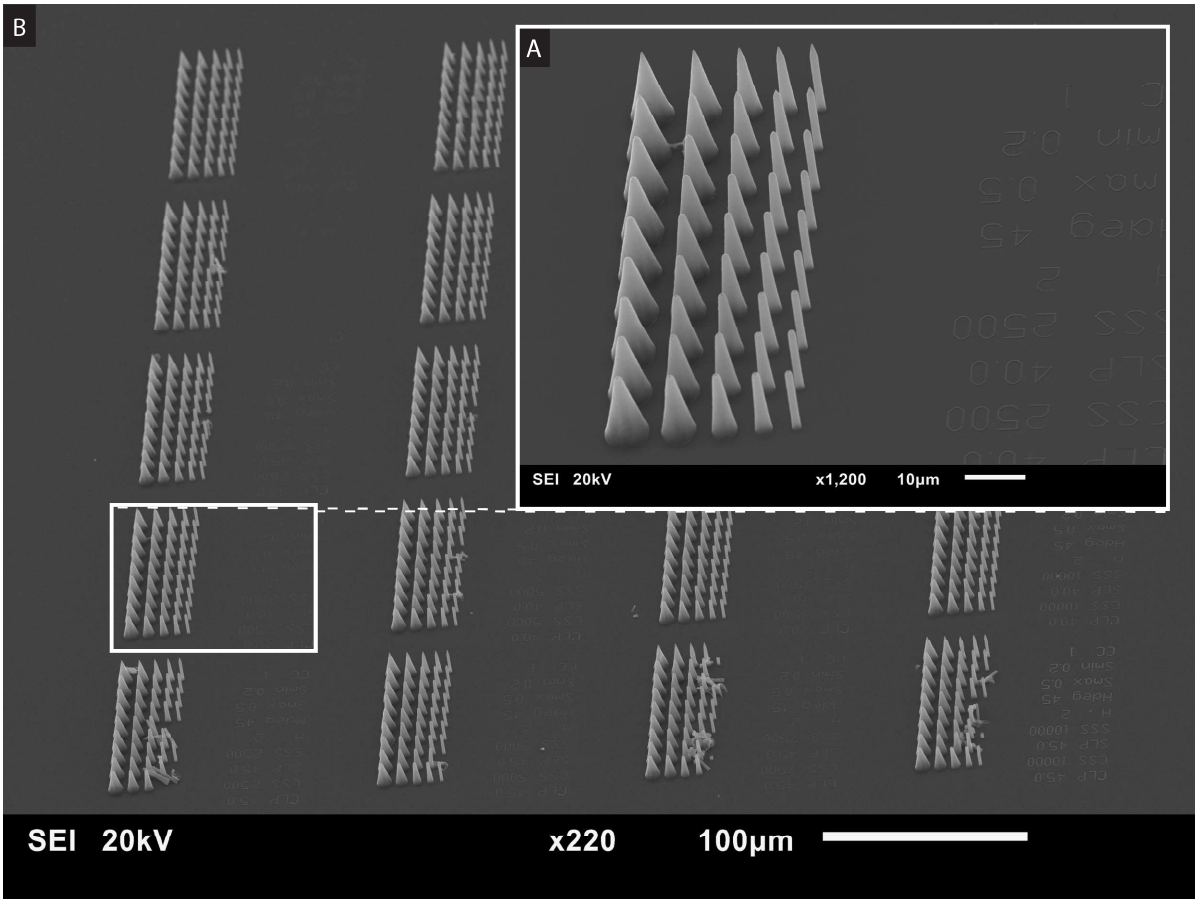

Figure C.21: Results of the printing pillars with sharp tips regarding the pillars with a diameter of 1 µm. A: Zoomed in on the set of pillars which looks the most like the modeled ones, printed with a laser power of 20.0 mW and a scan speed of 2500 µm s^{-1}. B: Overview of the printed pillars with a diameter of 1 µm.

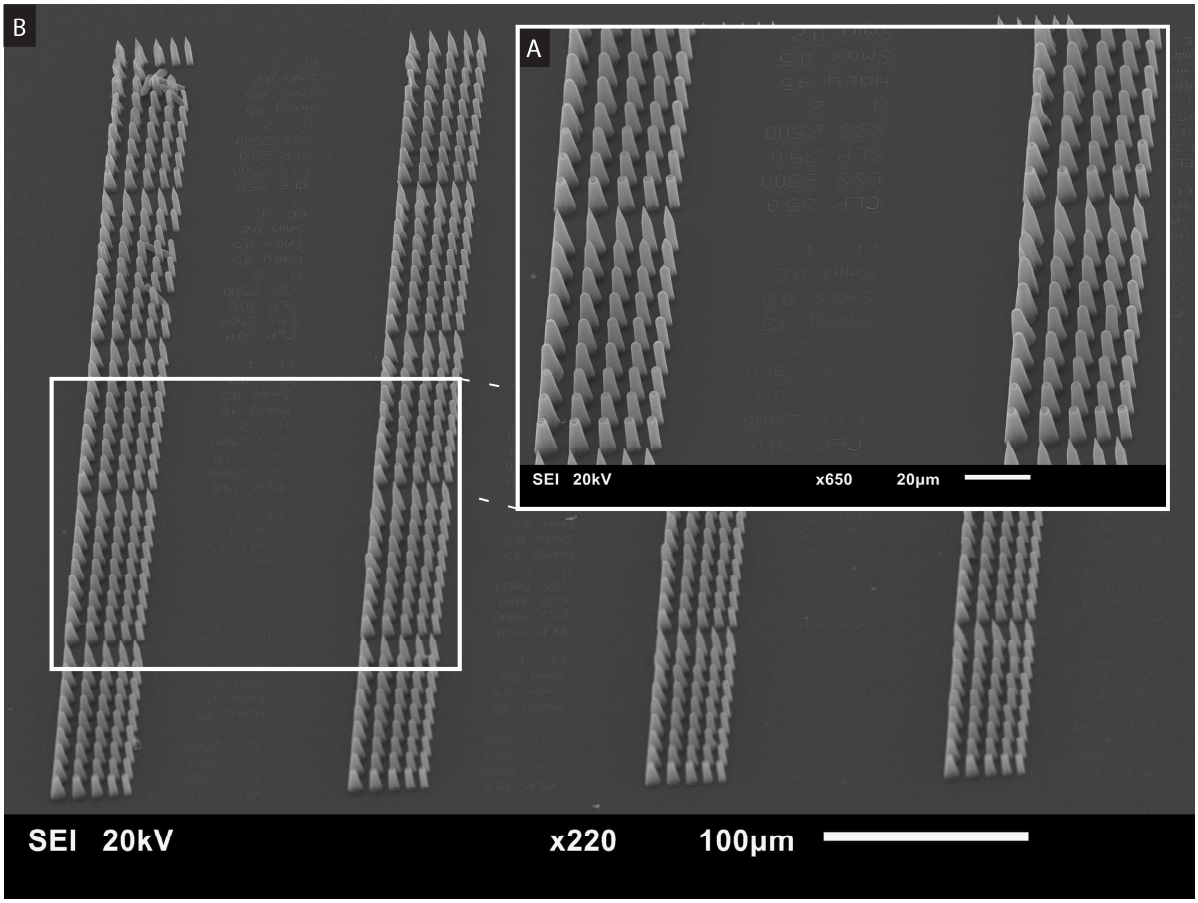

Figure C.22: Results of the printing pillars with sharp tips regarding the pillars with a diameter of 3 µm. A: Zoomed in on the set of pillars which looks the most like the modeled ones, printed with a laser power of 20.0 mW and a scan speed of 2500 µm s^{-1}. B: Overview of the printed pillars with a diameter of 3 µm.

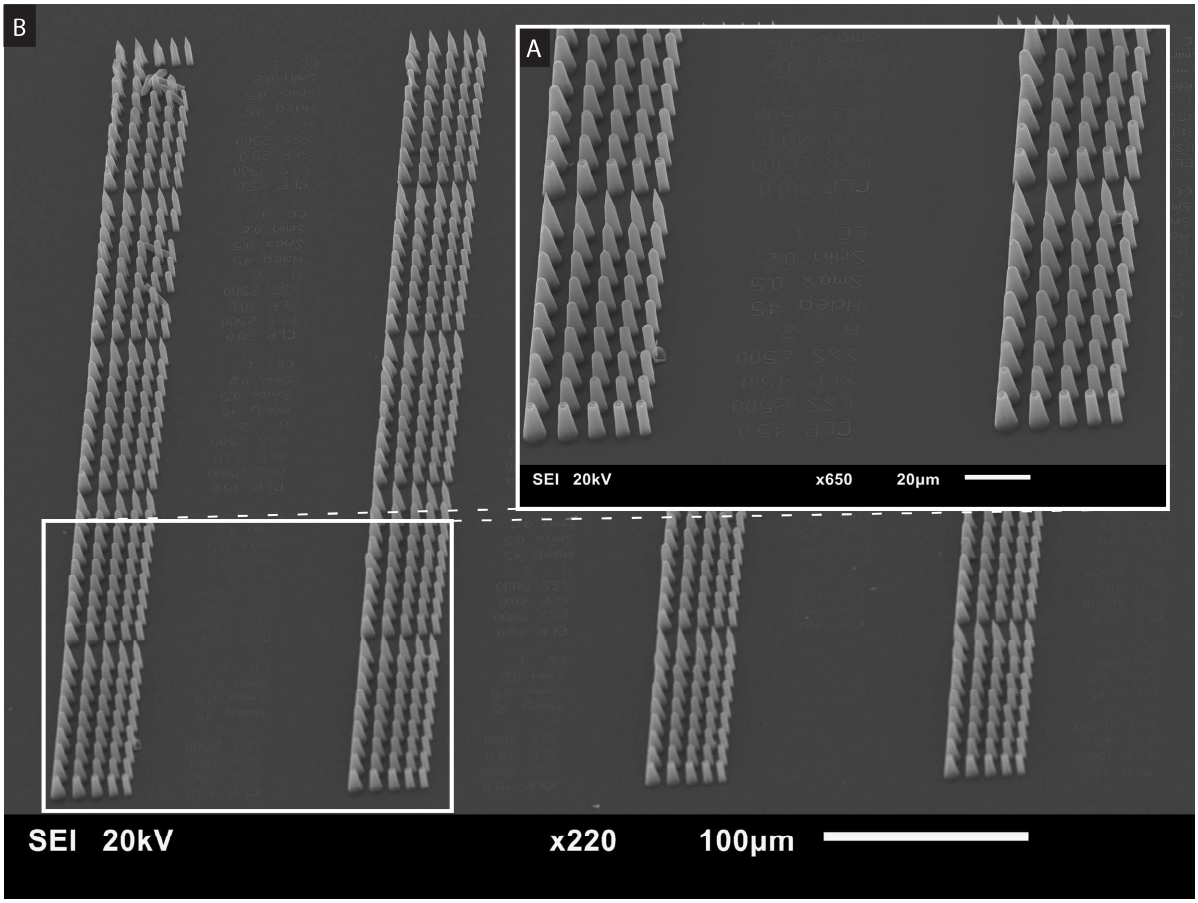

Figure C.23: Results of the printing pillars with sharp tips regarding the pillars with a diameter of 3 µm. A: Zoomed in on the set of pillars which looks the most like the modeled ones, printed with a laser power of 22.5 mW and a scan speed of 2500 µm s^{-1}. B: Overview of the printed pillars with a diameter of 3 µm.

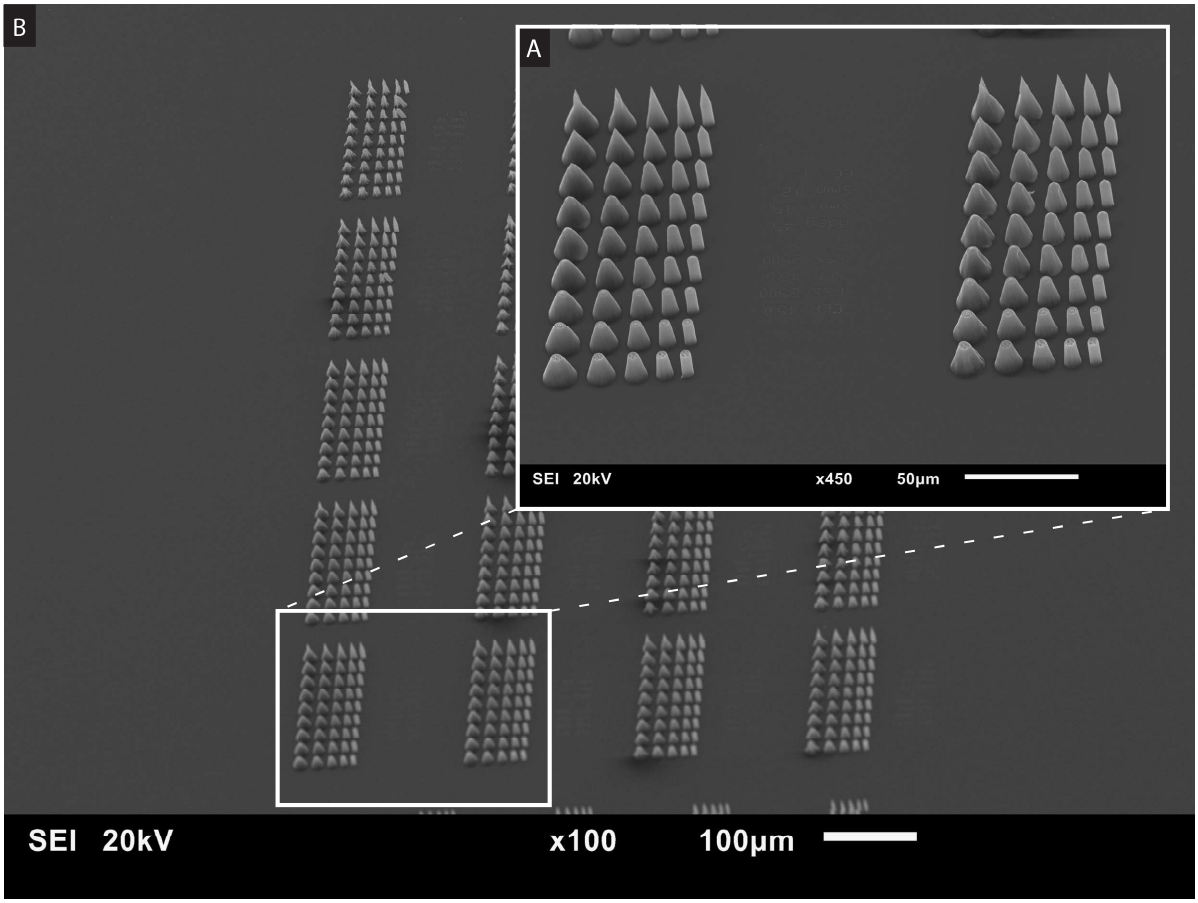

Figure C.24: Results of the printing pillars with sharp tips regarding the pillars with a diameter of 5 µm. A: Zoomed in on the set of pillars which looks the most like the modeled ones, printed with a laser power of 22.5 mW and a scan speed of 2500 µm s^{-1}. B: Overview of the printed pillars with a diameter of 5 µm.

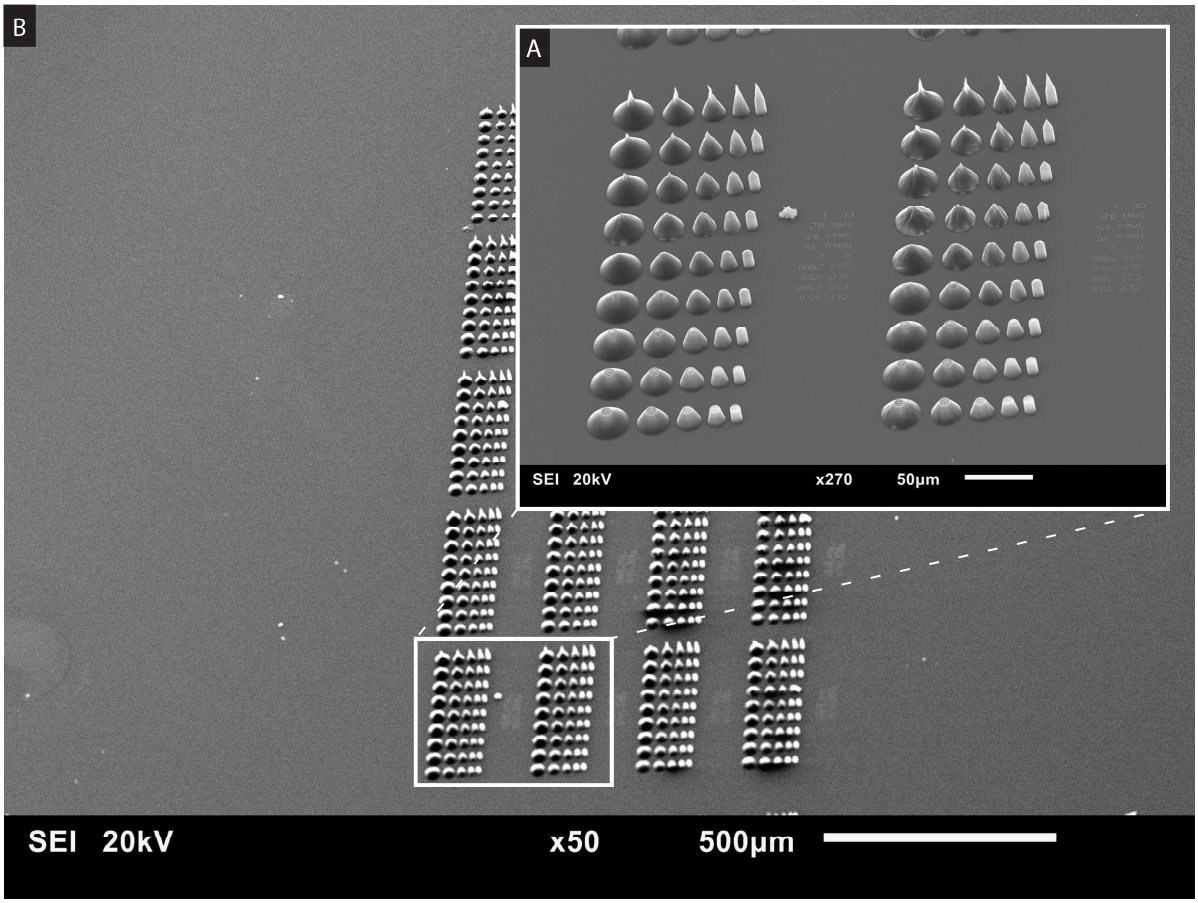

Figure C.25: Results of the printing pillars with sharp tips regarding the pillars with a diameter of 8 µm. A: Zoomed in on the set of pillars which looks the most like the modeled ones, printed with a laser power of 22.5 mW and a scan speed of 2500 µm s^{-1}. B: Overview of the printed pillars with a diameter of 8 µm.

Table C.3: Overview optimal parameters for printing pillars of different diameters with the 63x objective.

	8 µm pins	5 µm pins	3 µm pins	1 µm pins	0.4 µm pins
Laser power [mW]	22.5	22.5	22.5/20.0	20.0	20.0
Writing speed [µm s^{-1}]	2500	2500	2500	2500	2500
Minimum slicing distance [µm]	0.2	0.2	0.2	0.2	0.2
Maximum slicing distance [µm]	0.5	0.5	0.5	0.5	0.5
Hatching distance [µm]	2	2	2	2	2
Contour count	1	1	1	1	1
Hatching angle [°]	45	45	45	45	45

Influence of slicing distance

First, from figure C.26A, it can be seen that the pillars were not printed successfully with a laser power of 22.5 mW because the resist started to boil. So, the printing process was stopped. Zoomed in SEM images of the pillars which are printed with the optimal parameters are presented in the figures C.27, C.28, and C.29. Comparing figure C.27A with figure C.22A, figure C.28A with figure C.24A, and figure C.29A with figure C.25A, it can be seen that there was little to no improvement by printing the pillars with a smaller slicing distances. But it took much more time to print due to the smaller slicing distance. So, there is no advantage in decreasing the slicing distance.

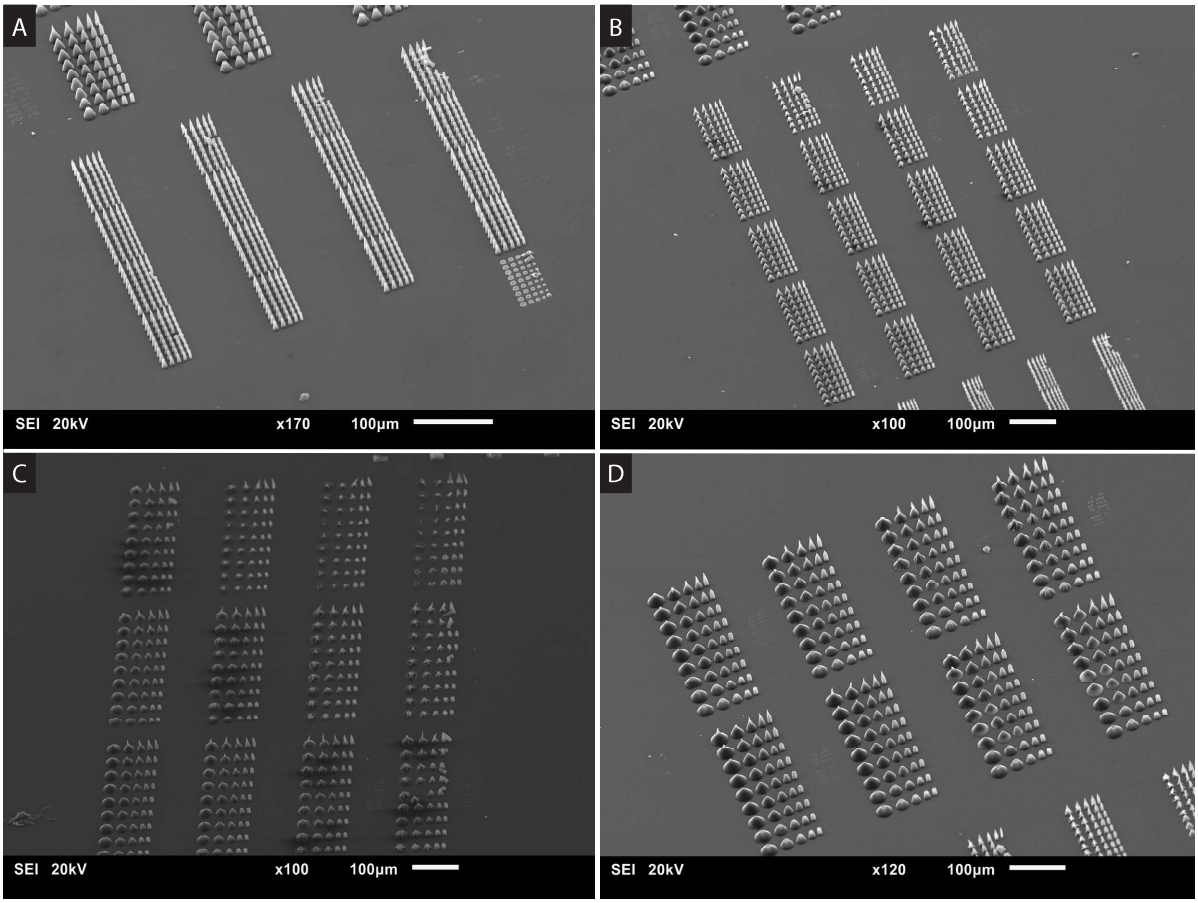

Figure C.26: Results of the printed pillars of different diameters regarding the influence of the slicing distance. A: Overview of the printed pillars with a diameter of 3 µm. B: Overview of the printed pillars with a diameter of 5 µm. C: Part one of the printed pillars with a diameter of 8 µm. D: Part two of the printed pillars with a diameter of 8 µm.

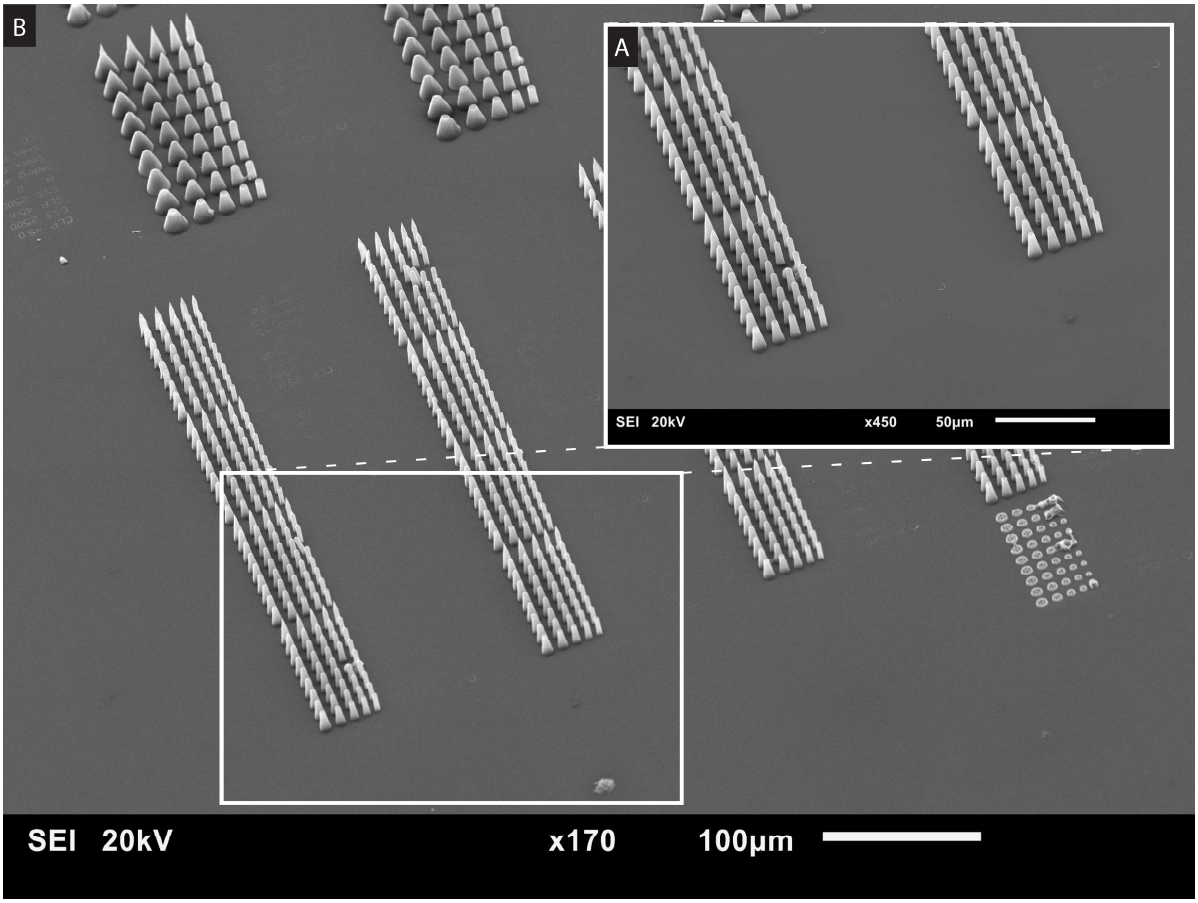

Figure C.27: Results of the pillars with a diameter of 3 µm. A: Zoomed in on the pillars printed with a laser power of 20 mW and a scan speed of 2500 µm s^{-1}. B: Overview of the printed pillars with a diameter of 3 µm.

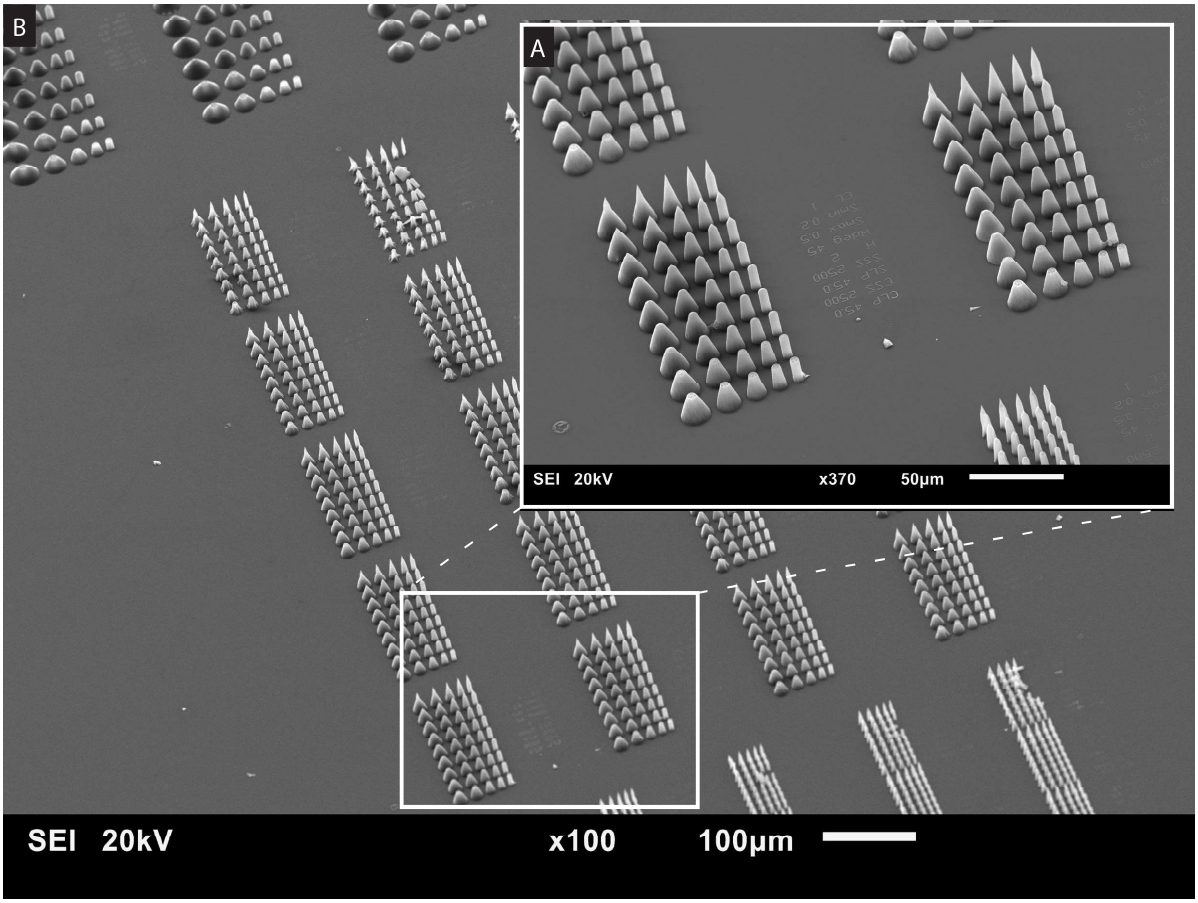

Figure C.28: Results of the pillars with a diameter of 5 µm. A: Zoomed in on the pillars printedwith a laser power of 22.5 mW and a scan speed of 2500 µm s^{-1}. B: Overview of the printed pillars with a diameter of 5 µm.

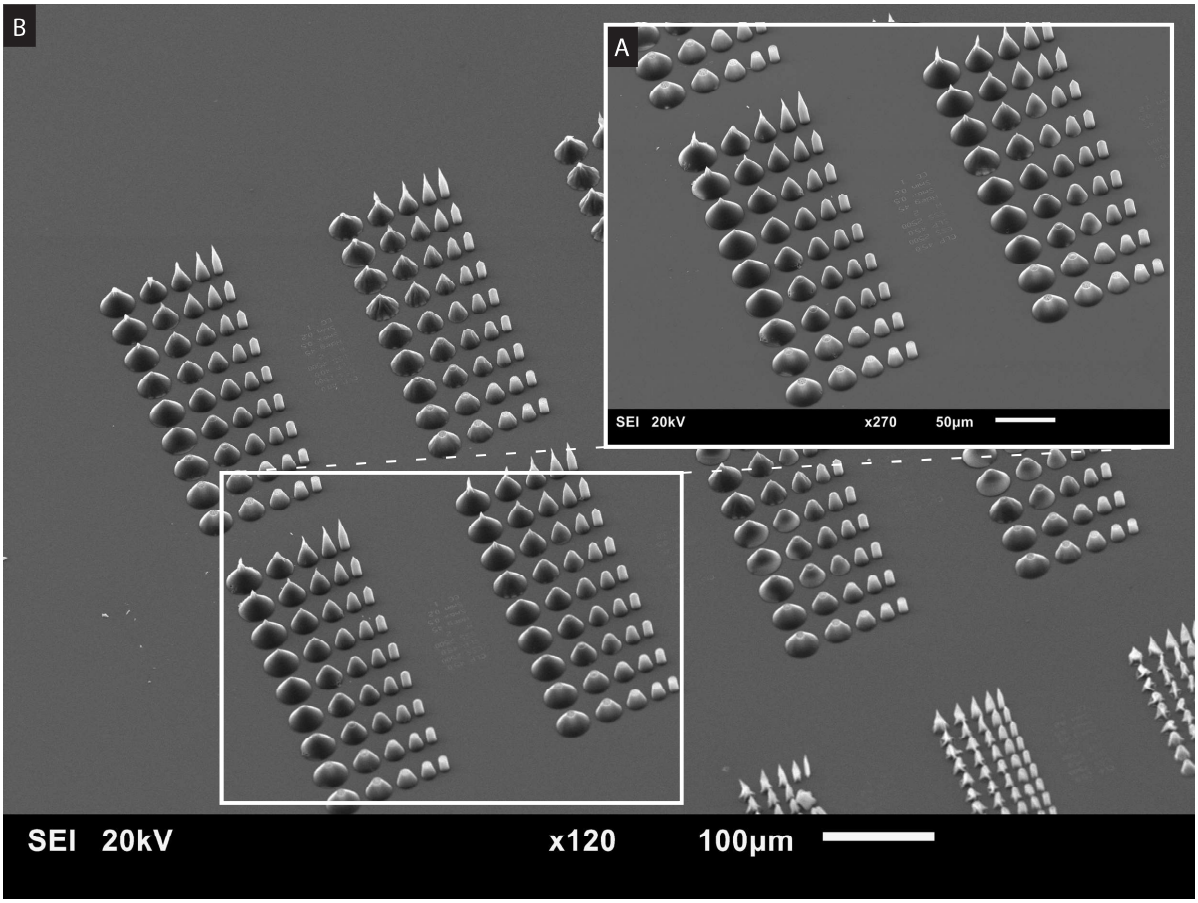

Figure C.29: Results of the pillars with a diameter of 8 µm. A: Zoomed in on the pillars printed with a laser power of 22.5 mW and a scan speed of 2500 µm s^{-1}. B: Overview of the printed pillars with a diameter of 8 µm.

Influence of the 25x objective in comparison with the 63x objective

The printed pillars are presented in figures C.30A to C.30F. And a close up of the pillars with different diameters is given in figures C.31A to C.31E.

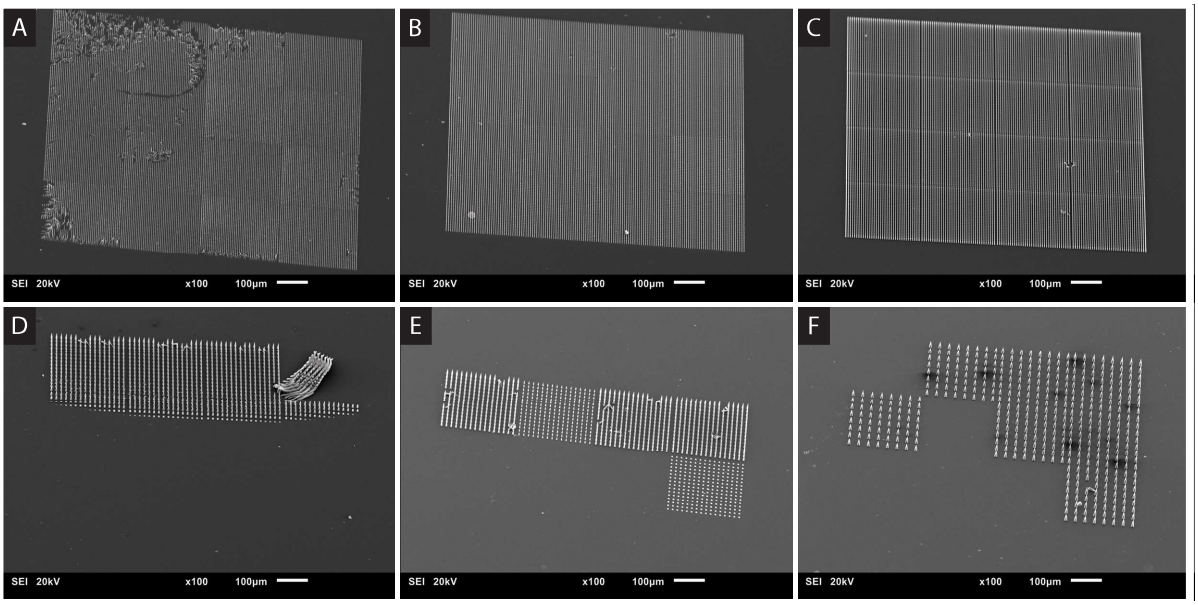

Figure C.30: Results of the printed 1 mm by 1 mm fields of pillars with the 25x objective. A: Overview of the printed pillars with a diameter of 0.4 µm. B: Overview of the printed pillars with a diameter of 1 µm. C: Overview of the printed pillars with a diameter of 3 µm. D: Part one of the printed pillars with a diameter of 5 µm. E: Part two of the printed pillars with a diameter of 5 µm. F: Overview of the printed pillars with a diameter of 8 µm.

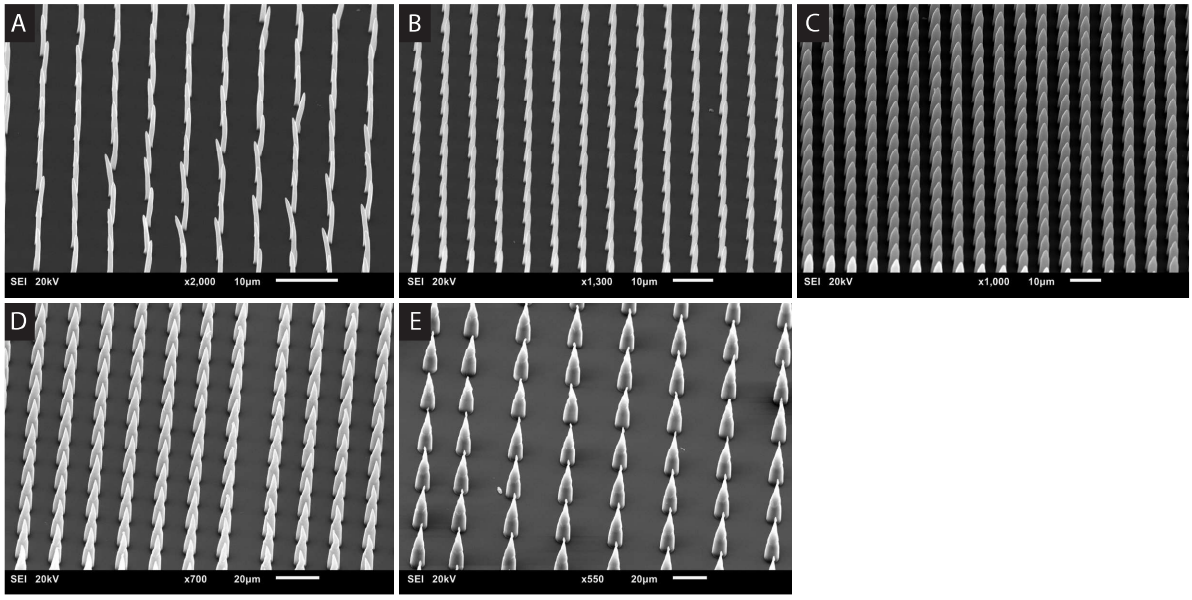

Figure C.31: Results of the printed 1 mm by 1 mm fields of pillars with the 25x objective. A: Close up of the printed pillars with a diameter of 0.4 µm. B: Close up of the printed pillars with a diameter of 1 µm. C: Close up of the printed pillars with a diameter of 3 µm. D: Close up of the printed pillars with a diameter of 5 µm. E: Close up of the printed pillars with a diameter of 8 µm.

The reason why there is only a partial field is printed, which can be seen in figure C.30D, is due to the fact that the droplet of IP-L 780 was not big enough and, therefore, the Photonic Professional GT tried to print the pillars in air. So, a new substrate was placed and the print job was modified to only print the fields of pillars with a diameter of 5 µm and 8 µm. But due to time constraint, they are not fully printed. In figure C.30E, a

part of smaller pillars can be observed. This was caused by the fact that the Photonic Professional GT was not able to find the interface successfully. The same cause led to missing parts of pillars in figure C.30F.

But the prints were succesfull enough to compare them with the pillars printed with the 63x objective. So figure C.31A can be compared with figure C.20A, figure C.31B can be compared with figure C.21A, figure C.31C can be compared with figure C.22A, figure C.31D can be compared with figure C.24A, and figure C.31E can be compared with figure C.25A. All the tips are almost the same except for the pillars with 3 µm in diameter. This could be solved by printing the pillars with a laser power of 22.5 mW instead of 20.0 mW.

Electrodes 5 µm in height

In figure C.32 the overview of the results is presented, but the best version of both of the printed contours are shown in C.33A (finger spacing of 1 µm) and C.33B (finger spacing of 0.5 µm). It can be seen that the contour of the interdigit sensors are stuck to each other. Also, in both cases, the big round circle fell inwards, probably due to the capillary forces during the development process. Therefore, this design of the contours of two different sensors of 5 µm in height are not able to be printed successfully due to their height.

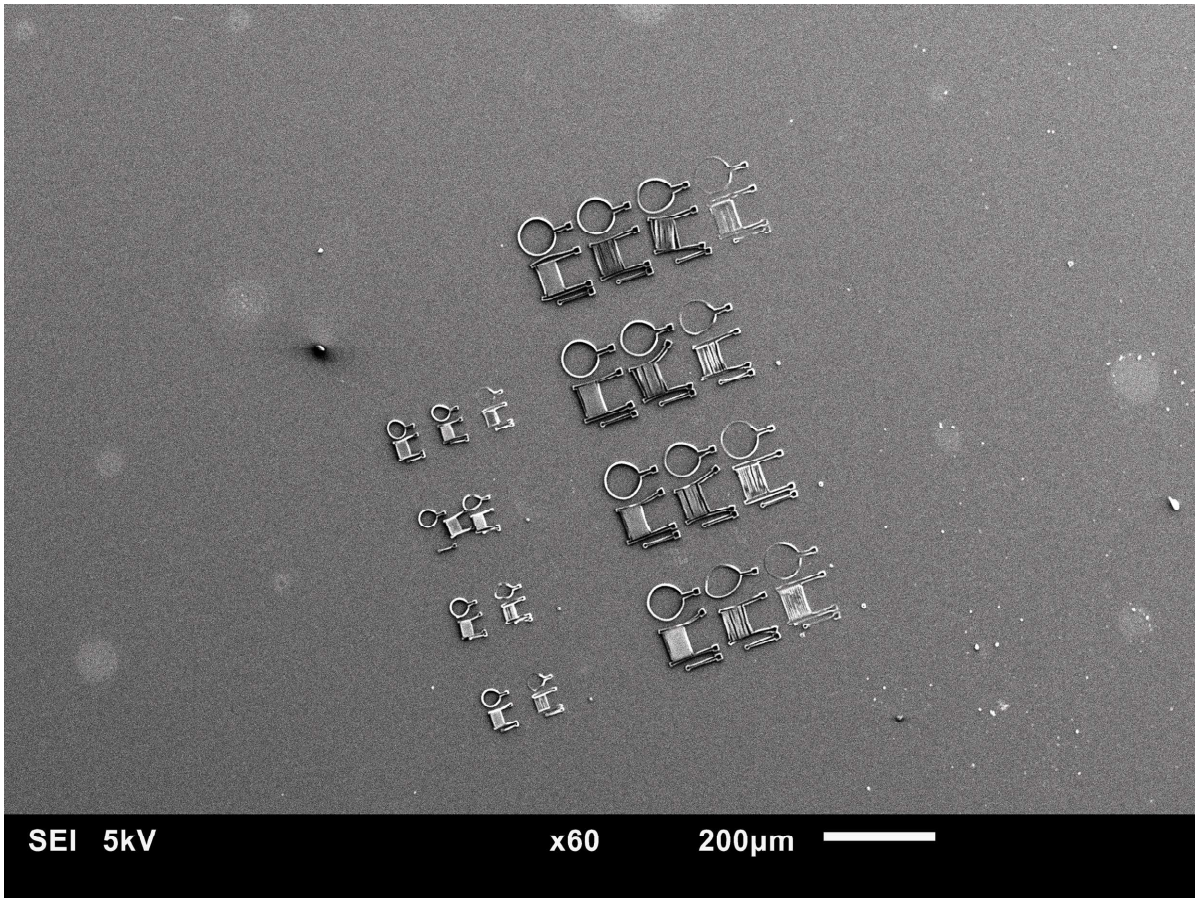

Figure C.32: Overview of the printed contours of the sensor, both with a finger spacing of 0.5 µm and 1 µm, 5 µm in height, at different laser powers and scan speeds.

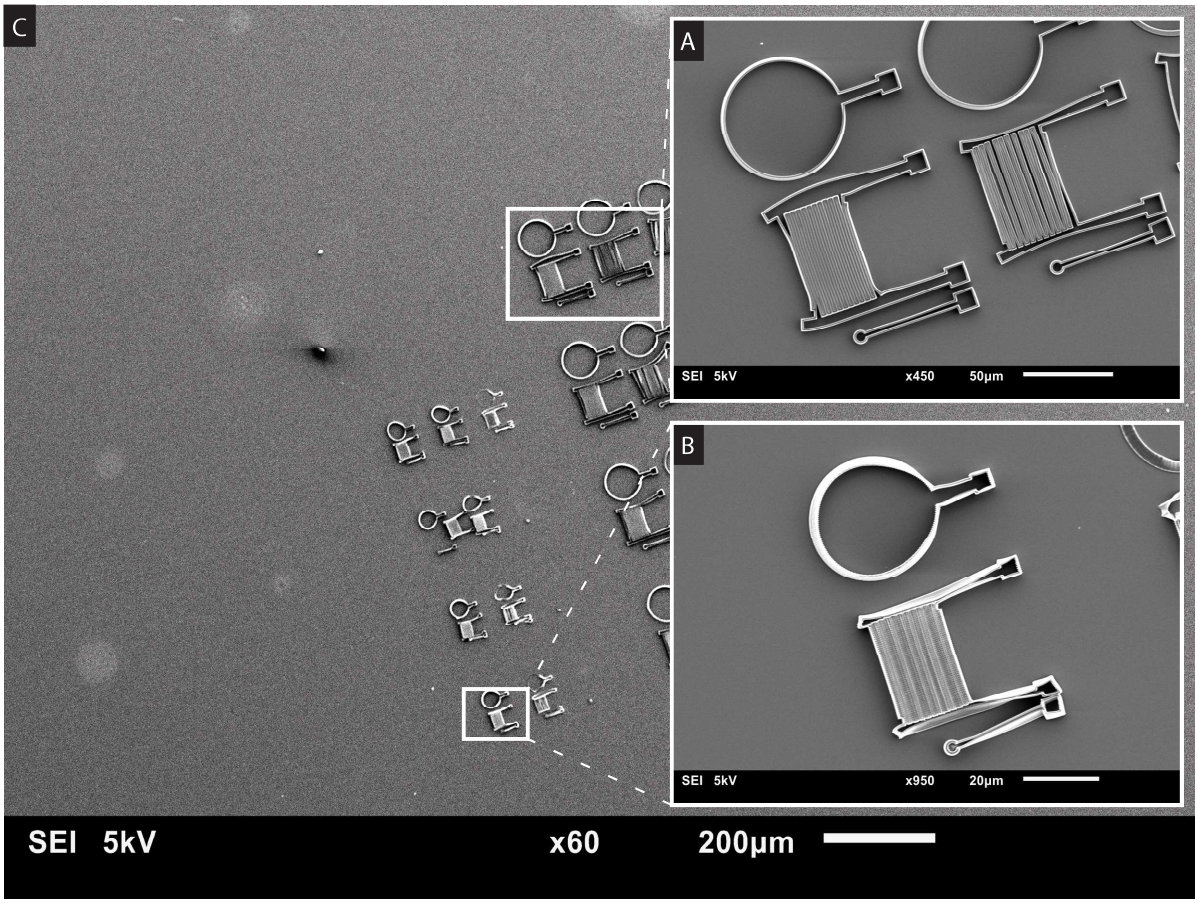

Figure C.33: Results of the printed contours of the sensor, both with a finger spacing of 0.5 µm and 1 µm, 5 µm in height, at different laser powers and scan speeds. A: Close up of the contour of the sensor which is the closest one to the designed contour with a finger spacing of 1 µm. B: Close up of the contour of the sensor which is the closest one to the designed contour with a finger spacing of 0.5 µm. C: Overview of the printed contours of the sensor.

Electrodes 1 µm, 2 µm, 3 µm and 4 µm in height

Figure C.34 contains an overview of the printed contours of the sensor at different heights and finger spacings. The sensor with the dimension of 1 µm in finger spacing and 4 µm in height is particially succesfull, but it is good enough to be used for the imprinting for at least the counter electrode and the reference electrode which is presented in figure C.35A. This one is printed with a laser power of 20.0 mW and a scan speed of 5000 µm s^{-1}. For the dimensions of 1 µm in finger spacing and a maximum of 3 µm in height the contours polymarized successfully. For the sensors with a finger spacing of 0.5 µm, a maximum height of 2 µm was achieved of which the structure did not collapse. These printing parameters are summed up in table C.4. Zoomed in SEM images of the pillars which are printed with the optimal parameters are presented in the figures C.35, C.36, C.37, and C.38.

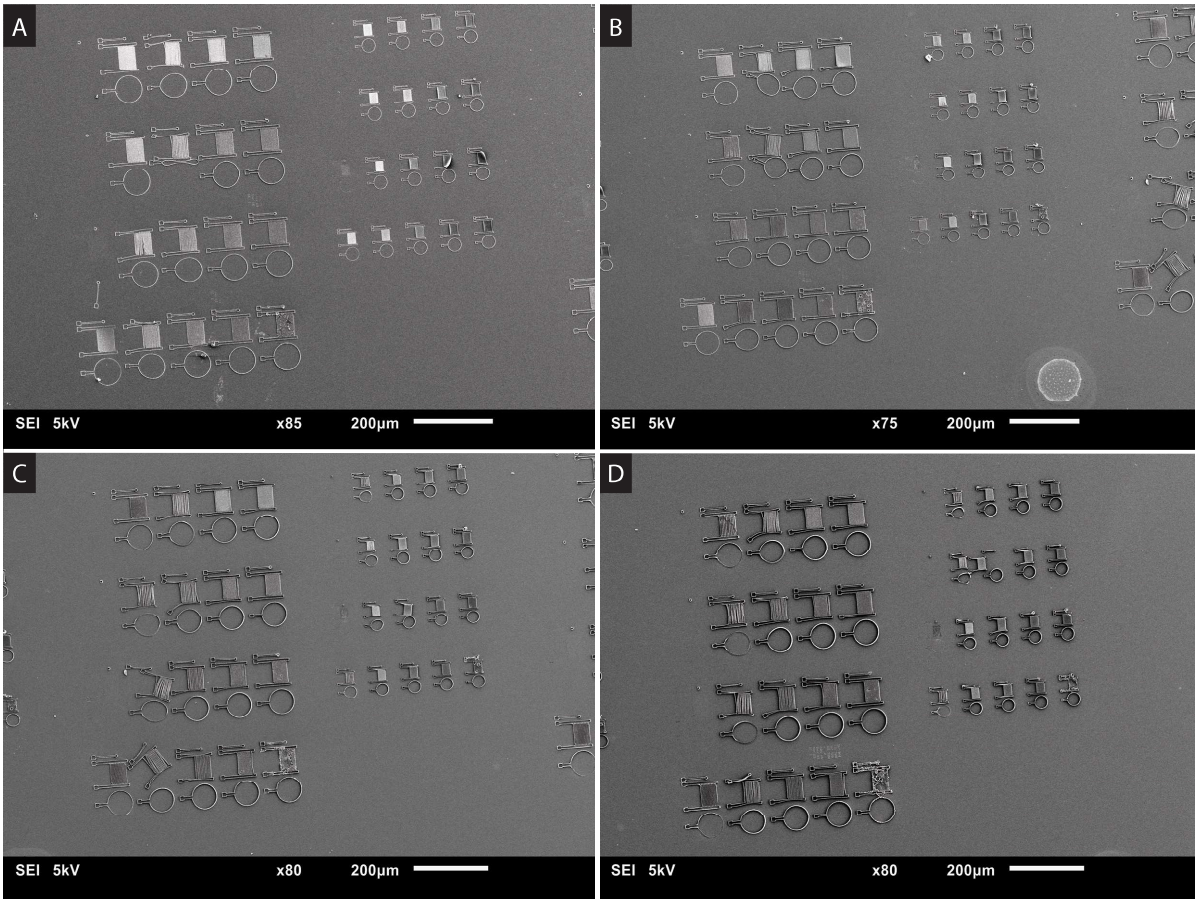

Figure C.34: Overview of the printed contours of the sensor, with a finger spacing of 0.5 µm and 1 µm, different heights, with different laser powers, and scan speeds. A: Contours of the sensor which is 1 µm in height. B: Contours of the sensor which is 2 µm in height. C: Contours of the sensor which is 3 µm in height. D: Contours of the sensor which is 4 µm in height.

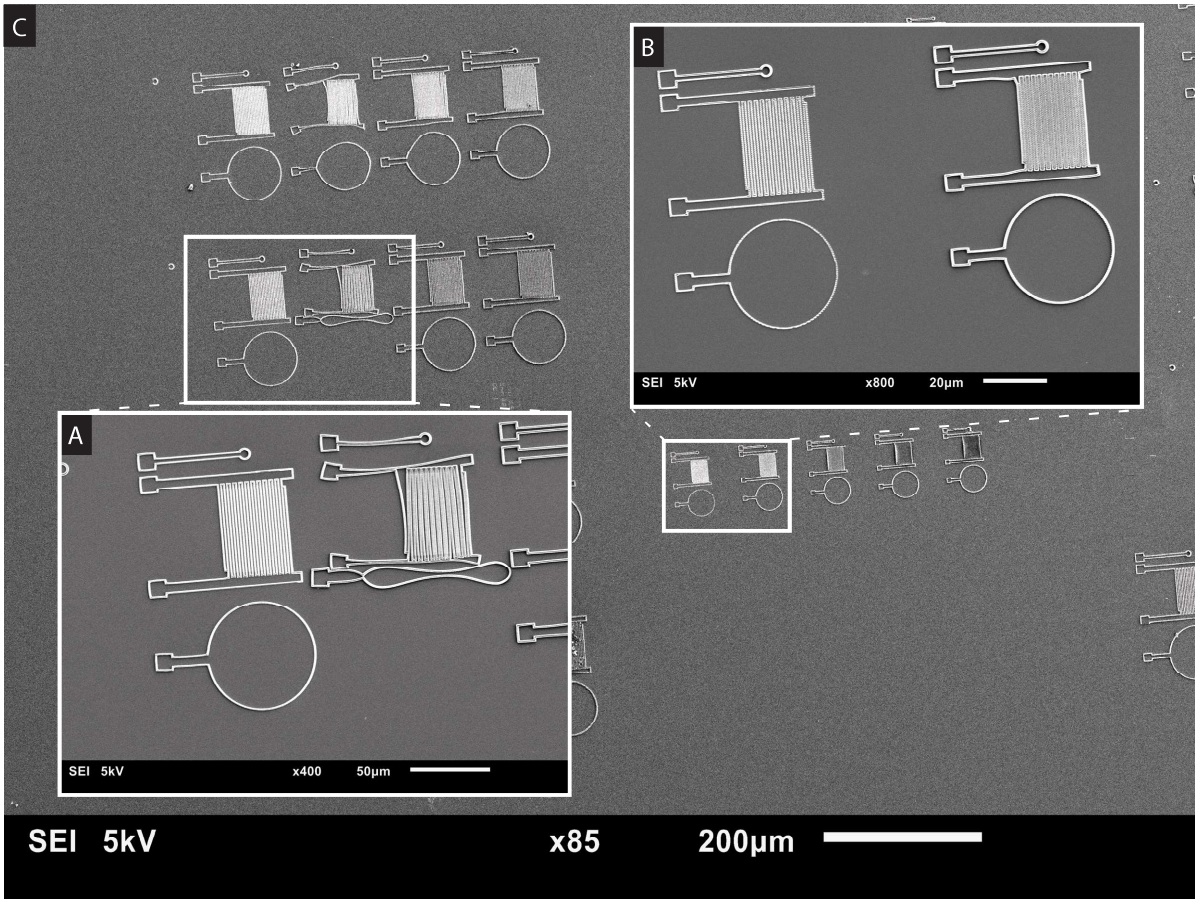

Figure C.35: Results of the printed contours of the sensor, with a finger spacing of 0.5 µm and 1 µm, 1 µm in height, at different laser powers and scan speeds. A: Close up of the contour of the the sensor which is the closest one to the designed contour with a finger spacing 1 µm, printed with a laser power of 15.0 mW and a scan speed of 15 000 µm s^{-1}. B: Close up of the contour of the sensor which is the closest one to the designed contour with a finger spacing 0.5 µm, printed with a laser power of 15.0 mW and a scan speed of 5000 µm s^{-1}. C: Overview of the printed contours of the sensor.

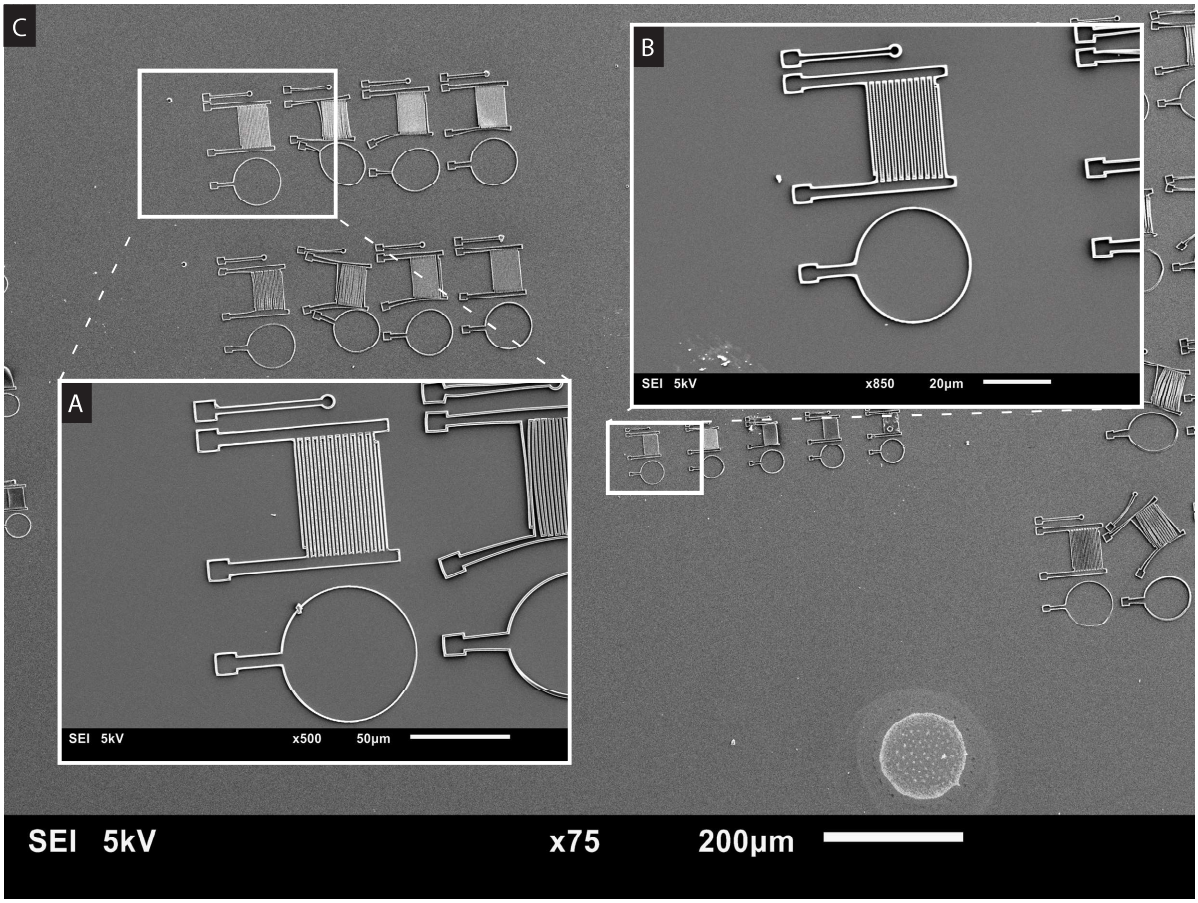

Figure C.36: Results of the printed contours of the sensor, with a finger spacing 0.5 µm and 1 µm, 2 µm in height, at different laser powers and scan speeds. A: Close up of the contour of the sensor which is the closest one to the designed contour with a finger spacing of 1 µm, printed with a laser power of 15.0 mW and a scan speed of 20 000 µm s^{-1}. B: Close up of the contour of the sensor which is the closest one to the designed contour with a finger spacing of 0.5 µm, printed with a laser power of 10.0 mW and a scan speed of 5000 µm s^{-1}. C: Overview of the printed contours of the sensor.

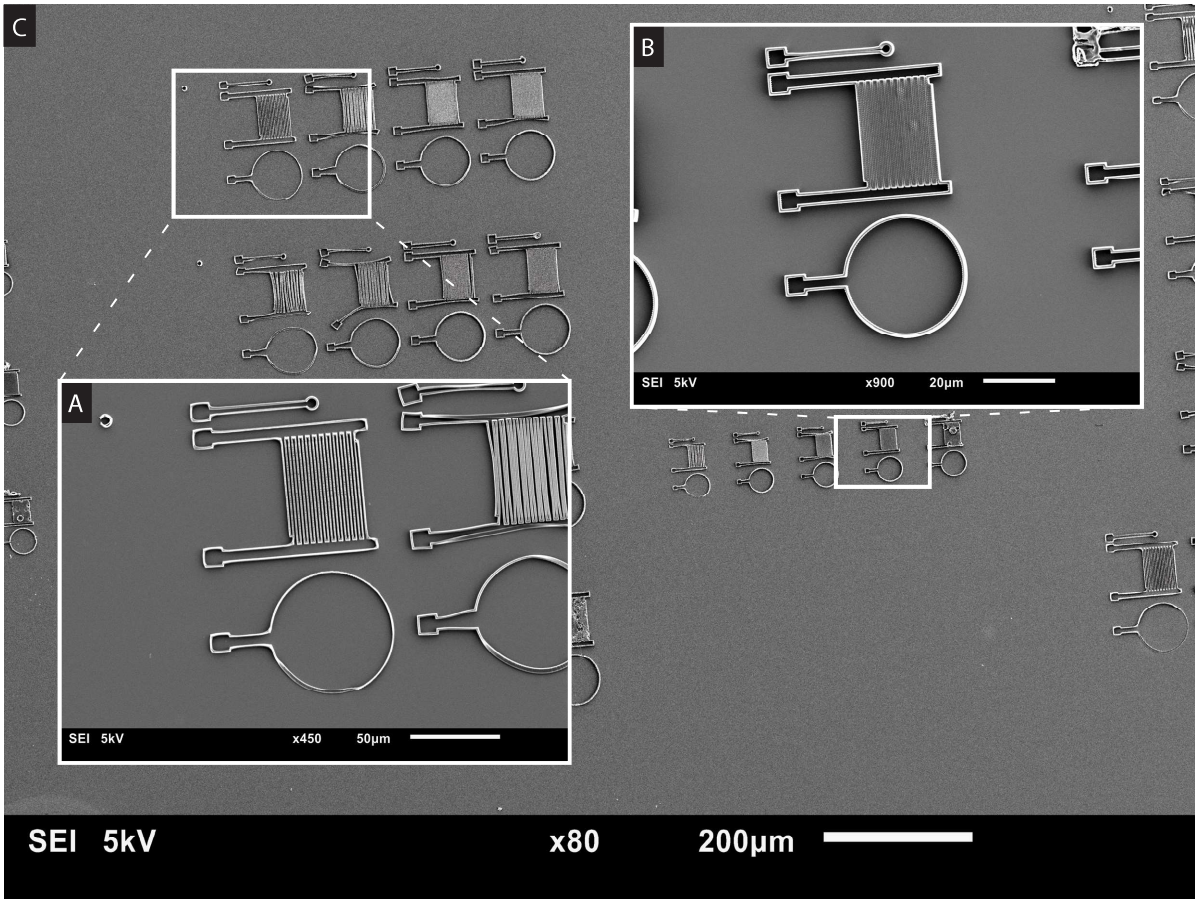

Figure C.37: Results of the printed contours of the sensor, with a finger spacing of 0.5 µm and 1 µm, 3 µm in height, at different laser powers and scan speeds. A: Close up of the contour of the sensor which is the closest one to the designed contour with a finger spacing of 1 µm, printed with a laser power of 15.0 mW and a scan speed of 20 000 µm s^{-1}. B: Close up of the contour of the sensor which is the closest one to the designed contour with a finger spacing of 0.5 µm, printed with a laser power of 25.0 mW and a scan speed of 5000 µm s^{-1}. C: Overview of the printed contours of the sensor.

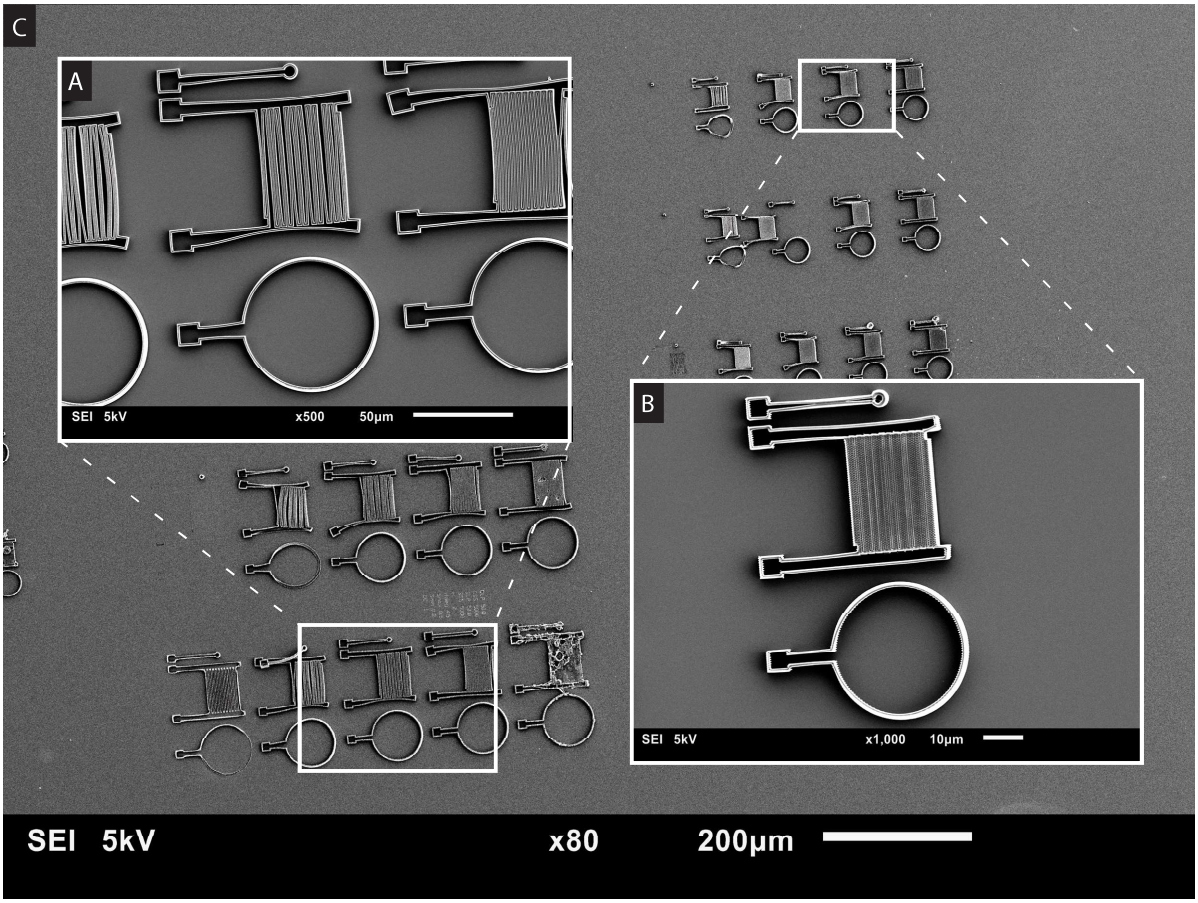

Figure C.38: Results of the printed contours of the sensor, with a finger spacing of 0.5 µm and 1 µm, 4 µm in height, at different laser powers and scan speeds. A: Close up of the contour of the sensor which is the closest one to the designed contour with a finger spacing of 1 µm, printed with a laser power of 20.0 mW and a scan speed of 5000 µm s^{-1}. B: Close up of the contour of the sensor which is the closest one to the designed contour with a finger spacing of 0.5 µm, printed with a laser power of 25.0 mW and a scan speed of 20 000 µm s^{-1}. C: Overview of the printed contours of the sensor.

Table C.4: Overview optimal parameters for printing contours of the sensor.

	1 x 4 µm electrodes	1 x 3 µm electrodes	1 x 2 µm electrodes	1 x 1 µm electrodes	0.5 x 2 µm electrodes	0.5 x 1 µm electrodes
Laser power [mW]	20.0	15.0	15.0	15.0	10.0	10.0
Writing speed [µm s^{-1}]	5000	20000	20000	15000	5000	5000
Minimum slicing distance [µm]	0.2	0.2	0.2	0.2	0.2	0.2
Maximum slicing distance [µm]	0.4	0.4	0.4	0.4	0.4	0.4
Hatching distance [µm]	0.3	0.3	0.3	0.3	0.3	0.3
Contour count	1	1	1	1	1	1
Hatching angle [°]	0	0	0	0	0	0

Contours of the sensor with a sharp edge
An overview of the contours of the sensor with a sharp edge are presented in figure C.39.

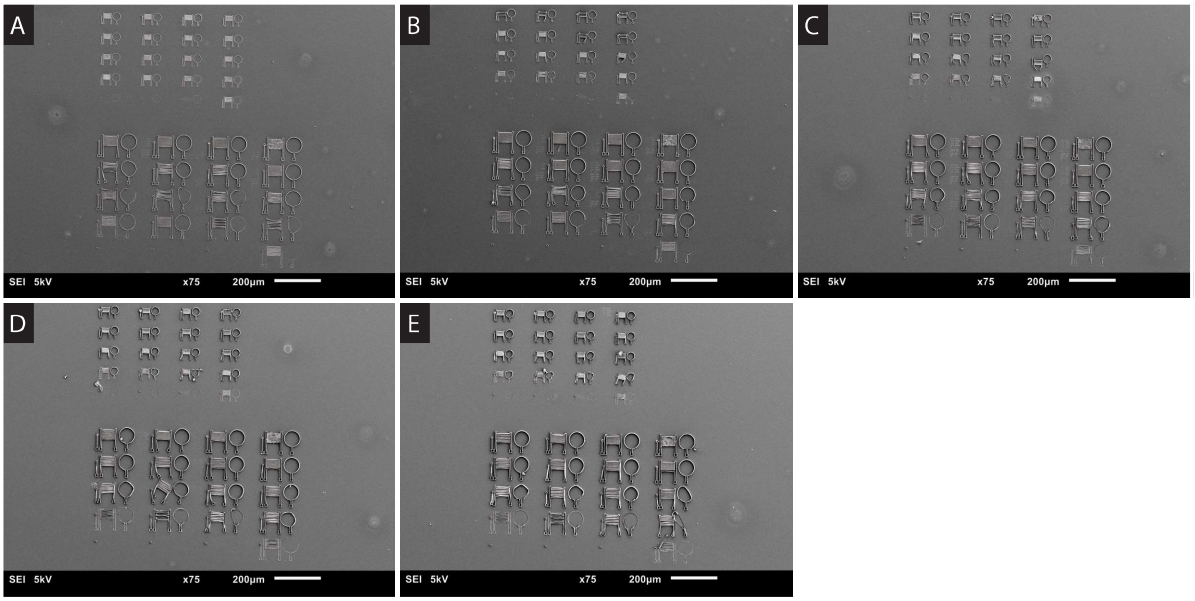

Figure C.39: Overview of the printed contours of the sensor with a sharp edge, with a finger spacing of 0.5 µm and 1 µm, at different laser powers and scan speeds. A: Contours of the sensor successfully with a sharp edge which are 0 µm in height. B: Contours of electrodes with a sharp edge which are 1 µm in height. C: Contours of the sensor with a sharp edge which are 2 µm in height. D: Contours of the sensor with a sharp edge which are 3 µm in height. E: Contours of the sensor with a sharp edge which are 3 µm in height.

Only the contours of the sensor with a height of 0 µm and 1 µm were printed successfully with the Photonic Professional GT. The optimal printing parameters are summarized in table C.5. For the contours of the sensor with a finger spacing of 0.5 µm two good combinations of laser power and scan speed are found. Version 1 is prefered while the higher scan speed will result in a print job which takes less time to execute. Zoomed in SEM images of the contours of the sensor with a sharp edge which are printed with these optimal printing parameters are presented in the figures C.40, C.41, and C.42.

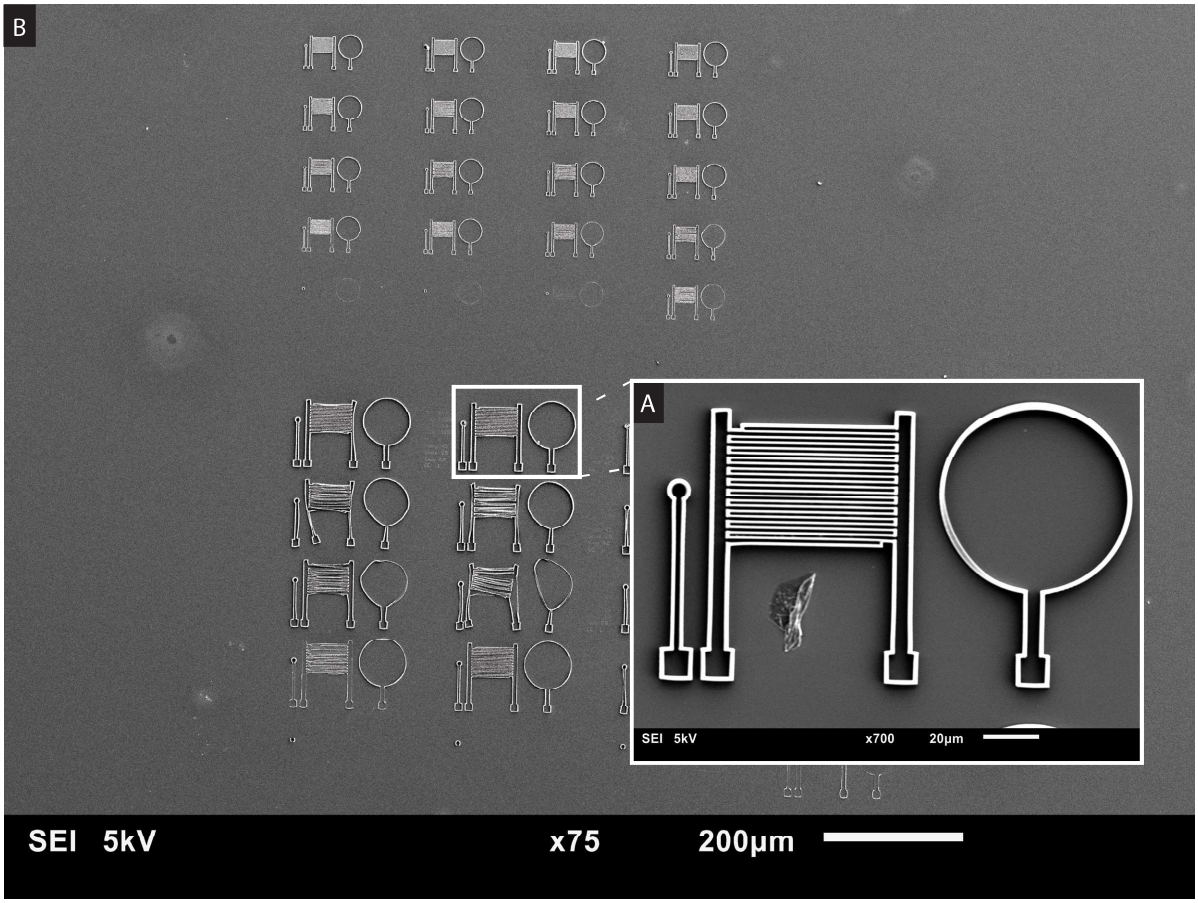

Figure C.40: Results of the printed contours of the sensor with a sharp edge, with a finger spacing of 0.5 µm and 1 µm, 1 µm in height, at different laser powers, and scan speeds. A: Close up of the contour of the sensor which is the closest one to the designed contour with a finger spacing of 1 µm and 1 µm in height excluding the sharp edge, printed with a laser power of 30.0 mW and a scan speed of 15 000 µm s^{-1}. B: Overview of the printed contours of the sensor with a sharp edge.

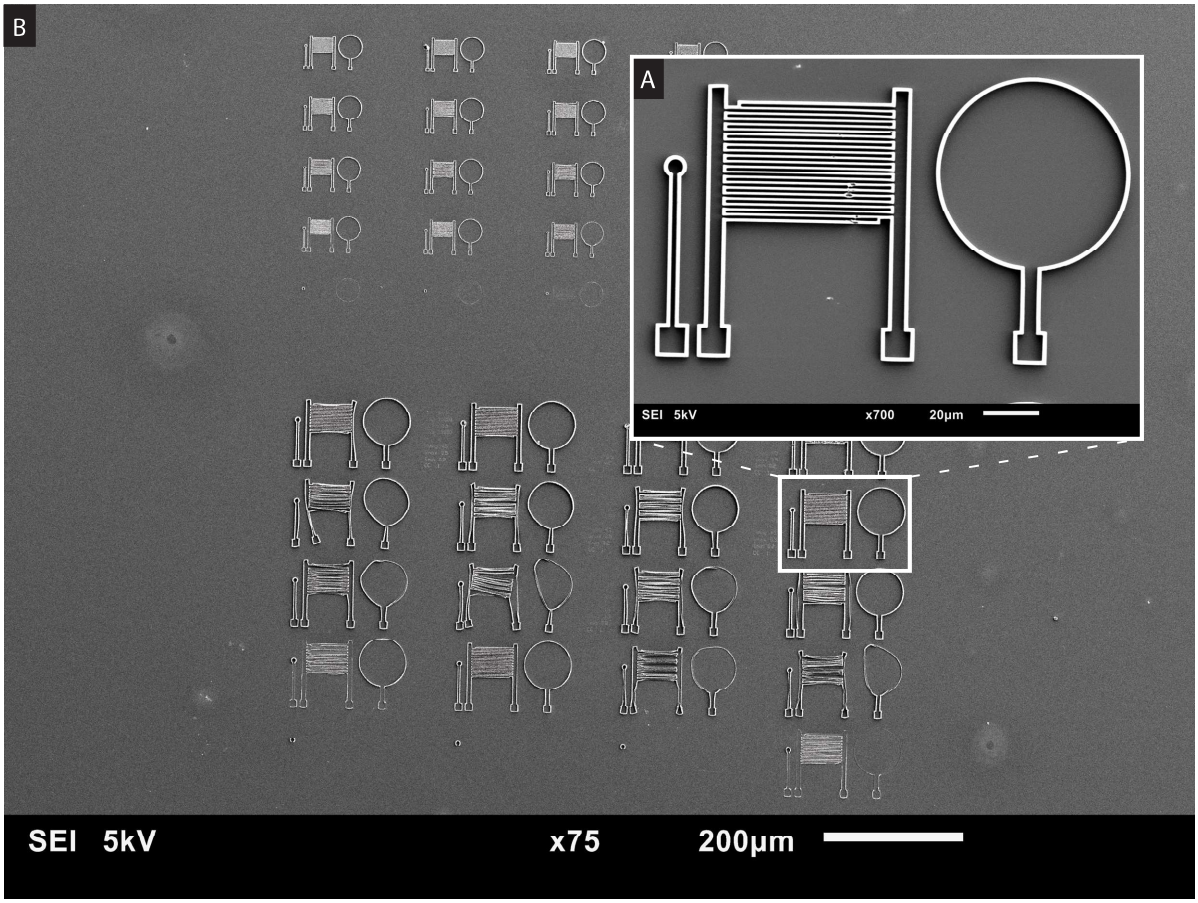

Figure C.41: Results of the printed contours of the sensor with a sharp edge, with a finger spacing of 0.5 µm and 1 µm, 1 µm in height, at different laser powers, and scan speeds. A: Close up of the contour of the sensor which is the closest one to the designed contour with a finger spacing of 1 µm and 0 µm in height excluding the sharp edge, printed with a laser power of 25.0 mW and a scan speed of 5000 µm s^{-1}. B: Overview of the printed contours of the sensor with a sharp edge.

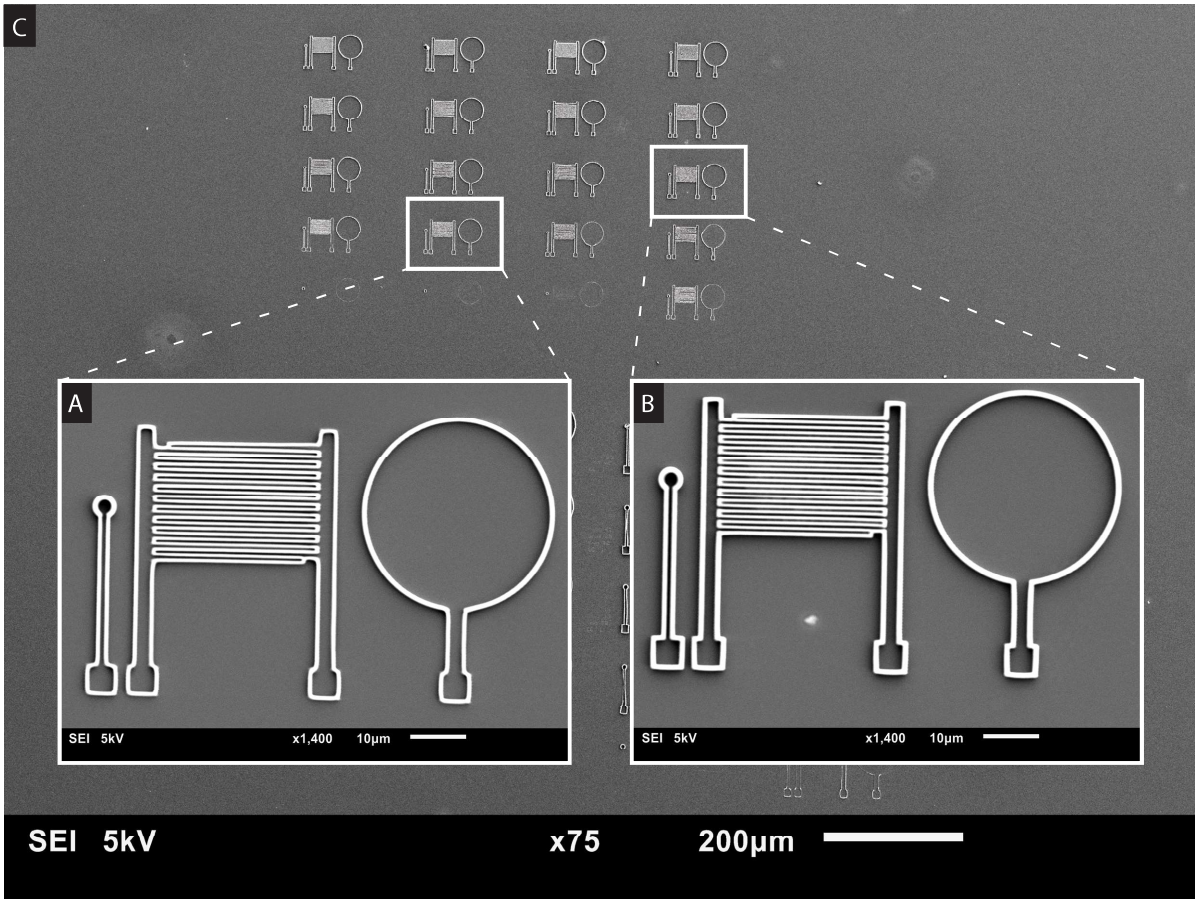

Figure C.42: Results of the printed contours of the sensor with a sharp edge, with a finger spacing of 0.5 µm and 1 µm, 1 µm in height, at different laser powers, and scan speeds. A: Close up of the first contour of the sensor which is close to the designed contour with a finger spacing of 0.5 µm and 0 µm in height excluding the sharp edge, printed with a laser power of 15.0 mW and a scan speed of 15 000 µm s^{-1}. B: Close up of the second contour of the sensor which is the close to the designed contour of 0.5 µm in finger spacing and 0 µm in height excluding the sharp edge, printed with a laser power of 20.0 mW and a scan speed of 5000 µm s^{-1}. C: Overview of the printed contours of the sensor with a sharp edge.

Table C.5: Overview optimal parameters for the contours of the sensor with a sharp edge.

	1 x 1 µm electrodes with a sharp edge	1 x 0 µm electrodes with a sharp edge	0.5 x 0 µm electrodes with a sharp edge V1	0.5 x 0 µm electrodes with a sharp edge V2
Laser power [mW]	30.0	25.0	20.0	15.0
Writing speed [µm s^{-1}]	15000	5000	5000	15000
Minimum slicing distance [µm]	0.2	0.2	0.2	0.2
Maximum slicing distance [µm]	0.4	0.4	0.4	0.4
Hatching distance [µm]	0.3	0.3	0.3	0.3
Contour count	1	1	1	1
Hatching angle [°]	0	0	0	0

C.3.2. Substrate protocols

Uniform layers TOPAS

The steps taken to create a TOPAS:toluene 20wt% solution are summed up below with comments of what was observed.

1. Clean a bottle with ethanol and let it evaporate for one hour
2. Weigh 10.84 g of TOPAS gradules
3. Fill bottle with 50 mL toluene
4. Add the TOPAS gradules
5. Ultrasonic cleaner with a full sinus wave for 15 min at 20 °C (start: temperature of 30 °C, end: temperature of 39 °C)
6. Wooden stick to stir TOPAS and toluene mixture
7. Ultrasonic cleaner with a full sinus wave for 15 min at 20 °C (start: temperature of 38 °C, end: temperature of 44 °C)
8. Ultrasonic cleaner with a full sinus wave for 15 min at 20 °C (start: temperature of 44 °C, end: temperature of 48 °C)
9. Solution rested for 1.25 h
10. Ultrasonic cleaner with a full sinus wave for 15 min at 20 °C
11. Wooden stick to stir the glue like TOPAS which was stuck on the bottom of the bottle (It got stuck to the wooden stick)
12. Ultrasonic cleaner with a full sinus wave for 15 min at 20 °C (end: temperature of 46 °C)
13. Rotate/spin the bottle by hand
14. Ultrasonic cleaner with a full sinus wave for 15 min at 20 °C (end: temperature of 47 °C)
15. Rotate/spin the bottle by hand (still only a bit dissolved)
16. Solution rested overnight, 18.75 h (still not dissolved)
17. Shake it a lot by hand (alsmost dissolved)
18. Ultrasonic cleaner with a full sinus wave for 15 min at 20 °C (end: temperature of 47 °C, still no progess)
19. Orbital shaker for 5 min at 1500 RPM
20. Solution rested for 1.5 h to 2 h
21. Orbital shaker for 3 min at 2200 RPM
22. Solution rested for 45 min
23. Orbital shaker for 5 min at 1500 RPM (TOPAS 'glue' still stuck at the edges of the bottle, but almost completely dissolved)
24. Ultrasonic cleaner with a full sinus wave for 15 min at 20 °C (start: temperature of 30 °C, end: temperature of 38 °C)
25. Orbital shaker for 7 min at 2200 RPM (TOPAS completely dissolved)

The most important conclusion for dissolving TOPAS granules into toluene is that placing it on an orbital shaker speeds up the process. While after shaking it, a real difference was observed. Stirring the solution with a wooden stick did not help, and the TOPAS got stuck to the wooden stick which influences the final concentration. The results of the spin coated films of TOPAS are shown in figure C.43.

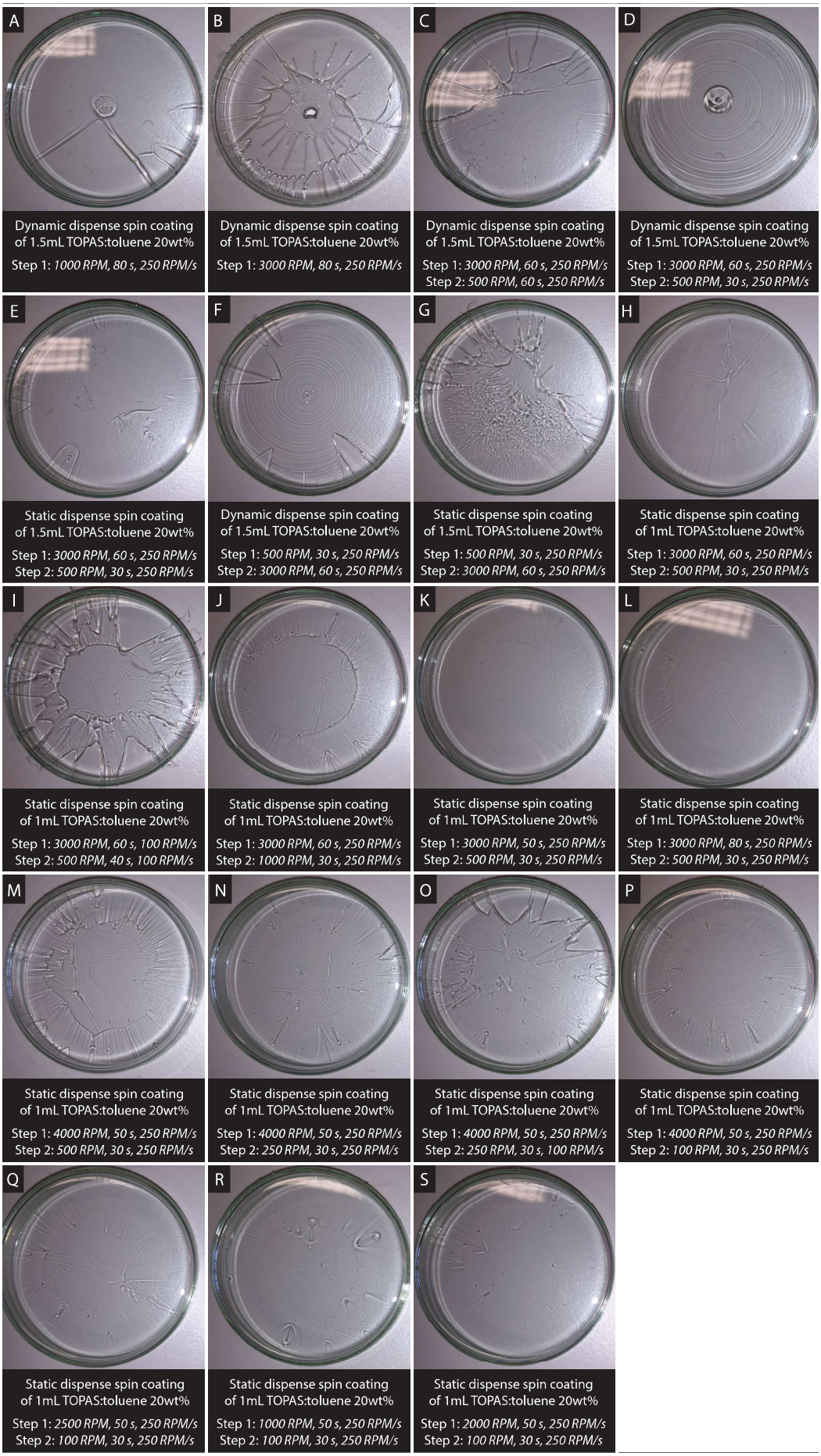

Figure C.43: Results of spin coating TOPAS onto a glass Petri dish to develop a general spin coating protocol to manufacture uniform layers of TOPAS. The used parameters to spin coat the layers of TOPAS are presented below the corresponding Petri dish.

For creating uniform layers of TOPAS a spin coat step of 1000 RPM, for 80 s, with a spin acceleration of 250 RPM/s and 1.5 mL is dynamically dispensed during the spin coating. The resulting film is shown in figure C.43A. The spin speed was changed to 3000 RPM to see the effect of changing the spin speeds to create films of different thicknesses. The spin coated film is presented in figure C.43B. Because this spin speed gave a worse result than the first one, this one will be tweaked to create an uniform layer of which one step is at 3000 RPM. A spin coat step of was added after the 3000 RPM spin coat step to spread the solution more slowly on the substrate, which has the same settings as the first one but only the spin speed was changed to 500 RPM. The resulting TOPAS film is shown in figure C.43C. Subsequently, the duration of the final step was decreased to reduce the influence of the second step, shown in figure C.43D. While the coverage of the layer is better, a wave pattern can be observed. The difference between a dynamic dispense spin coat technique and a static dispense spin coat technique was investigated. The difference can be seen by comparing figure C.43D and figure C.43E. The two spin coating steps were flipped to see the difference in spreading the solution before and after the initial step. Also, the difference between a dynamic dispense spin coat technique and a static dispense spin coat technique was investigated. These films are shown in figure C.43F and figure C.43G. Again, the wave pattern can be observed for the dynamic dispense spin coat technique. A static dispense spin coat technique will be used from now on to eliminate the wave pattern. Flipping the steps did not improve the spin coated layer of TOPAS. So, the first step will be the one which will be used to change the spin speeds in the following experiments. Using 1 mL of TOPAS:toluene solution instead of 1.5 mL slightly increased the uniformity of the layer, figure C.43H. In figure C.43I can be observed that increasing the time of the second spin coat step by 10 s ruins the film. Increasing the spin speed of the second step also does not improve the uniformity. Decreasing the duration of the first results in an uniform film of TOPAS, shown in figure C.43K. Increasing the duration results in a slightly less uniform layer, figure C.43L. When a different spin speed is used for the first step, which is the goal of the experiment, it no longer results in an uniform layer, shown in figure C.43M. As shown in figure C.43N, changing the spin speed of the second step from 500 RPM to 250 RPM increases the uniformity of the film. But decreasing the acceleration of the last step does not, figure C.43O. Decreasing the spin speed even more results in uniform layers again, which remain uniform for different spin coat speeds of the first steps. These are presented in figure C.43P, C.43Q, C.43R and C.43S. The final protocol will, therefore, consists of two steps. The first step has a spin time of 50 s, of which the spin speed can be varied. Next, the sample is spin coated for 30 s at 100 RPM. The acceleration for both steps is 250 RPM/s. 1 mL of the TOPAS solution is spin coated, on the outside of the Petri dish, with a static dispense spin coating technique.

TOPAS film thickness

From figure C.44 it can be seen that a minimum spin speed of 1000 RPM is required to cover the Petri dish completely with an TOPAS layer.

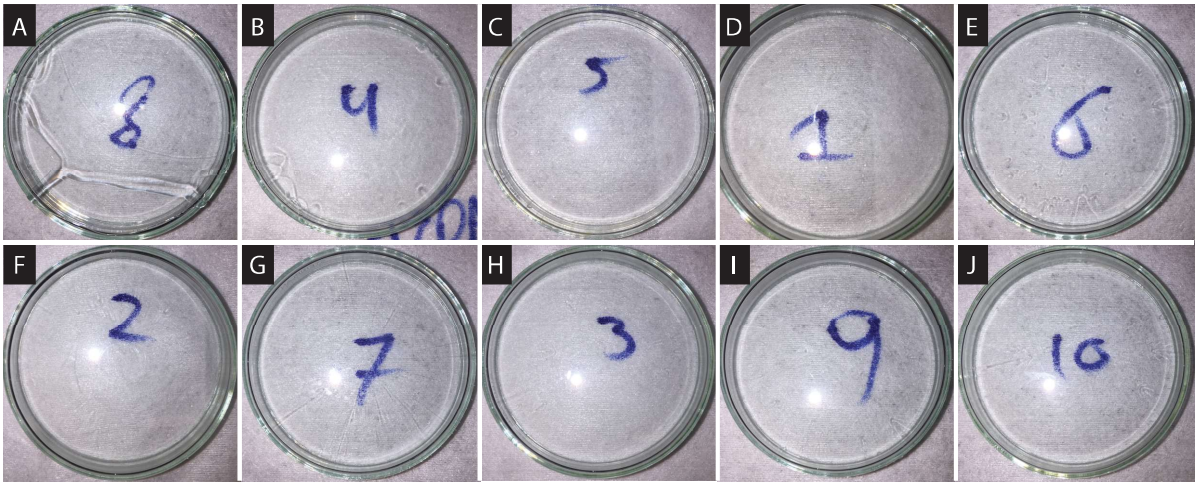

Figure C.44: Results of spin coating the TOPAS layer at different spin speeds of the second step. A: Image of the spin coated layer of TOPAS at 500 RPM. B: Image of the spin coated layer of TOPAS at 1000 RPM. C: Image of the spin coated layer of TOPAS at 1500 RPM. D: Image of the spin coated layer of TOPAS at 2000 RPM. E: Image of the spin coated layer of TOPAS at 2500 RPM. F: Image of the spin coated layer of TOPAS at 3000 RPM. G: Image of the spin coated layer of TOPAS at 3500 RPM. H: Image of the spin coated layer of TOPAS at 4000 RPM. I: Image of the spin coated layer of TOPAS at 4500 RPM. J: Image of the spin coated layer of TOPAS at 5000 RPM.

The results regarding the measured thickness and uniformity of the different TOPAS films are shown in figure C.45. According to literature, the thickness of the layer scales proportional to the inverse of the spin speed squared.[111] The fitted function (black dashed line) with this relationship has a coefficient of determination, R^2, of 0.91. A thickness of 10 µm is required while commercial porous membranes for cell culturing are available with that thickness as presented in table 2.1. To get a TOPAS layer of the required thickness (red dashed line), a spin coating speed of 3900 RPM is needed as indicated by the crossing of the two dashed lines.

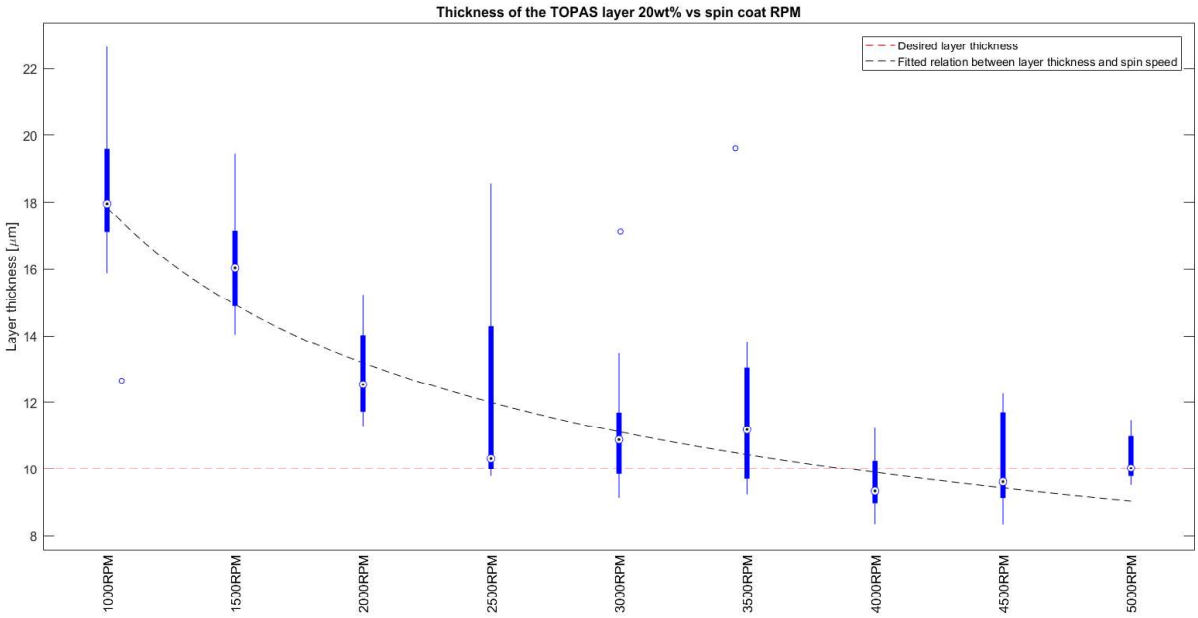

Figure C.45: Boxplot (showing the median, 25th percentile, 75th percentile, and data points outside the inter-quartile range) for the thickness of each of the different spin speeds of spin coated TOPAS films. A line is fitted with the known relation between spin speed and layer thickness.

PEDOT:PSS film thickness

The resulting spin coated layers are presented in figure C.46. The results regarding the thickness measurements of the PEDOT:PSS films are shown in figure C.47.

Figure C.46: Results of spin coating the PEDOT:PSS layer at different spin speeds of the second step. A: Image of the spin coated layer of PEDOT:PSS at 500 RPM. B: Image of the spin coated layer of PEDOT:PSS at 750 RPM. C: Image of the spin coated layer of PEDOT:PSS at 1000 RPM. D: Image of the spin coated layer of PEDOT:PSS at 1250 RPM. E: Image of the spin coated layer of PEDOT:PSS at 1500 RPM.

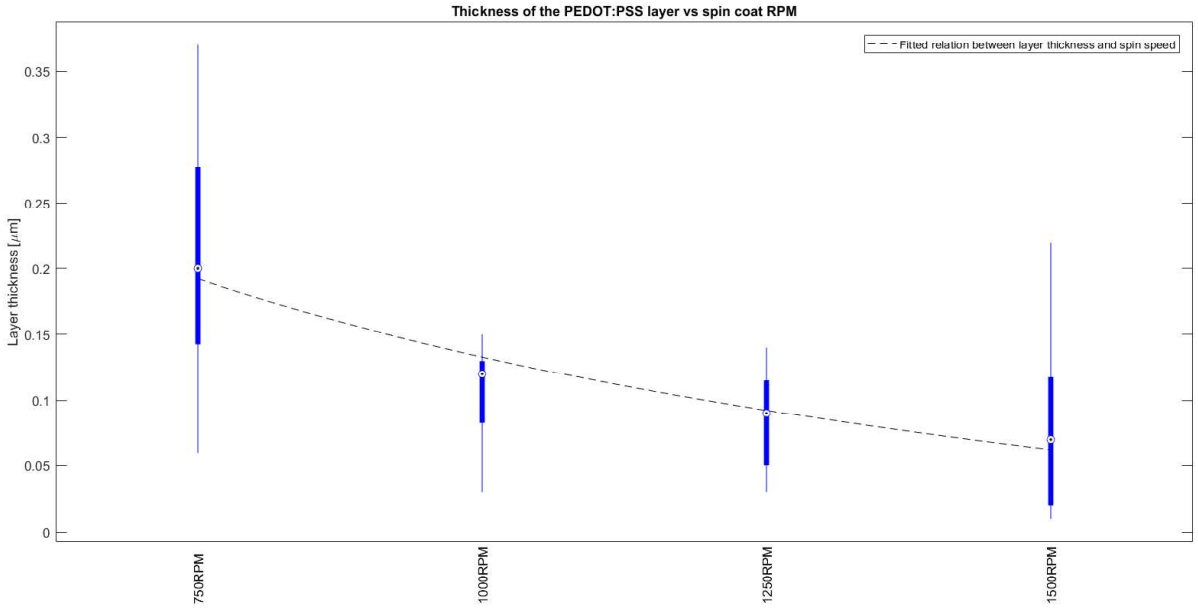

Figure C.47: Boxplot (showing the median, 25th percentile, 75th percentile, and data points outside the inter-quartile range) for the thickness of each of the different spin speeds of spin coating PEDOT:PSS films. A line is fitted with the known relation between spin speed and layer thickness.

The results regarding the sheet resistance of the PEDOT:PSS films are shown in figure C.48.

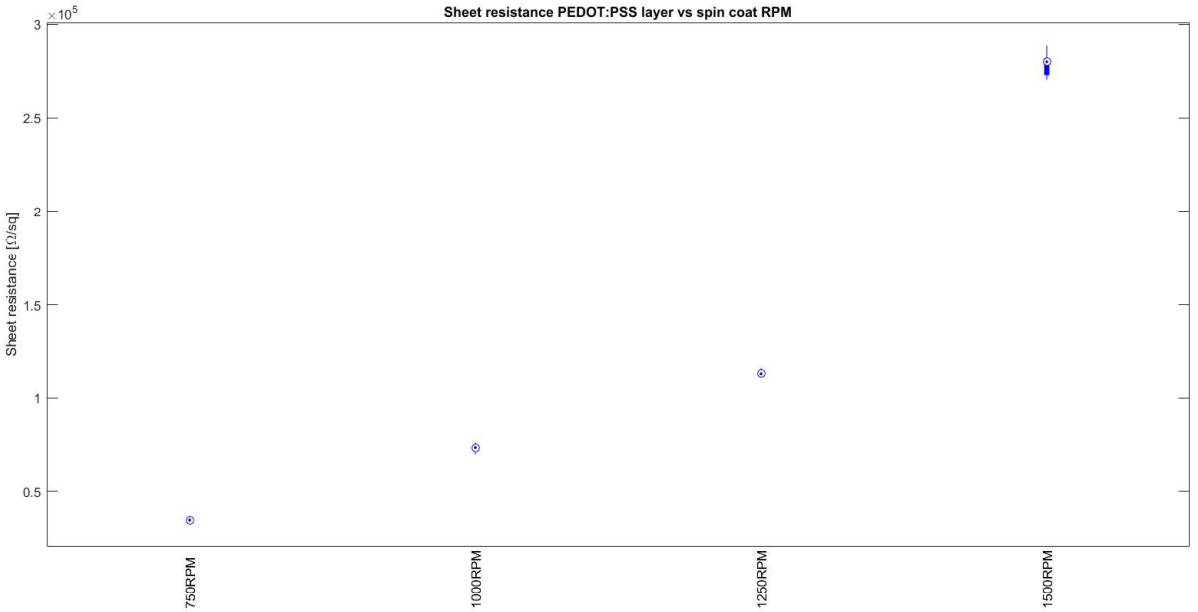

Figure C.48: Boxplot (showing the median, 25th percentile, 75th percentile, and data points outside the inter-quartile range) for the sheet resistance of each of the different spin speeds of spin coating PEDOT:PSS films.

From figure C.46 it can be seen that a minimum spin speed of 750 RPM is required to cover the Petri dish completely. The results regarding the measured thickness and uniformity of the PEDOT:PSS films are shown in figure C.47. The found thickness of the film spin coated at 1000 RPM is in line with the resulting thickness found in literature with the same spin coating settings.[19] According to literature, the thickness of the layer scales proportional to the inverse of the spin speed squared.[111] The fitted function (black dashed line) with this relationship has a coefficient of determination, R^2, of 0.97.

A spin coating speed of 750 RPM is selected while this layer results in an uniform layer with the lowest sheet resistance. As presented in figure C.49, the measured resistance can be used to determine, roughly, the

expected thickness of the layers while the bulk resistance of the spin coated PEDOT:PSS solution is known. The expected thicknesses are in line with the measured thicknesses.

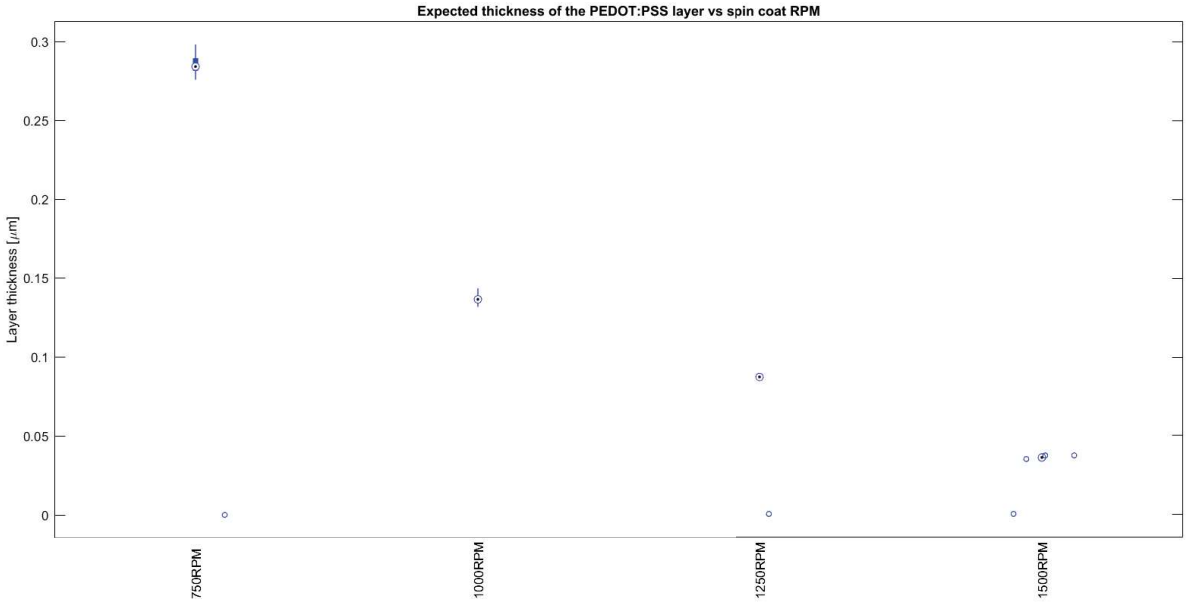

Figure C.49: Boxplot (showing the median, 25th percentile, 75th percentile, and data points outside the inter-quartile range) for the expected thickness for each of the different spin speeds of spin coating PEDOT:PSS films.

PAA film thickness

The resulting spin coated layers is presented in figure C.50.

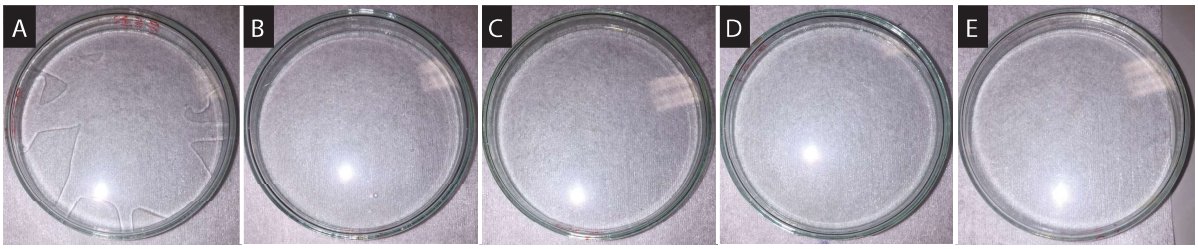

Figure C.50: Results of spin coating the PAA layer at different spin speeds of the second step. A: Image of the spin coated layer of PAA at 250 RPM. B: Image of the spin coated layer of PAA at 500 RPM. C: Image of the spin coated layer of PAA at 750 RPM. D: Image of the spin coated layer of PAA at 1000 RPM. E: Image of the spin coated layer of PAA at 1250 RPM.

The results regarding the measured thicknesses of the PAA films are shown in figure C.51.

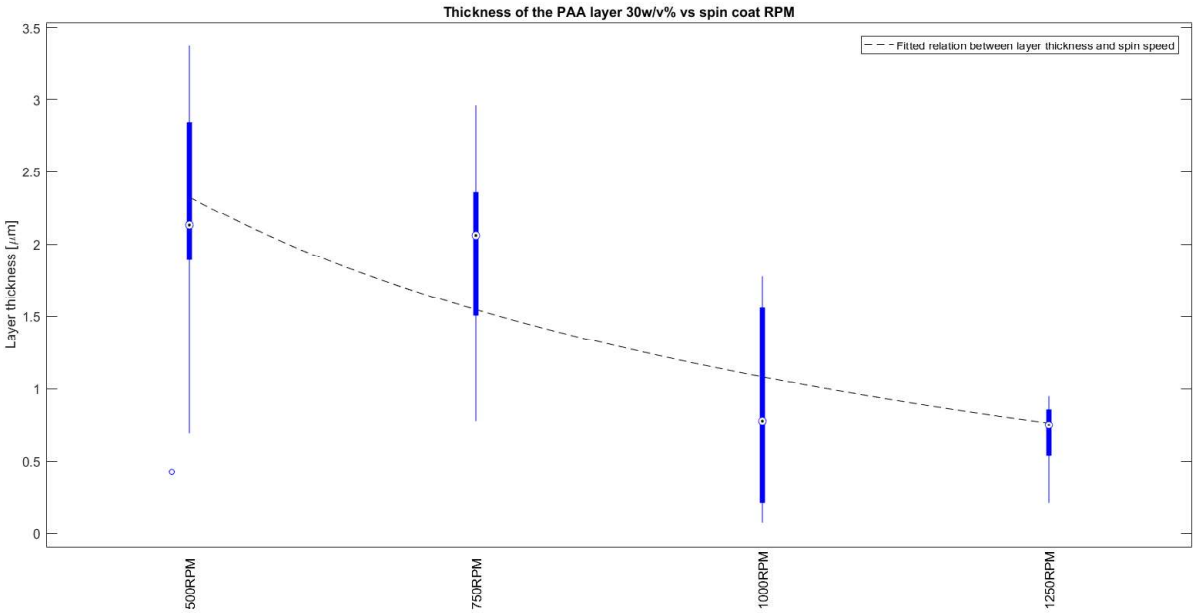

Figure C.51: Boxplot (showing the median, 25th percentile, 75th percentile, and data points outside the inter-quartile range) for the thickness of each of the different spin speeds of spin coating PAA films. A line is fitted with the known relation between spin speed and layer thickness.

From figure C.50 it can be seen that a minimum spin speed of 750 RPM is required to cover the Petri dish completely. According to literature, the thickness of the layer scales proportional to the inverse of the spin speed squared.[111] The fitted function (black dashed line) with this relationship has a coefficient of determination, R^2, of 0.78. The measured thicknesses differ significantly from literature, probably due to the difference in substrate material, variations in the cleaning procedure and spin coat procedures.[61] Additional experiments were performed to get thicker films, of which the results are presented in figure C.52.

Additional experiments PAA

The results regarding the measured thicknesses of the spin coated layers are presented in figure C.52.

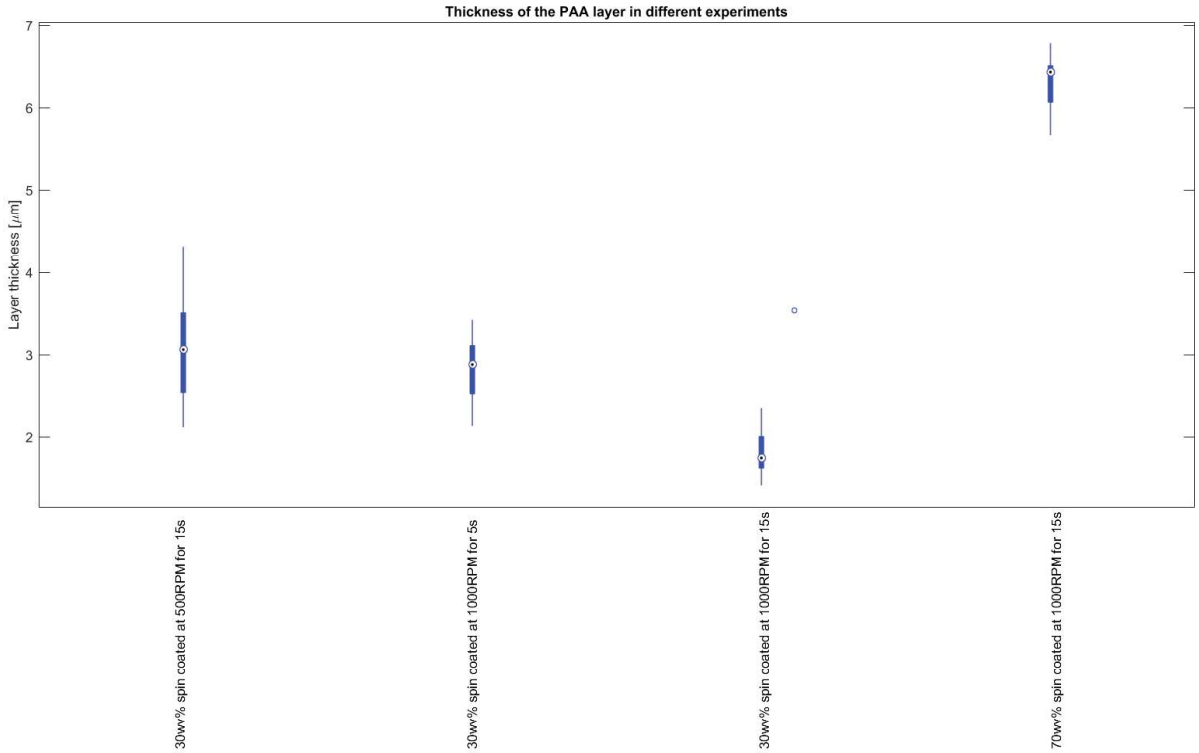

Figure C.52: Boxplot (showing the median, 25th percentile, 75th percentile, and data points outside the inter-quartile range) for the thickness of each of the different spin speeds of spin coating PAA films.

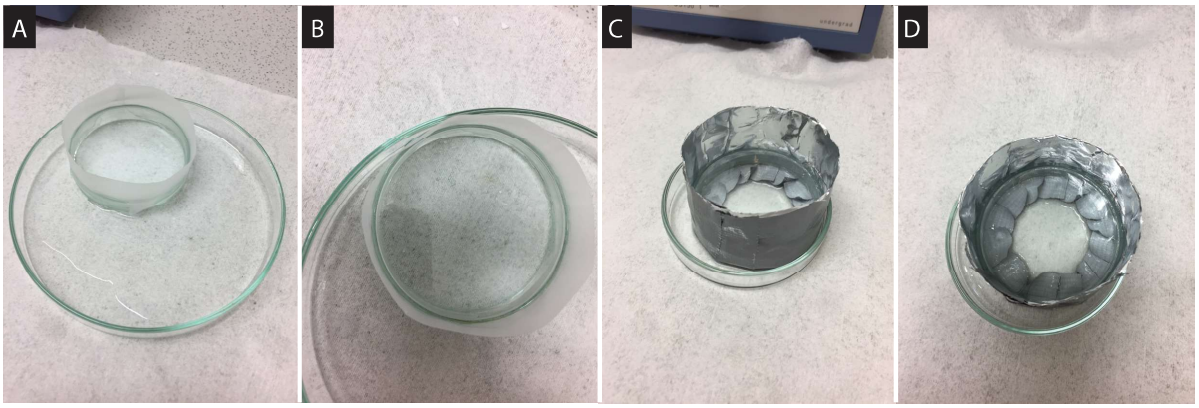

Figure C.53: Results of the casting experiment of PAA onto a glass Petri dish. A-B: Experiment with the side walls made out of tape. C-D: Experiment with the side walls made out of duct tape and aluminium foil.

Looking at the measured thicknesses of the films in figure C.52, none of them come close to the desired values. That is why a casting method is tried as well. Looking at the pictures in figure C.53 regarding the casting experiments, both times the PAA solution started leaking through the side walls which can be seen by the solution in the Petri dishes. So creating the sidewalls like it is shown in figure C.53 is not a valid possibility in this case because of the high viscosity of the PAA 70wv% PAA solution. Therefore, it is decided to use a TOPAS sheet as second sacrificial layer.

Multilayer substrate manufacturing protocol
Results of stacking the layers in the described different orders is presented in figure C.54.

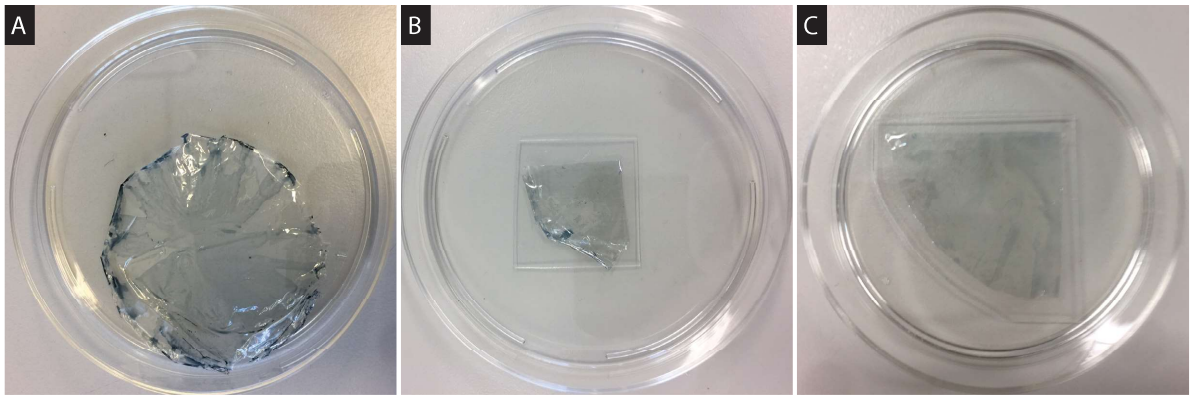

Figure C.54: Results from the different ways of stacking the layers on top of each other. A: First, a PAA film is spin coated on the spin coated TOPAS film. Subsequently, a film of PEDOT:PSS is spin coated on the other side of the TOPAS film. B: First, a PEDOT:PSS film is spin coated on the spin coated TOPAS film. Subsequently, a film of PAA is spin coated on the other side of the TOPAS film. These layers are placed on top of a sheet of TOPAS. C: First, a PAA film is spin coated on a TOPAS sheet. Subsequently, a film of PEDOT:PSS is spin coated on the spin coated TOPAS film. Which is placed on top of the TOPAS sheet with the PAA film.

First spin coating the PAA layer followed by the PEDOT:PSS layers results in a non uniform layer of PEDOT:PSS, which is seen in figure C.54A. This is caused due to the flipping over of the layer. Because it is almost impossible to place it back, manually, on a Petri dish without introducing rimples due to the folding and tendency to roll up of the PAA layer and the TOPAS layer. In figure C.54B, the result is shown were the PEDOT:PSS layer is spin coated on top of the TOPAS film, flipped, and the PAA film is spin coated on the back of it. The stacking of the layers was successful. But to ensure a complete coverage by the PAA film, a large amount has to be spin coated on top of it. This could have as a result that the PAA solution will get between the glass Petri dish and the PEDOT:PSS layer. Finally, the protocol were the PAA solution was spin coated on the TOPAS sheet was also successful, shown in figure C.54C. While this method has not the risk of getting PAA on top of the PEDOT:PSS layer, which will be an additional layer to imprint, it is selected as the best one.

In figure C.55A, the layer are stacked manually on to op of each other. Placing the substrate in the desiccator for 10 min min has little to no effect on the amount of air trapped between the layers, shown by comparing the figures C.55A and C.55B. Pushing away the air bubbles with the back of a tweezer improved the substrate locally. The imprinted part of the substrate would have a lot less air bubbles but due to the pushing of the air bubbles, some relative heigh rimples formed in the top layers of the substrate. This is presented in figure C.55C. A large number of air bubbles is removed by the last method which can be seen in figure C.55D.

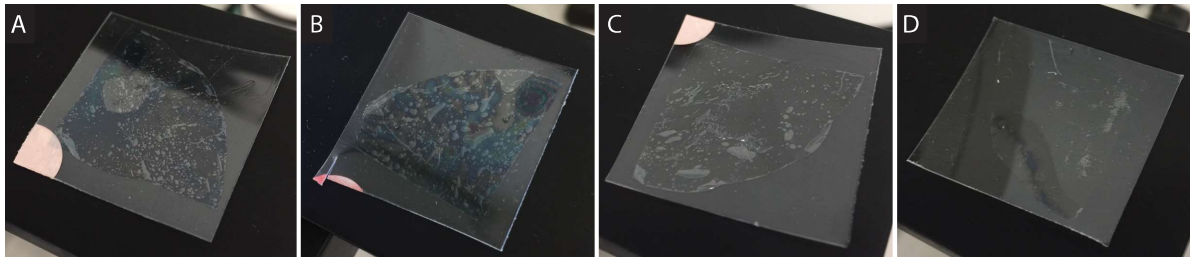

Figure C.55: Results from the experiment to minimalize the number of air bubbles trapped between the layers. A: Pushing the bubbles away by hand. B: Placing it in vacuum for 10 min in a desiccator. C: Pushing the air bubbles with the backside of a pair of tweezers. D: Pushing the air bubbles away by sliding a red stirring stick across the layers.

C.3.3. Imprinting protocol

Imprinting force
The results of imprinting at 4000 N is presented in figure C.56 and figure C.57. The results of imprinting at 5000 N is presented in figure C.58.

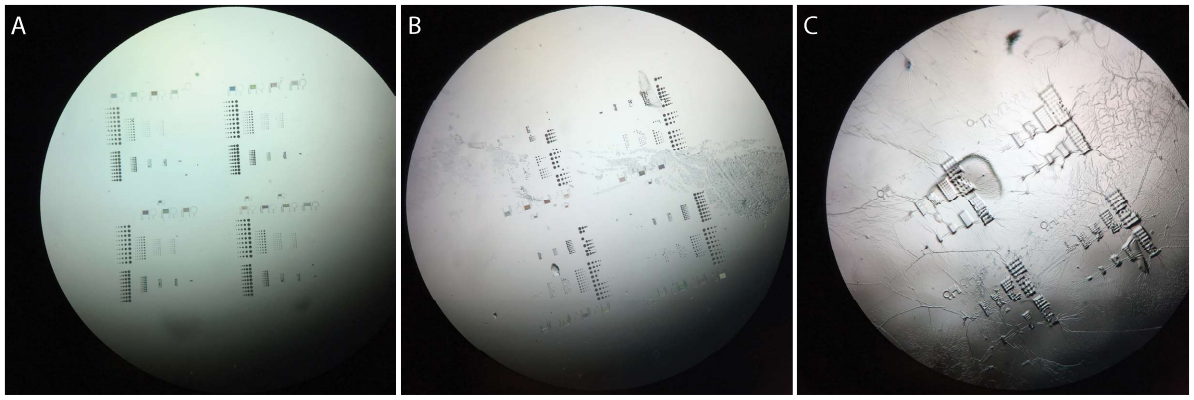

Figure C.56: Results of imprinting at 120 °C, 4000 N, with a holding time of 10 min. A: Mold before imprinting. B: Mold after imprinting. C: Substrate after imprinting and treatment with EG.

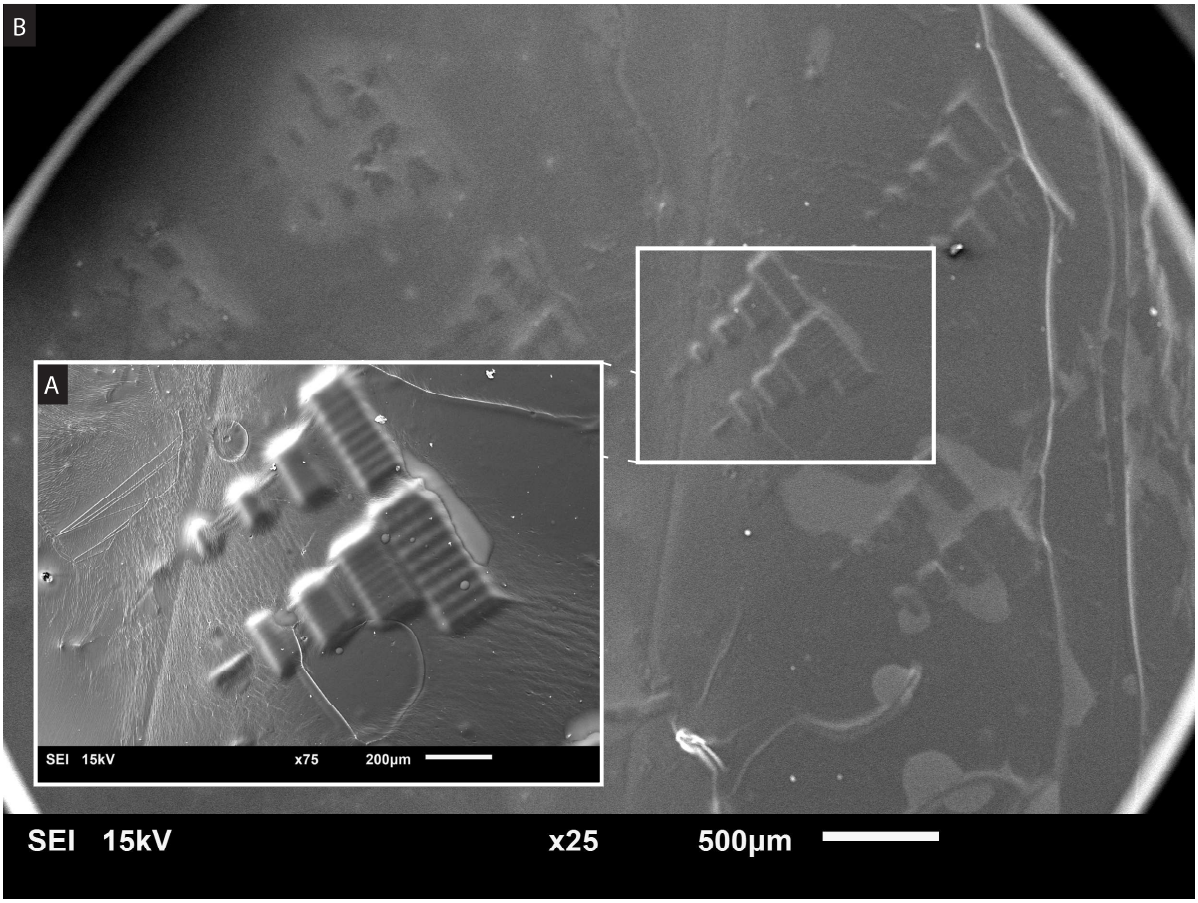

Figure C.57: SEM images of the multilayer substrate after imprinting at 120 °C, 4000 N, with a holding time of 10 min. A: Close up of one matrix with all the different elements. B: Overview of the non conductive side of the imprinted multilayer substrate.

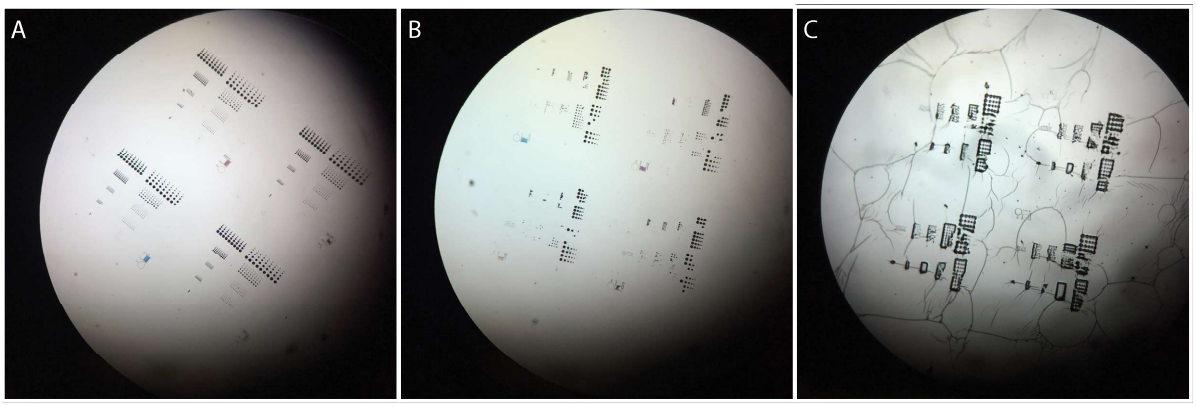

Figure C.58: Results of imprinting at 120 °C, 5000 N, with a holding time of 10 min. A: Mold before imprinting. B: Mold after imprinting. C: Substrate after imprinting and treatment with EG.

Comparing figure C.58A with C.58B, some of the pillars are gone. these got stuck in the substrate shown in figure C.58C. While comparing figure C.56A with C.56B shows that none of the pillars transferred into the substrate. Therefore, it can be concluded that a maximum force of 4000 N can be used without destroying the soft mold. But looking at the backside of the imprinted membrane, figure C.57, no through-holes were manufactured. It looks like the pillars with a small to no tip angle at all prevented the pillars with sharp tips of creating through-holes. Because the PEDOT:PSS layer does not become "soft" during the imprinting process and has to be ripped.[93] Helping to visually imagine this, it could be compared to puncturing a rubber glove a stick without a sharp tip and to puncture it with a stick with a sharp tip. A sharper tip (bigger tip angle) requires a lower force to puncture a rubber substrate than a tip with a smaller tip angle.[112] So, the influence of the tip angle has to be investigated while this influences the force which is needed to penetrate the PEDOT:PSS layer.

Influence tip angle of the pillars with sharp tips

Results of imprinting with pillar with tip angles of 60°, 70°, and 80° are presented in figure C.59. Results of imprinting with pillar with tip angles of 80° are presented in figure C.60. Results of imprinting with pillar with tip angles of 70° are presented in figure C.61. Comparing the figure C.59A with C.59B and figure C.61A with C.61B, some of the pillars are lost. But this does not influence the experiment to find the required tip angle to create through-holes. The big number of transferred pillars from the mold to the substrate in figure C.61 can be explained by the fact that the used glass coverslip was already used before and was cleaned with acetone and 2-propanol to reuse it. This has apparently influence on the adhesion between the pillars and the glass coverslip.

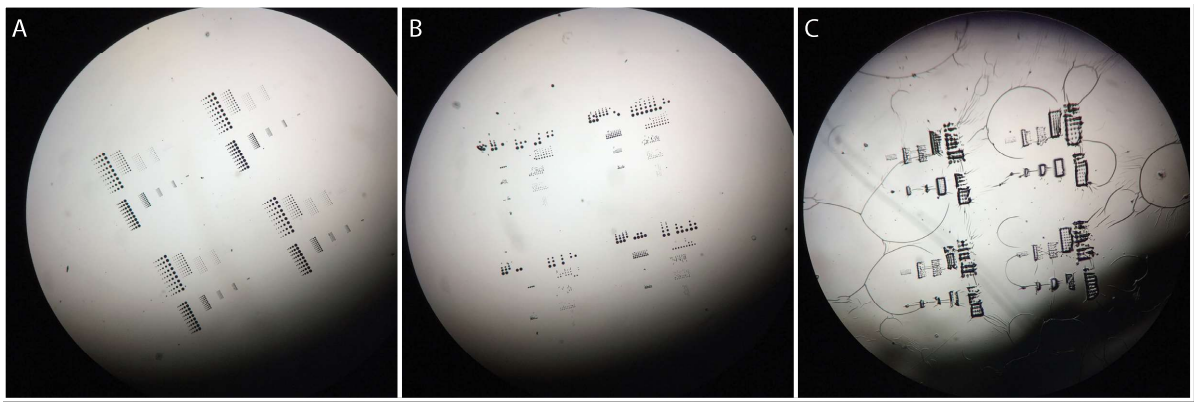

Figure C.59: Results of imprinting at 120 °C, 4000 N, with a holding time of 10 min with a mold which contains pillars with tip angles of 60°, 70°, and 80°. A: Mold before imprinting. B: Mold after imprinting. C: Substrate after imprinting and treatment with EG.

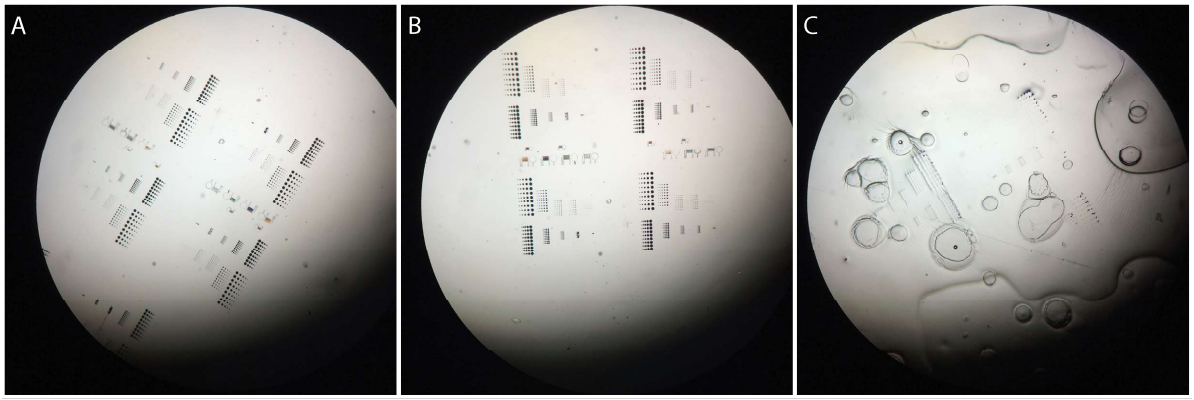

Figure C.60: Results of imprinting at 120 °C, 4000 N, with a holding time of 10 min with a mold which contains pillars with a tip angles 80°. A: Mold before imprinting. B: Mold after imprinting. C: Substrate after imprinting and treatment with EG.

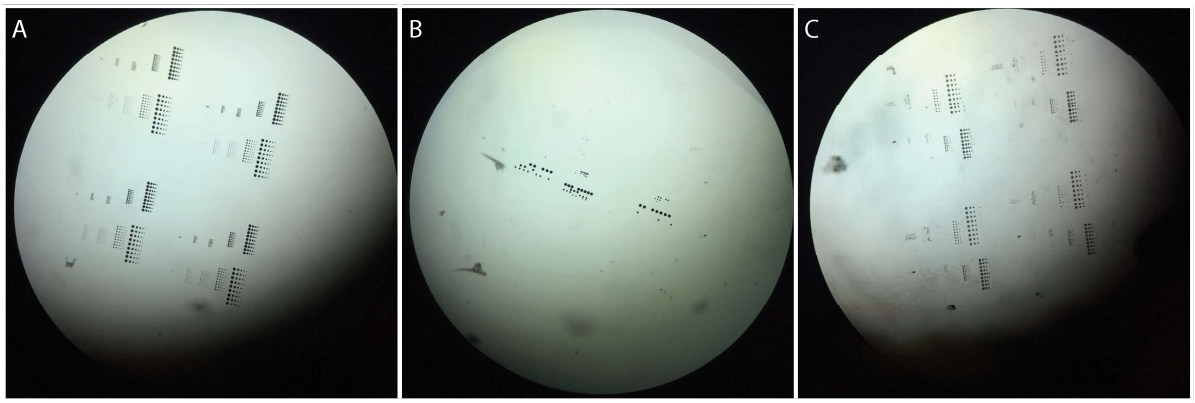

Figure C.61: Results of imprinting at 120 °C, 4000 N, with a holding time of 10 min with a mold which contains pillars with tip angles of 70°. A: Mold before imprinting. B: Mold after imprinting. C: Substrate after imprinting and treatment with EG.

In figure C.62A, two through-holes can be seen, but it is still believed that the pillars with a lower tip angle kept all the other pillars of puncturing through the PEDOT:PSS layer as discussed earlier. While only two through-holes are created with the first version, the experiments with only 70° tip angles and 80° tip angles were performed. From figure C.63, it can be seen that a large number of the pillars created through-holes. And with pillars with a tip angle of 70° did not puncture through the PEDOT:PSS layer, of which the SEM images are shown in figure C.64. From these three experiments, it can be concluded that a tip angle of at least 80° is required for creating through-holes.

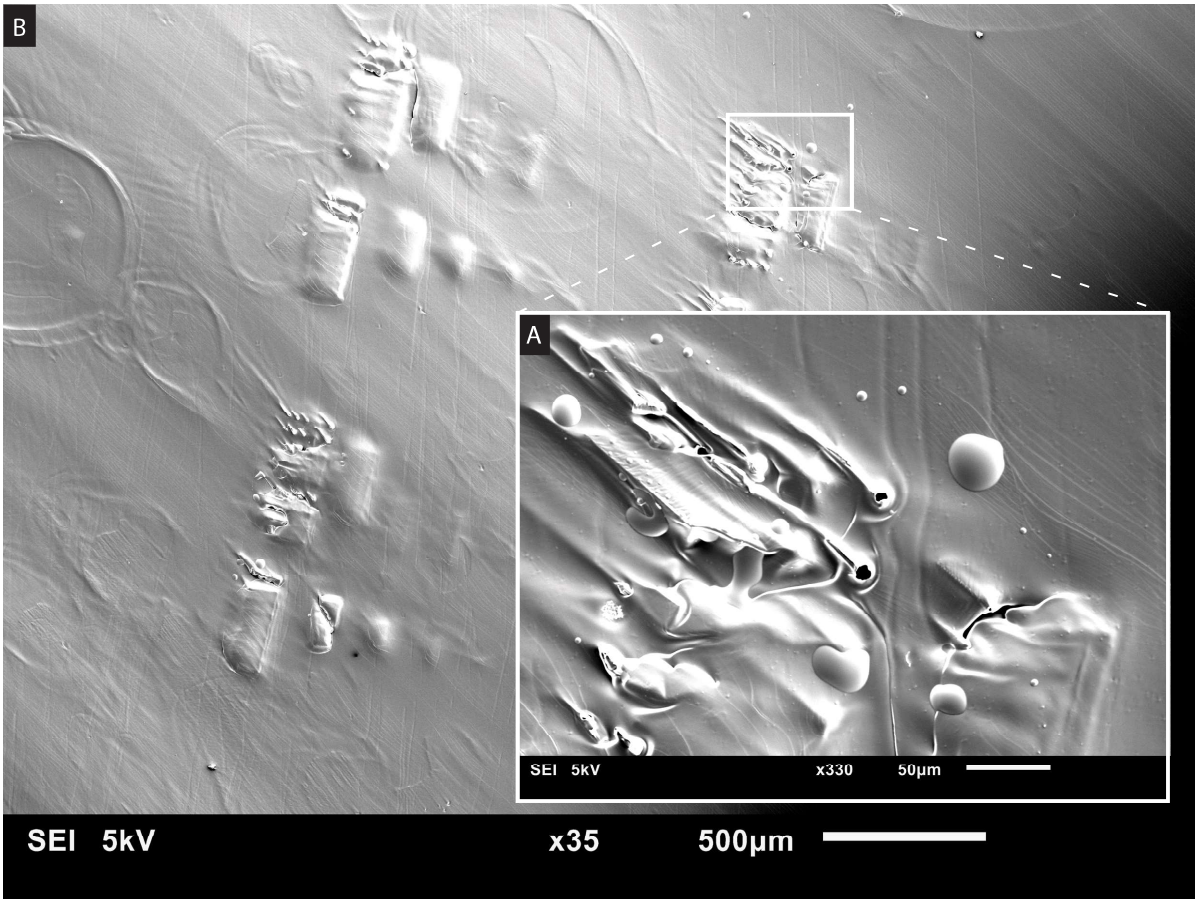

Figure C.62: SEM images of the multilayer substrate after imprinting at 120 °C, 4000 N, with a holding time of 10 min with a mold which contains pillars with tip angles of 60°, 70°, and 80°. A: Close up of one matrix with all the different elements. B: Overview of the non conductive side of the imprinted multilayer substrate.

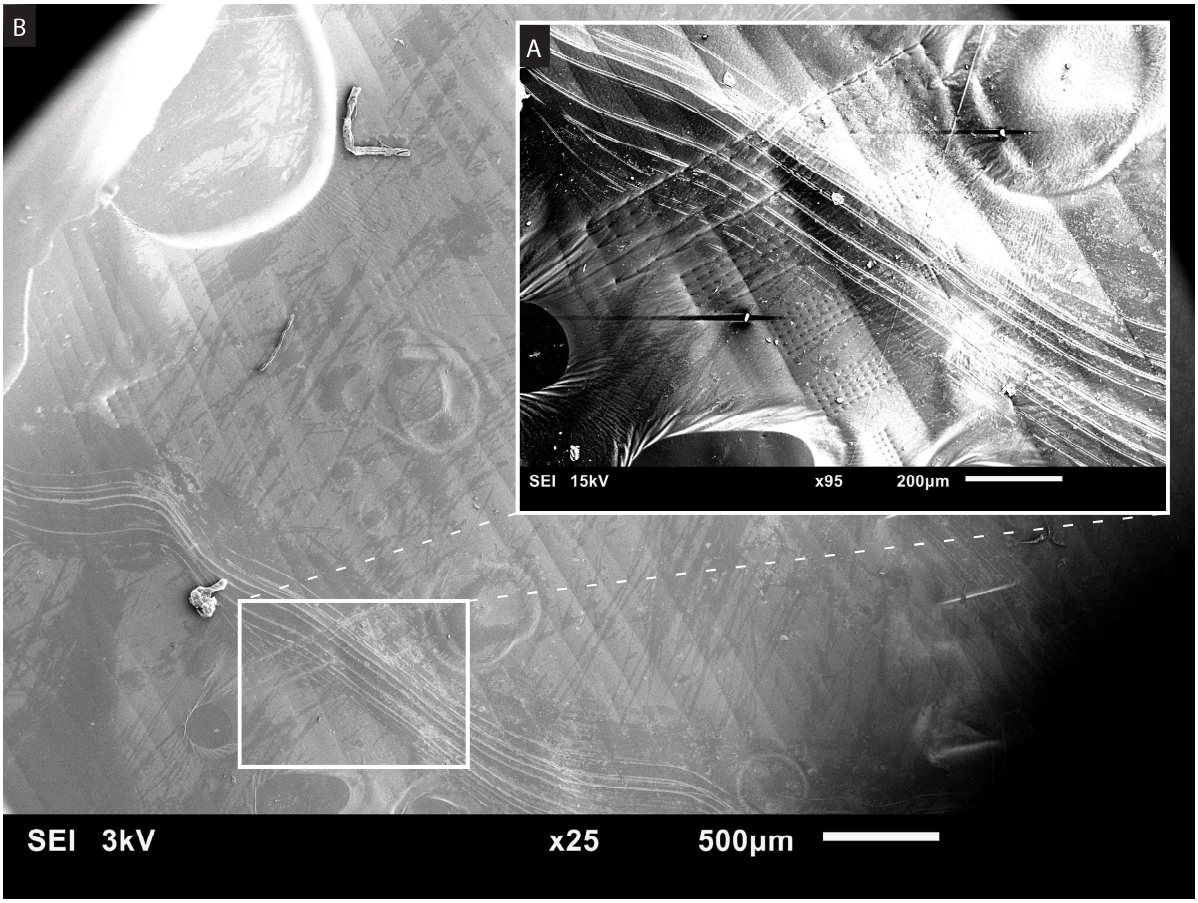

Figure C.63: SEM images of the multilayer substrate after imprinting at 120 °C, 4000 N, with a holding time of 10 min with a mold which contains pillars with tip angles of 80°. A: Close up of one matrix with all the different elements. B: Overview of the non conductive side of the imprinted multilayer substrate.

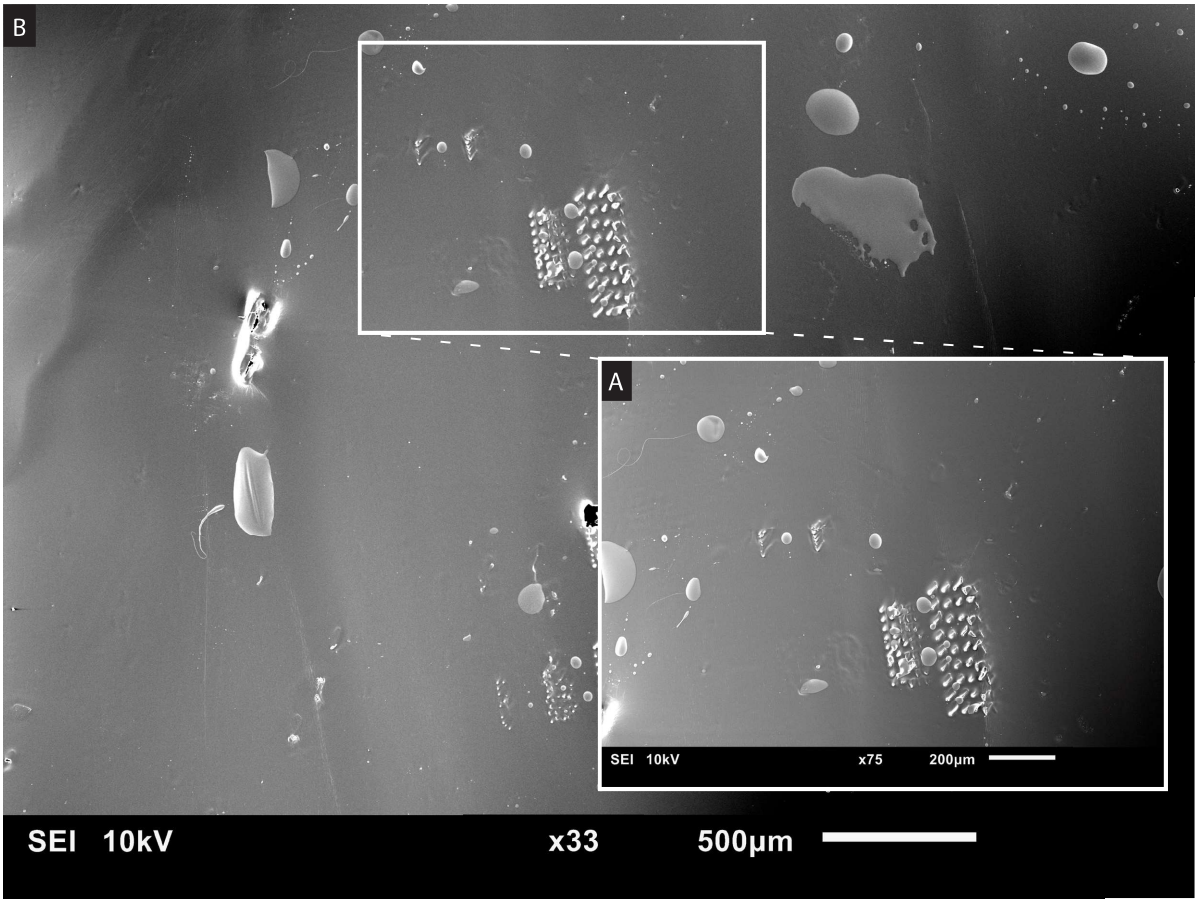

Figure C.64: SEM images of the multilayer substrate after imprinting at 120 °C, 4000 N, with a holding time of 10 min with a mold which contains pillars with tip angles of 70°. A: Close up of one matrix with all the different elements. B: Overview of the non conductive side of the imprinted multilayer substrate.

Imprinting temperature

The results of imprinting with an imprinting temperature of 130 °C is presented in figure C.65.

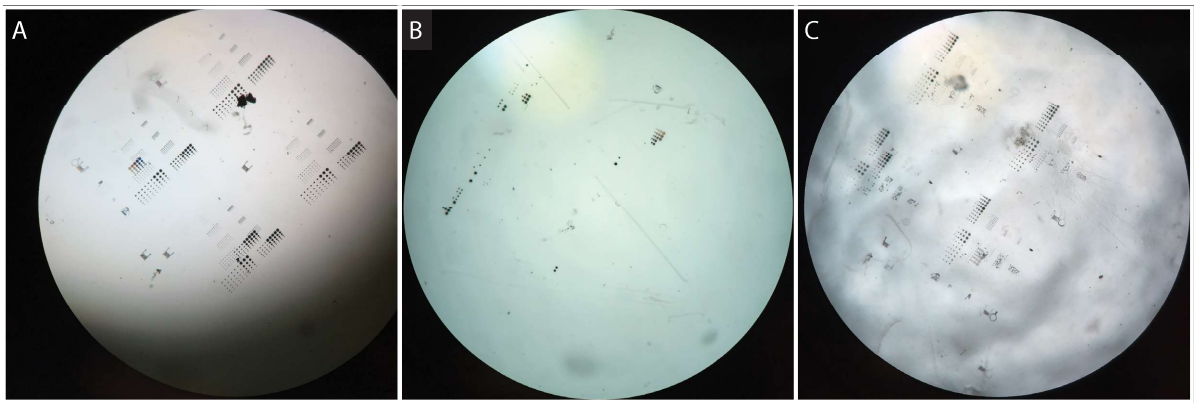

Figure C.65: Results of imprinting at 130 °C, 4000 N, with a holding time of 10 min. A: Mold before imprinting. B: Mold after imprinting. C: Substrate after imprinting and treatment with EG.

There is no need to compare the results of figure C.65 with the results presented in figure C.59 while almost all pillars transferred from the soft mold to the multilayer substrate. From the results, there can be concluded that a maximum imprinting temperature of 120 °C can be used to imprint the multilayer substrate without losing the features of the soft mold which can be seen by comparing figure C.65A with figure C.65B.

Holding time
The results of imprinting with a holding time of 20 min is presented in figure C.66.

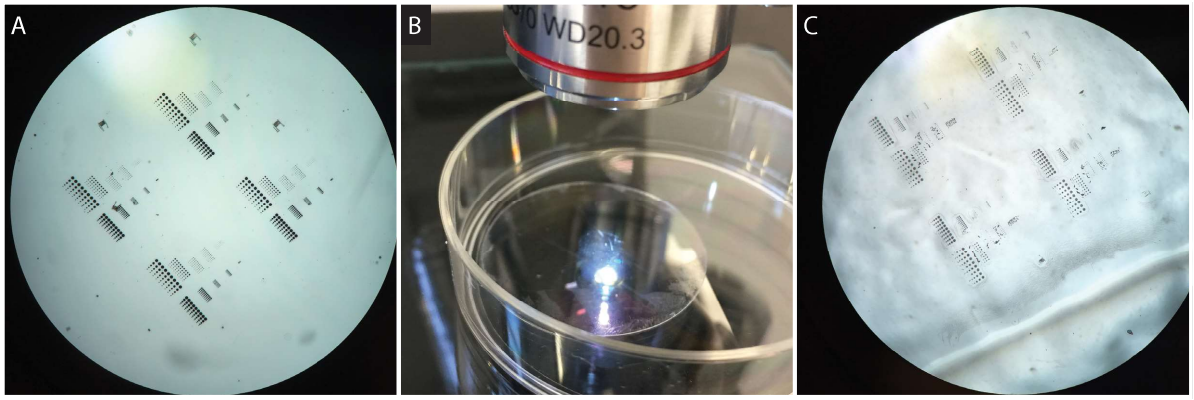

Figure C.66: Results of imprinting at 120 °C, 4000 N, with a holding time of 20 min. A: Mold before imprinting. B: Mold after imprinting. C: Substrate after imprinting and treatment with EG.

All the features transfered from the soft mold, figure C.66A, into the substrate, C.66C. This is confirmed by the glass cloverslip without any pillars shown in figure C.66B. While the holding time of 20 min resulted in the loss of all printed features, a maximum holdingtime of 10 min minutes can be used.

C.3.4. Post treatment

Dissolving the PAA layer
The results of the first protocol and the second protocol to see whether there is an improvement in the peeling of procedure of the membrane are already presented in figure C.63 and C.63. The straight lines which can be seen in figure C.64 are caused by peeling of the membrane while it was not completely separated from the sacrificial TOPAS sheet. This was not the case after an immersion of 2 h anymore.

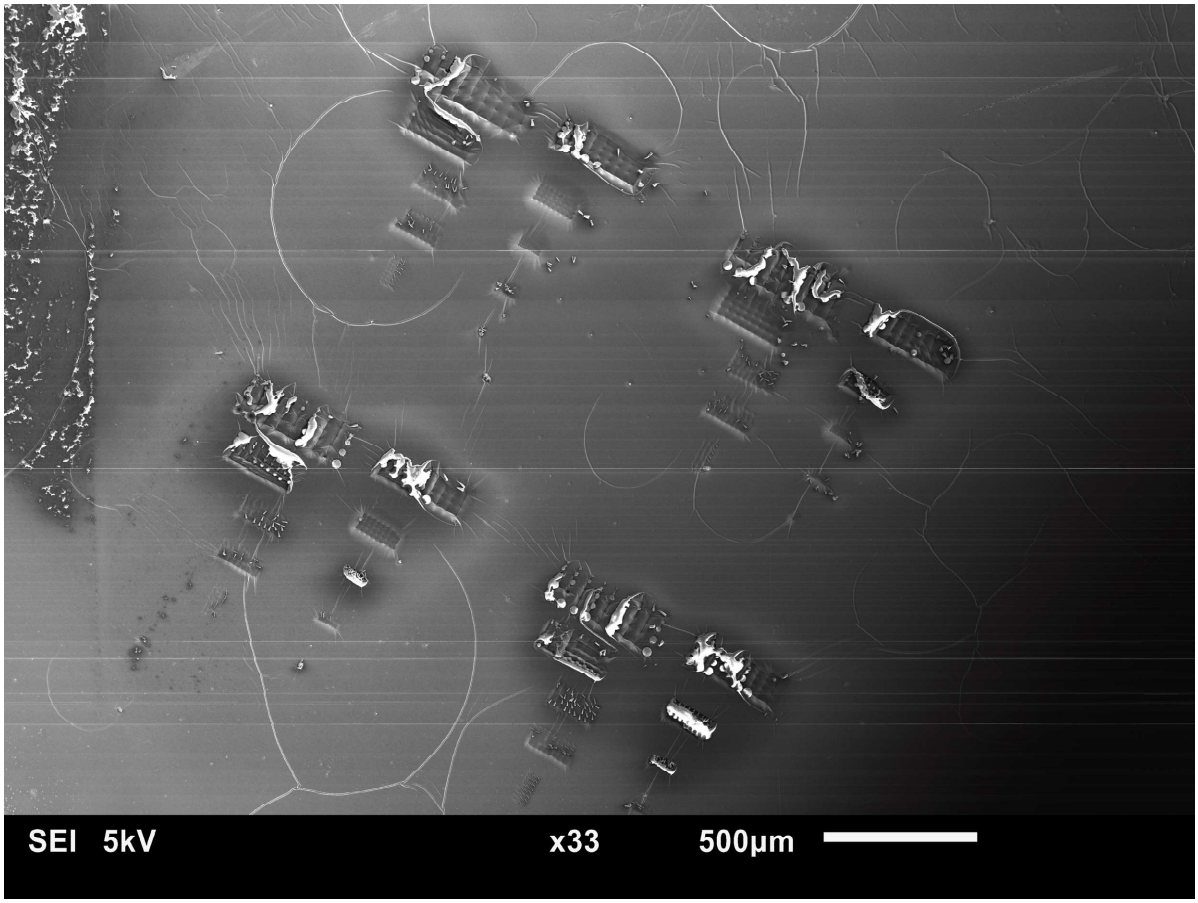

Figure C.67: SEM image of the PEDOT:PSS layer before immersion in EG for 15 min.

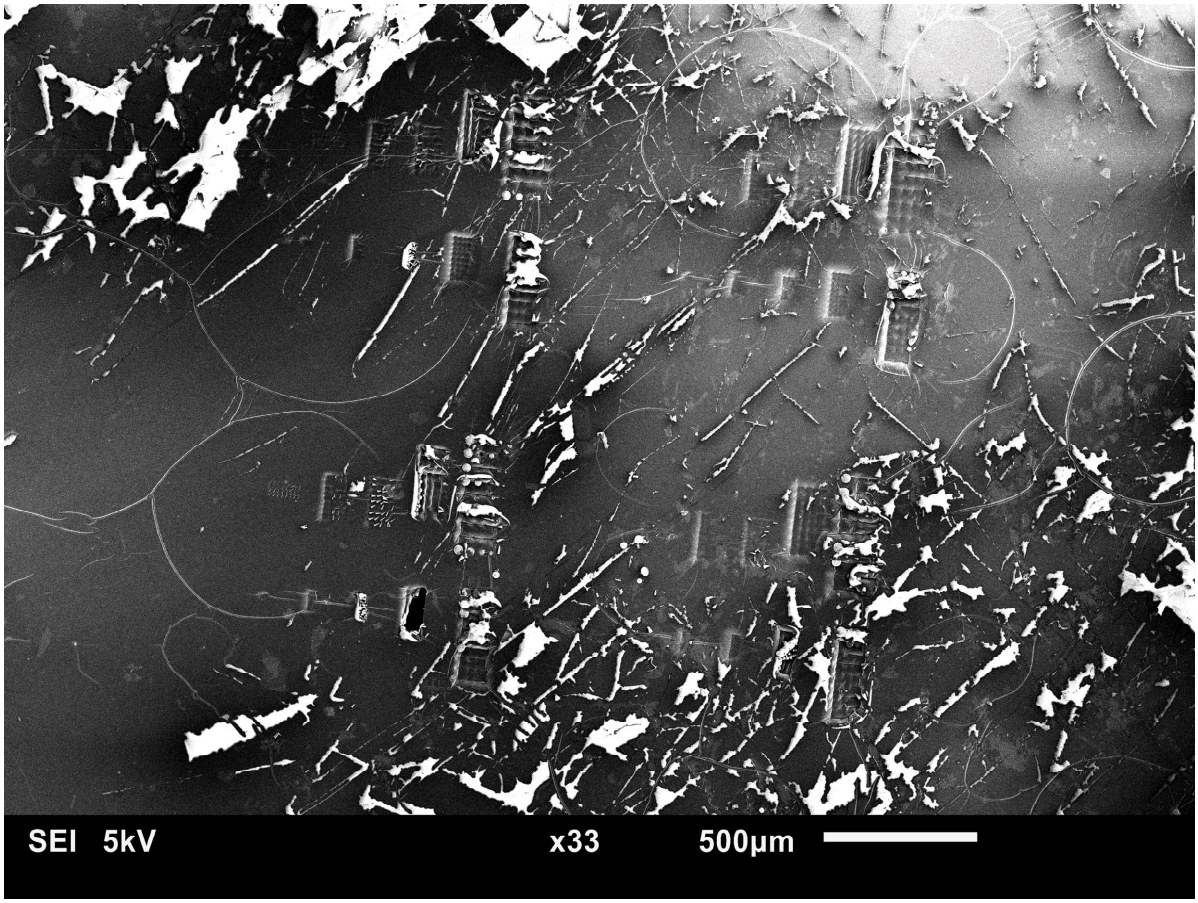

Figure C.68: SEM image of the PEDOT:PSS layer after immersion in EG for 15 min.

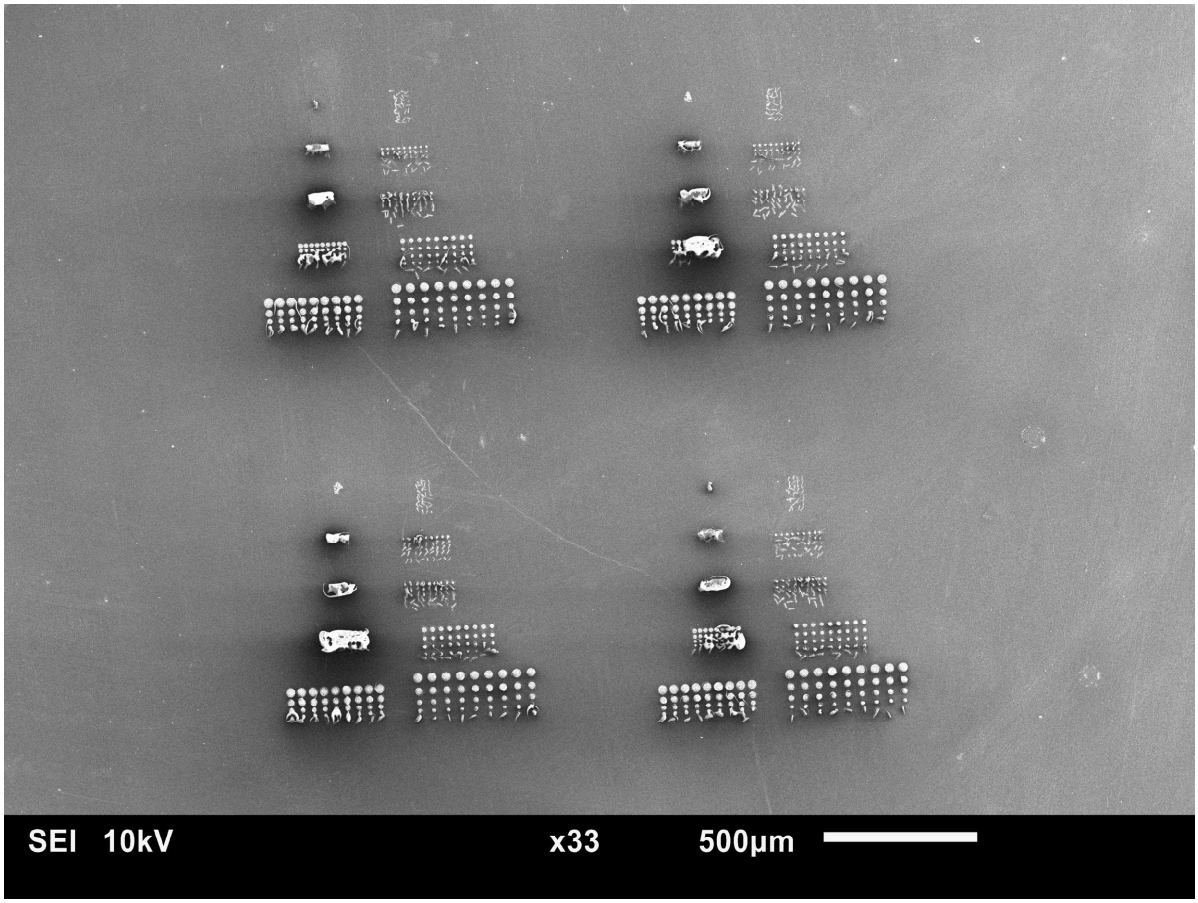

Figure C.69: SEM image of the PEDOT:PSS layer before immersion in EG for 2 h.

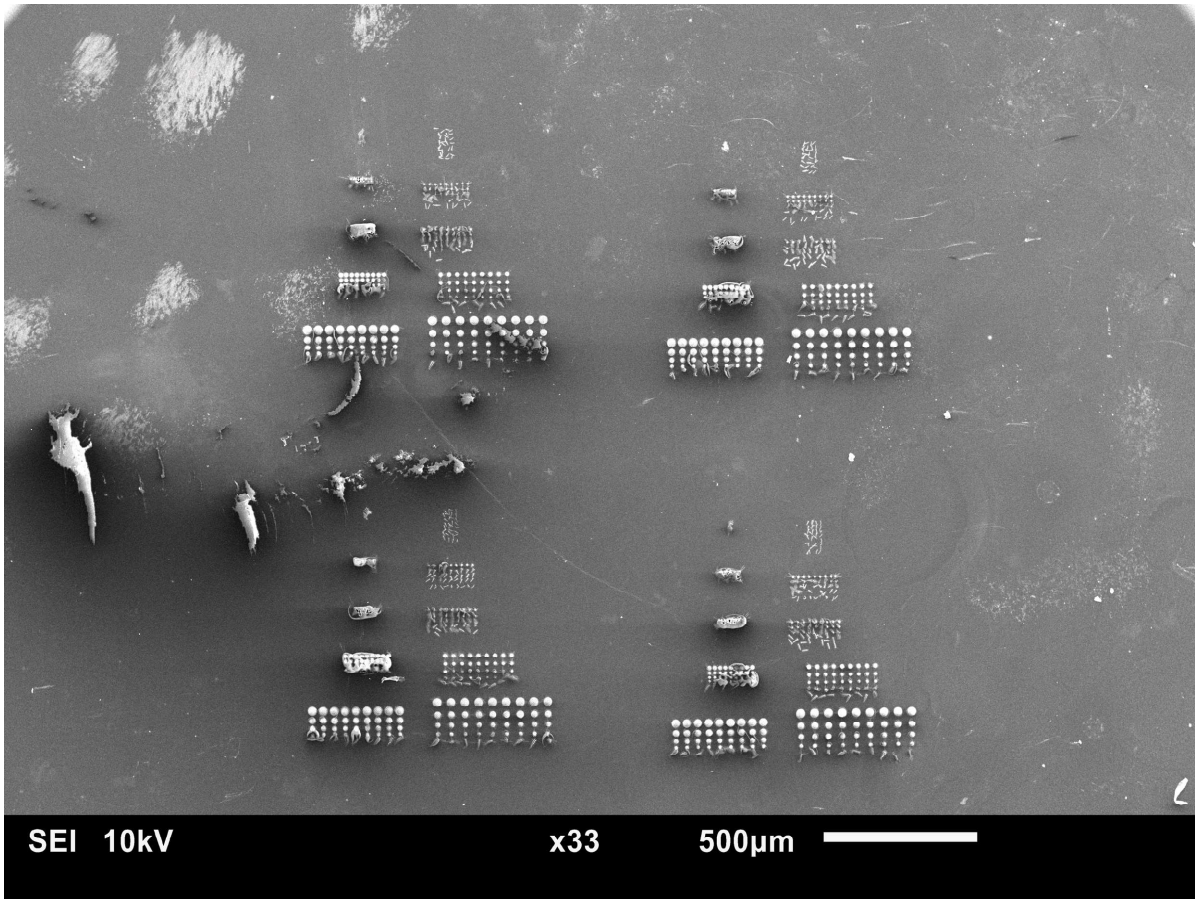

Figure C.70: SEM image of the PEDOT:PSS layer after immersion in EG for 2 h.

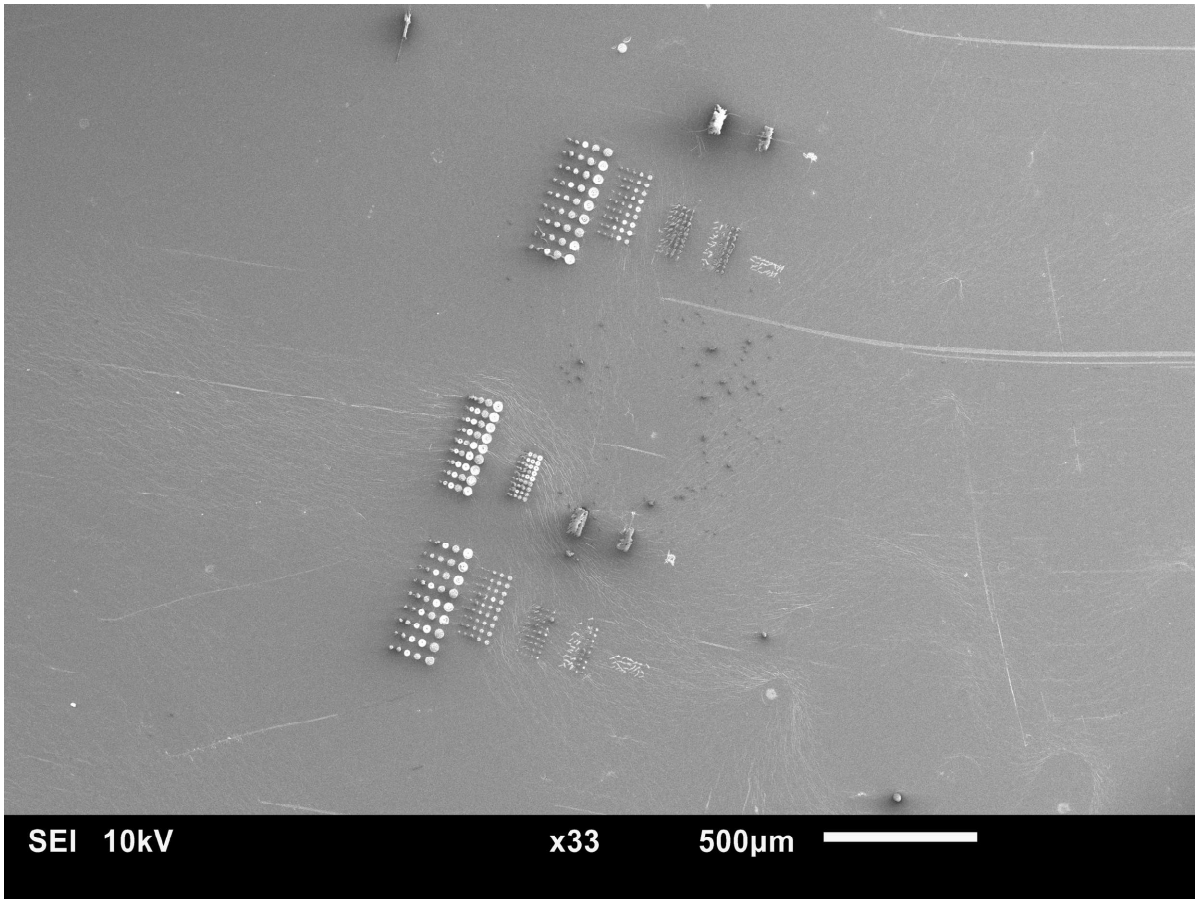

Figure C.71: SEM image of the PEDOT:PSS layer before immersion in EG for 14 min in an ultrasonic cleaner followed by letting it rest for 2 h immersed in EG.

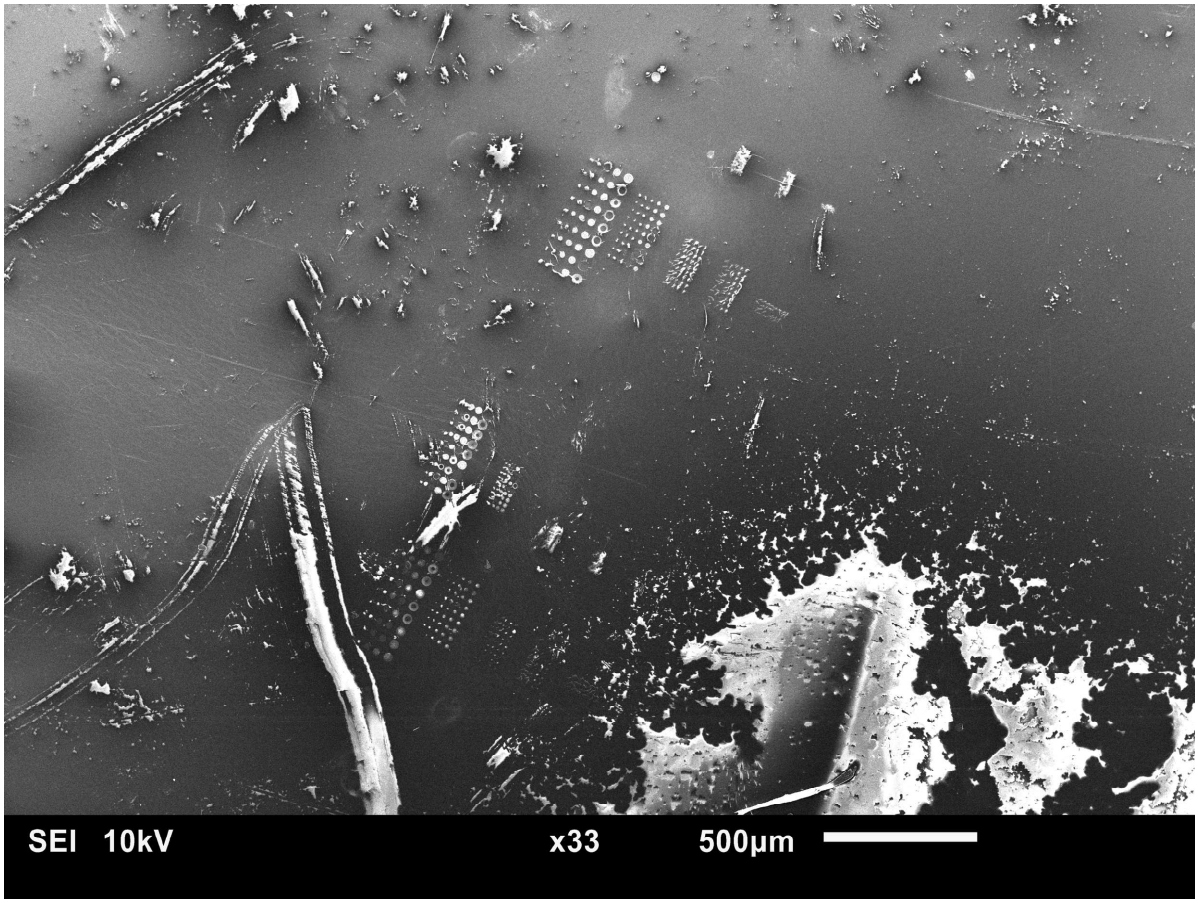

Figure C.72: SEM image of the PEDOT:PSS layer after immersion in EG for 14 min in an ultrasonic cleaner followed by letting it rest for 2 h immersed in EG.

Comparing figure C.67 with C.68, figure C.69 with C.71, and figure C.70 with C.72 it can be seen that bigger non-conductive spots are formed after EG treatment. Less conductive spots were seen when the multilayer substrate was immersed for 2 hours instead of 15 min, seen by comparing figures C.68, C.70, and C.72. But placing the substrate in an ultrasonic cleaner for 15 min did not decrease the size and the number of non-conductive spots which can be seen by comparing figure C.70 with figure C.72.

C.4. Conclusions

From the established protocols, a final manufacturing overview for manufacturing a polymeric membrane with integrated porous electrode can be created. This overview schematically presented in figure C.73.

C.4.1. Manufacturing of the soft mold (figure C.73A)

A glass coverslip of 30 mm in diameter with a thickness of 0.17 mm +/- 0.01 mm is cleaned with acetone and followed by isopropanol. A drop of immersion oil is placed on the bottom of the coverslip and a drop of IPL-780 is placed on top of it. The coverslip is placed on a holder and placed in the Photonic Professional GT. A STL-file is created with Solidworks and converted into job-files with Describe and printed with the Photonic Professional GT. The optimal parameters for converting the STL files into job files and to the optimal parameters writing the pillars, the contours of the sensor, and the electrodes with a sharp edge are presented in table C.3, table C.4, and table C.5. When the print job is finished, the coverslip with the printed structure on top of it is developed for 25 min in PGMEA, followed by 5 min in 2-propanol.

C.4.2. Substrate preparation (figure C.73D)

TOPAS
From the results, the following protocol is created to dissolve TOPAS granules into toluene.

1. Clean bottle with ethanol and let it evaporate for an hour
2. Weigh the correct amount of TOPAS granules
3. Fill the bottle with the correct amount of toluene
4. Add the TOPAS granules
5. Put the bottle in the ultrasonic cleaner for 15 min
6. Put the bottle on an orbital shaker at 2200 RPM for 10 min
7. Repeat last two steps until, when you tilt the bottle, the solution is viscous and fluidic

The final protocol for spin coating the TOPAS film with the desired thickness of 10 µm, will start with a cleaning procedure of the glass Petri dish. The Petri dish is cleaned with ethanol, followed by 2-propanol. Subsequently, the Petri dish is placed in the oven at 150 °C for 15 min to dehydrate. The Petri dish is placed in the fume hood to cool down. 1 mm of the TOPAS solution is spin coated, on the outside of the Petri dish, with a static dispense spin coating technique. The first step of the spin coat protocol has a spin time of 50 s, at 3900 RPM. Subsequently, the sample is spin coated for 30 s at 100 RPM. The acceleration for both steps is 250 RPM/s. The sample is left to dry overnight in the fume hood.

PEDOT:PSS
The final protocol for manufacturing the thin film of PEDOT:PSS is concluded to be as following, a glass Petri dish is treated for 5 min with oxygen plasma at 60 W. Two milliliters of PEDOT:PSS is dynamically dispended on the TOPAS film during the spin coating process. A spin speed of 750 RPM, a spin coat time is 60 s, and an acceleration of 1000 RPM/s will be used. The sample is left to dry overnight in the fume hood.

PAA
A minimum required thickness of the PAA film without a safety margin is the height of the highest pillar of the experiment in chapter C.2.1 minus the thickness of the TOPAS layer and the PEDOT:PSS layer, which is 27.5 µm. While none of the manufactured layers of this experiment and the experiment in appendix C.3.2 came close to the required thickness, there is decided to add a sheet of TOPAS as an additional sacrificial layer instead of spin coating multiple layers on top of each other. Because this takes less time and the TOPAS sheet has a large safety margin in thickness. Because there is a layer of PAA between it, it is still possible to chemically peel of the manufactured membrane.

So, a 30 wv% solutions of PAA and DI water is prepared by adding the correct amounts into a Falcon tube, and place it on an orbital shaker at 2200 RPM until the PAA is completely dissolved. 1.5 mL of the solution, is dynamically dispended on the TOPAS sheet during the spin coating process. The final spin coat protocol for creating the PAA film is to spin coat a 30w/v% PAA in DI water solution at 500 RPM for 45 s while this results in a thicker layer which is still uniform. This layer will be baked for 20 min at 60 °C afterwards.

Stacking layers
A layer of TOPAS is spin coated on the outside of a glass Petri dish. On top is a layer of PEDOT:PSS spin coated. The PAA layer will be spin coated on top of the TOPAS sheet. The substrate with the PEDOT:PSS and TOPAS layers will be placed on top of the substrate which consists of a PAA layer and a TOPAS sheet. The air bubbles will be removed by sliding them away with a red stirring stick across the substrate while this method had the best results.

C.4.3. Soft mold imprint process (figure C.73B)
The soft mold nano imprint lithography process is performed with an wafer bonder system (EVG 510, EV Group). The mold and the multilayer substrate were placed between kapton foil with on top two graphene sheets. The multilayer substrate will be imprinted at an imprinting temperature of 120 °C, with an imprinting force 4000 N, and a holding time of 10 min.

C.4.4. Post treatment process (figure C.73C)

The final protocol is to immerse the imprinted multilayer substrate in ethylene glycol for 2 h. Because this improves the dissolving of the PAA layer and placing it in the ultrasonic cleaner did not decrease the number and the size of the non-conductive spots, which makes it an unnecessary additional step.

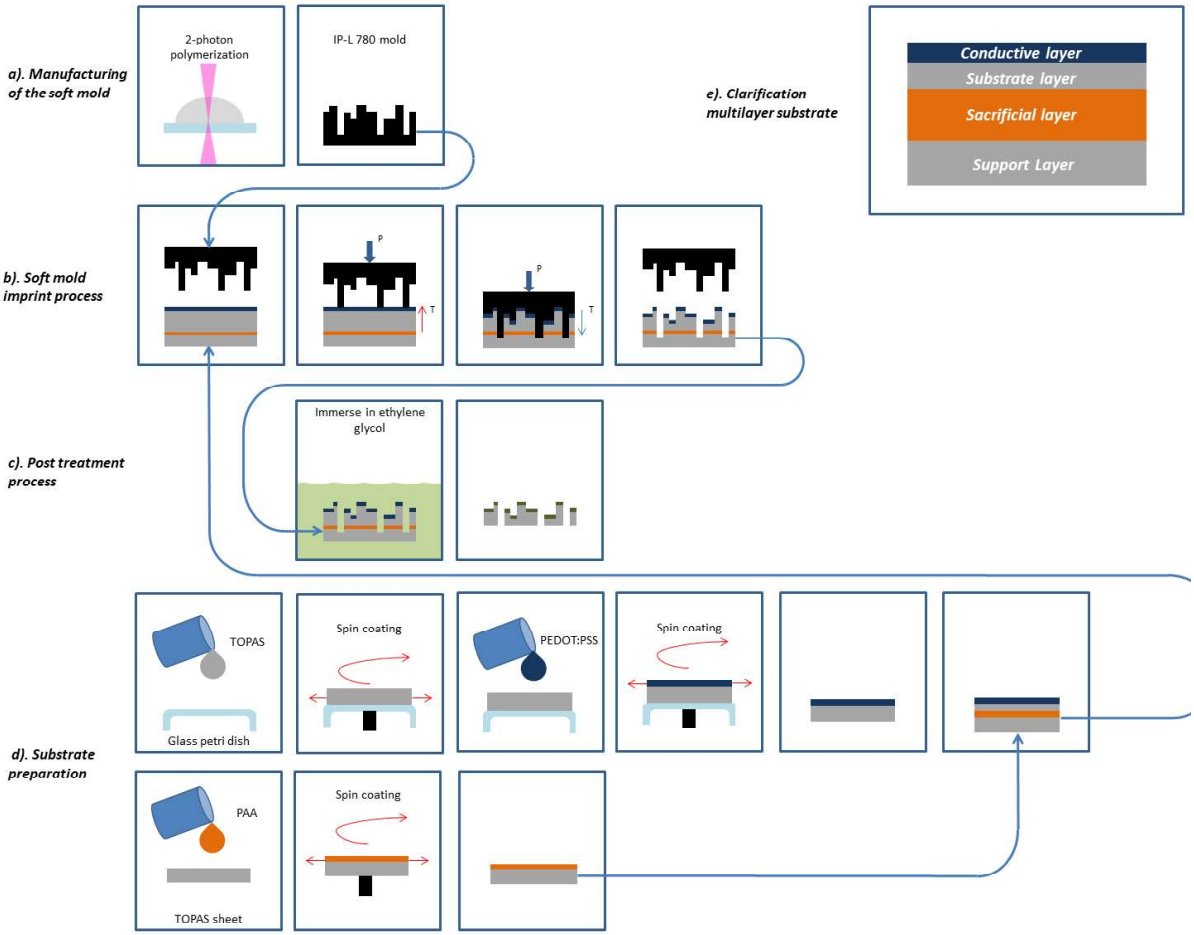

Figure C.73: Schematic overview of the final manufacturing process divided into four steps. A: The soft mold is manufactured with a two-photon polymerization process. D: The substrate consists of four polymeric layers, a conductive layer (PEDOT:PSS), a substrate layer (TOPAS), a sacrificial layers (PAA) and a support layer (TOPAS), which are spin coated and placed on top of each other. B: The multilayer substrate is imprinted (soft NIL) to create the porous electrode and the through-holes. C: A post treatment step is performed to enhance the conductivity of the conductive layer, to decrease the water solubilty of the conductive layer and to dissolve the sacrificial layer which helps the demolding of the soft mold.

D

Experiments performed for establishing manufacturing protocols to scale up the process

D.1. Introduction

A, yet non explainable shift, occurred in the quality of the printed structures by the Photonic Professional GT. A clear shift in quality was seen in the printed pillars as presented in figure D.1. For images in figure D.1E to D.1L , the pillars printed at their optimal parameters are the ones on the outside. The pillars with a diameter of 0.4 µm and 1 µm do not experience that much of a difference in quality as it can been seen by comparing figure D.1A with figure D.1B and figure D.1C with figure D.1D. But all the other pillars look more wrinkled then they were before the shift in quality. Therefore, the previously developed protocols to manufacture a polymeric membrane with integrated porous electrode does not work anymore. This is illustrated by performing an imprinting experiment which before resulted in successful through-holes before, but now result in the transferring of all the pillars from the soft mold to the multilayer substrate as shown in figure D.2A.

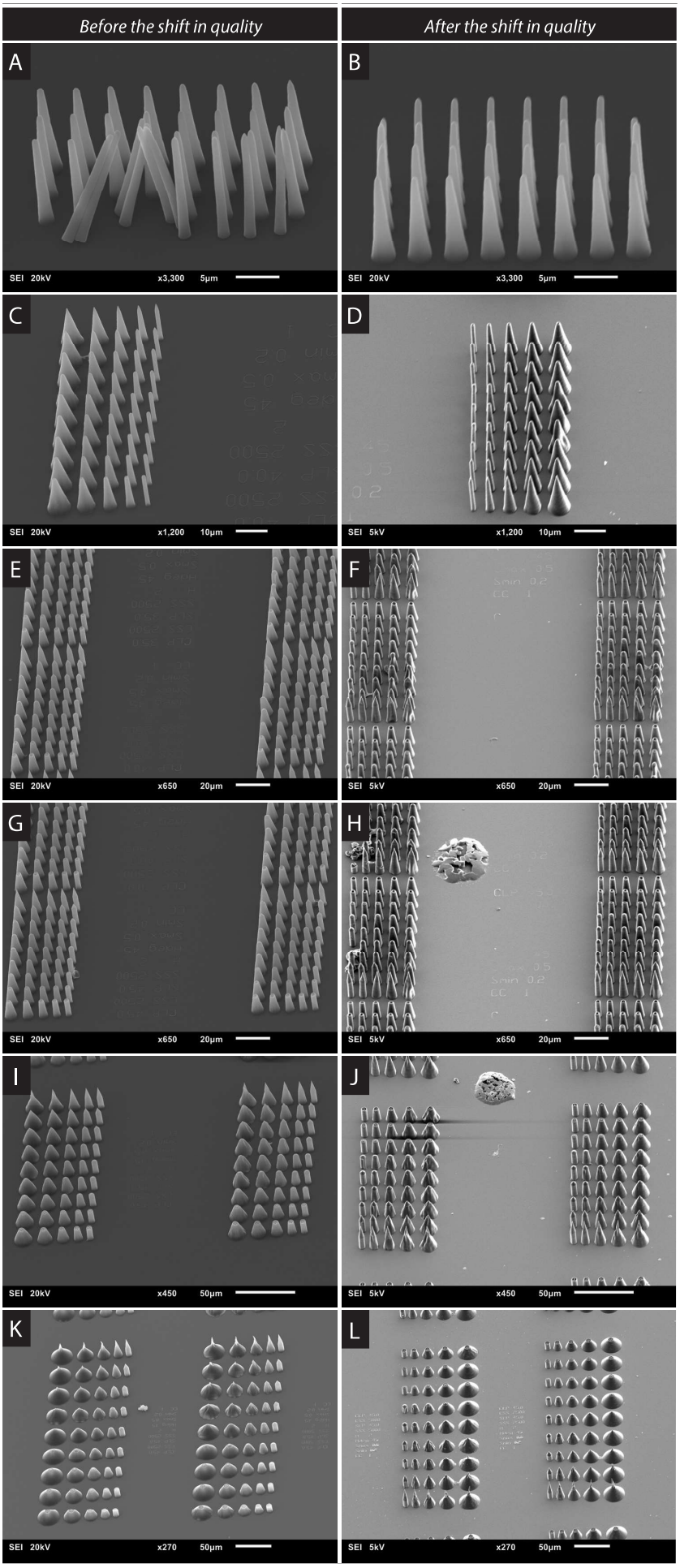

Figure D.1: Overview of the shift in quality of the printed structures with the Nanoscribe with on the left side before the shift and on the right side afterwards. From top to bottom are the printed pillars of different diameters at their optimal laser power and a scan speed of 2500 µm s^{-1} (0.4 µm at 20.0 mW, 1 µm at 20.0 mW, 3 µm at 20.0 mW, 3 µm at 22.5 mW, 5 µm at 22.5 mW, and 8 µm at 22.5 mW.

The shift in the quality of the printed pillars also resulted in bended pillars laying on top of the multilayer substrate and pillars which got stuck into the substrate during the imprinting process. This is shown in figure D.2B and figure D.2C.

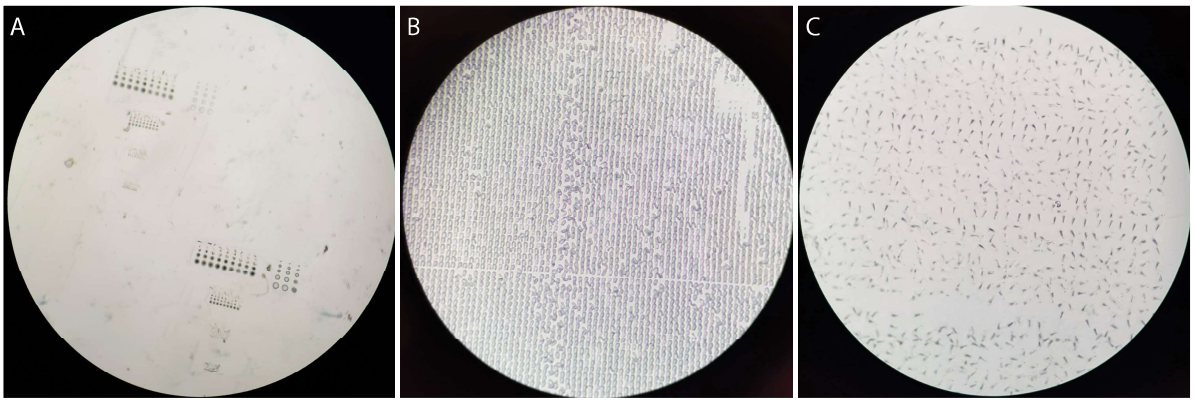

Figure D.2: A: Example of transfering pillars from the soft mold to the multilayer substrate. B: Example of bended pillars. C: Example of collapsed pillars.

The quality of the print was changed due to the Photonic Professional GT. That is why there is decided to first try to get the same results by changing the parameters used to manufacture the soft mold. While this alone did not solve the problem, the parameters used to imprint the multilayer substrate and to the manufacture the multilayer substrate had to be adjusted as well. To determine how to solve the current issues (figure D.2), a mind map was created per observed problem. These mind maps are shown in figure D.3 (the collapsing of the pillars), figure D.4 (the bending of the pillars), and figure D.5 (the sticking of the pillars). In the middle of the mind map, the problem is visualized. What could have been the cause of this problem and potential solutions are written down around the visualization.

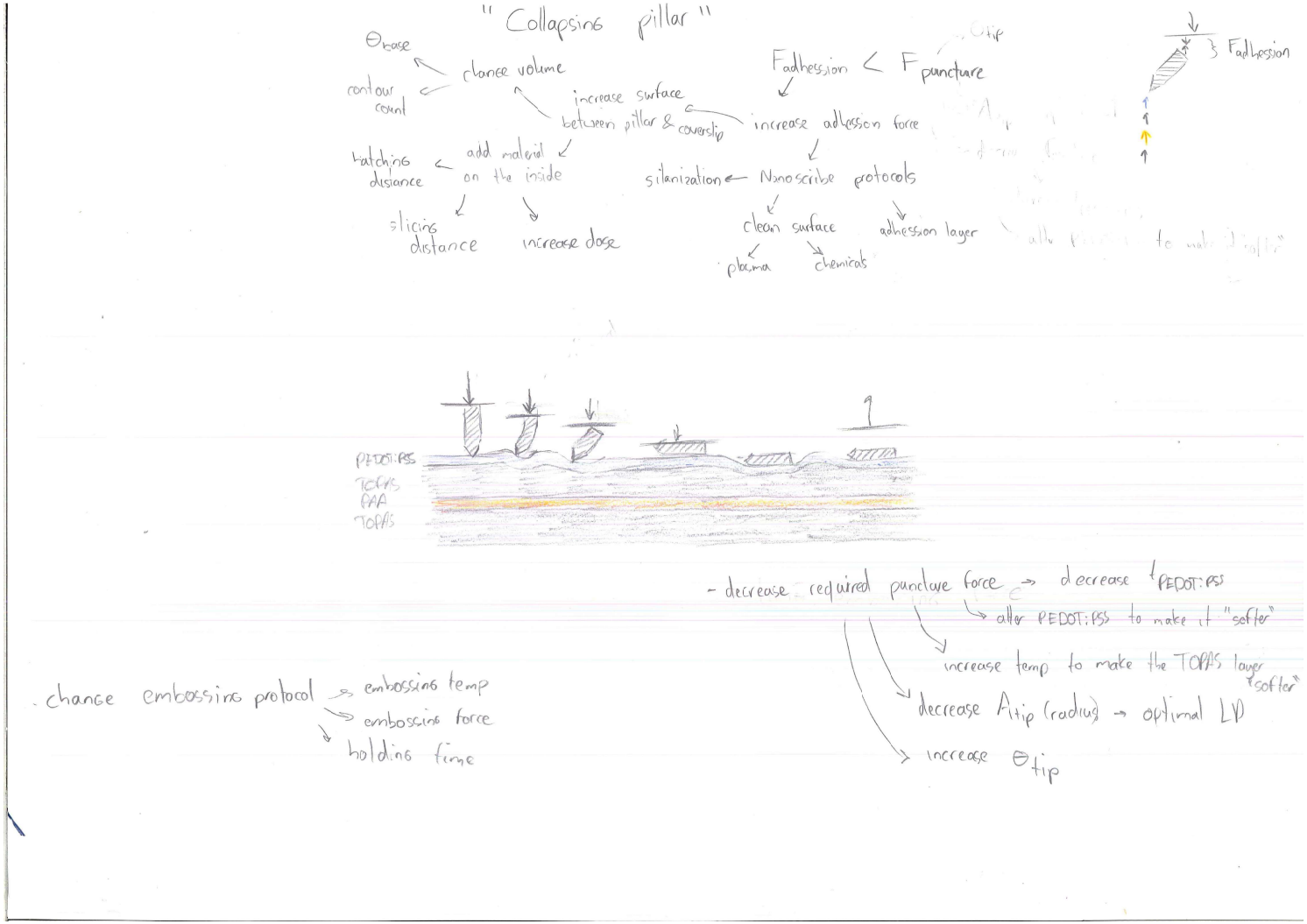

Figure D.3: The visualization of the collapsing the pillar problem with a mindmap of solutions around it.

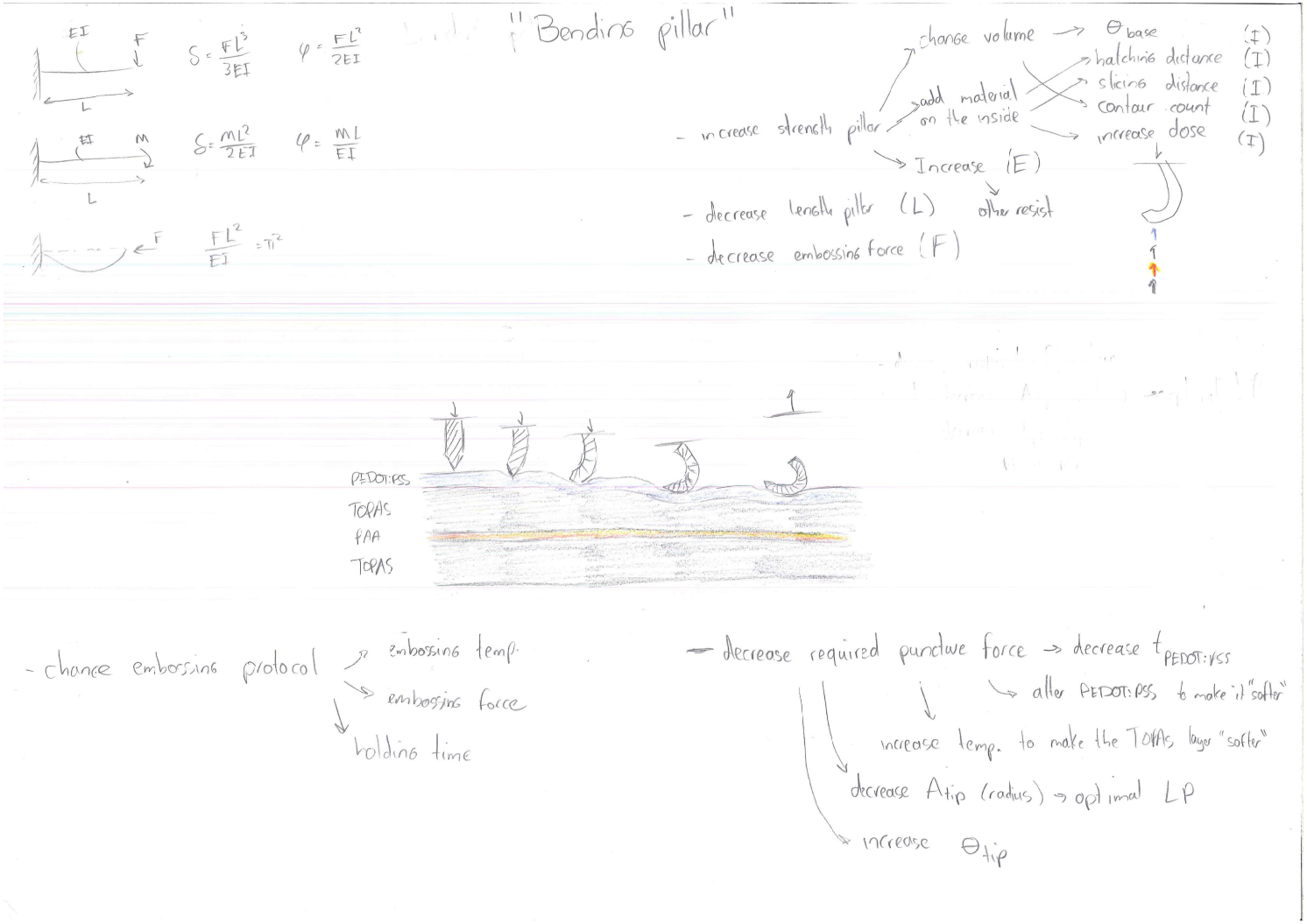

Figure D.4: The visualization of the collapsing the pillar problem with a mindmap of solutions around it.

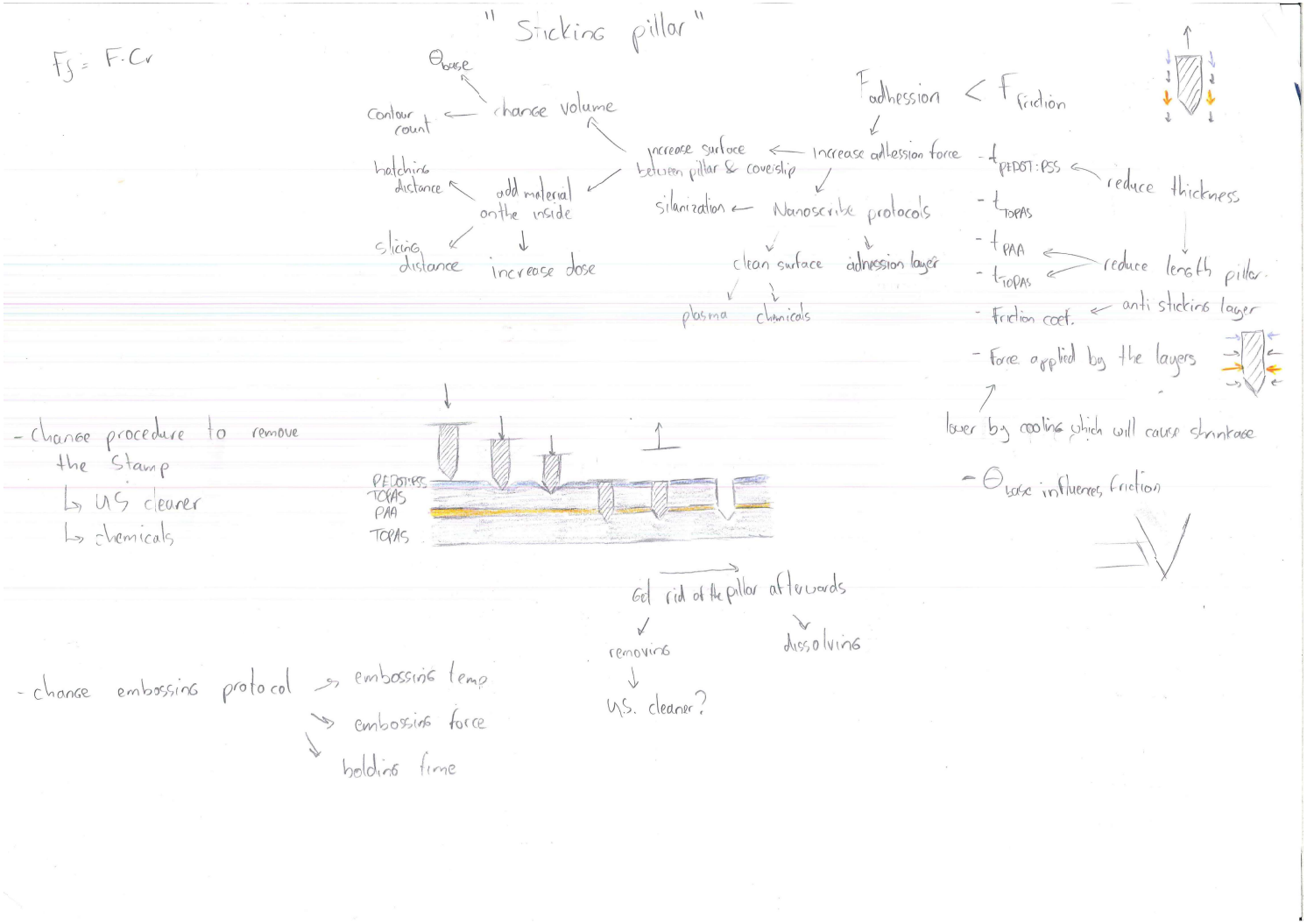

Figure D.5: The visualization of the collapsing the pillar problem with a mindmap of solutions around it.

In this appendix, the performed experiments will be described in section D.2. Subsequently, the results of these experiments are presented and discussed in section D.3. Finally, the conclusions will contain the final protocols which are developed to manufacture a polymeric membranes with an integrated porous electrode can be found in section D.4. The work performed in this appendix is reflected on the roadmap to success, which is presented in figure D.6.

Figure D.6: Roadmap to success with symbols indicating which experiments are already furfilled and which are performed in this appendix.

D.2. Experimental

The established protocols from appendix C are used in this appendix unless stated differently.

Printing cones and pillars with sharp tips, 63x objective

The same print job is used as in figure C.5. This experiment is performed to determine the optimal laser power and scan speed (the combination is called dose) per different diameter of the pillars. For each pore size, the maximum area per pore is calculated for which it is still possible to create the highest number of pores/cm^2, which are commercially available. Subsequently, the maximum diameter of a circle is calculated which would fit in the area, which can be used to determine the maximum base angle which can be used to still be able to fit the number of pillars next to each other to create the highest number of pores/cm^2 which are commercially available. There is decided to use 5 pillars with different base angles per pore size. In the case for a pore size of 0.4 µm, it is decided to use 4 pillars with a base angle from 1° to 4° in steps of 1° while the maximum base angle is only 1.14°. The used base angles are all rounded and this all is summarized in table D.1.

The tip angle varies also for each pore size from 0° to 80° in steps of 10°. The tip angle will influence whether the pillar/cone is able to create through-holes of which we already know that a tip angle of 80° is required. The pillars have a height of 15 µm excluding the tip. Looking at one square of pillars, in the x-direction, the base angle varies and in the y-direction, the tip angle varies, shown in figure D.7A. Next to this square of pillars, a text is written with information regarding the printing parameters used to print that particular square of pillars. Out of this square, a matrix of squares is created. In the x-direction the scan

Table D.1: Overview of the values used to determine the maximum base angle per pore size. This is done by looking at the maximum pore density commercially available per pore diameter. This value is used to determine the maximal area available per pillar. Which leads to a maximum diameter at the base. Which can be used to calculate the maximum base angle. The base angles used are determined by round the maximum base angle and dividing it by 5 to have the step size between the different base angles from zero to the maximum base angle.

Pore size [µm]	Max pore density [pores/cm^2]	Max area per pore [µm]	Max diameter [µm]	Max base angle [◦]	Base angles used [◦]
0.4	1×10^8	1.0	1.0	1.1	1, 2, 3, 4
1.0	2×10^6	50	7.1	11.4	0, 3, 6, 9, 12
3.0	2×10^6	50	7.1	7.7	0, 2, 4, 6, 8
5.0	4×10^5	250	15.8	19.8	0, 5, 10, 15, 20
8.0	1×10^5	1000	31.6	38.2	0, 10, 20, 30, 40

speed varies from 10 000 µm s^{-1} to 2500 µm s^{-1} in steps of 2500 µm s^{-1} and in the y-direction the laser power varies from 17.5 mW to 30.0 mW in steps of 2.5 mW. The scan speed is reduced in the x-direction and the laser power increased in the y-direction to have the pillars printed with the highest dose at last. Because there will be a dose which starts to boil the photoresist which can influence the photoresist around it as well. By printing those at last, the effect of the boiling of the resist on the other pillars is limited. Multiple of these matrices are placed behind each other, in the y-direction, varying the diameter of the pillar for the different pore diameters, shown in figure D.7B.

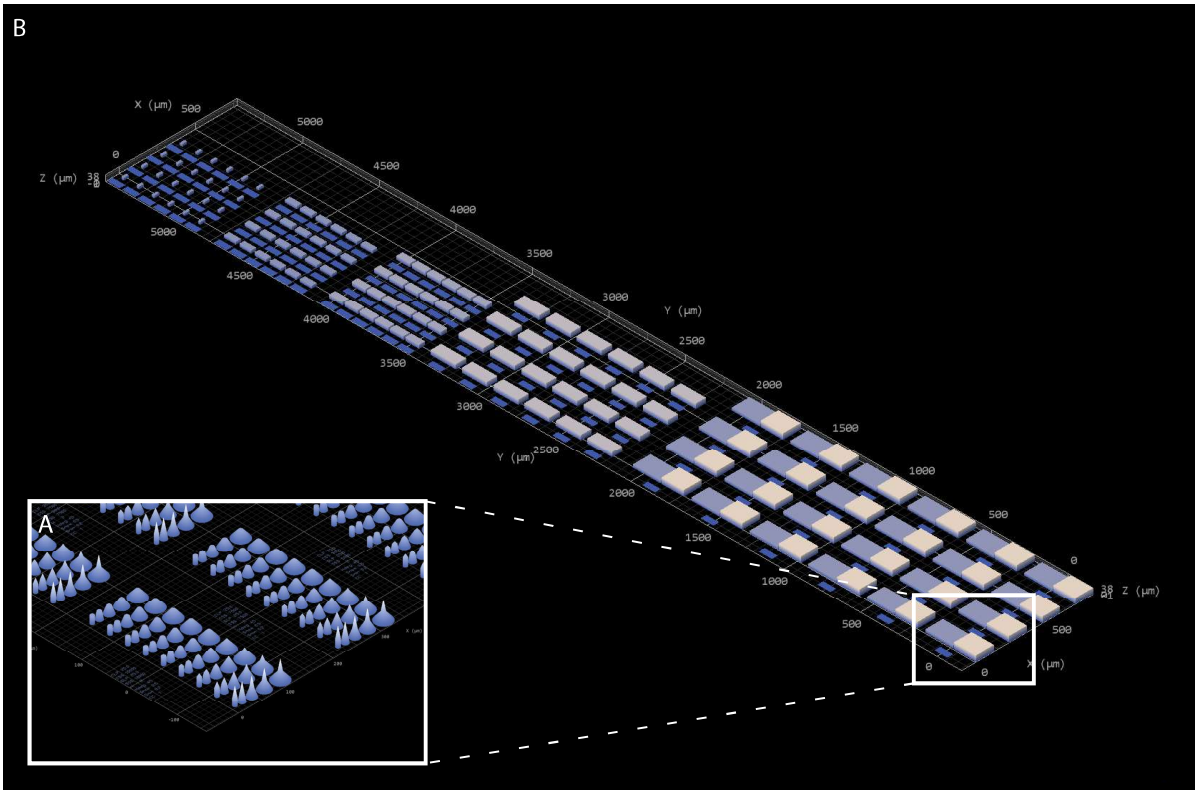

Figure D.7: 3D preview of the print job to determine the optimal dose for printing pillars with different diameters, base angles, and tip angles. A: Close up of one square of pillars in which the base angle is varied in the x-direction and the tip angle is varied in the y-direction. B: Overview of the complete print job in which the scan speed is varied in the x-direction and the laser power is varied in the y-direction. This is done per diameter pillar.

Small fields of pillars, 25x objective

After redefining the optimal values to print pillars with the 63x objective, an experiment is performed to find the optimal values for the 25x objective as well. The scan field of the 25x objective is larger and, therefore, more pillars at the same time can be printed which reduces the total printing time. A scan speed of

2500 µm s^{-1} was, again, found as the optimal scan speed (Table D.2). The laser power did vary in comparison with the optimal values found before the quality problems with the Photonic Professional GT. Therefore, in this experiment, the soft mold designed to be used to manufacture the 1 mm by 1 mm membrane are printed with laser powers +2.5 mW, 0 mW, and -2.5 mW of the found optimal values, varied in the x-direction of the print job, to find the optimal values for printing the soft mold to manufacture membranes of 1 mm by 1 mm with the 25x objective. A small range around the optimal laser powers of the 63x objective is selected, while before the shift in the quality of the printed structures, it was already seen that the optimal values of the 63x and the 25x objective are really close to each other. A 3D preview of the print job is given in figure D.8. Following the y-axis, the first field of pillars consists of 0.4 µm pillars in diameter with a center to center spacing of 7 µm between them. This is also shown in figure D.8A. Subsequently, pillars which are 1 µm in diameter are placed with a spacing of 7.04 µm center to center. The field in the middle consists of pillars which are 3 µm in diameter and with a center to center spacing of 7.04 µm. The next field has pillars of 5 µm in diameter which is placed 15.63 µm, center to center, apart from each other. The last field consists of pillars which are 8 µm in diameter and have a center to center spacing of 31.25 µm. All the pillars have a base angle of 0° and a tip angle of 80°. The pillars have a height of 15 µm excluding the tip.

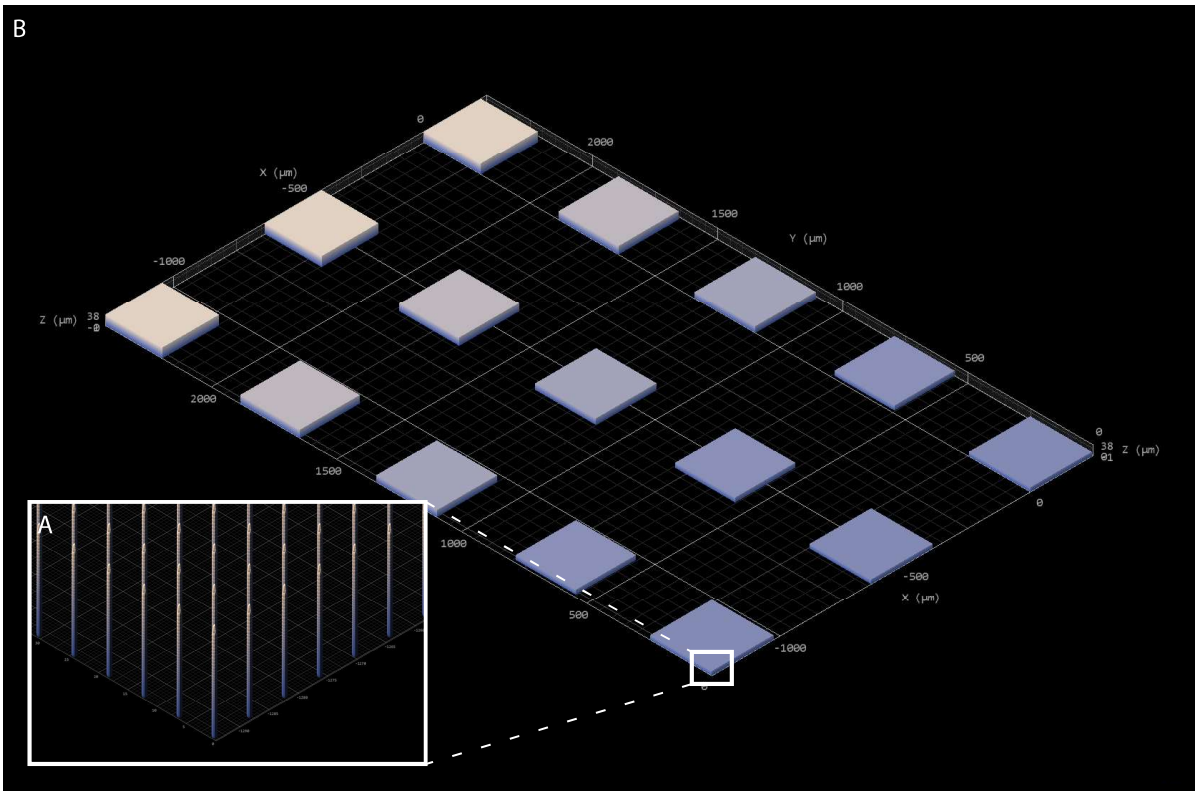

Figure D.8: 3D preview of the print job to determine the optimal values to print fields of pillars of different diameters with the 25x objective. A: Close up of the print job regarding small fields of pillars which are in this field 0.4 µm in diameter. B: Overview of the complete print job with varying the laser power in the x-direction and the diameter of the pillars in the y-direction.

Minimum distance required to prevent pillars with a diameter of 0.4 µm from falling over due to the capillary forces

It is expected that the pillars of 0.4 µm in diameter to fall over, as observed in figure D.1A, due to the capillary forces between them during the evaporation of isopropanol/drying of the sample during the development process. The capillary forces between the pillars depends on the spacing of the pillars and their height.[113] To find the minimal spacing required per height of the pillars to prevent them from falling over, the following experiment is carried out. The height of the pillars is varied from 2.5 µm to 15 µm in steps of 2.5 µm in the direction of the x-axis. The spacing between the pillars is varied from 1 µm to 14 µm in steps of 1 µm in the direction of the y-axis. A base angle ranging from 0° to 4° in steps of 1° are used. All the pillars have a tip angle of 80°. The resulting matrix of pillars is printed ten times to eliminate any fluctuations during the printing process which can boil the photoresist locally or any interface finding problems by the software itself. The

resulting print job is shown in figure D.9B and partially zoomed in in figure D.9A. The pillars with a height of 15 µm excluding the tip and a tip angle of 80° are printed with a laser power of 22.5 mW and a scan speed of 2500 µm s^{-1} with the 25x objective.

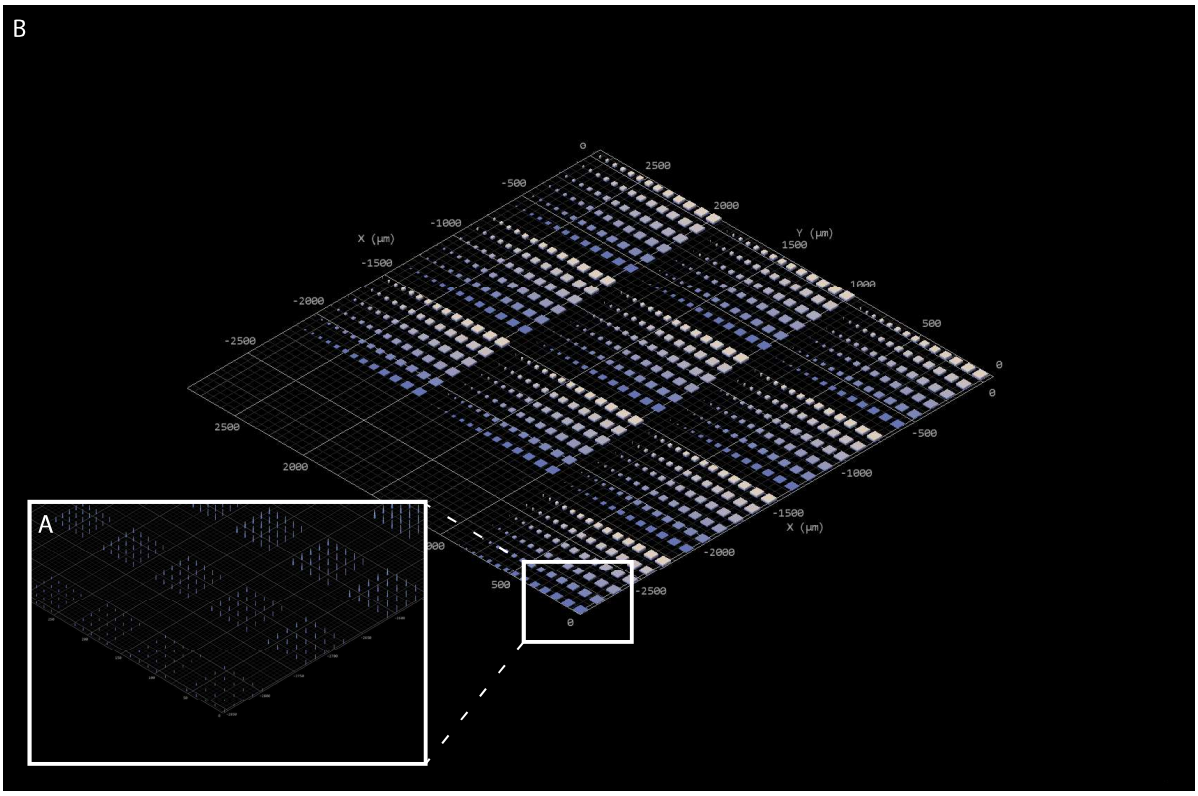

Figure D.9: 3D preview of the print job to investigate the minimum distance required to prevent the 0.4 µm pillars from falling over. A: Close up of one matrix in which the base angle is varied in the y-direction per small block. Within the matrix, the pillars increase in height in the x-direction and decrease in center to center spacing in the y-direction. B: Overview in which the ten matrices can be seen.

Imprinting 1mm by 1mm membrane with optimal printing parameters, 63x objective

The same experiment with the 1mm by 1mm field of pillars as described in figure C.7 is performed, but this time with the redefined optimal laser power for the 63x objective as presented in table D.2. Five STL files are created which could be used to imprint 1 mm by 1 mm membranes with pillars with a base angle of 0°, a tip angle of 80° and a height of 15 µm excluding the tip. A 3D preview of the final job file in Describe is given in figure D.10. Following the y-axis, the first field of pillars consists of 0.4 µm pillars in diameter with a center to center spacing of 7 µm between them. This is also shown in figure D.10A. Subsequently, pillars which are 1 µm in diameter are placed with a spacing of 7.04 µm center to center. The field in the middle consists of pillars which are 3 µm in diameter and with a center to center spacing of 7.04 µm. The next field has pillars of 5 µm in diameter which is placed 15.63 µm, center to center, apart from each other. The last field consists of pillars which are 8 µm in diameter and have a center to center spacing of 31.25 µm. These STL files are converted to job files to create the 5 fields of pillars placed behind each other of which each field is 1 mm by 1 mm, which is presented in figure D.10B. Due to the smaller scan field of the 63x objective, the blocks are a bit smaller than in figure C.7.

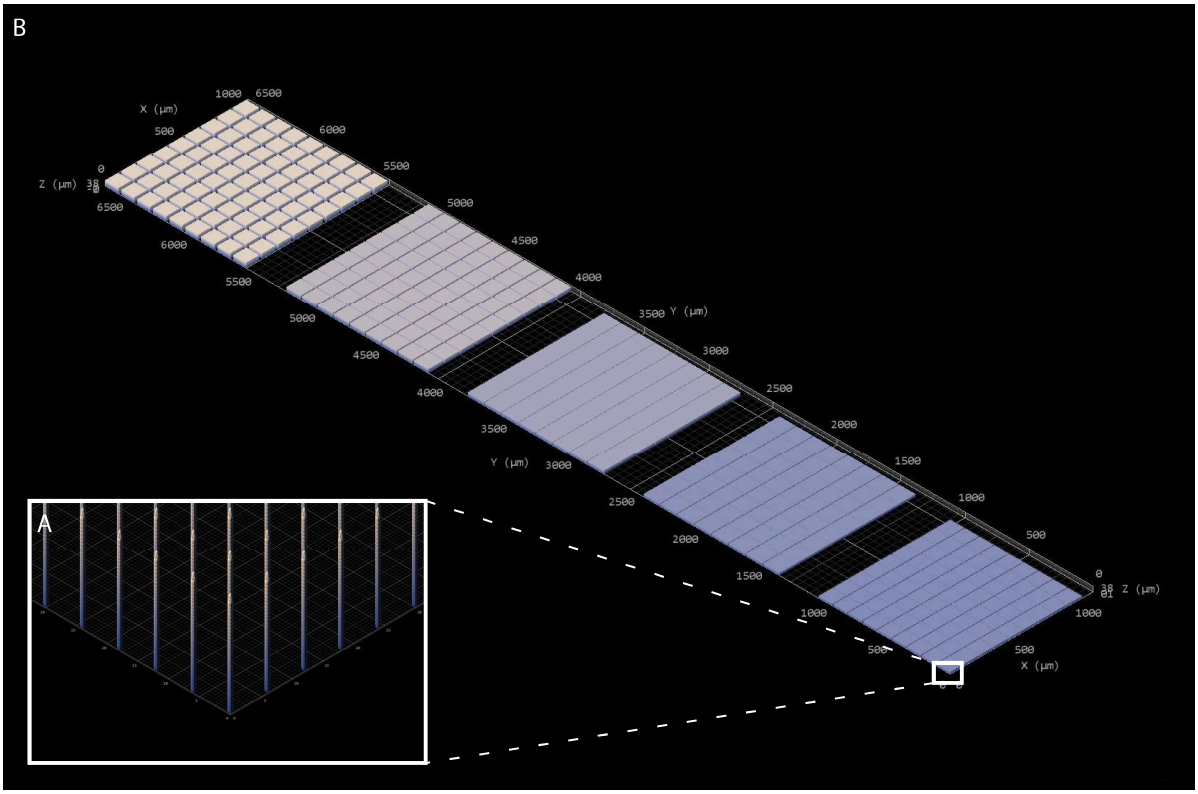

Figure D.10: 3D Preview of the print job for printing 1 mm by 1 mm fields of pillars with different diameters. A: Close up of the field of pillars with a diameter of 4 µm. B: Overview of the print job with the varying laser power in the x-direction and the different diameters of pillars in the y-direction.

Imprinting 1mm by 1mm membrane with optimal printing parameters, 25x objective

The same job-file with the 1mm by 1mm field of pillars, as shown in figure D.10, is printed with the 25x objective. This time the mold is printed with the redefined optimal printing values as summarized in table D.3. Because of the bigger scan field of the 25x objective, more pillars can be printed at the same time which reduces the number of blocks each square contains. A 3D preview of the print job is given in figure D.11. To imprint the multilayer substrate, the earlier determined imprinting protocol is used with an imprinting temperature of 120 °C, an imprinting force of 4000 N, and a holding time of 10 min. After demolding the mold from the substrate, the imprinted substrate is placed in an ultrasonic bath for 10 min to remove any transferred pillars.

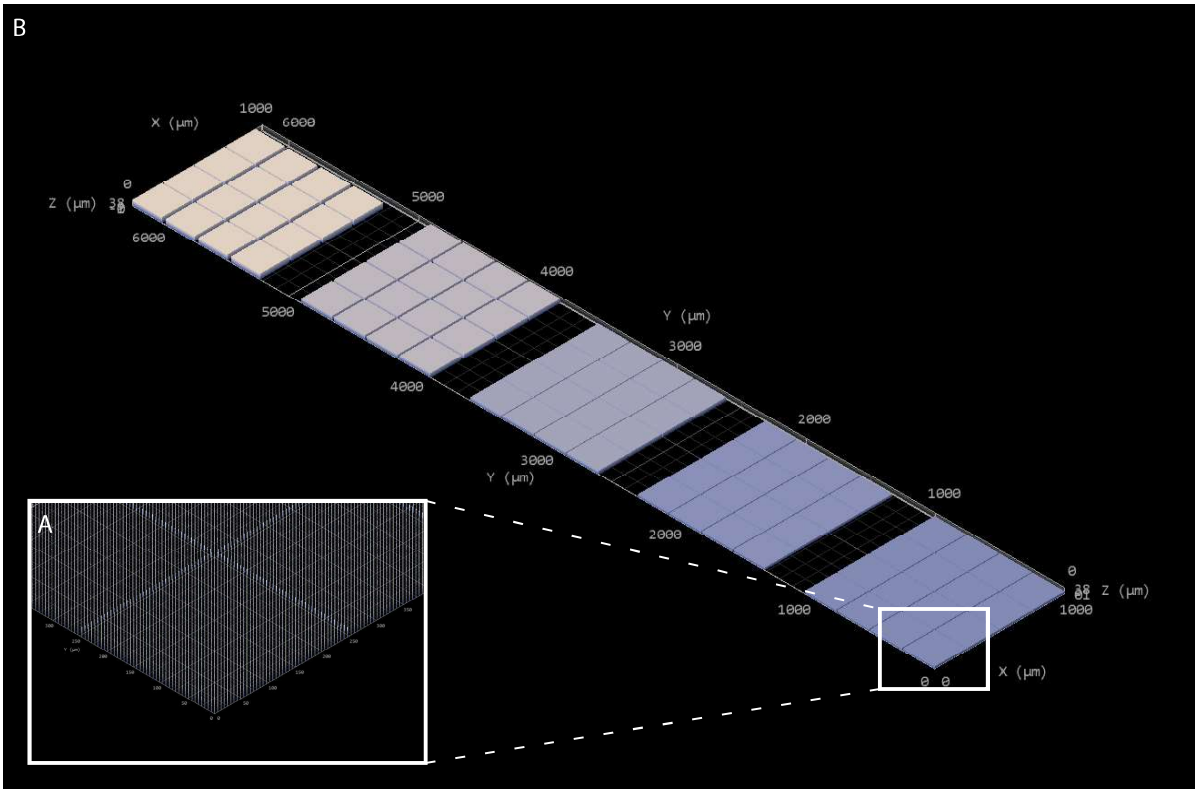

Figure D.11: 3D Preview of the print job for printing 1 mm by 1 mm fields of pillars with different diameters. A: Close up of the field of pillars with a diameter of 4 µm. B: Overview of the print job with the varying laser power in the x-direction and the different diameters of pillars in the y-direction.

Imprinting 1mm by 1mm membrane with optimal printing parameters and demolding in US cleaner
The same experiment with the 1mm by 1mm field of pillars, as shown in figure D.11, is printed with the 25x objective with the optimal printing parameters (table D.3). But this time the mold is demolded from the multilayer substrate after placing it in an ultrasonic cleaner for 10 min in an attempt to make the demolding step easier. The goal of this experiment is to verify whether this will reduce the number of transferred pillars significantly.

Small field of pillars, 25x objective and maximal laser power
After redefining the optimal values to print pillars with the 25x objective, an experiment is performed to find the maximum laser power values which can be used to print pillars with 25x objective per different diameter of the pillar. An increased laser power will polymerize more material and, therefore, the pillars will be less likely to bend. But increasing the laser power too much will boil the photoresist and this will destroy all the pillars. So, a maximum laser power per diameter of the pillar has to be found. A scan speed of 2500 µm s^{-1} is used as the optimal scan speed. The optimal laser power of each pillar with a different diameter, as presented in table D.2, was increased by 2.5 mW and 5.0 mW. A 3D preview of the print job is given in figure D.12. The laser power is varied in the x-direction and the diameter of the pillars in the y-direction per square. The same parameters regarding the center to center spacing, base angle, and tip angle are used.

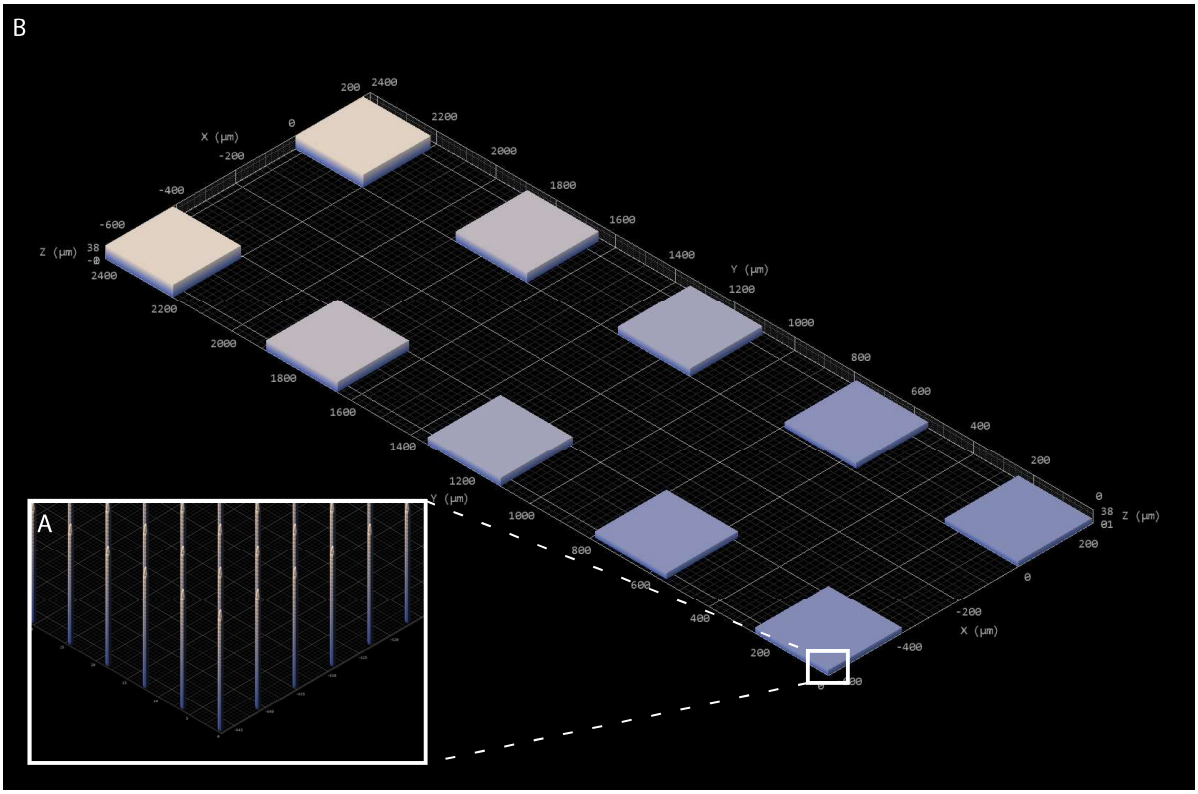

Figure D.12: 3D preview of the print job used to determine the maximal laser power to print pillars with different diameters. A: Close up of the print job regarding small fields of pillars to find the maximal laser power to print such pillars with the 25x objective. B: Overview of the complete print job with varying the laser power in the x-direction and the diameter of pillars per square in the y-direction.

Imprinting 1mm by 1mm membrane with maximal laser power settings

The same experiment is performed with the 1mm by 1mm field of pillars, as presented in figure D.11. But this time the maximum allowable laser power is used to print the soft mold as presented in table D.4. The soft mold will be demolded by hand after the post treatment in EG of 20 min.

Threshold experiment difference between the old resist and the new resist

When the photoresist gets older, it could lower the effectiveness of the photosensitivity of the resist. It could be that the lower quality of the printed pillars is caused by this phenomena, while the resist that is used passed its expiration date. Therefore, a threshold experiment is performed to see the difference in the dose that is required to polymerize the old photoresist (which passed its expiration date) and the same photoresist from a new bottle (which did not pass its expiration date). A 3D preview of this print job is given in figure D.13. Looking at a small part of the print job, presented in figure D.13A, it can been seen that lines are printed at different scan speeds (1000 µm s^{-1}, 5000 µm s^{-1}, 10 000 µm s^{-1}, 30 000 µm s^{-1}, 80 000 µm s^{-1}, and 160 000 µm s^{-1}) which is written down underneath these lines. The laser power is varied from 0 mW to 50.0 mW while the polymerization starts somewhere between those values. This is done by printing the small lines. The threshold test is printed 25 times, with a pause of 10 min between them, to evaluate at the same time whether the needed dose to polymerize the resist fluctuates over time. This could be the case when the Photonic Professional GT starts to warm up for example.

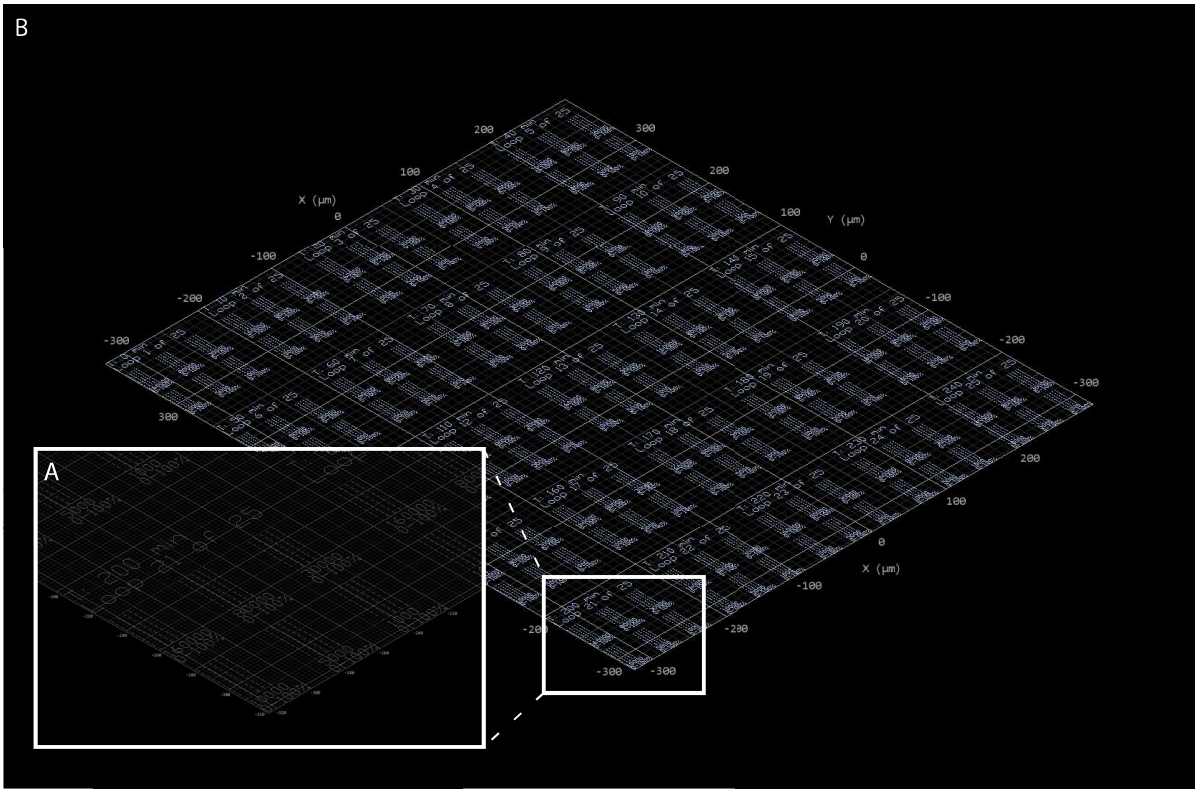

Figure D.13: 3D preview of the print job used to find the difference between the old resist and the new resist. A: Close up of the print job regarding the threshold test at different scan speeds and different laser powers. B: Overview of the complete print job in which 5 by 5 individual threshold tests can be seen.

Imprinting 1mm by 1mm membrane with optimal printing parameters, no PEDOT:PSS layer

The design presented in figure D.11 is used as a soft mold during the imprinting process. The mold is printed with the 25x objective at the optimal laser powers, presented in table D.3. But this time, the multilayer substrate is altered by not spin coating a PEDOT:PSS film on top of it. While PEDOT:PSS is a thermosetting polymer, it will not get "soft" during the imprinting process. Therefore, it normaly cannot be imprinted by such a process. This could be the cause of the problem of the transferring of all the pillars from the soft mold onto and into the substrate. The imprinting is performed at as temperature of 120 °C, imprinting force of 4000 N, and a holding time of 10 min. This is the protocol was established before the shift in the quality of the printed structures.

Imprinting LP array, no PEDOT:PSS layer

Instead of determining the optimal printing parameters and trying those to imprint the multilayer substrate, different laser power are all tried at once to imprint a multilayer substrate. This will give information which diameter at which laser power can be used for imprinting without transferring the pillars from the mold into the multilayer substrate. The laser power (LP) is varied from 20.0 mW to 27.5 mW in steps of 1.25 mW. The scan speed was kept constant at 2500 µm s^{-1}. A 3D preview of the print job is given in figure D.14, in which the diameter of the pillars is varied in the x-direction and the laser power in the y-direction. In figure D.14A, a close up from the print job regarding the one square of pillars is presented. The base angles is varied in the x-direction according to table D.1 and the tip angle is varied in the y-direction from 0° to 80° in steps of 10°. Next to this square of pillars, text is printed with information regarding the printing parameters used to print that particular square of pillars. The pillars have a height of 15 µm excluding the tip. Again, a multilayer substrate without the PEDOT:PSS film is used for this experiment. The imprinting temperature is increased from 120 °C to 130 °C to further mobilize the polymer.[88] The imprinting force of 4000 N and a holding time of 10 min are not altered.

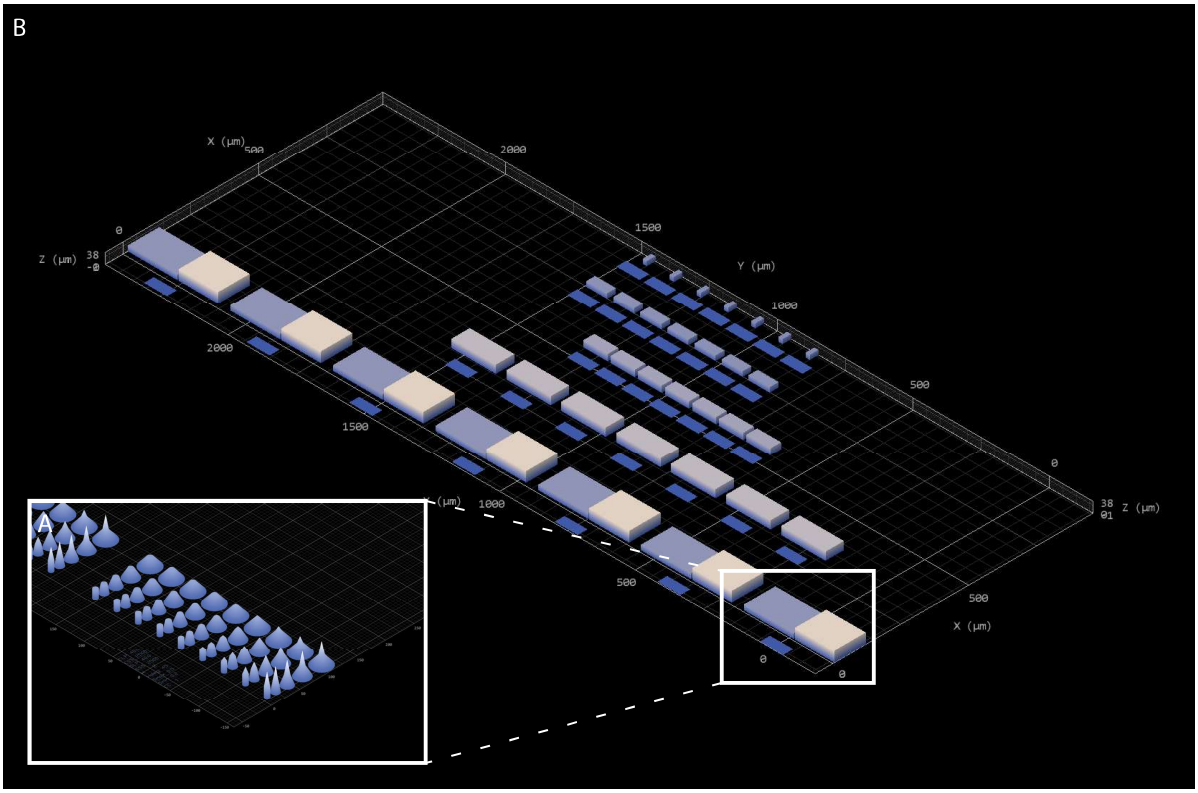

Figure D.14: 3D preview of the print job used to find the laser powers per pillar diameter to imprint a multilayer substrate without transferring of the pillars. A: Close up from the print job regarding the one square of pillars with varying base angles in the x-direction and varying tip angles in the y-direction. B: Overview of the complete print job in which the diameter of the pillars is varied in the x-direction and the laser power in the y-direction.

Improve adhesion between pillars and glass coverslip by oxygen plasma treatment

Instead of determining optimal printing parameters and trying those to imprint the multilayer substrate, different laser power and different scan speeds are all tried simultaneously to imprint a multilayer substrate. This will give information which diameter pillar printed at which laser power (LP) and which scan speed (SS) can be used for imprinting successfully. The laser power is varied from 17.5 mW to 30.0 mW in steps of 2.5 mW and the scan speed is varied from 10 000 µm s^{-1} to 2500 µm s^{-1} in steps of 2500 µm s^{-1}, again, to print the pillars at a dose which will locally boil the photoresist at last. A 3D preview of the print job is given in figure D.15. Five matrices of pillars are placed behind each other in the y-direction of which the pillar diameter varies (8 µm, 5 µm, 3 µm, 1 µm, and 0.4 µm). Within such a matrix, the scan speed in varied in the x-direction and the laser power is varied in the y-direction. A close up of the print job is given in figure D.15A. The base angle is varied from 0° to 80° in steps of 10° and tip angle is kept constant at 80°. Next to this square of pillars, text is printed with information regarding the printing parameters used to print that particular square of pillars. The pillars have a height of 15 µm excluding the tip. The glass coverslip was cleaned with oxygen plasma before placing the immersion oil and photoresist on it, in an attempt to increase the adhesion between the printed pillars and the glass coverslip.[114]

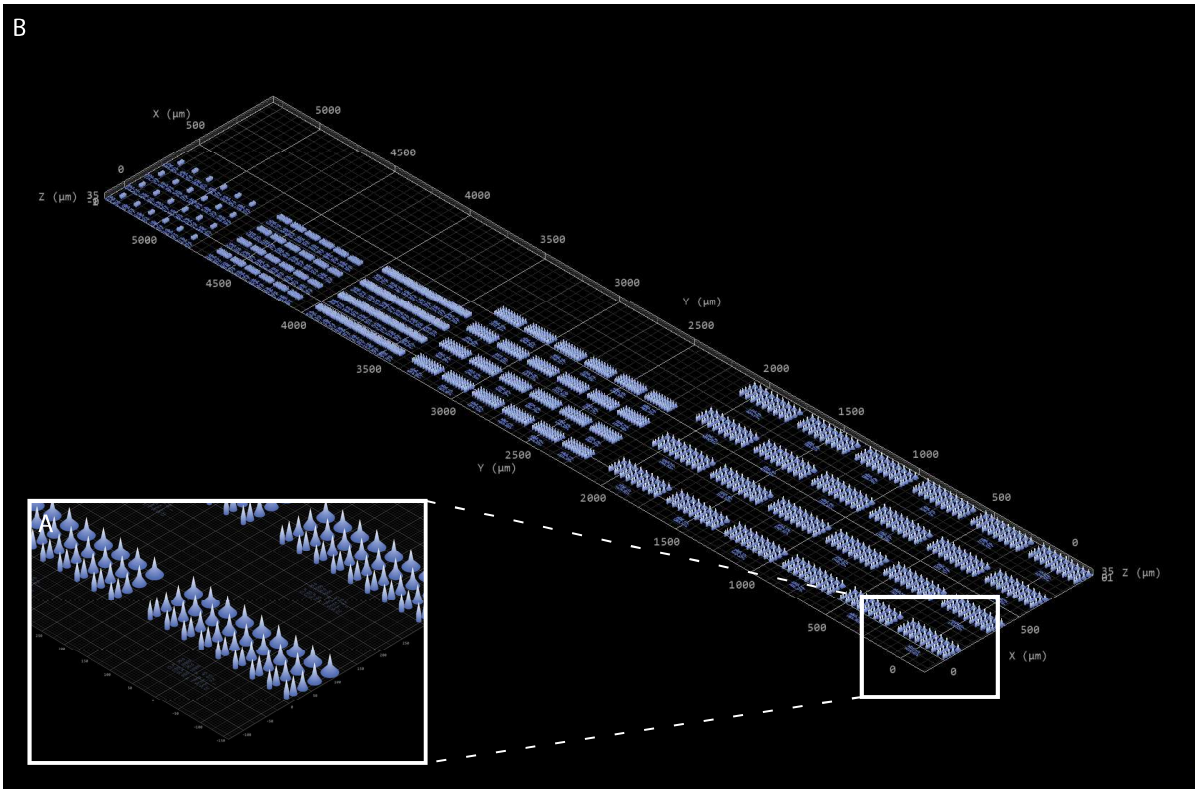

Figure D.15: 3D preview of the print job used to find the laser powers and scan speed per pillar diameter to imprint a multilayer substrate without transferring of the pillars. A: Close up from the print job regarding the one square of pillars with varying base angles in the x-direction. B: Overview of the complete print job in which 5 matrices of pillars with different diameters are placed behind each other in the y-direction. Within such a matrix, the scan speed in varied in the x-direction and the laser power is varied in the y-direction.

Imprint two LP & SS matrices

The same print job with the LP & SS matrix as in figure D.15 is printed twice. This shown in the 3D preview of the print job in figure D.16. The LP & SS matrix on the right has a hatching distance of 0.5 µm and the LP & SS matrix on the left has a hatching distance of 2 µm. A smaller hatching distance is used while this results in more material inside the pillars, which increases the strength of the pillars. But it will also increase the adhesion strength between the pillars and the coverslip while the effective area of the pillars is larger.[114] Also, the height of the pillars is reduced from 15 µm to 12.5 µm excluding the tip. This decreases the friction force on the pillars during the demolding step. The imprinting temperature is increased from 130 °C to 140 °C to further mobilize the polymer.[88] The imprinting force of 4000 N and a holding time of 10 min are not altered. A multilayer substrate without PEDOT:PSS film is used.

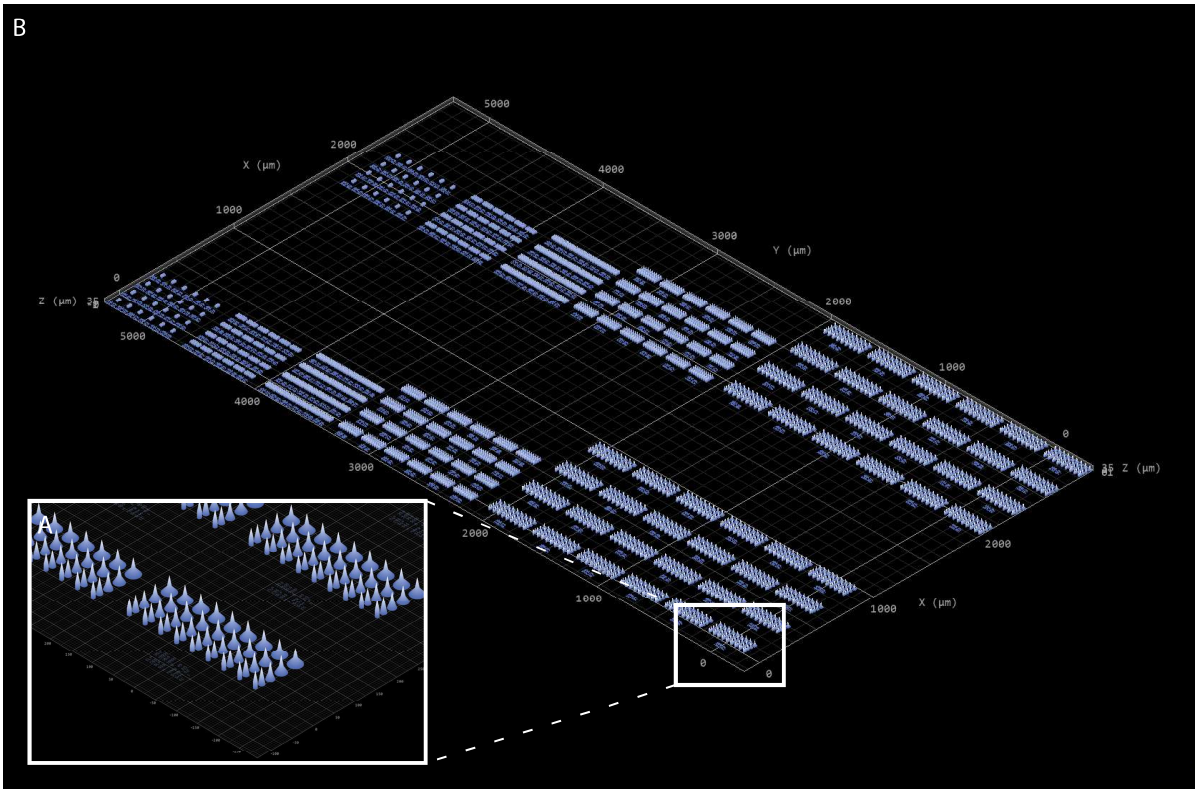

Figure D.16: 3D preview of the print job used to find the laser powers, scan speed, and hatching distance per pillar diameter to imprint a multilayer substrate without transferring of the pillars. A: Close up from the print job regarding the one square of pillars with varying base angles in the x-direction. B: Overview of the complete print job of which the LP & SS matrix on the right has a hatching distance of 0.5 µm and the LP & SS matrix on the left has a hatching distance of 2 µm. Five matrices of pillars with different diameters are placed behind each other in the y-direction. Within such a matrix, the scan speed in varied in the x-direction and the laser power is varied in the y-direction.

Imprint two LP & SS matrices, reduced imprinting force

The same print job with the two LP & SS matrices as shown in figure D.16, is used. The imprinting force is reduced from 4000 N to 3000 N. The imprinting temperature of 130 °C and a holding time of 10 min are not altered. A multilayer substrate without PEDOT:PSS film is used.

0.5mm/1mm by 0.5mm/1mm membrane with optimal imprinted values

A new job file was created of which a 3D preview is given in figure D.17. It consists of two fields of pillars of 1 mm by 1 mm and two fields of pillars which are 0.5 mm by 0.5 mm. The pillars used in this field have a diameter of 8 µm, a base angle of 40°, a tip angle of 80°, are 12.5 µm in height, and have a center to center spacing of 31.25 µm. If the imprinting is successful, it results in four membranes which still can be separated by hand due to the relative large spacing between them. The results of the 0.5 mm by 0.5 mm imprinted membranes and the results of the 1 mm by 1 mm imprinted membranes can be compared to see the effect of the bigger field of pillars on the imprinting. The field of pillars is printed with the 25x objective. A laser power of 30.0 mW and a scan speed of 2500 µm s^{-1} are used while these led to promising results in the previous experiment. A multilayer substrate without PEDOT:PSS film is imprinted with an imprinting temperature of 130 °C, an imprinting force of 3000 N, and a holding time of 10 min is used.

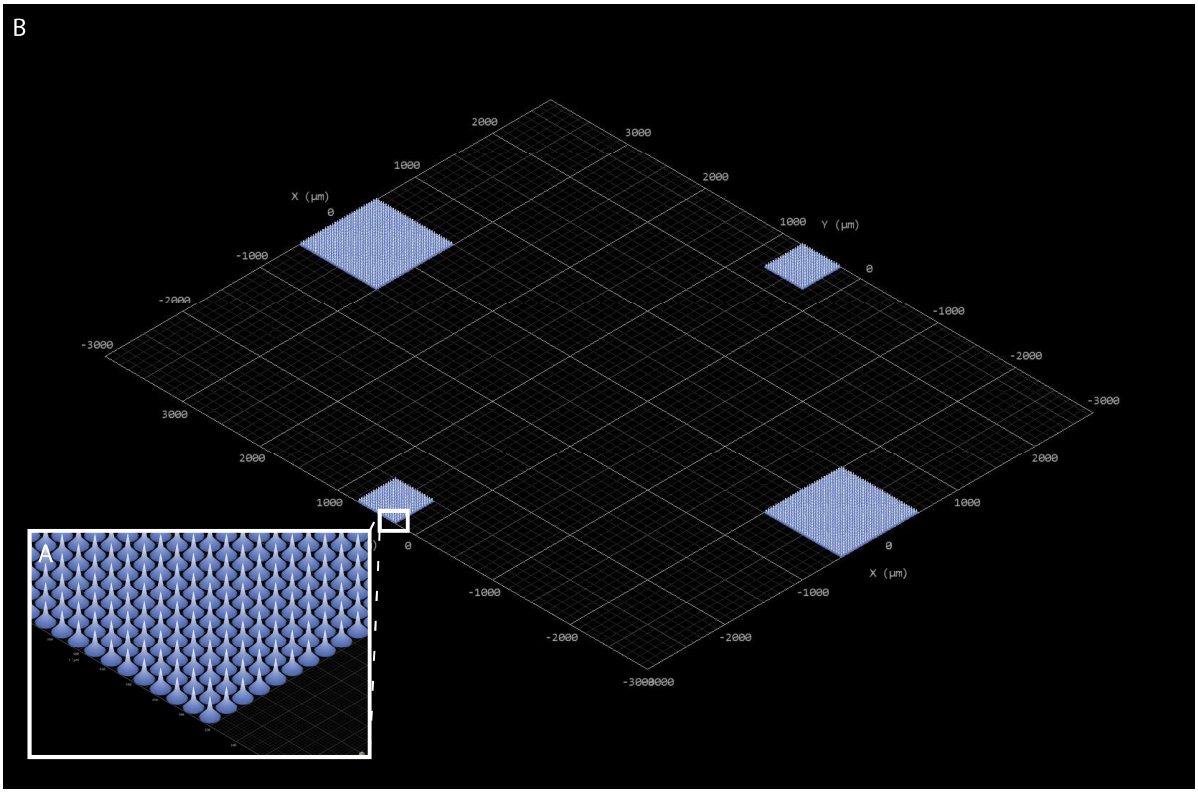

Figure D.17: 3D preview of the print job used to imprint a multilayer substrate to manufacture two membranes of 1 mm by 1 mm and two membranes 0.5 mm by 0.5 mm. A: Close up from the print job one field of pillars. B: Overview of the complete print job which has two fields of pillars of 1 mm by 1 mm and two fields of pillars which are 0.5 mm by 0.5 mm.

LP & SS matrices with optimal imprinted values, anti stiction layer
The same print job with the two LP & SS matrices as shown in figure D.16 is used. Again, the height of the pillars excluding the tip was deceased from 15 µm to 12.5 µm. An anti stiction layer (EVG) was spin coated on top of the soft mold at 2000 RPM for 60 s, rinsed afterwards with HFE7100 (HG Chemicals), and baked for 10 min at 120 °C. Decreasing the height and adding an anti stiction layer is done to decrease the friction forces experienced by the pillars during the demolding step to decrease the number of pillars transferring from the mold to the multilayer substrate. And, preventing the pillars of nailing the membrane to the support layer. The imprinting temperature of 130 °C, an imprint force of 3000 N, and a holding time of 10 min is used for imprinting the multilayer substrate which does not contain a PEDOT:PSS layer.

LP & SS matrices with optimal imprinted values, anti stiction layer and PEDOT:PSS layer
The same print job with the two LP & SS matrices presented in figure D.16 is used. But the height of the pillars excluding the tip was decreased from 15 µm to 12.5 µm. An anti stiction layer is spin coated on top of the soft mold at 2000 RPM for 60 s, rinsed afterwards with HFE7100, and baked for 10 min at 120 °C. The imprinting temperature of 130 °C, an imprint force of 3000 N, and a holding time of 10 min is used for imprinting the multilayer substrate which, this time, does contain a PEDOT:PSS layer.

LP & SS matrices with optimal imprinted values, anti stiction layer and just PAA and TOPAS sheet
The same print job with the two LP & SS matrices as in figure D.16 is used. The height of the pillars is 12.5 µm excluding the tip. An anti stiction layer is spin coated on top of the soft mold at 2000 RPM for 60 s, rinsed afterwards with HFE7100, and baked for 10 min at 120 °C. The imprinting temperature of 140 °C, an imprint force of 3000 N, and a holding time of 10 min is used for imprinting the multilayer substrate which this time does only consist out of the sacrificial layer (PAA) and support layer (TOPAS sheet).

Improve adhesion between pillars and glass coverslip by acid cleaning the glass coverslip
The same print job with the two LP & SS matrices is used as presented in figure D.16. Again, the height of the pillars excluding the tip is 12.5 µm. The glass coverslip is acid cleaned before placing the immersion oil and photoresist on it, in an attempt to increase the adhesion between the printed pillars and the glass

coverslip.[114] This was done by boiling the glass coverslip for 10 min in a mixture which contains 70% concentrated nitric acid (HNO_3), 95% concentrated sulphuric acid (H_2SO_4), and 38% concentrated hydrochloric acid (HCl) in a 1:1:1 volume rate.[115]

0.5mm/1mm by 0.5mm/1mm membrane with optimal imprinted values
The same job-file with the 0.5mm/1mm by 0.5mm/1mm membrane, as shown in figure D.17, is printed with the 25x objective. A laser power of 22.5 mW and a scan speed of 10 000 µm s^{-1} are used while these led to promising results in the previous experiment. A hatching distance of 0.5 µm is used and the height of the pillars is 12.5 µm excluding the tip. An anti stiction layer is spin coated on top of the soft mold at 2000 RPM for 60 s, rinsed afterwards with HFE7100, and baked for 10 min at 120 °C. An imprinting temperature of 130 °C, an imprinting force of 3000 N, and a holding time of 10 min is used. A multilayer substrate without PEDOT:PSS film is used.

0.5mm/1mm by 0.5mm/1mm membrane with optimal imprinted values, reinforcement layer
The same job-file with the 0.5mm/1mm by 0.5mm/1mm membrane as shown in figure D.17 is printed with the 25x objective. A laser power of 22.5 mW and a scan speed of 10 000 µm s^{-1} are used. A hatching distance of 0.5 µm is used and the height of the pillars is reduced from 15 µm to 12.5 µm excluding the tip. The soft mold is reinforced by sputter coating a 10 nm layer of Au/Pd on top of it. An anti stiction layer is spin coated on top of the sputter coated layer at 2000 RPM for 60 s, rinsed afterwards with HFE7100, and baked for 10 min at 120 °C. An imprinting temperature of 130 °C, an imprinting force of 3000 N, and a holding time of 10 min is used. A multilayer substrate without PEDOT:PSS film is used.

Casting PAA experiment
To reduce the amount of contact between the pillars and the material of the multilayer substrate during the demolding process, rises the need to increase the thickness of the PAA layer. Because this layer can be dissolved before the demolding of the mold. Making this layer thick enough will also prevent the pillars from nailing the membrane to the support layer. Additional experiments are performed to be able to create a thick layer of PAA by a casting method. First, a wall of aluminum foil was made around a square sheet of TOPAS. The walls were connected to this sheet of TOPAS with duct tape. To prevent leaking of the 30 wv% of PAA in DI water, glue was applied in around the edges of the TOPAS sheet, shown in figure D.18.

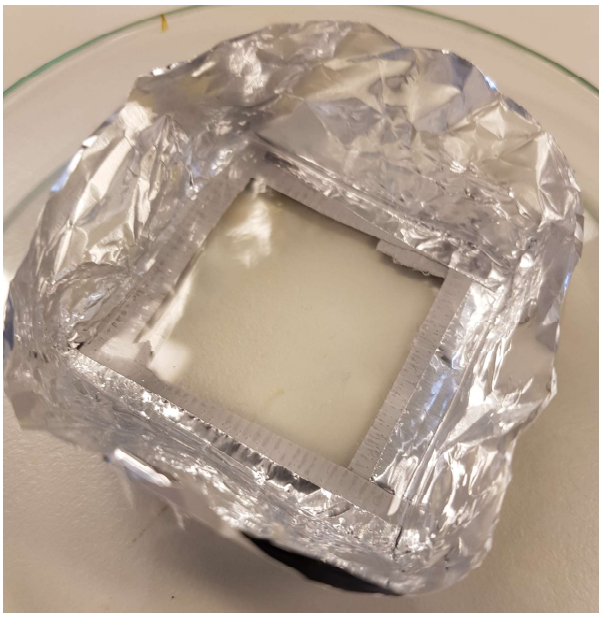

Figure D.18: A square sheet of TOPAS with walls made out of aluminum foil which is attached with duct tape and glue to the TOPAS sheet.

The PAA solution was poured onto the TOPAS sheet and placed in the oven at 60 °C for 2 h to ensure that the PAA layer is cured below the glass transition temperature of TOPAS.[108] The second experiment was by dispensing around 1 mL of 100 wv% of PAA in DI water directly on top of a square piece of TOPAS sheet. Subsequently, the PAA was cured by placing it on a hot plate at 60 °C for 15 min and is cooled down on the

hotplate as well. This will allow the substrate to slowly cool down. The last experiment was by dispensing around 1 mL of 100 wv% of PAA in DI water directly on top of a square piece of TOPAS sheet and let it cure overnight in the fume hood at room temperature.

0.5mm/1mm by 0.5mm/1mm membrane with optimal imprinted values, EG experiment
The same job-file with the 0.5mm/1mm by 0.5mm/1mm membrane, as shown in figure D.17, is printed with the 25x objective. A laser power of 22.5 mW and a scan speed of 10 000 µm s^{-1} are used. A hatching distance of 0.5 µm is used and the height of the pillars is 12.5 µm excluding the tip. An anti stiction layer is spin coated on top of the soft mold at 2000 RPM for 60 s, rinsed afterwards with HFE7100, and baked for 10 min at 120 °C. An imprinting temperature of 130 °C, an imprinting force of 3000 N, and a holding time of 10 min is used. A multilayer substrate with PEDOT:PSS film which is spin coated at 1500 RPM is used to verify whether the created protocol also works for a multilayer substrate with a conductive layer. A thinner layer of PEDOT:PSS, spin coated at 1500 RPM instead of 750 RPM, is used to make the puncturing of this layer easier. The multilayer substrate is placed in the US cleaner for 2.5 h in EG to help the demolding process and left overnight in EG to let in demold chemically.

0.5mm/1mm by 0.5mm/1mm membrane with optimal imprinted values, increased temperature
The same job-file with the 0.5mm/1mm by 0.5mm/1mm membrane, as shown in figure D.17, is printed with the 25x objective. A laser power of 22.5 mW and a scan speed of 10 000 µm s^{-1} are used. A hatching distance of 0.5 µm is used and the height of the pillars is 12.5 µm excluding the tip. An anti stiction layer is spin coated on top of the soft mold at 2000 RPM for 60 s, rinsed afterwards with HFE7100, and baked for 10 min at 120 °C. An imprinting temperature of 140 °C, an imprinting force of 3000 N, and a holding time of 10 min is used. A multilayer substrate with PEDOT:PSS film spin coated at 1500 RPM is used.

Influence of a tip angle of 85°
A print job similar the two LP & SS matrices, as presented in figure D.16, is created. The only difference is that the pillars on the left have a tip angle of 85° and the hatching distance of those pillars is 0.5 µm as well. This experiment is performed to verify whether a sharper tip results in more through-holes than found by the pillars on the right with a tip angle of 80° of this experiment. A 3D preview of this print job is presented in figure D.19.

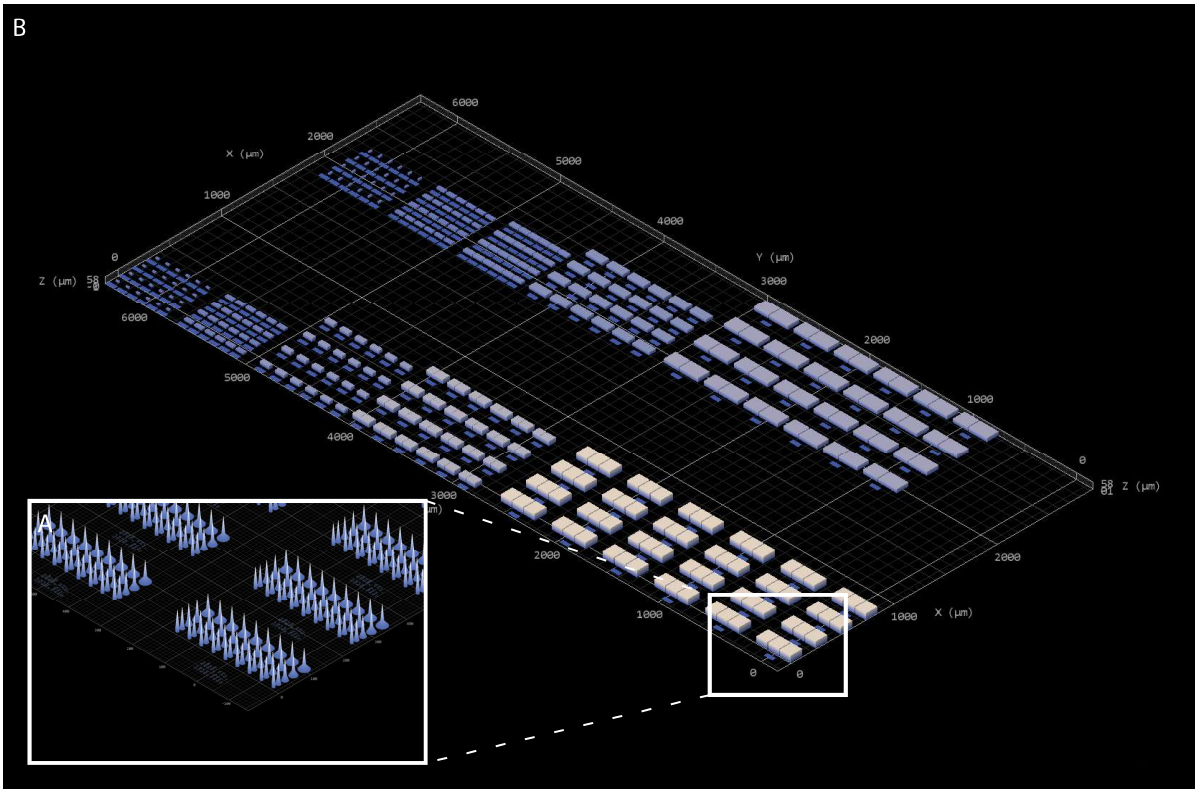

Figure D.19: 3D preview of the print job used to find the laser powers, scan speed, and hatching distance per pillar diameter to imprint a multilayer substrate without transferring of the pillars. A: Close up from the print job regarding the one square of pillars with varying base angles in the x-direction. B: Overview of the complete print job of which the LP & SS matrix on the right has pillars with a hatching distance of 0.5 µm and a tip angle of 80°. The LP & SS matrix on the left has a hatching distance of 0.5 µm and a tip angle of 85°. Five matrices of pillars with different diameters are placed behind each other in the y-direction. Within such a matrix, the scan speed in varied in the x-direction and the laser power is varied in the y-direction.

An anti stiction layer is spin coated on top of the soft mold at 2000 RPM for 60 s, rinsed afterwards with HFE7100, and baked for 10 min at 120 °C. The imprinting temperature of 130 °C, an imprint force of 3000 N, and a holding time of 10 min is used for imprinting the multilayer substrate. The multilayer substrate contains a PEDOT:PSS layer spin coated at 1500 RPM. The imprinted substrate was immersed in EG overnight. Afterwards, it was placed for 30 min in EG in the US cleaner to remove sticking pillars.

D.3. Results and discussion

Printing cones and pillars with sharp tips, 63x objective

An overview of the printed pillars per diameter (0.4 µm, 1 µm, 3 µm, 5 µm, and 8 µm) is given in the figures D.20B, D.21B, D.22B, D.23B, and D.24B. By visually inspecting the SEM images, the pillars are selected which looked the most like the original print job. These selected pillars are shown in the figures D.20A, D.21A, D.22A, D.23A, and D.24A. The corresponding laser powers and scan speeds of these pillars are summed up in table D.2. A comparison is made with the previous found optimal printing parameters before the experienced shift in the quality of the printed structures. The optimal scan speed did not change, but the optimal laser power increased with 2.5 mW. So, the optimal values to print pillars with a diameter of 5 µm or larger are a laser power of 25.0 mW and a scan speed of 2500 µm s^{-1}. And the optimal printing parameters for printing pillars with a diameter of 3 µm or smaller are a laser power of 22.5 mW and a scan speed of 2500 µm s^{-1}. The transition diameter of the optimal laser power is not 3 µm anymore, which had previously an optimal laser power of 20.0 mW and 22.5 mW. This transitioning diameter is somewhere between 3 µm and 5 µm. So nothing can be concluded about the optimal laser power between those diameters after the quality shift of the Photonic Professional GT.

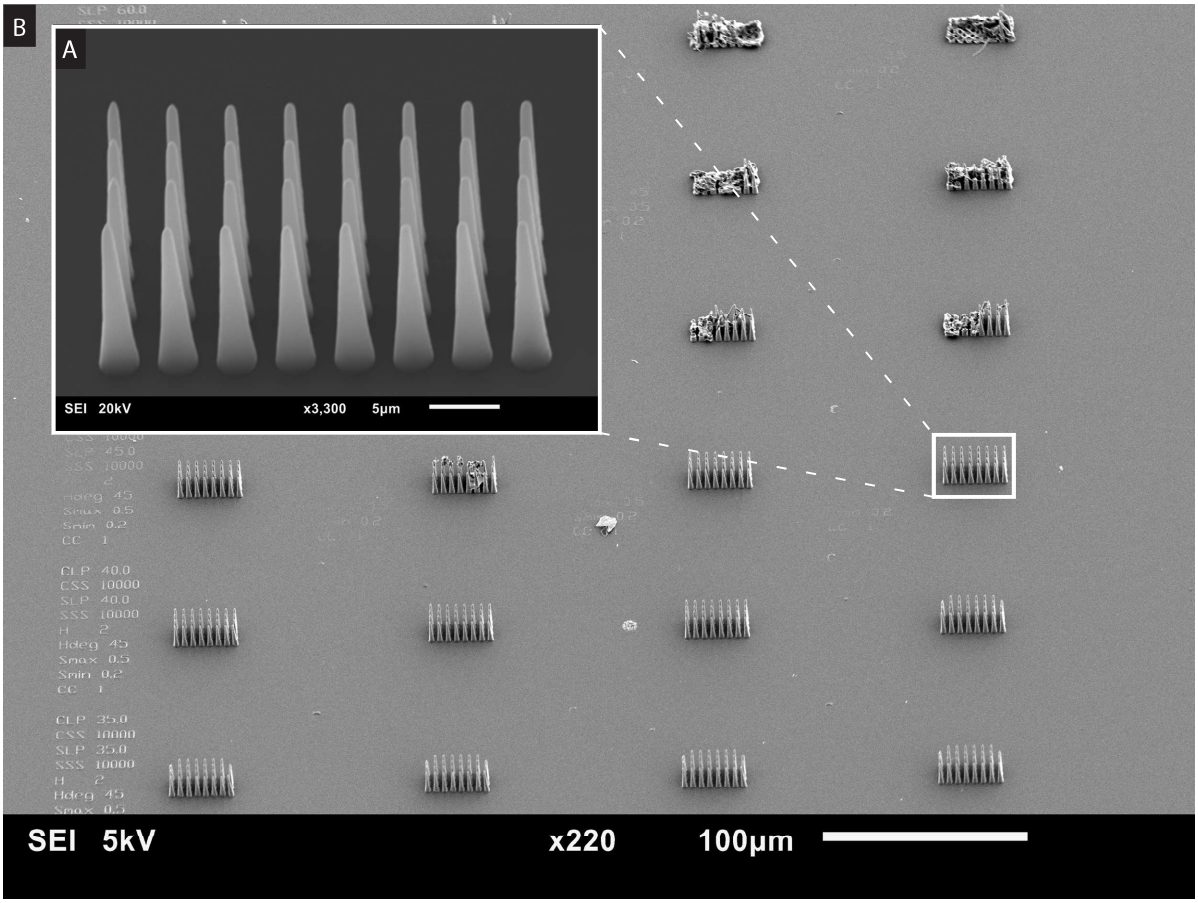

Figure D.20: Results of the printing cones and pillars with sharp tips, 63x objective experiment regarding the pillars with a diameter of 0.4 µm. A: Zoomed in on the set of pillars which looks the most like the modeled ones, printed with a laser power of 22.5 mW and a scan speed of 2500 µm s^{-1}. B: Overview of the printed pillars with a diameter of 0.4 µm.

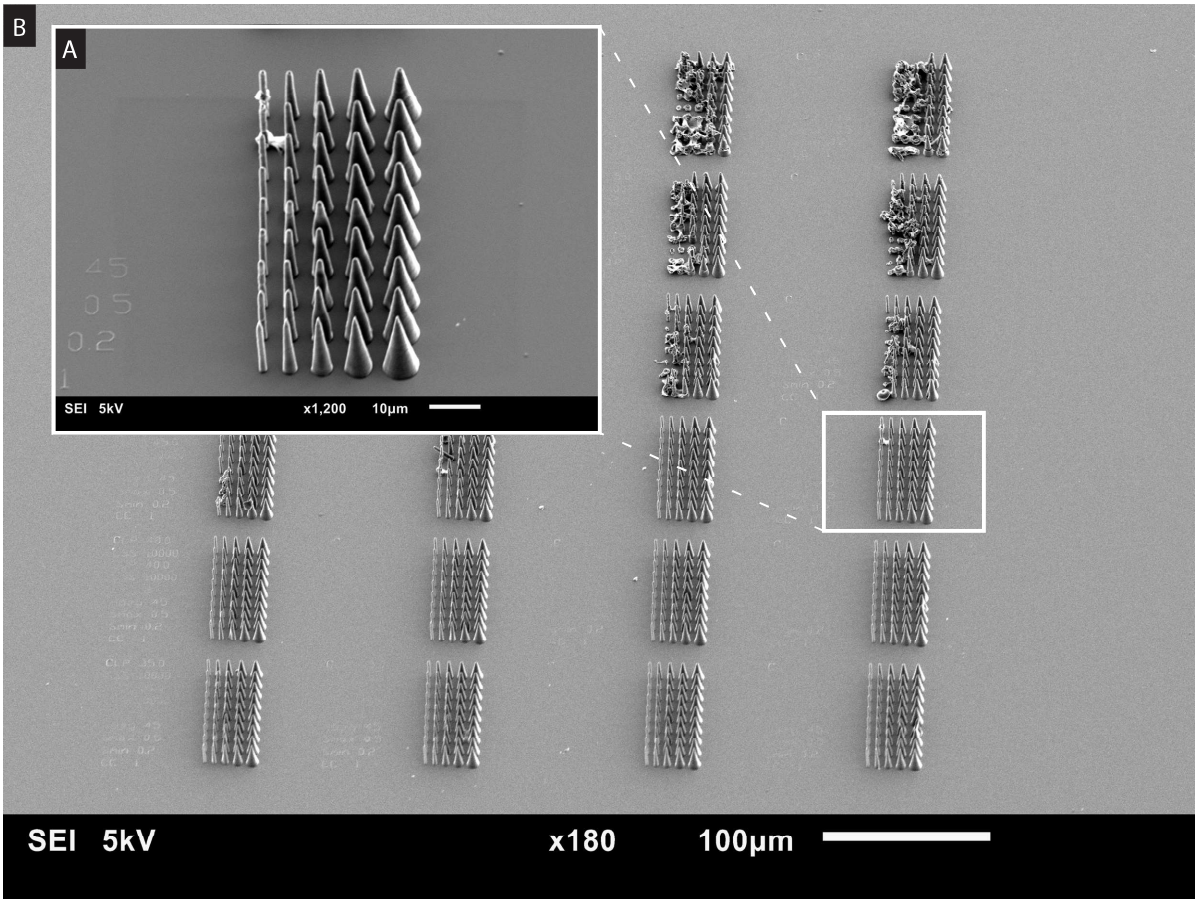

Figure D.21: Results of the printing cones and pillars with sharp tips, 63x objective experiment regarding the pillars with a diameter of 1 µm. A: Zoomed in on the set of pillars which looks the most like the modeled ones, printed with a laser power of 22.5 mW and a scan speed of 2500 µm s^{-1}. B: Overview of the printed pillars with a diameter of 1 µm.

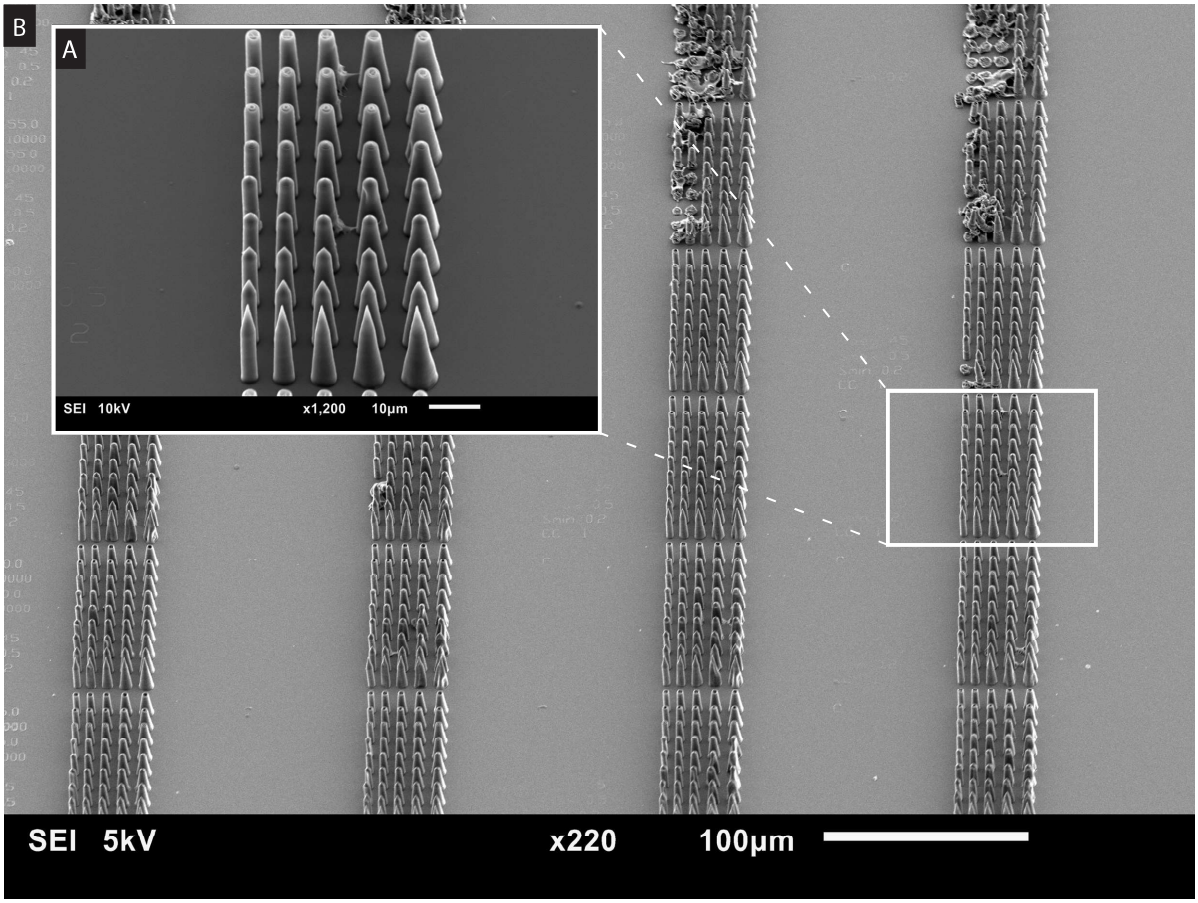

Figure D.22: Results of the printing cones and pillars with sharp tips, 63x objective experiment regarding the pillars with a diameter of 3 µm. A: Zoomed in on the set of pillars which looks the most like the modeled ones, printed with a laser power of 22.5 mW and a scan speed of 2500 µm s^{-1}. B: Overview of the printed pillars with a diameter of 3 µm.

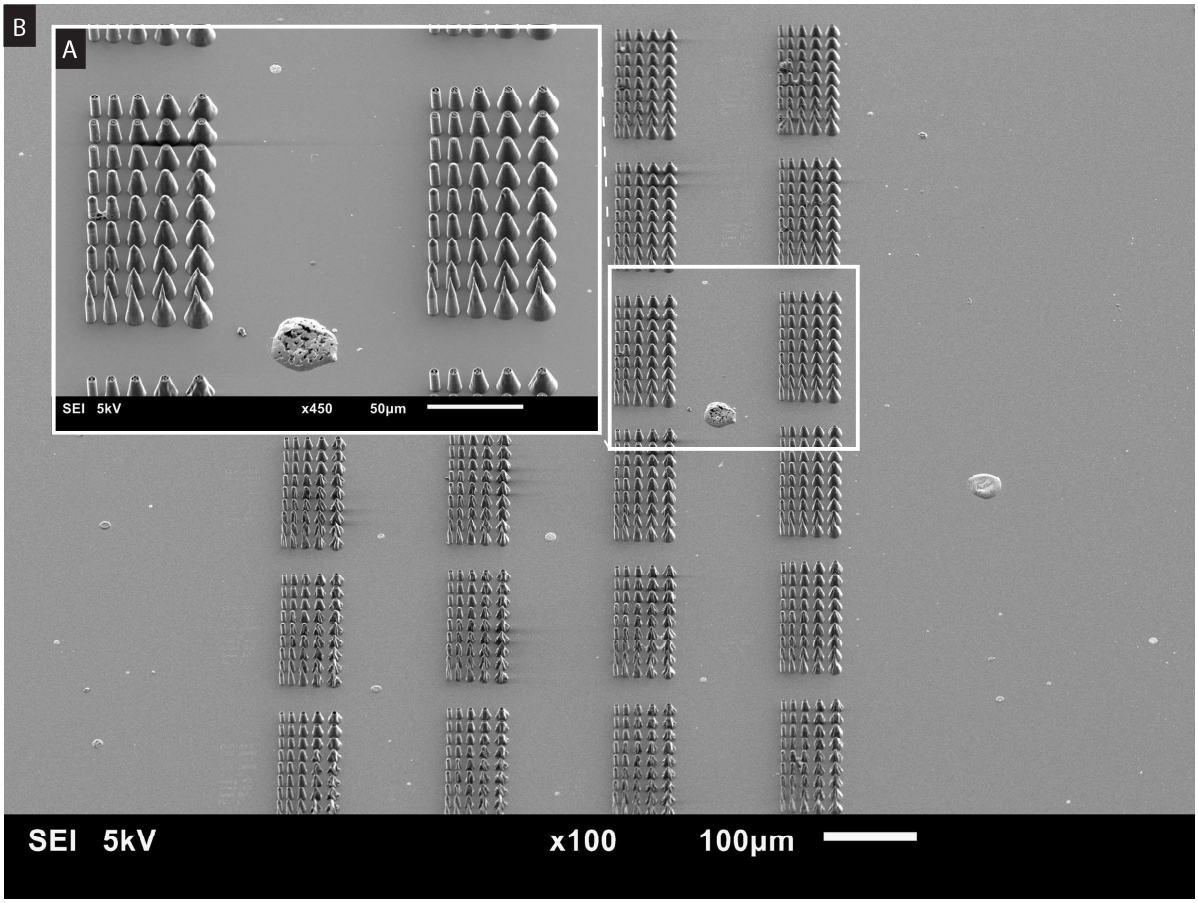

Figure D.23: Results of the printing cones and pillars with sharp tips, 63x objective experiment regarding the pillars with a diameter of 5 µm. A: Zoomed in on the set of pillars which looks the most like the modeled ones, printed with a laser power of 25.0 mW and a scan speed of 2500 µm s^{-1}. B: Overview of the printed pillars with a diameter of 5 µm.

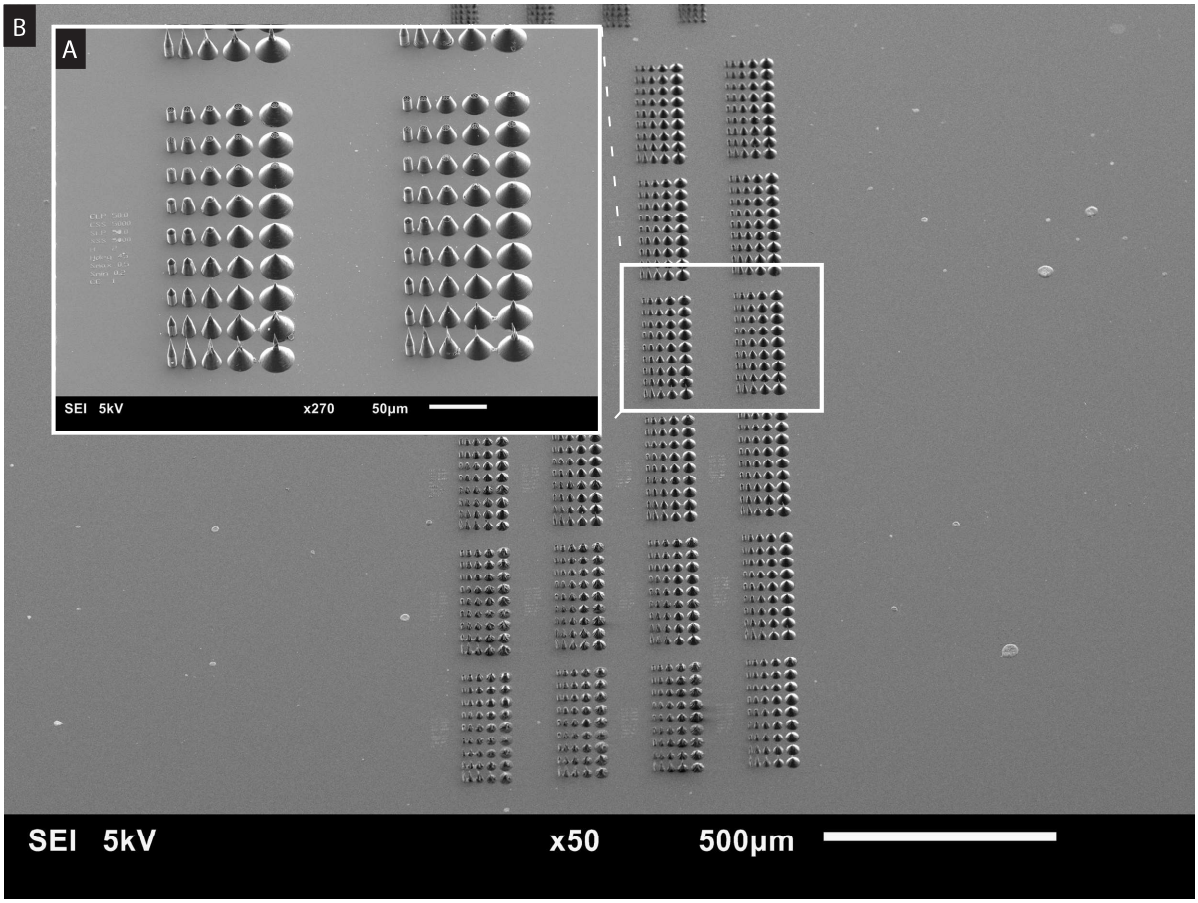

Figure D.24: Results of the printing cones and pillars with sharp tips, 63x objective experiment regarding the pillars with a diameter of 8 µm. A: Zoomed in on the set of pillars which looks the most like the modeled ones, printed with a laser power of 25.0 mW and a scan speed of 2500 µm s^{-1}. B: Overview of the printed pillars with a diameter of 8 µm.

Table D.2: Overview of the optimal parameters, before and after the experienced shift in the quality of the printed structures, for printing pins with sharp tips with the 63x objective.

	0.4 µm pins	1 µm pins	3 µm pins	5 µm pins	8 µm pins
Laser power (old) [mW]	20.0	20.0	20.0/22.5	22.5	22.5
Laser power (new) [mW]	22.5	22.5	22.5	25.0	25.0
Writing speed (old) [µm s^{-1}]	2500	2500	2500	2500	2500
Writing speed (new) [µm s^{-1}]	2500	2500	2500	2500	2500

Small fields of pillars, 25x objective

The printed pillars per diameter (0.4 µm, 1 µm, 3 µm, 5 µm, and 8 µm) are shown in figures D.25, D.26, D.27, D.28, and D.29. It can be seen that there is little difference between the pillars per diameter. So, the sharpest lookings ones are selected as the best ones. In the case when there is little to no difference (the pillars with a diameter of 0.4 µm, 1 µm, and 8 µm) the laser power is selected of the corresponding figure B. Because these pillars will still be good ones when the Photonic Professional GT fluctuates a bit during the printing process. The determined optimal printing parameters of the pillars with the 25x objective are summarized in table D.3. The pillars in figure D.25B and D.25C are bend. This phenomenon happened during the imaging of the pillars in the SEM.

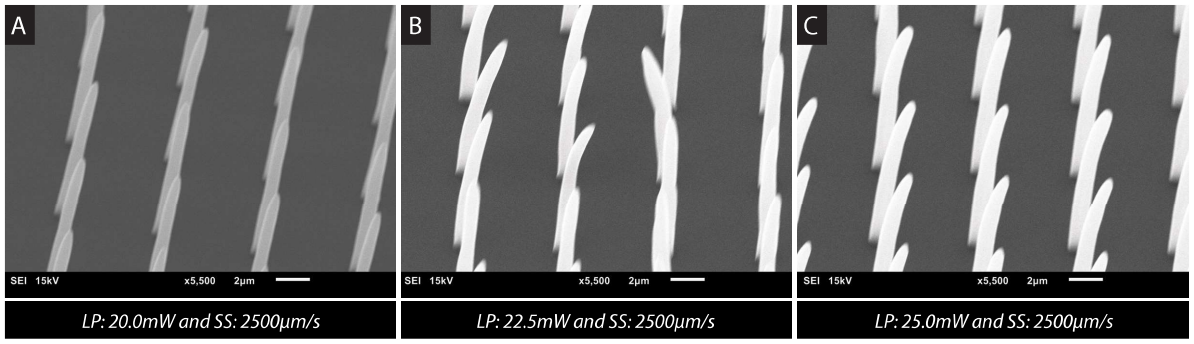

Figure D.25: Results of the Small fields of pillars, 25x objective experiment regarding the pillars with a diameter of 0.4 µm. The used laser power and scan speed are presented below each SEM image.

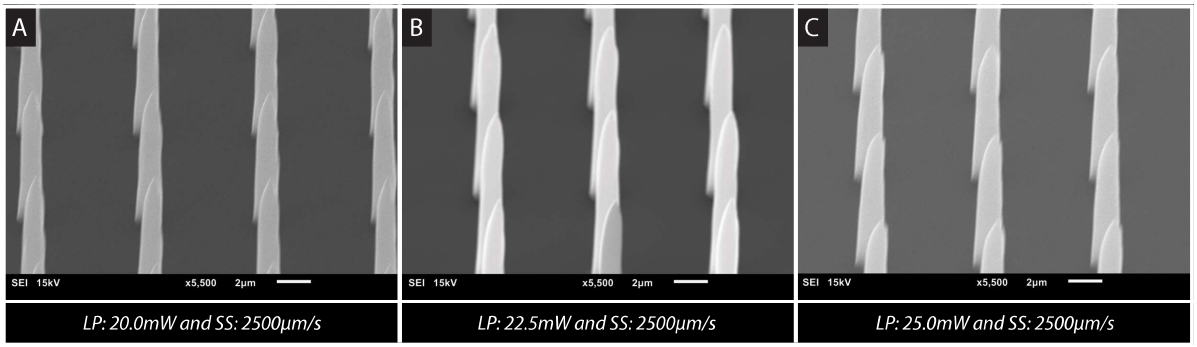

Figure D.26: Results of the Small fields of pillars, 25x objective experiment regarding the pillars with a diameter of 1 µm. The used laser power and scan speed are presented below each SEM image.

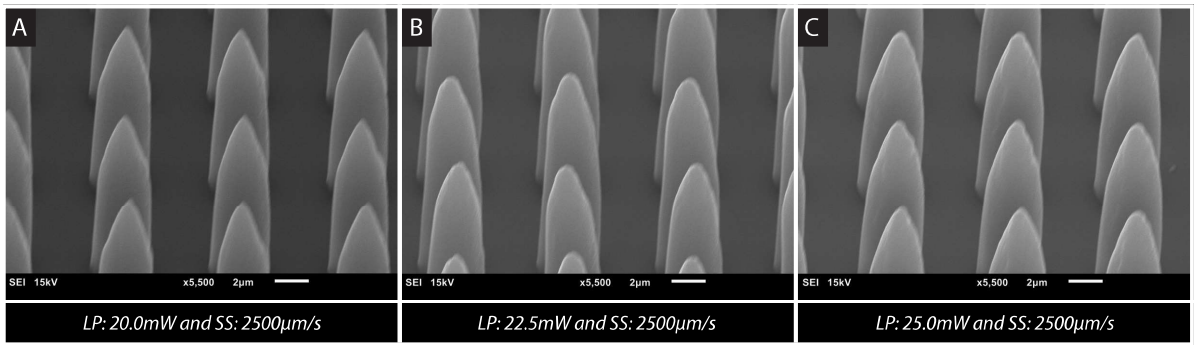

Figure D.27: Results of the Small fields of pillars, 25x objective experiment regarding the pillars with a diameter of 3 µm. The used laser power and scan speed are presented below each SEM image.

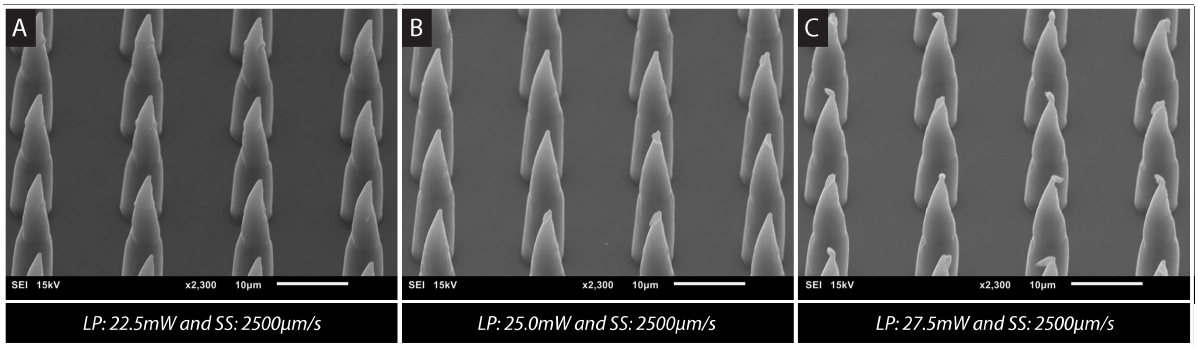

Figure D.28: Results of the Small fields of pillars, 25x objective experiment regarding the pillars with a diameter of 5 µm. The used laser power and scan speed are presented below each SEM image.

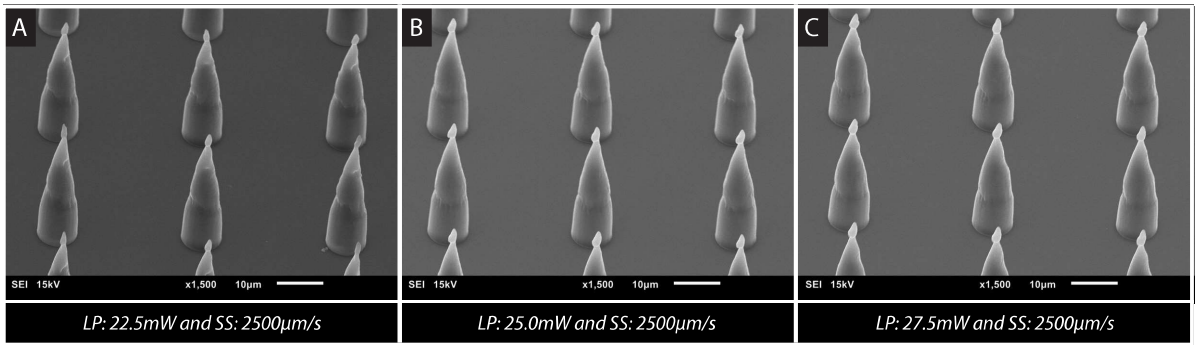

Figure D.29: Results of the Small fields of pillars, 25x objective experiment regarding the pillars with a diameter of 8 µm. The used laser power and scan speed are presented below each SEM image.

Table D.3: Overview of the optimal parameters for printing pins with sharp tips with the 25x objective.

	0.4 µm pins	1 µm pins	3 µm pins	5 µm pins	8 µm pins
Laser power [mW]	22.5	22.5	20.0	25.0	22.5
Writing speed [µm s^{-1}]	2500	2500	2500	2500	2500

Minimum distance required to prevent pillars with a diameter of 0.4 µm from falling over due to the capillary forces

The printed pillars of this experiment are shown in figures D.30B to D.39B. And a close up of the critical center to center spacing of pillars with a height 15 µm to 10 µm are presented in figures D.30A to D.39A. A close up of the critical center to center spacing of pillars with a height 7.5 µm to 2.5 µm are presented in figures D.30C to D.39C.

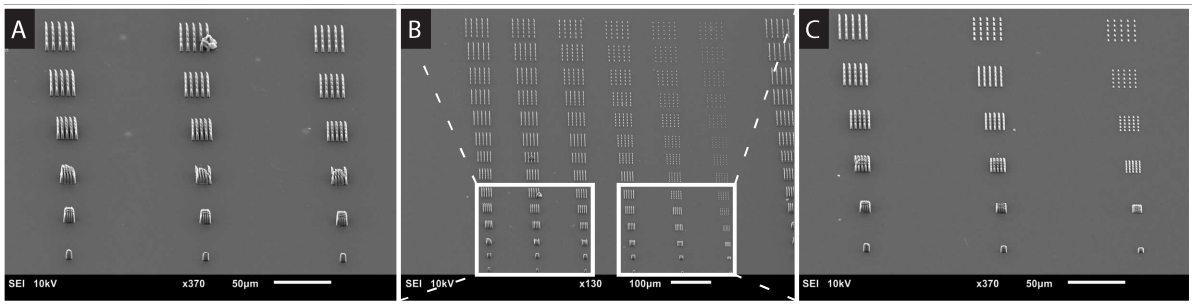

Figure D.30: Results of the first matrix of the print job used to determine the minimum distance required to prevent the pillars which are in 0.4 µm diameter from falling over due to the capillary forces. The height of the pillars is varied from 2.5 µm to 15 µm in steps of 2.5 µm in the direction of the x-axis. The spacing between the pillars is varied from 1 µm to 14 µm in steps of 1 µm in the direction of the y-axis. A: Close up of the critical center to center spacing of pillars with a height 15 µm to 10 µm. B: Overview of the printed pillars. C: Close up of the critical center to center spacing of pillars with a height 7.5 µm to 2.5 µm.

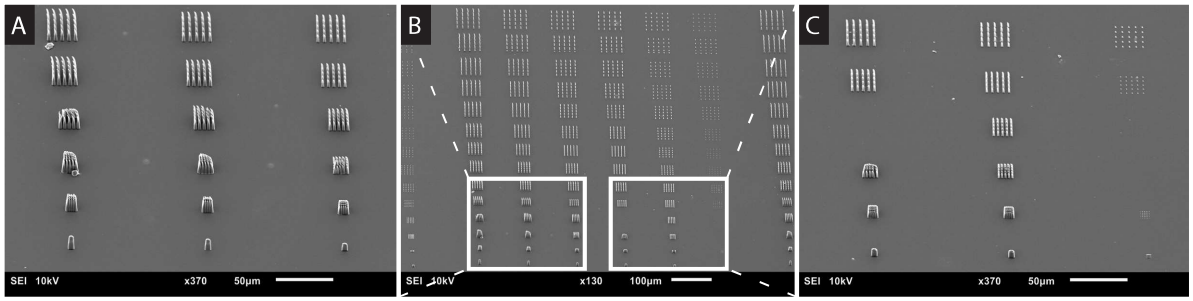

Figure D.31: Results of the second matrix of the print job used to determine the minimum distance required to prevent the pillars which are in 0.4 µm diameter from falling over due to the capillary forces. The height of the pillars is varied from 2.5 µm to 15 µm in steps of 2.5 µm in the direction of the x-axis. The spacing between the pillars is varied from 1 µm to 14 µm in steps of 1 µm in the direction of the y-axis. A: Close up of the critical center to center spacing of pillars with a height 15 µm to 10 µm. B: Overview of the printed pillars. C: Close up of the critical center to center spacing of pillars with a height 7.5 µm to 2.5 µm.

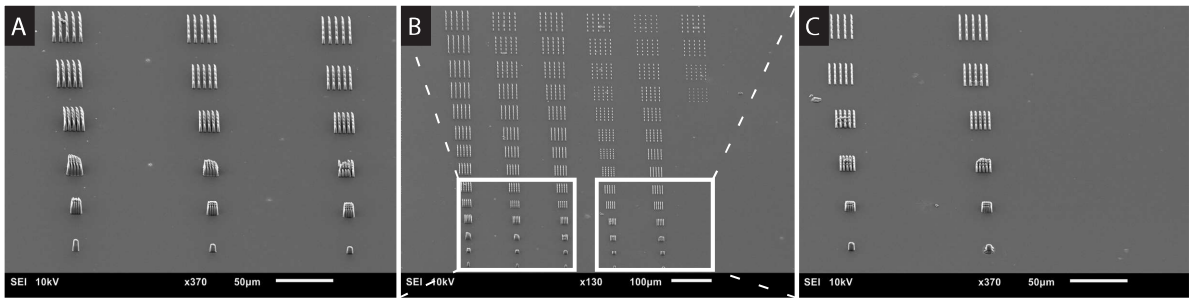

Figure D.32: Results of the third matrix of the print job used to determine the minimum distance required to prevent the pillars which are in 0.4 µm diameter from falling over due to the capillary forces. The height of the pillars is varied from 2.5 µm to 15 µm in steps of 2.5 µm in the direction of the x-axis. The spacing between the pillars is varied from 1 µm to 14 µm in steps of 1 µm in the direction of the y-axis. A: Close up of the critical center to center spacing of pillars with a height 15 µm to 10 µm. B: Overview of the printed pillars. C: Close up of the critical center to center spacing of pillars with a height 7.5 µm to 2.5 µm.

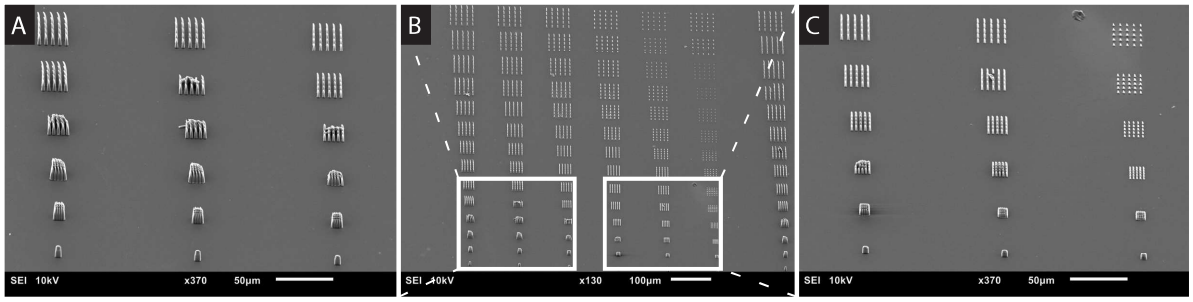

Figure D.33: Results of the fourth matrix of the print job used to determine the minimum distance required to prevent the pillars which are in 0.4 µm diameter from falling over due to the capillary forces. The height of the pillars is varied from 2.5 µm to 15 µm in steps of 2.5 µm in the direction of the x-axis. The spacing between the pillars is varied from 1 µm to 14 µm in steps of 1 µm in the direction of the y-axis. A: Close up of the critical center to center spacing of pillars with a height 15 µm to 10 µm. B: Overview of the printed pillars. C: Close up of the critical center to center spacing of pillars with a height 7.5 µm to 2.5 µm.

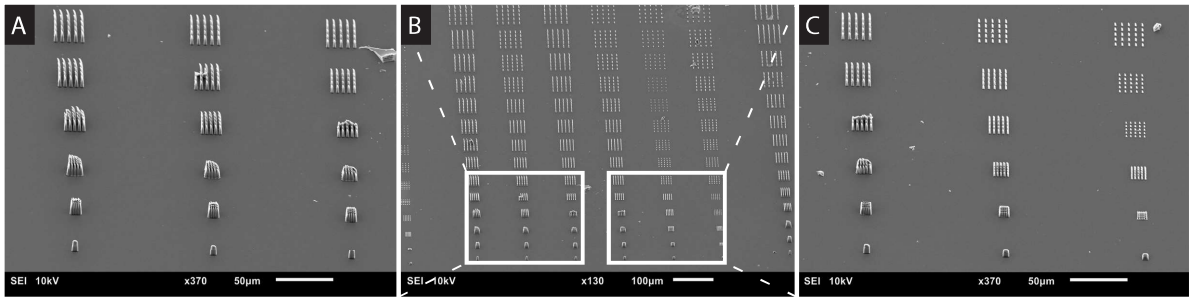

Figure D.34: Results of the fifth matrix of the print job used to determine the minimum distance required to prevent the pillars which are in 0.4 µm diameter from falling over due to the capillary forces. The height of the pillars is varied from 2.5 µm to 15 µm in steps of 2.5 µm in the direction of the x-axis. The spacing between the pillars is varied from 1 µm to 14 µm in steps of 1 µm in the direction of the y-axis. A: Close up of the critical center to center spacing of pillars with a height 15 µm to 10 µm. B: Overview of the printed pillars. C: Close up of the critical center to center spacing of pillars with a height 7.5 µm to 2.5 µm.

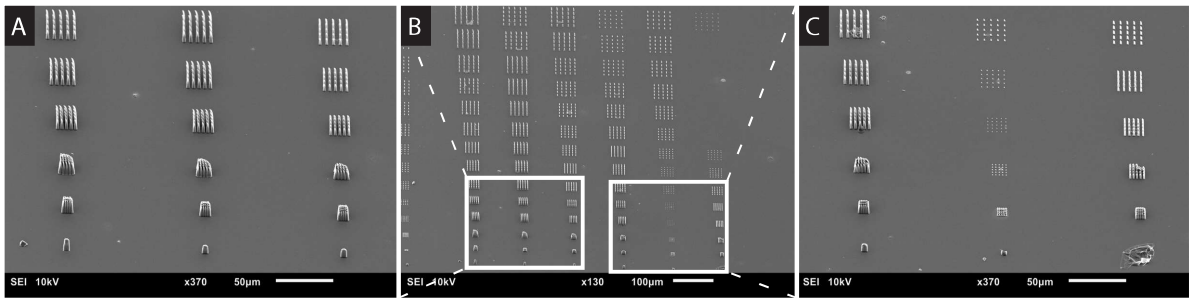

Figure D.35: Results of the sixth matrix of the print job used to determine the minimum distance required to prevent the pillars which are in 0.4 µm diameter from falling over due to the capillary forces. The height of the pillars is varied from 2.5 µm to 15 µm in steps of 2.5 µm in the direction of the x-axis. The spacing between the pillars is varied from 1 µm to 14 µm in steps of 1 µm in the direction of the y-axis. A: Close up of the critical center to center spacing of pillars with a height 15 µm to 10 µm. B: Overview of the printed pillars. C: Close up of the critical center to center spacing of pillars with a height 7.5 µm to 2.5 µm.

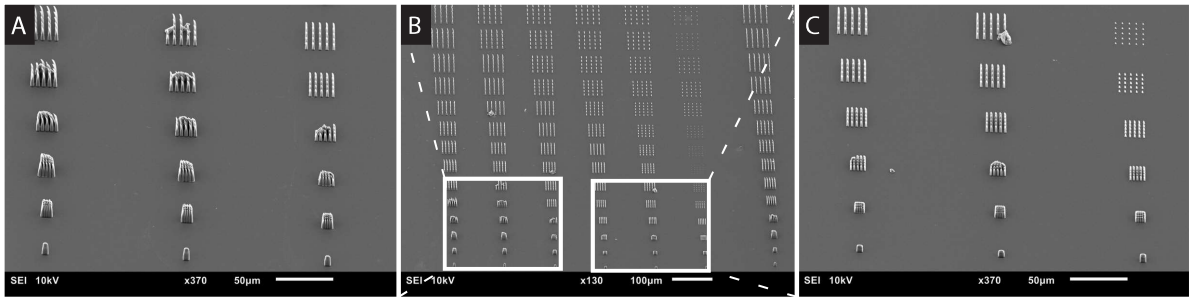

Figure D.36: Results of the seventh matrix of the print job used to determine the minimum distance required to prevent the pillars which are in 0.4 µm diameter from falling over due to the capillary forces. The height of the pillars is varied from 2.5 µm to 15 µm in steps of 2.5 µm in the direction of the x-axis. The spacing between the pillars is varied from 1 µm to 14 µm in steps of 1 µm in the direction of the y-axis. A: Close up of the critical center to center spacing of pillars with a height 15 µm to 10 µm. B: Overview of the printed pillars. C: Close up of the critical center to center spacing of pillars with a height 7.5 µm to 2.5 µm.

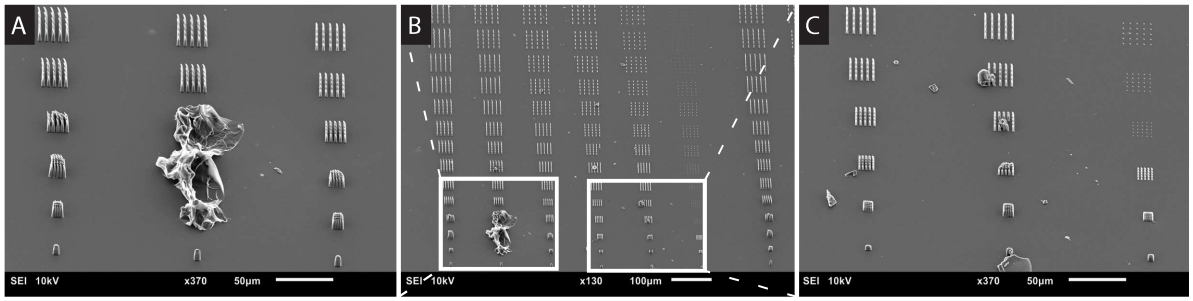

Figure D.37: Results of the eigthth matrix of the print job used to determine the minimum distance required to prevent the pillars which are in 0.4 µm diameter from falling over due to the capillary forces. The height of the pillars is varied from 2.5 µm to 15 µm in steps of 2.5 µm in the direction of the x-axis. The spacing between the pillars is varied from 1 µm to 14 µm in steps of 1 µm in the direction of the y-axis. A: Close up of the critical center to center spacing of pillars with a height 15 µm to 10 µm. B: Overview of the printed pillars. C: Close up of the critical center to center spacing of pillars with a height 7.5 µm to 2.5 µm.

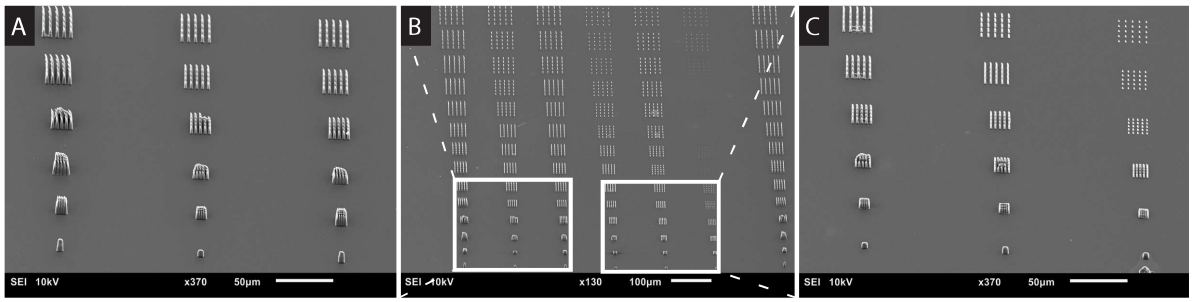

Figure D.38: Results of the ninth matrix of the print job used to determine the minimum distance required to prevent the pillars which are in 0.4 µm diameter from falling over due to the capillary forces. The height of the pillars is varied from 2.5 µm to 15 µm in steps of 2.5 µm in the direction of the x-axis. The spacing between the pillars is varied from 1 µm to 14 µm in steps of 1 µm in the direction of the y-axis. A: Close up of the critical center to center spacing of pillars with a height 15 µm to 10 µm. B: Overview of the printed pillars. C: Close up of the critical center to center spacing of pillars with a height 7.5 µm to 2.5 µm.

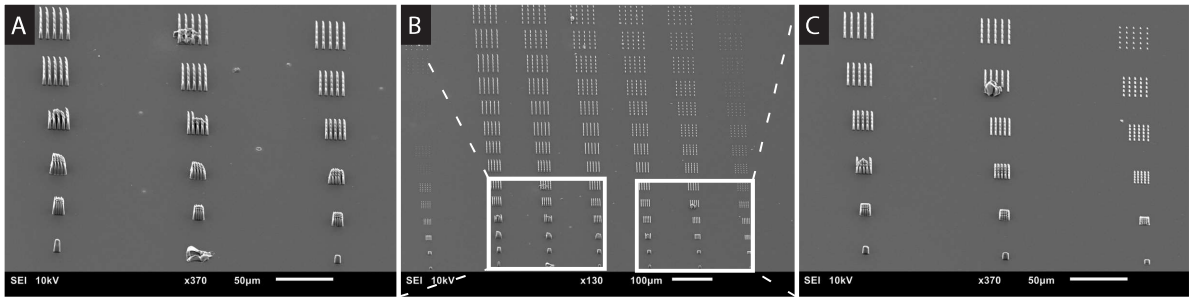

Figure D.39: Results of the tenth matrix of the print job used to determine the minimum distance required to prevent the pillars which are in 0.4 µm diameter from falling over due to the capillary forces. The height of the pillars is varied from 2.5 µm to 15 µm in steps of 2.5 µm in the direction of the x-axis. The spacing between the pillars is varied from 1 µm to 14 µm in steps of 1 µm in the direction of the y-axis. A: Close up of the critical center to center spacing of pillars with a height 15 µm to 10 µm. B: Overview of the printed pillars. C: Close up of the critical center to center spacing of pillars with a height 7.5 µm to 2.5 µm.

Except from collapsing of the pillars, some other phenomena can be seen in the figures as well. Some of the photoresist started to boil which ruined the pillars at those locations and there was some problem with finding the correct interface which resulted in pillars which are lower in height, or no pillars at all. The minimal center to center spacing required to prevent the pillars per height and per base angle from collapsing due to the capillary forces are selected by hand per SEM image. The resulting boxplots with the minimal center to center spacing are presented in figure D.40. Of all the boxplots it can be seen that a bigger base angle needs a smaller center to center distance to prevent the pillars from collapsing. Also, the shorter pillars require a smaller center to center spacing than the taller ones, which is in line with literature.[113]

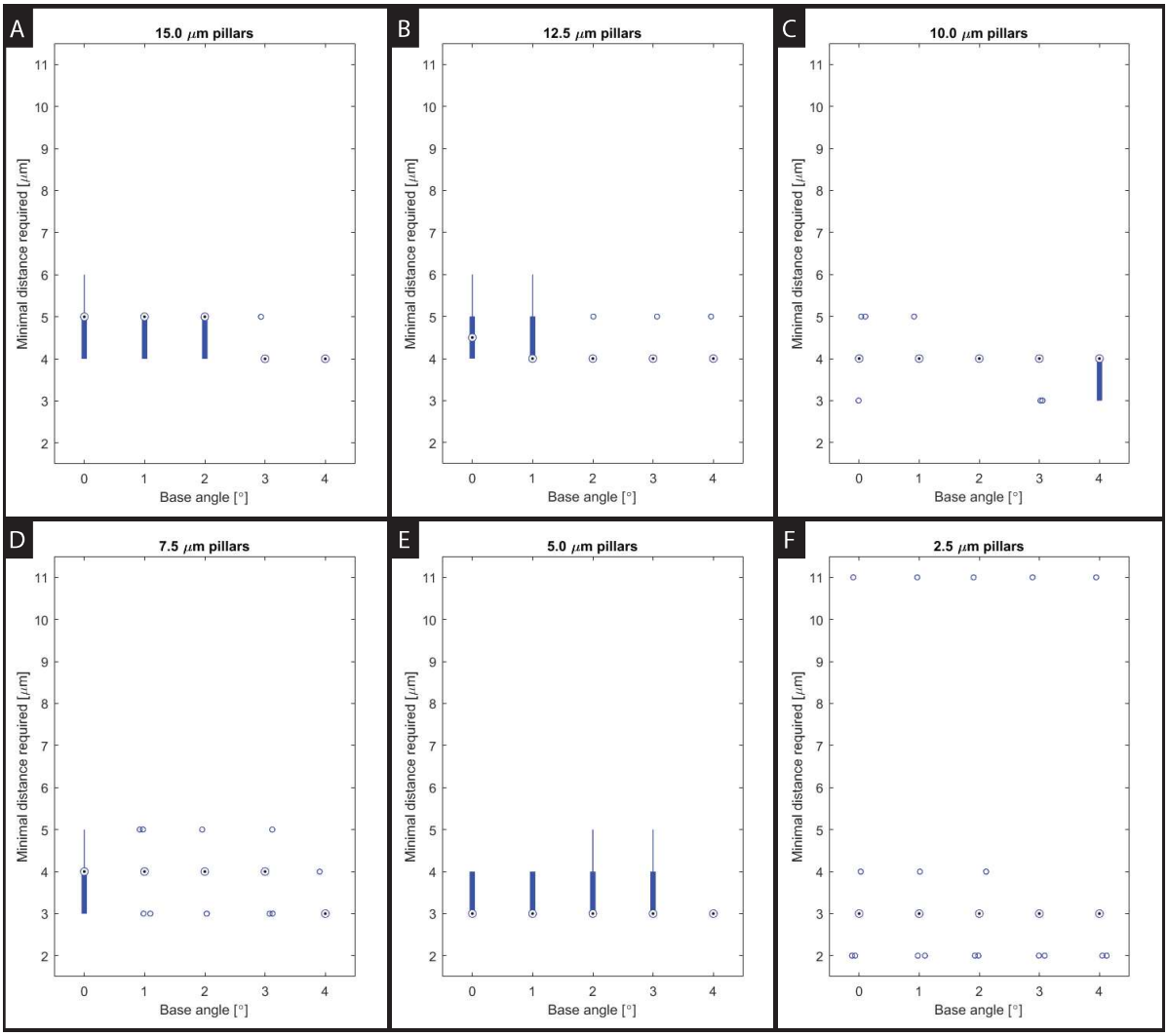

Figure D.40: Boxplots (showing the median, 25th percentile, 75th percentile, and data points outside the inter-quartile range) for the minimal distance required to prevent the pillars of 0.4 µm in diameter from collapsing due to the capillary forces. A: Boxplot of the minimal distance required per base angle of pillars which are 15 µm in height. B: Boxplot of the minimal distance required per base angle of pillars which are 12.5 µm in height. C: Boxplot of the minimal distance required per base angle of pillars which are 10 µm in height. D: Boxplot of the minimal distance required per base angle of pillars which are 7.5 µm in height. E: Boxplot of the minimal distance required per base angle of pillars which are 5 µm in height. F: Boxplot of the minimal distance required per base angle of pillars which are 2.5 µm in height.

Imprinting 1mm by 1mm membrane with optimal printing parameters, 63x objective

The mold before imprinting, mold after imprinting, and the substrate after imprinting are shown in figure D.41A to D.41C. All the pillars transferred from the mold to the substrate, which can be seen by the empty coverslip in figure D.41B. Looking at figure D.41C, it can be seen that the pillars are stuck in the substrate. The 0.4 µm pillars did collapse, which can been seen in figure D.41A. The center to center spacing of those pillars was 2 µm above the minimum required distance. But the difference is that the 63x objective was used to print the pillars instead of the 25x objective. This could explain the difference. But that would mean that the pillars printed with the 25x objective have a better adhesion with the glass coverslip in comparison when they are printed with the 63x objective. Therefore, the same experiment will be performed but printed with the 25x objective to see if there is a difference.

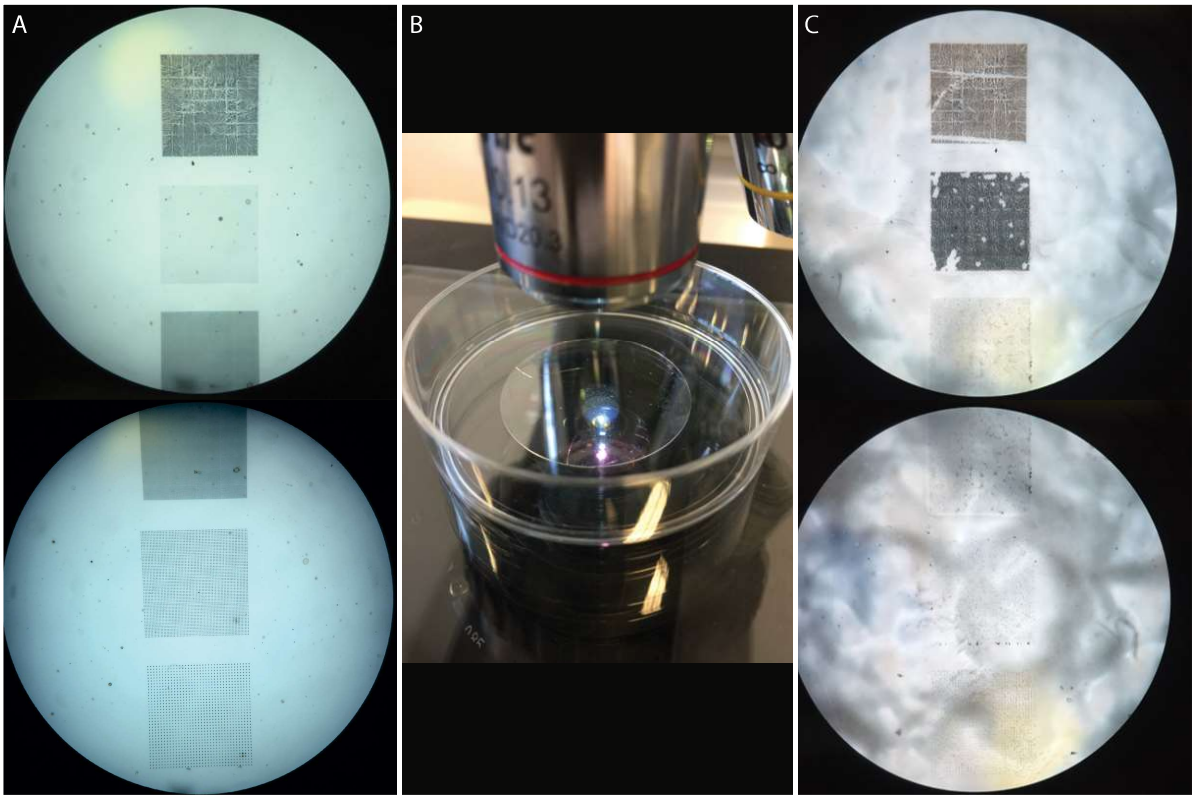

Figure D.41: Results of imprinting at 120 °C, 4000 N, with a holding time of 10 min with a mold which is printed with the optimal printing parameters with the 63x objective. A: Mold before imprinting. B: Mold after imprinting. C: Substrate after imprinting and treatment with EG.

Imprinting 1 mm by 1 mm membrane with optimal printing parameters, 25x objective

The mold before imprinting is shown in figure D.42A. The second field of pillars is incomplete. This happened during the printing of the mold. The Photonic Professional GT tried to find, probably, the interface at a location of one the already printed pillars or really close to it. Therefore, the Photonic Professional GT was most of the time not able to find the correct interface what resulted in missing pillars on the mold. The mold after imprinting is shown in figure D.42B and the substrate after imprinting is shown in figure D.42C. From figure D.42B, it can be seen that all the pillars were lost after the imprinting step. But most of the pillars got removed by cleaning the substrate after imprinting in the US bath, while almost no pillars can be seen in figure D.42C. While all the pillars got removed from the mold, it is hard to say whether printing the pillars with the 25x objective results in better adhesion between the pillars and the glass coverslip. But the pillars of 0.4 µm in diameter did not collapse, which can been seen in figure D.42A.

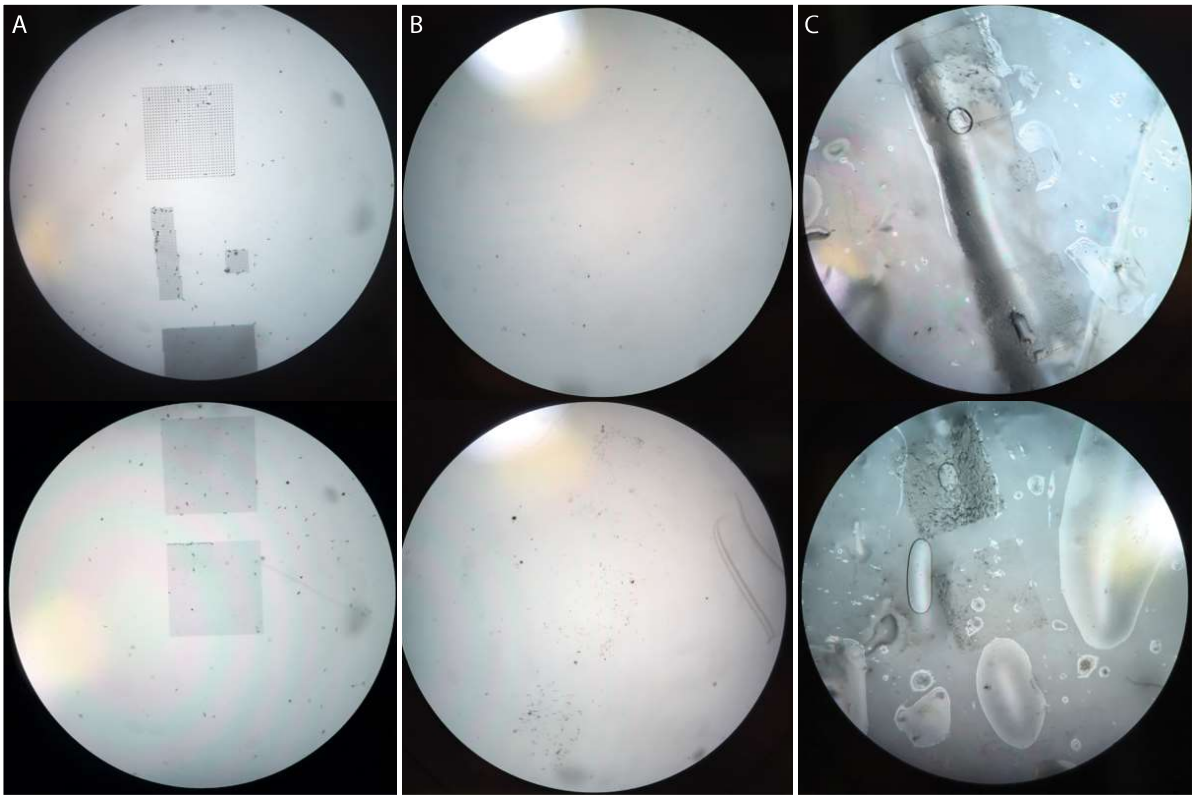

Figure D.42: Results of imprinting at 120 °C, 4000 N, with a holding time of 10 min with a mold which is printed with the optimal printing parameters with the 25x objective. A: Mold before imprinting. B: Mold after imprinting. C: Substrate after imprinting and post treatment with EG and removing the pillars in the US cleaner.

Imprinting 1 mm by 1 mm membrane with optimal printing parameters and demolding in US cleaner
The mold before imprinting is shown in figure D.43A. The third and fourth field of pillars are the same one. The order from top to bottom in diameter of the pillars are 1 µm, 3 µm, 5 µm, 8 µm, and 0.4 µm. The order changed while during the printing process the results from the capillary force experiment were imaged and processed to make sure that the pillars of this mold would not collapse due to capillary forces. If necessary, the mean center to center spacing could be changed after already printing the first four fields of pillars. The mold after imprinting is shown in figure D.43B and the substrate after imprinting is shown in figure D.43C. As clearly can be seen in these images, the demolding of the mold after a treatment in the US cleaner did not prevent the pillars from transferring from the mold to the substrate.

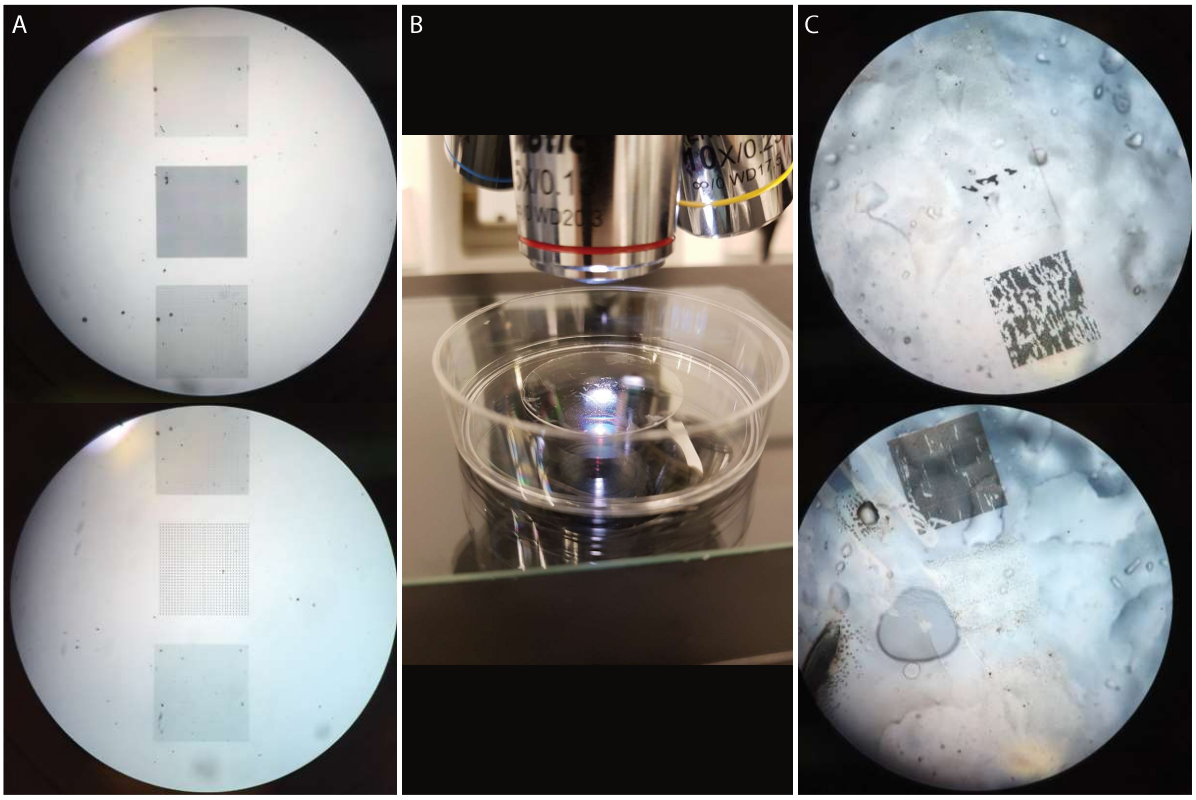

Figure D.43: Results of imprinting at 120 °C, 4000 N, with a holding time of 10 min with a mold which is printed with the optimal printing parameters with the 25x objective. A: Mold before imprinting. B: Mold after imprinting and demolding it in the US cleaner. C: Substrate after imprinting and post treatment with EG.

Small field of pillars, 25x objective and maximal laser power

The printed pillars per diameter (0.4 µm, 1 µm, 3 µm, 5 µm, and 8 µm) are shown in figures D.44, D.45, D.46, D.47, and D.48. As expected, a lot of boiling of the photoresist is seen. This limits the maximal laser power that can be used. Therefore, the laser powers with little to no boiling of the photoresist are selected as the maximum allowable ones. This is summarized in table D.4.

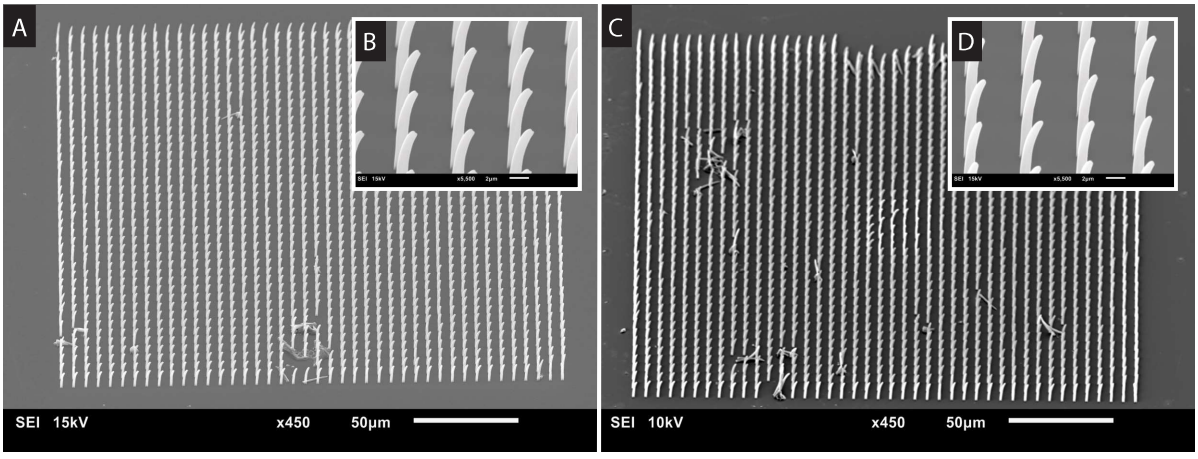

Figure D.44: Results of printing pillars with a diameter of 0.4 µm at their maximum laser power. A: Overview of the printed pillars with a laser power of 30.0 mW and a scan speed of 2500 µm s^{-1}. B: Close up of the pillars printed with a laser power of 30.0 mW and a scan speed of 2500 µm s^{-1}. C: Overview of the printed pillars with a laser power of 27.5 mW and a scan speed of 2500 µm s^{-1}. D: Close up of the pillars printed with a laser power of 27.5 mW and a scan speed of 2500 µm s^{-1}.

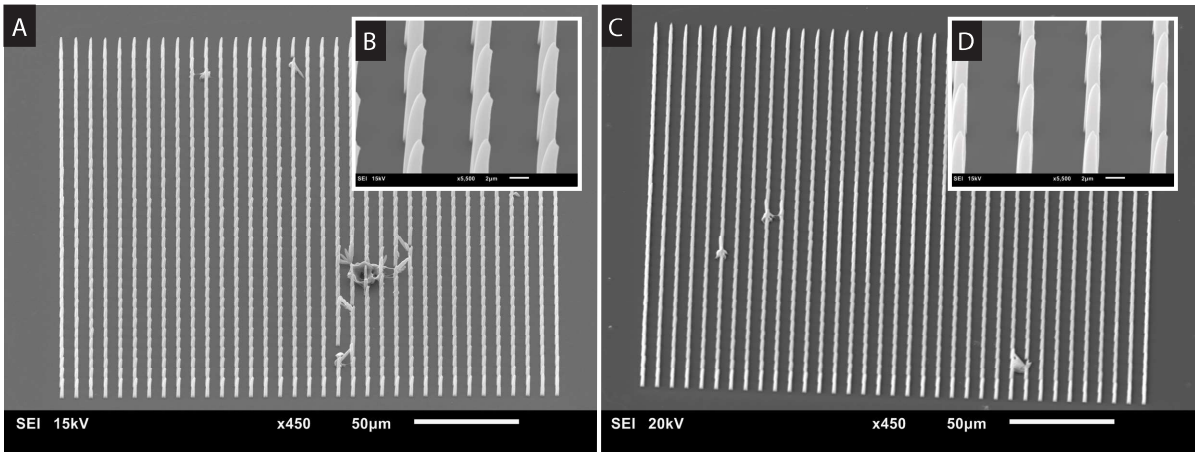

Figure D.45: Results of printing pillars with a diameter of 1 µm at their maximum laser power. A: Overview of the printed pillars with a laser power of 30.0 mW and a scan speed of 2500 µm s^{-1}. B: Close up of the pillars printed with a laser power of 30.0 mW and a scan speed of 2500 µm s^{-1}. C: Overview of the printed pillars with a laser power of 27.5 mW and a scan speed of 2500 µm s^{-1}. D: Close up of the pillars printed with a laser power of 27.5 mW and a scan speed of 2500 µm s^{-1}.

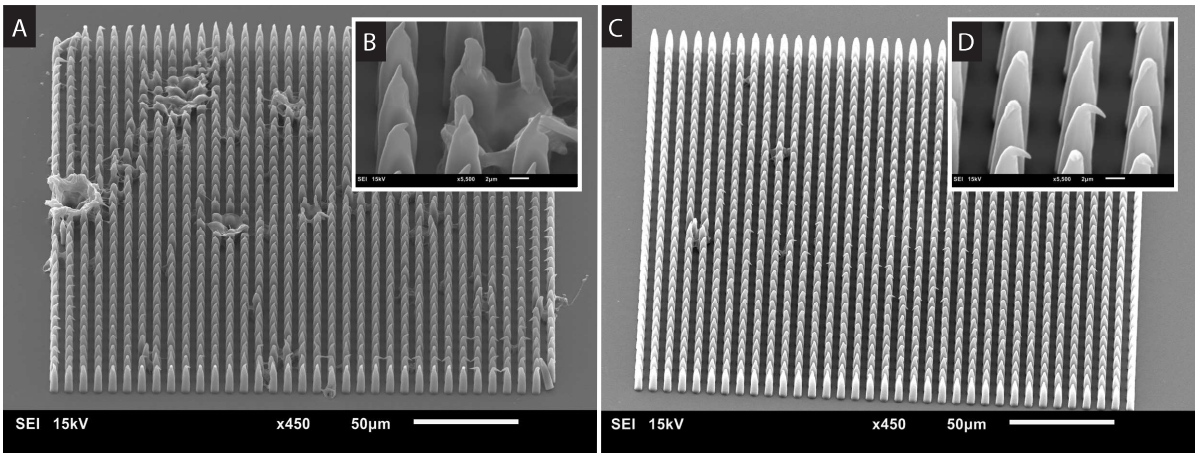

Figure D.46: Results of printing pillars with a diameter of 3 µm at their maximum laser power. A: Overview of the printed pillars with a laser power of 30.0 mW and a scan speed of 2500 µm s^{-1}. B: Close up of the pillars printed with a laser power of 30.0 mW and a scan speed of 2500 µm s^{-1}. C: Overview of the printed pillars with a laser power of 27.5 mW and a scan speed of 2500 µm s^{-1}. D: Close up of the pillars printed with a laser power of 27.5 mW and a scan speed of 2500 µm s^{-1}.

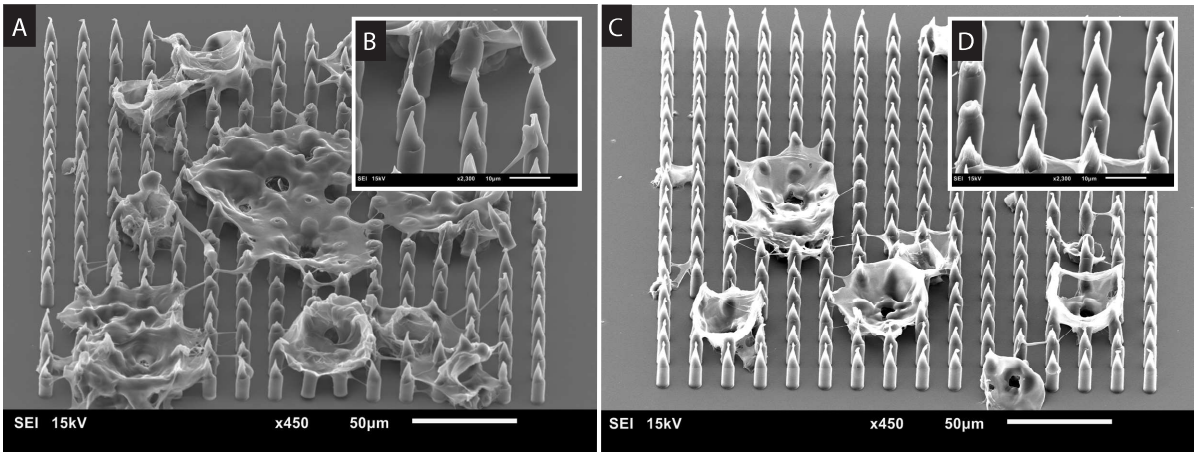

Figure D.47: Results of printing pillars with a diameter of 5 µm at their maximum laser power. A: Overview of the printed pillars with a laser power of 32.5 mW and a scan speed of 2500 µm s^{-1}. B: Close up of the pillars printed with a laser power of 32.5 mW and a scan speed of 2500 µm s^{-1}. C: Overview of the printed pillars with a laser power of 30.0 mW and a scan speed of 2500 µm s^{-1}. D: Close up of the pillars printed with a laser power of 30.0 mW and a scan speed of 2500 µm s^{-1}.

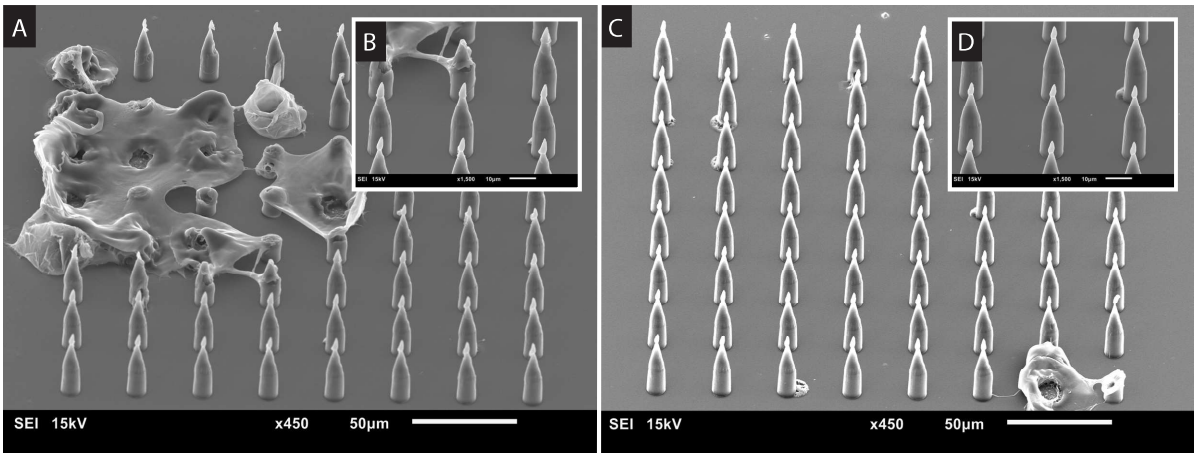

Figure D.48: Results of printing pillars with a diameter of 8 µm at their maximum laser power. A: Overview of the printed pillars with a laser power of 32.5 mW and a scan speed of 2500 µm s^{-1}. B: Close up of the pillars printed with a laser power of 32.5 mW and a scan speed of 2500 µm s^{-1}. C: Overview of the printed pillars with a laser power of 30.0 mW and a scan speed of 2500 µm s^{-1}. D: Close up of the pillars printed with a laser power of 30.0 mW and a scan speed of 2500 µm s^{-1}.

Table D.4: Overview of the maximal laser power and scan speed for printing pins with sharp tips with the 25x objective.

	0.4 µm pins	1 µm pins	3 µm pins	5 µm pins	5 µm pins
Laser power [mW]	22.5	25.0	25.0	27.5	27.5
Writing speed [µm s^{-1}]	2500	2500	2500	2500	2500

Imprinting 1 mm by 1 mm membrane with maximal laser power settings

The mold before imprinting, mold after imprinting, and the substrate after imprinting with pillars printed at the maximal laser power with the 25x objective are shown in figure D.49A to D.49C. In figure D.49A, the black dots are spots of boiled photoresist which have ruined those pillars locally. While it looks from figure D.44 that the pillars with a diameter of 0.4 µm can be printed at an even higher laser power. Therefore, they are printed with a laser power of 28.75 mW and a scan speed of 2500 µm s^{-1}. But the resist started to boil and was, therefore, not further printed. So, all the other fields of pillars are printed according to the printing parameters presented in table D.4. Looking at figure D.49B, the upper small field of pillars survived the demolding step.

And the resulting imprint can be seen in figure D.49C. But everything, or at least a large number of the pillars, of the other fields did transfer again.

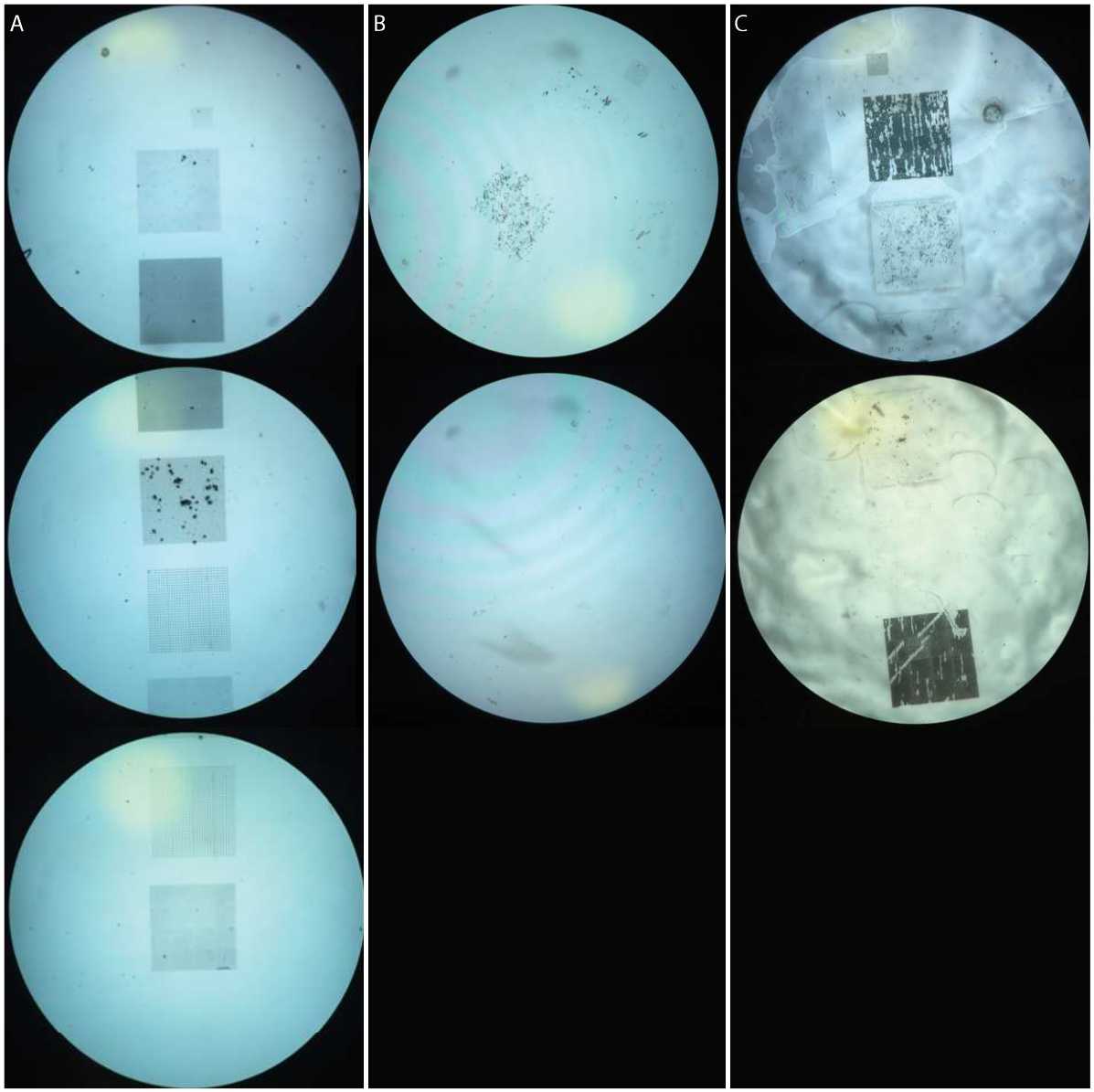

Figure D.49: Results of imprinting at 120 °C, 4000 N, with a holding time of 10 min with a mold which is printed with the maximal laser power with the 25x objective. A: Mold before imprinting. B: Mold after imprinting. C: Substrate after imprinting and post treatment with EG.

The substrate, regarding the small field of pillars which survived, is imaged on the conductive side (top), D.50A, and the non conductive side (bottom) in figure D.50B. No through-holes can been seen in in figure D.50B. Not even dents in the substrate can be seen, therefore, it is believed that there was a problem with finding the interface during the printing process which resulted in much shorter pillars. And due to their decrease in height, they survived the demolding step.

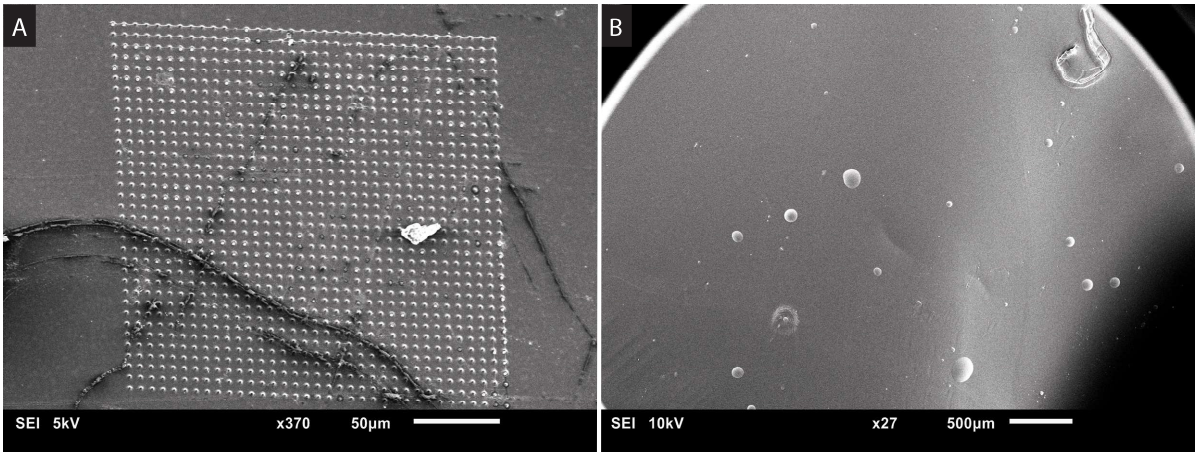

Figure D.50: SEM images of the imprinted substrate with a mold which contains pillars of 0.4 µm in diameter. A: Conductive side of the membrane (top). B: Non conductive side of the mebrane (bottom).

Threshold experiment difference between the old resist and the new resist

The results of the threshold test of the old resist are shown in figure D.51 and of the results of the threshold test with the new resist are shown in figure D.52. Some contamination of the resulting printed structures can be seen in figure D.51H, D.51I, D.51W, D.51Y, D.52A, D.52D, and D.52F. And in some cases the dose was to high which caused some boiling of the resist due to small fluctuations during the printing process which can been observed in figures D.51T, D.52I, D.52O, and D.52X. But overall, between all the images in figures D.51 and D.52 there is little to no difference in polymerization dose over time and between the old and new resist. Therefore, it can be ruled out that the expiration of the resist caused the quality problems of the printed structures. And it can be ruled out that there is a fluctation during the printing process.

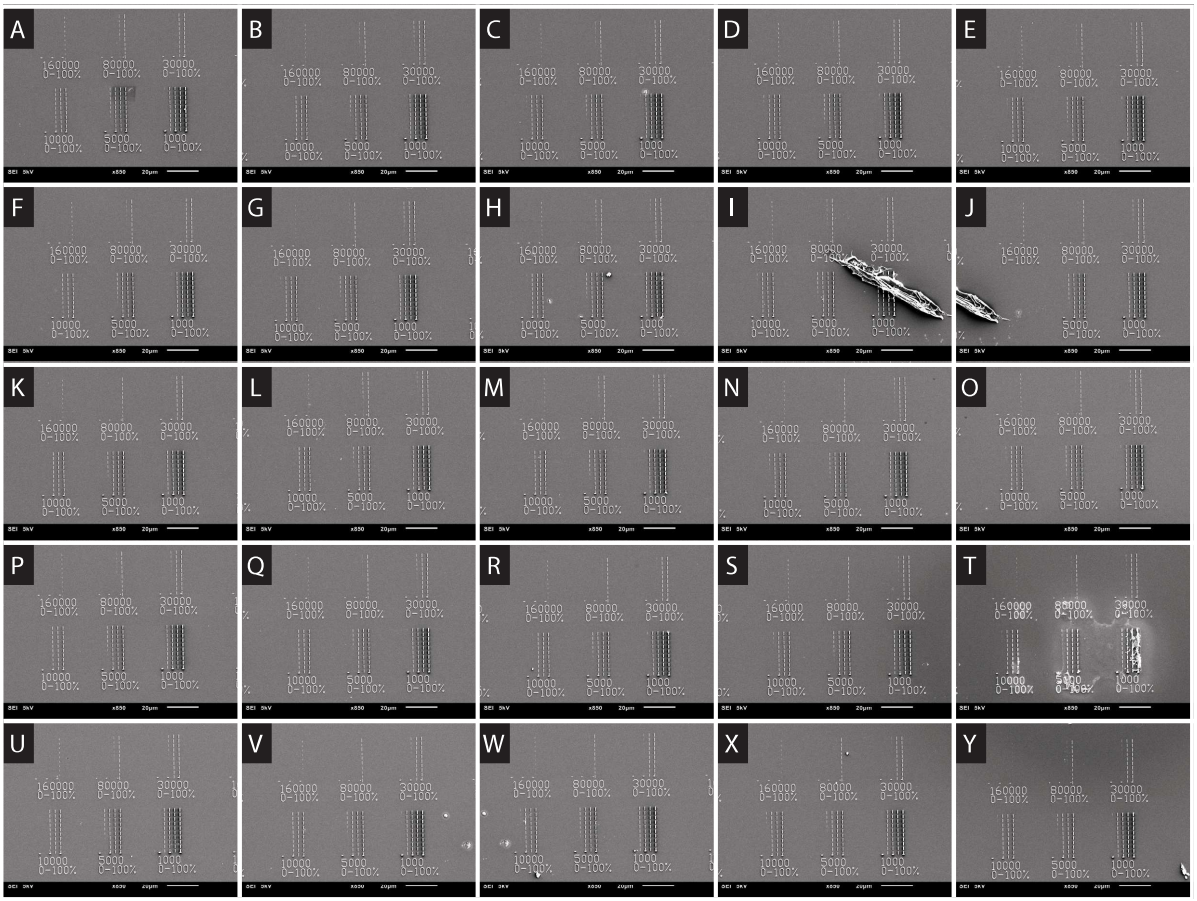

Figure D.51: SEM images of the threshold test performed with the expired resist. Each subfigure (A to Y) contains one threshold experiment which was performed every 10 min.

Figure D.52: SEM images of the threshold test performed with the new resist. Each subfigure (A to Y) contains one threshold experiment which was performed every 10 min.

Imprinting 1mm by 1mm membrane with optimal printing parameters, no PEDOT:PSS layer

The PEDOT:PSS layer was removed while this is a thermosetting polymer. This means that it will not become 'soft' when heated up which is normally one of the requirements to be able to imprint a polymer which such a technique. This layer will introduce a lot of stress on the pillars during the printing which could cause them to transfer from the mold to the substrate. The substrate after imprinting with pillars printed at the redefined optimal laser power and the already defined imprinting protocol is shown in figure D.53. The blue like color of the image was caused by a filter which was placed in the microscope which was not removed by the user. It can be seen that the pillars still transferred from the mold into the substrate. So, it can be concluded that not just the PEDOT:PSS layer caused the transferring of the pillars from the mold to the multilayer substrate.

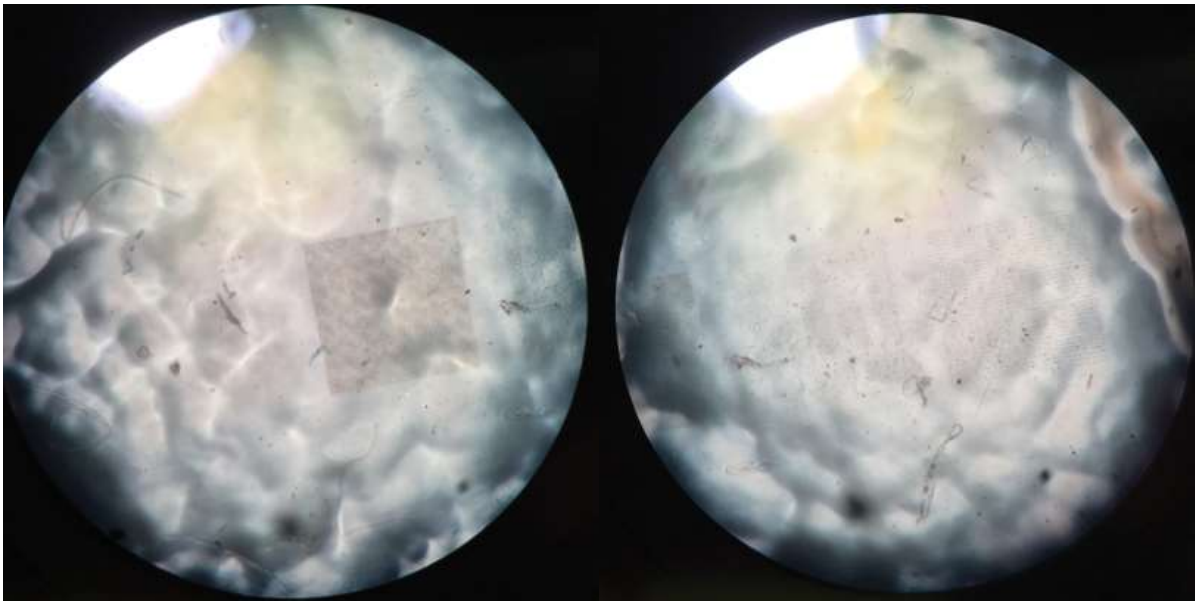

Figure D.53: Multilayer substrate without the PEDOT:PSS layer after imprinting at 120 °C, 4000 N, with a holding time of 10 min with a mold which is printed with the optimal printing parameters with the 25x objective.

Imprinting LP array, no PEDOT:PSS layer

Again, the PEDOT:PSS layer was no part of the imprinted multilayer substrate because it is a thermosetting polymer. But this time the imprinting temperature was increased while this increases the mobilization of the polymer chains.[88] By imprinting rows of pillars printed at different laser power, it can be investigated which laser powers are successful for imprinting. The mold before imprinting, mold after imprinting, and the substrate after imprinting are shown in figure D.54A to D.54C. Looking at figure D.54B, just some pillars with a diameter of 8 µm did not transfer from the mold to the substrate of which most of them are the pillars with a base angle of 40°. Only at a laser power of 20.0 mW, some of the pillars with a diameter of 8 µm, with a base angle of 30°, and one pillar, with a base angle 20°, survived.

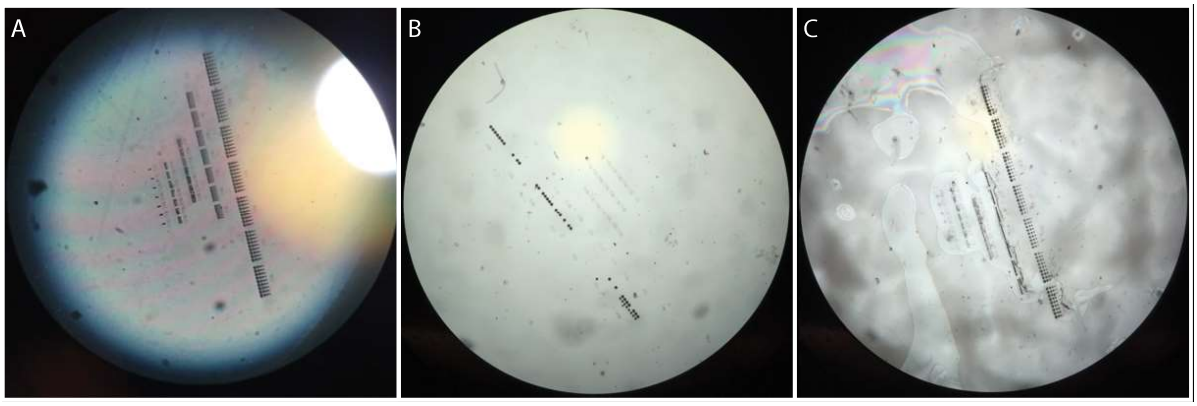

Figure D.54: Results of imprinting at 130 °C, 4000 N, with a holding time of 10 min with a mold which is printed with the 25x objective. A: Mold before imprinting. B: Mold after imprinting. C: Substrate after imprinting and post treatment with EG.

Improve adhession between pillars and glass coverslip by oxygen plasma treatment

The resulting mold printed after an improved cleaning step by oxygen plasma treatment is presented in figure D.55. A lot of pillars are missing or lighter in color. They are lighter in color because they are shorter in height. These fluctuations were caused by the fact that the Photonic Professional GT was not able to find the interface of the glass coverslip successfully anymore.

Figure D.55: Resulting mold when printed with the 25x objective onto an oxygen plasma cleaned glass coverslip.

Imprint two LP & SS matrices

Again, the PEDOT:PSS layer was no part of the imprinted multilayer substrate because it is a thermosetting polymer. And this time, the imprinting temperature was even further increased to 140 °C. The mold before imprinting, mold after imprinting, and the substrate after imprinting are shown in figure D.56A to D.56C. It can be seen that still a lot of pillars transferred from the mold into the multilayer substrate. Looking at figure D.56B, just some pillars with a diameter of 8 µm did not transfer from the mold to the substrate. All of them are the pillars with a base angle of 40°. No real difference can be seen between the pillars printed with a hatching distance of 2 µm and a hatching distance of 0.5 µm. Comparing the results from figure D.56B with figure D.54B it can be concluded that an imprinting temperature of 130 °C is preferred while with this temperature pillars with smaller base angles survived as well.

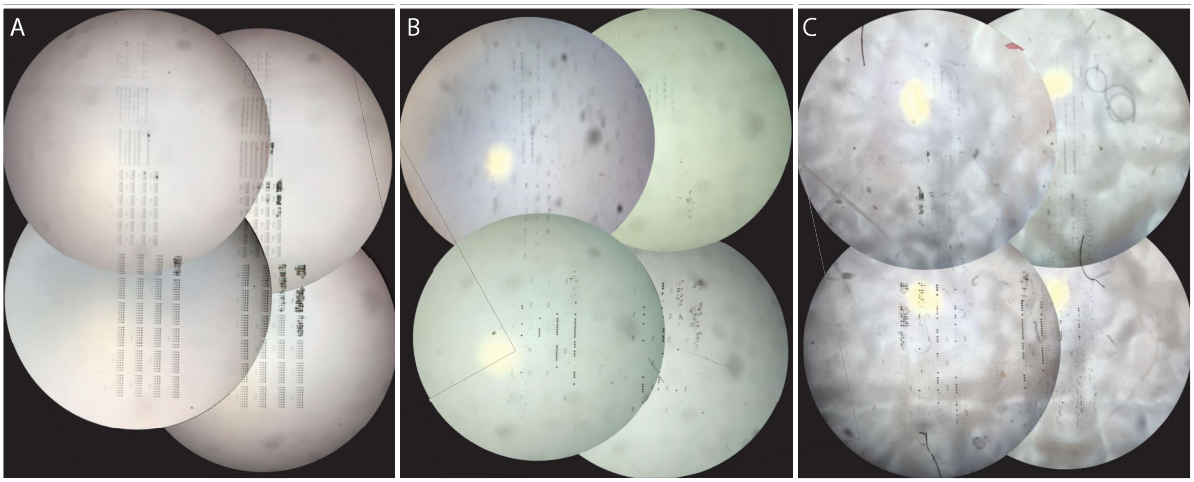

Figure D.56: Results of imprinting at 140 °C, 4000 N, with a holding time of 10 min with a mold which is printed with the 25x objective. A: Mold before imprinting. B: Mold after imprinting. C: Substrate after imprinting and post treatment with EG.

Imprint two LP & SS matrices, reduced imprinting force

This time, the imprinting force was lowered while this previously also resulted in a lower number of transfered pillars from the mold to the substrate (appendix C). The mold before imprinting, mold after imprinting, and the substrate after imprinting are shown in figure D.57A to D.57C. Still, almost all of the pillars transferred, but

a decent number of the pillars with a diameter 8 µm did not transfer. Looking at the mold after imprinting in figure D.57B, 8 µm pillars with a base angle as low as 20° survived. These were part of the best set, which was printed with a hatching distance of 2 µm, a laser power of 17.5 mW, and a scan speed of 10 000 µm s^{-1}. This is not what is expected while an increased laser power, decreased scan speed, and decreased hatching distance should have better adhesion.[114] But most of the pillars with a diameter of 8 µm, hatching distance of 0.5 µm, and a base angle of 40° survived. So, it looks like decreasing the hatching angle did have some positive effect on the adhesion. Comparing the results from figure D.56B with figure D.57B it can be concluded that an imprinting force of 3000 N is preferred while with this force more pillars survived the imprinting process. But this is below the imprinting force which was previously required to puncture the PEDOT:PSS layer, appendix C. But in this experiment the PEDOT:PSS layer was no part of the imprinted multilayer substrate.

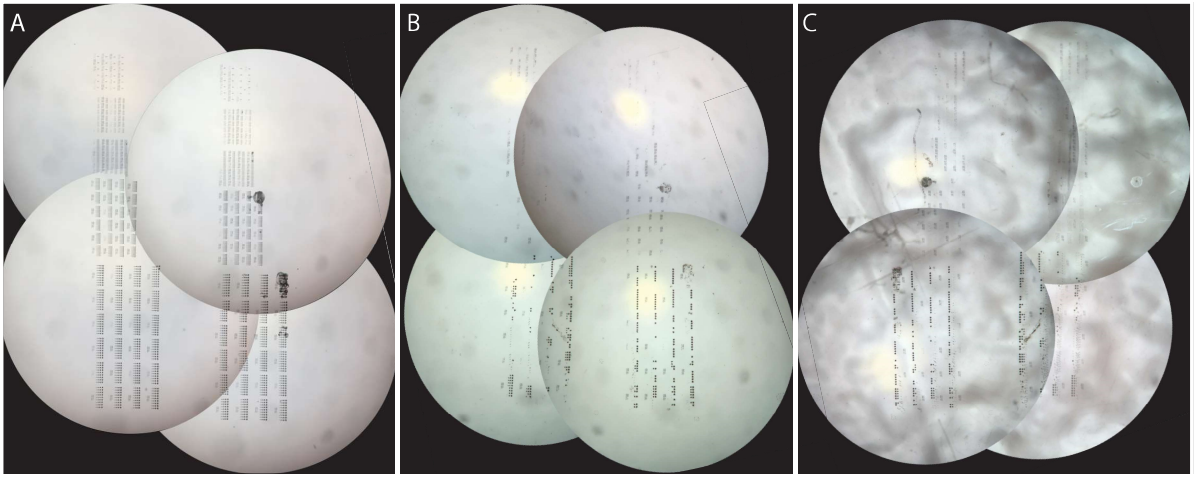

Figure D.57: Results of imprinting at 130 °C, 3000 N, with a holding time of 10 min with a mold which is printed with the 25x objective. A: Mold before imprinting. B: Mold after imprinting. C: Substrate after imprinting and post treatment with EG.

0.5mm/1mm by 0.5mm/1mm membrane with optimal imprinted values

The optimal imprinting temperature, imprinting force, and combination of laser power and scan speed for printing the pillars are used to imprint two membranes of 1 mm by 1 mm and two membranes of 0.5 mm by 0.5 mm. Figure D.58 shows the mold before and after imprinting. It can be seen that around half of the pillars did still transfer.

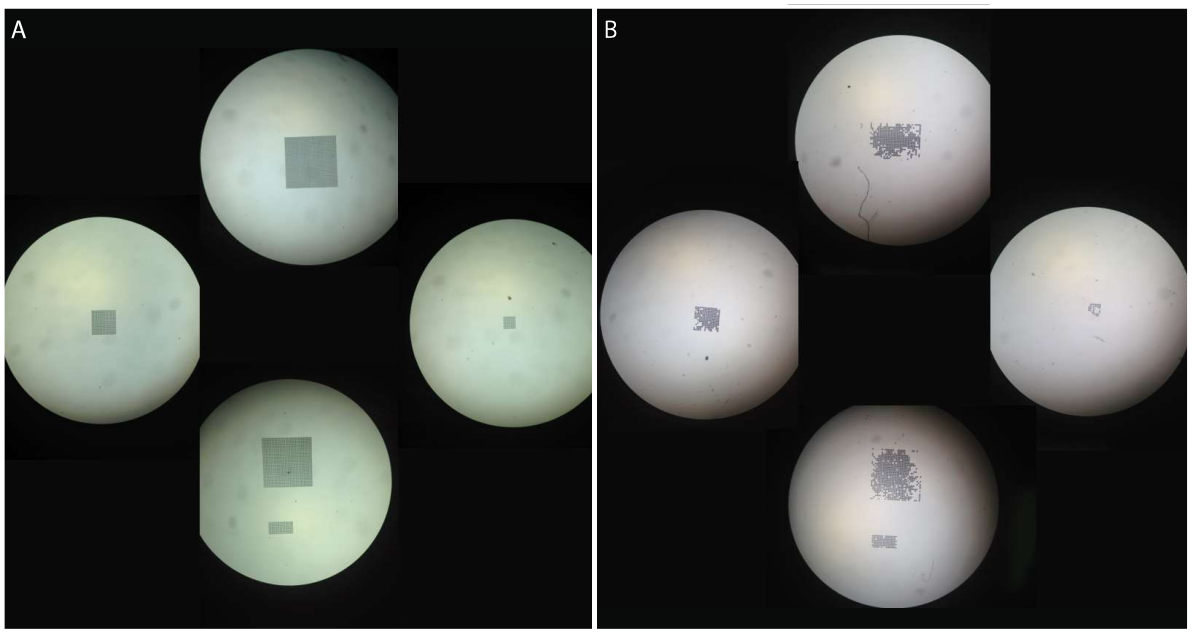

Figure D.58: Results of imprinting at 130 °C, 3000 N, with a holding time of 10 min with a mold which is printed with the 25x objective. A: Mold before imprinting. B: Mold after imprinting.

But dissolving the sacrificial layer did not release the manufactured membranes. They have been peeled off by hand of which the results can been seen in D.59. Only three membranes are shown twice (D.59A and D.59D, D.59B and D.59E, D.59C and D.59F) because the fourth one did not imprint the multilayer substrate. All the manufactured membranes figures D.59A, figures D.59B, and D.59C are stuck the on the support layer while they are nailed down by the pillars which transferred from the mold to the substrate.

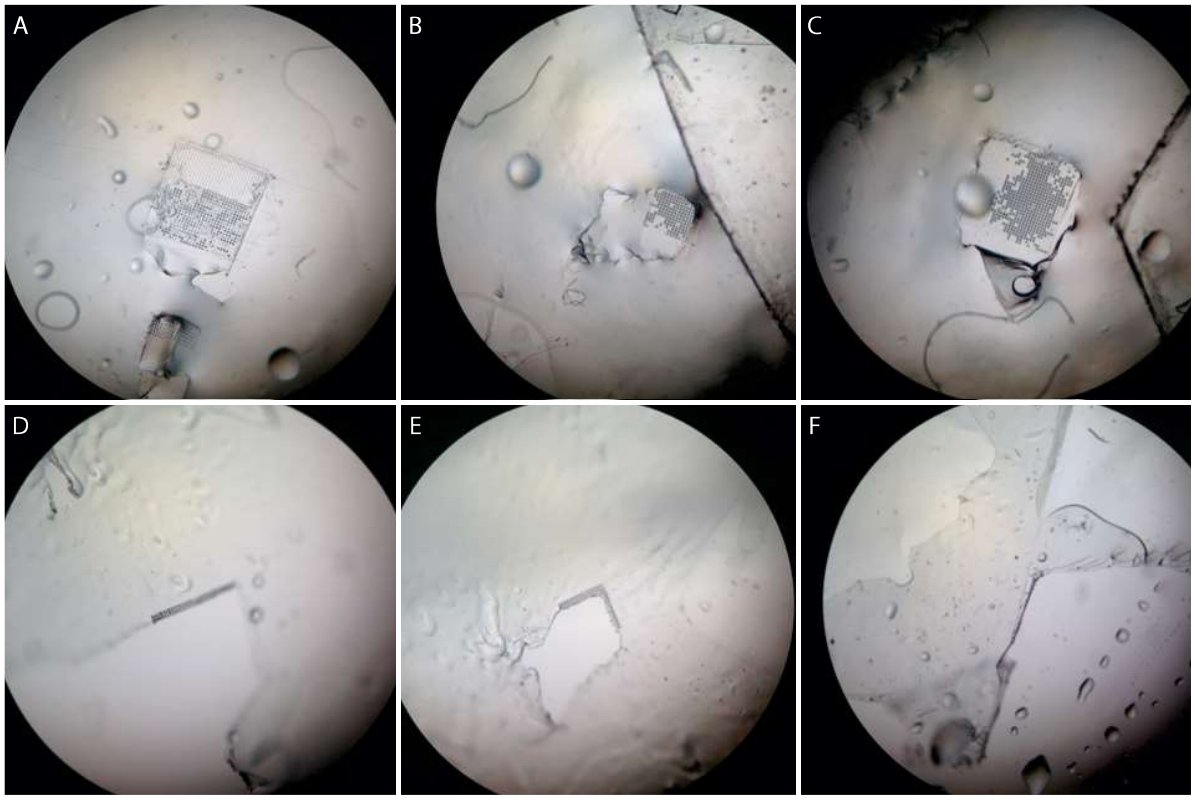

Figure D.59: Results of imprinting a multilayer substrate without the PEDOT:PSS layer after imprinting at 130 °C, 3000 N, with a holding time of 10 min. A-C: The support layer after removing the membrane where it can be seen that the imprinted membranes are stuck to the support layer. D-F: The resulting membrane after removing it from the support layer were it can be seen that the imprinted membranes are missing.

LP & SS matrices with optimal imprinted values, anti stiction layer

To help the pillars to release from the substrate, an anti stiction layer is added and the height of the pillars is decreased. The experiment with the two LP & SS matrices is performed to determine which parameters of the printing process has to be used. The mold before and after imprinting are shown in figure D.60. Still a lot of pillars transferred from the mold to the substrate which can be seen in figure D.60. Mainly, the pillars of 8 µm with a base angle of 40° and a hatching distance of 0.5 µm survived the imprinting process.

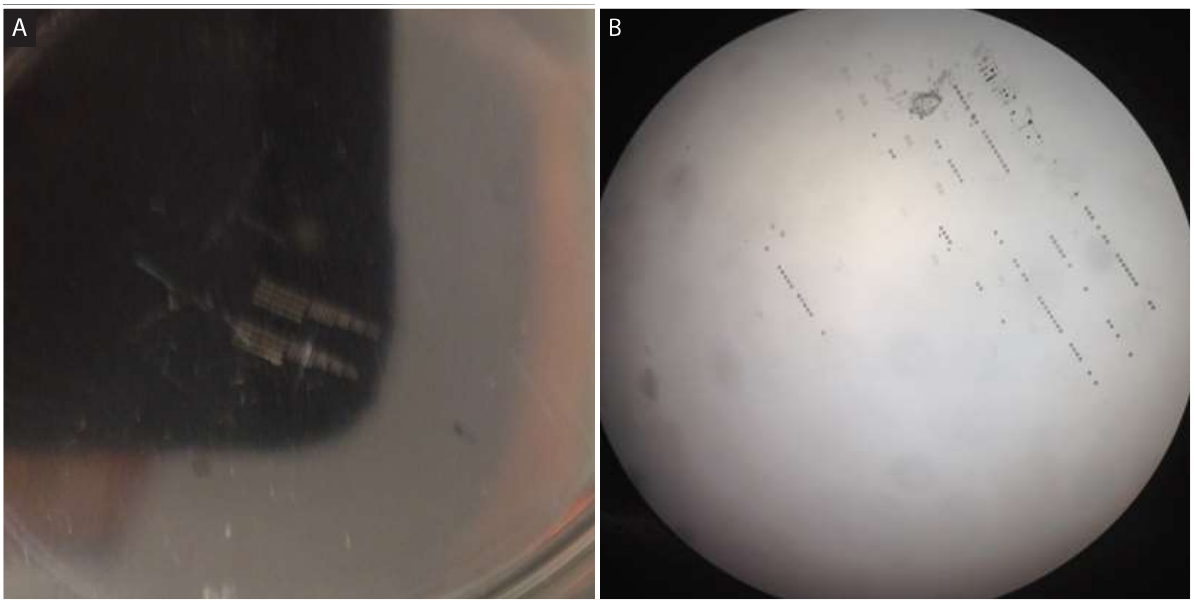

Figure D.60: Results of imprinting a multilayer substrate without PEDOT:PSS at 130 °C, 3000 N, with a holding time of 10 min. A: Mold before imprinting. B: Mold after imprinting.

But it was possible to partly peel off the membrane despite some pillars nailed the membrane to the support layer. The non conductive side of the membrane regarding the imprinting with pillars which have a hatching distance of 0.5 µm was imaged by the SEM, this is presented in figure D.61. The top part regarding the pillars with a diameter of 0.4 µm, 1 µm, and 3 µm did not result in any successful through-holes as shown in figure D.61A. In figure D.61B, the lower part regarding the pillars of 5 µm in diameter and the pillars of 8 µm in diameter are shown. A close up of the part regarding the 5 µm pillars are shown in figure D.61C. As can be seen in this figure, it was possible to manufacture through-holes with pillars of 5 µm in diameter. And in figure D.61B it can be seen that pillars of 8 µm in diameter were able to create through-holes as well.

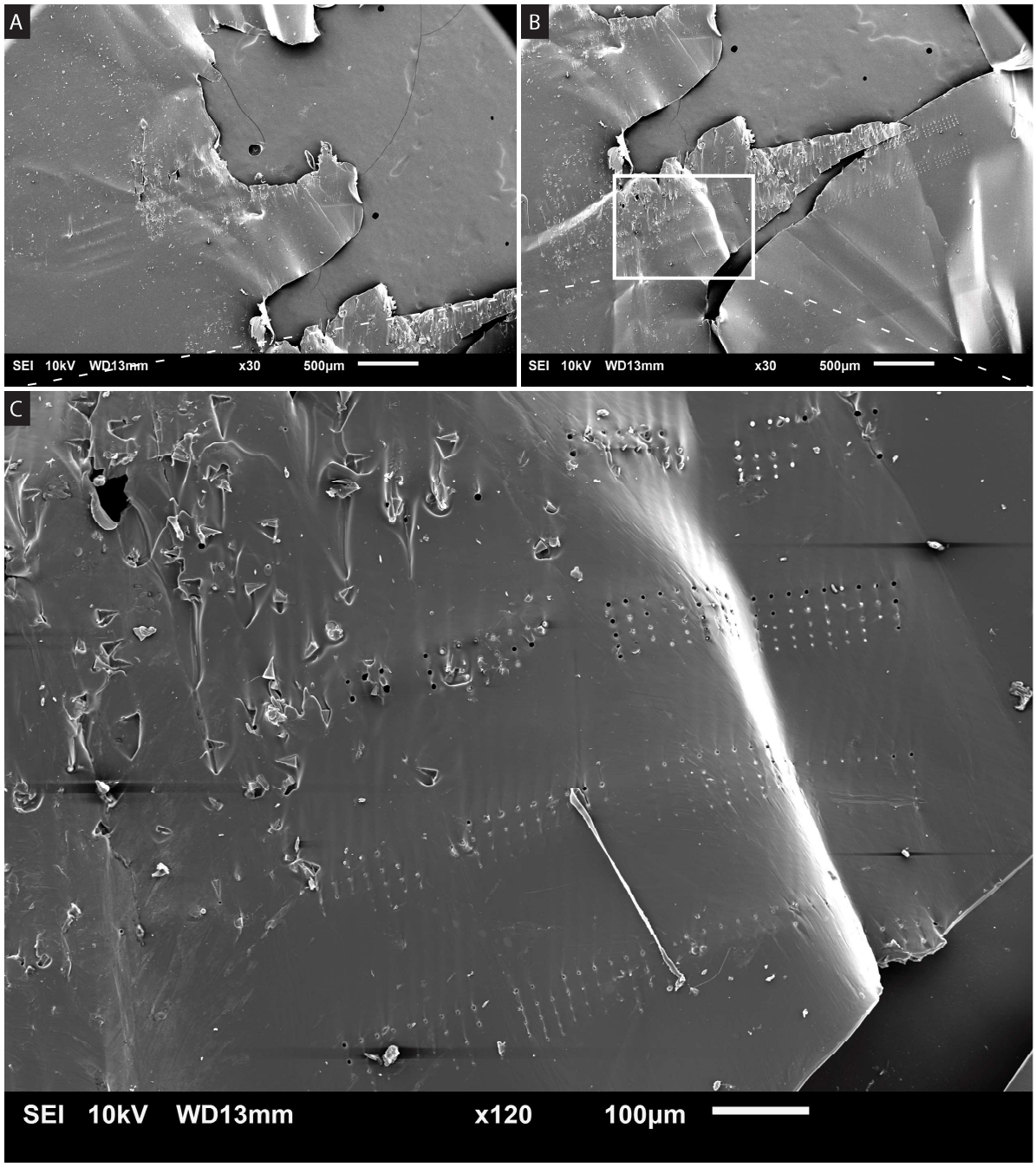

Figure D.61: Results of imprinting a multilayer substrate without the PEDOT:PSS layer after imprinting at 130 °C, 3000 N, with a holding time of 10 min. A: Top part of the LP & SS matrices with a hatching distance of 0.5 µm. B: Bottom part of the LP & SS matrices with a hatching distance of 0.5 µm. C: Close-up of the pillars with a diameter of 5 µm.

LP & SS matrices with optimal imprinted values, anti stiction layer and PEDOT:PSS layer
This time the PEDOT:PSS layer is added to see whether it is possible to manufacture successful through-holes in a bilayer membrane (TOPAS and PEDOT:PSS). The soft mold after imprinting is presented in figure D.62. The resulting through-holes created by the pillars with a hatching distance of 2 µm can be seen in figure D.63. The pillars with a diameter of 5 µm in diameter were able to create through-holes, as shown in figure D.63C. The pillars with a hatching distance of 2 µm were imaged while the part regarding the pillars with a hatching distance of 0.5 µm was destroyed during the peeling off of the membrane. But from the soft mold after imprinting, the best printing parameters are a laser power of 22.5 mW and a scan speed of 10 000 µm s^{-1}. Because the highest number, 7 out of 9, pillars which are 8 µm in diameter, have a base angle of 40°, and a tip angle of 80° survivied the imprinting and demolding process.

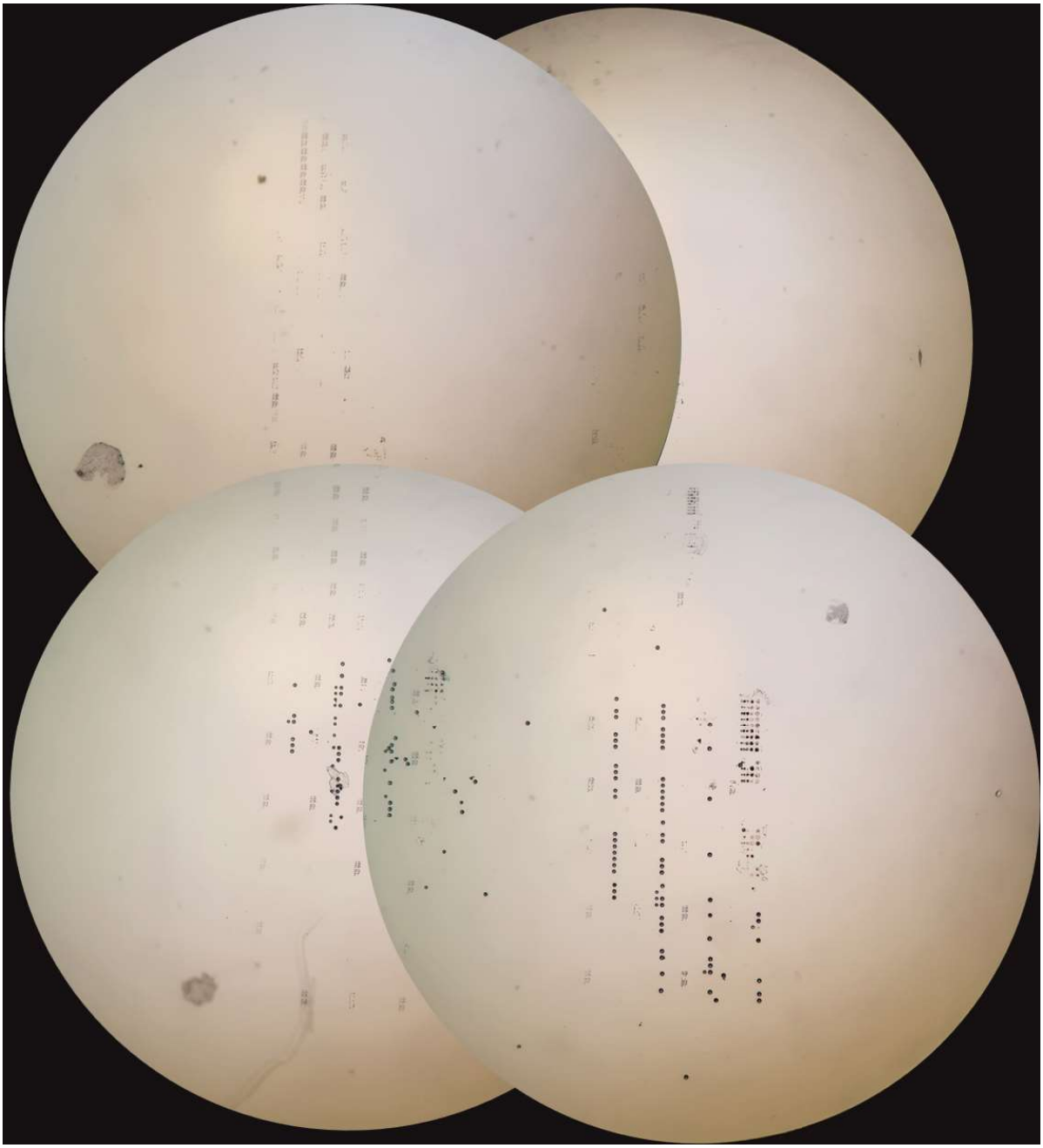

Figure D.62: Soft modl after imprinting a multilayer substrate at 130 °C, 3000 N, with a holding time of 10 min.

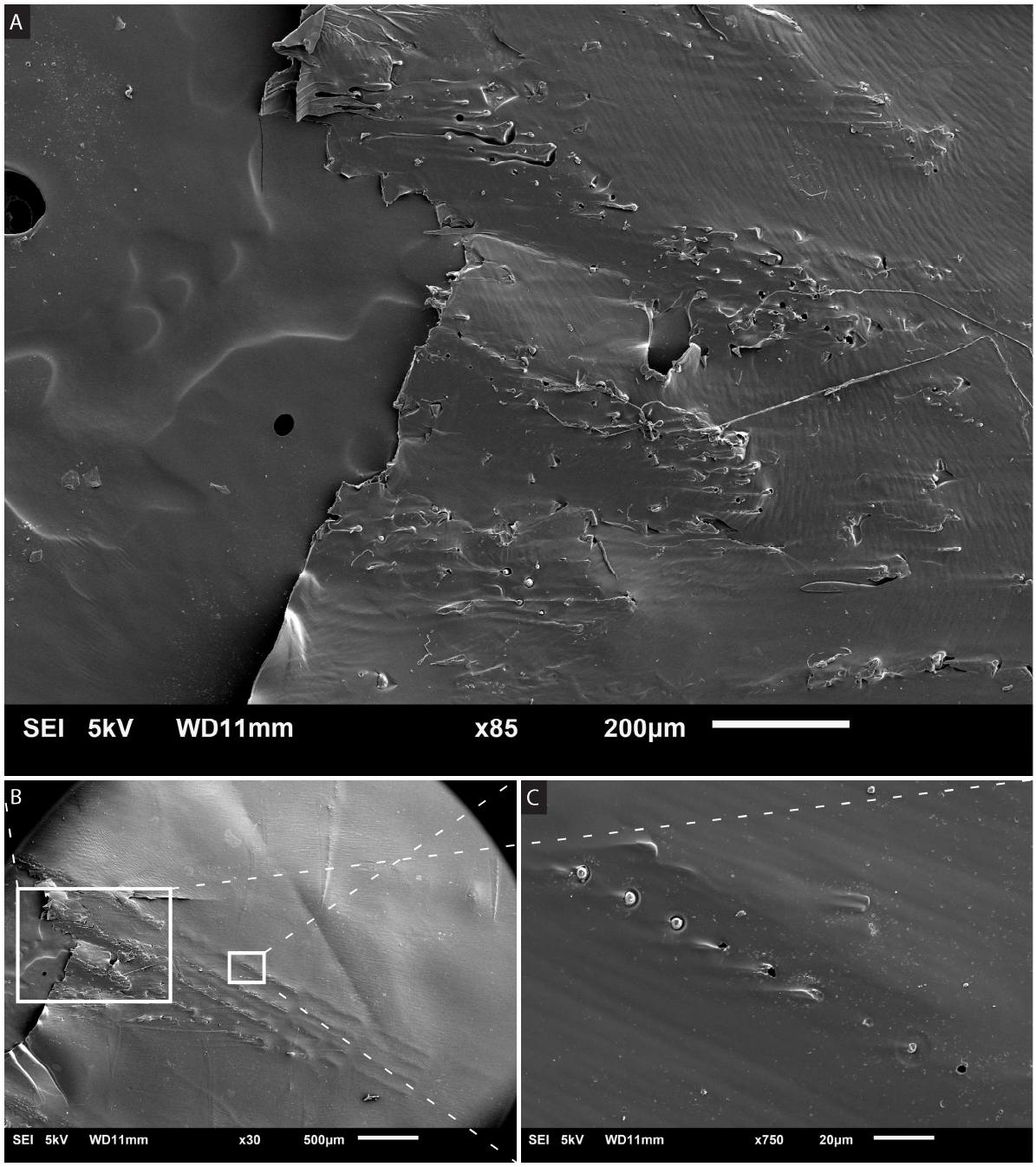

Figure D.63: Results of imprinting a multilayer substrate at 130 °C, 3000 N, with a holding time of 10 min. A: Close up of the 8 µm pores. B: Overview of the top matrices (2 µm hatch distance). C: Close-up of the 5 µm pores.

LP & SS matrices with optimal imprinted values, anti stiction layer and just PAA and TOPAS sheet

Imprinting the sacrificial layer (PAA) and the support layer (TOPAS) will help to understand what happens during the imprinting process and to determine what could cause the problems because the imprinted layer can be dissolved. The mold before imprinting is presented in figure D.64A, the mold after imprinting in figure D.64B, and the substrate after imprinting in figure D.64C. A lot of pillars did transfer from the mold (figure D.64B) to the substrate (figure D.64C). Again, most of the pillars that survived are 8 µm in diameter, have a base angle of 40°, and a hatching distance of 0.5 µm. It can be concluded that the transferring of the pillars is not caused by the PEDOT:PSS-TOPAS layer or just the TOPAS layer. Also, the demolding step is rather easy while the imprinted layer dissolves. Therefore, it is likely that the transferring from the pillars already happens during the imprinting step and is not only caused by the demolding step of the manufacturing process.

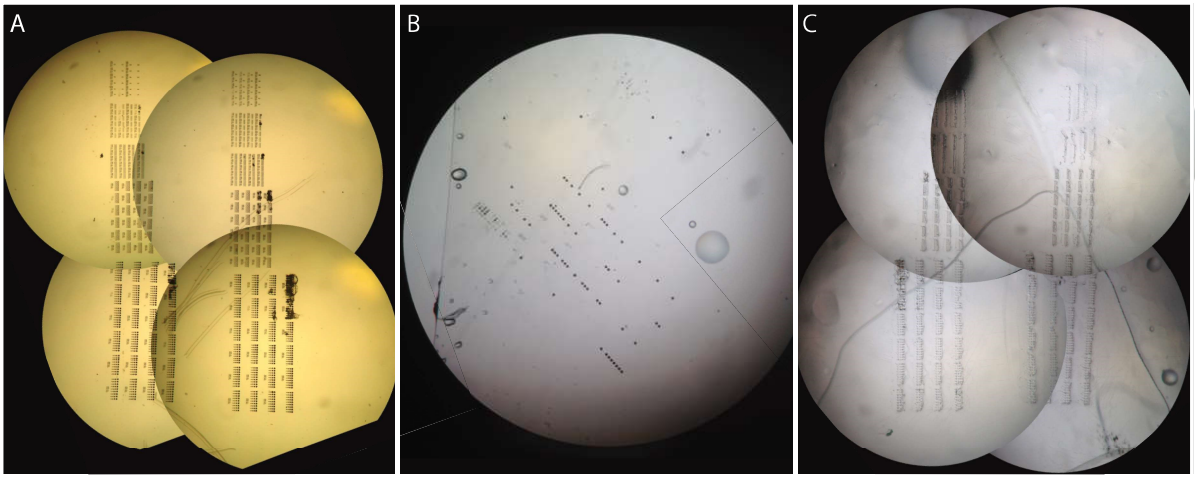

Figure D.64: Results of imprinting a multilayer substrate containing just the sacrificial layer and the support layer at 130 °C, 3000 N, with a holding time of 10 min. A: Mold before imprinting. B: Mold after imprinting. C: Substrate after imprinting and post treatment with EG.

Improve adhession between pillars and glass coverslip by acid cleaning the glass coverslip

The resulting printed structures onto the acid cleaned glass coverslip are shown in figure D.65. Almost all the structures are spread over the coverslip and almost no successful pillars were printed. This was caused while the Nanowrite software was not able to find the correct interface between the glass coverslip and the photoresist successfully. That is why (parts of) the pillars are spread across the glass coverslip instead of being attached to it.

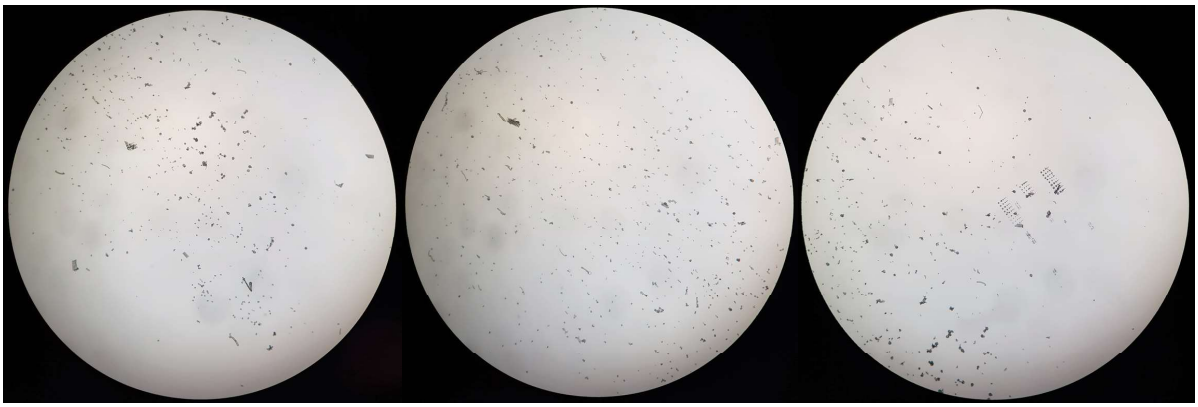

Figure D.65: Resulting mold when printed onto an acid cleaned glass coverslip.

0.5mm/1mm by 0.5mm/1mm membrane with optimal imprinted values

The mold after imprinting is presented in figure D.66A and the substrate after imprint is presented in figure D.66B. Only two out of the four printed fields of pillars resulted in successful imprints. Roughly half of the pillars did still transfer from the mold to the substrate. Therefore, it is investigated whether this can be improved.

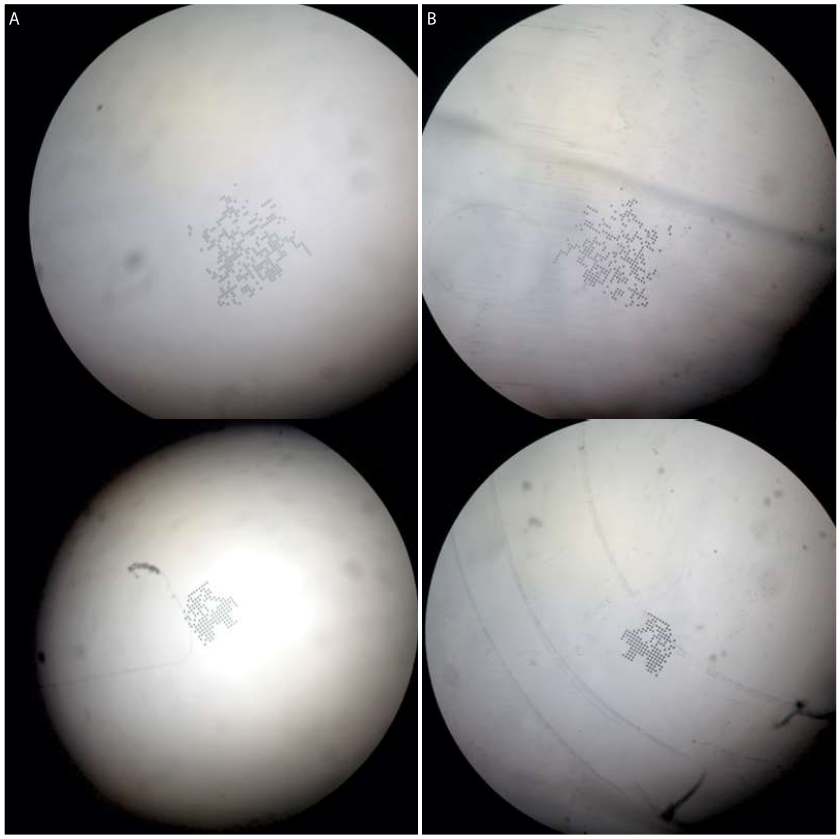

Figure D.66: Results of imprinting a multilayer substrate at 130 °C, 3000 N, with a holding time of 10 min. A: Mold after imprinting. B: Substrate after imprinting and post treatment with EG.

0.5mm/1mm by 0.5mm/1mm membrane with optimal imprinted values, reinforcement layer

The mold is shown in figure D.67A, the mold after sputter coating a 10 nm layer of Au/Pd and spin coating an anti-stiction layer is shown in figure D.67B, the mold after imprinting is shown in figure D.67C, and the multilayer substrate after imprinting is shown in figure D.67D. The mold did not drastically change after applying the Au/Pd layer and the ASL layer as can be seen by comparing figure D.67A with figure D.67B. But a lot of pillars did transfer from the mold to substrate during the imprinting process which can be seen in figure D.67C and figure D.67D. The reinforcement layer probably increased the roughness of the mold which had a more negative effect on the number of transferred pillars than the reinformed layer had a positive effect by increasing the strength of the mold on the number of the transferred pillars when compared to the results in figure D.66B.

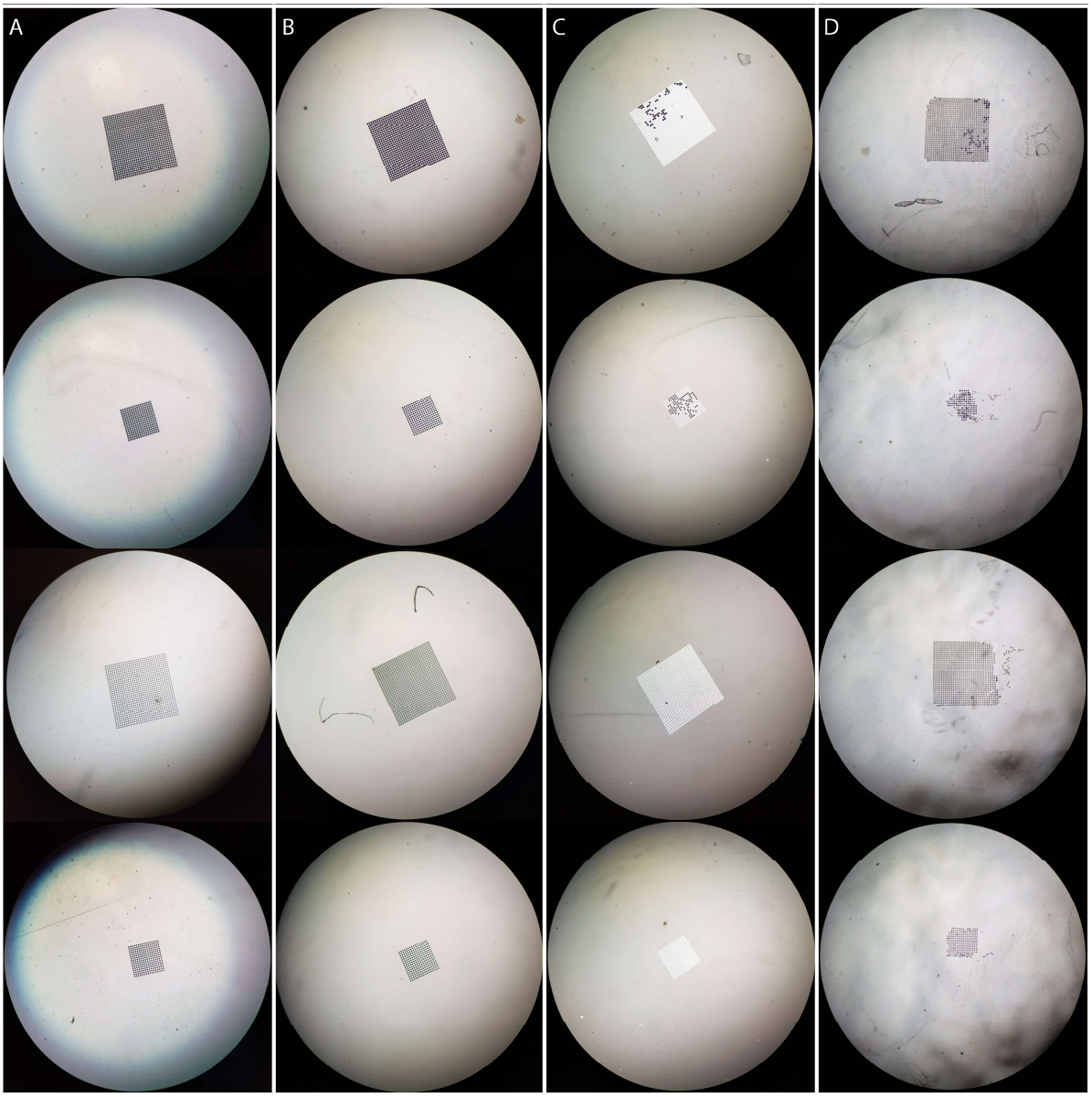

Figure D.67: Results of imprinting a multilayer substrate at 130 °C, 3000 N, with a holding time of 10 min. A: Mold after printing. B: Mold after sputter coating a 10 nm layer of Au/Pd and spin coating a layer of ASL. C: Mold after imprinting. D: Substrate after imprinting and post treatment with EG.

Casting PAA experiment

The resulting PAA layers on top of a TOPAS sheet are shown in figure D.68. Because the aluminum foil was attached so well to the TOPAS sheet it was not possible to remove it without destroying the PAA layer during the process of it. This explains the low quality of the PAA layer in figure D.68A. The PAA layers in figure D.68B and D.68C are both looking uniform. In figure D.68B some wrinkles in the layer can be seen which is probably caused due to the cooling down of the layer.

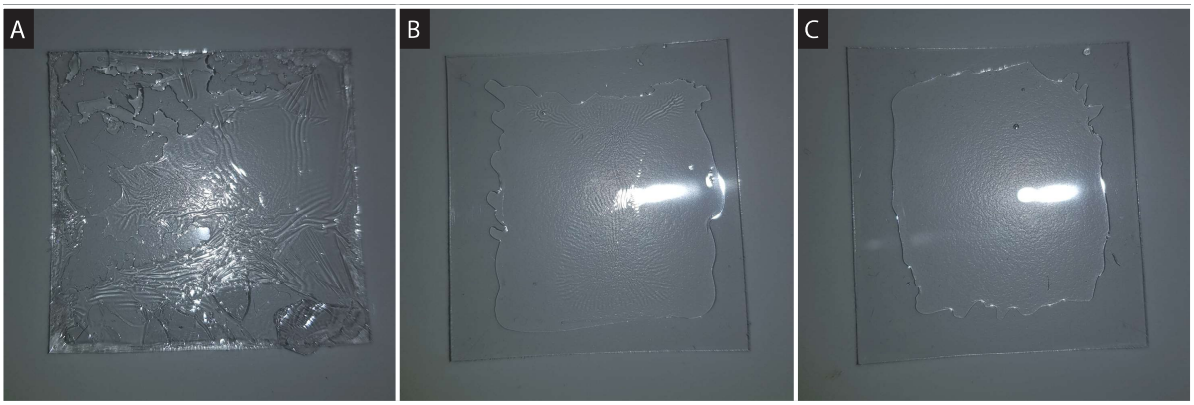

Figure D.68: Results of the second experiment to cast PAA onto a TOPAS sheet. A: Curing at 60 °C for 2 h in the oven and let it cool down at room temperature. B: Curing at 60 °C for 15 min on the hot plate and let it cool down on top of the hotplate which is also cooling down. C: Cure it at room temperature.

0.5mm/1mm by 0.5mm/1mm membrane with optimal imprinted values, EG experiment

The mold before imprinting, mold after imprinting, and the substrate after imprinting are presented in figure D.69A-D.69C. The mold broke during the imprinting process and all the pillars transferred from the mold to the substrate as can be seen in figure D.69B. But the post treatments of the substrate did remove a large number of pillars. These are the membranes which are also used for the paper which can be found in chapter 5, where the membranes are further characterized and discussed.

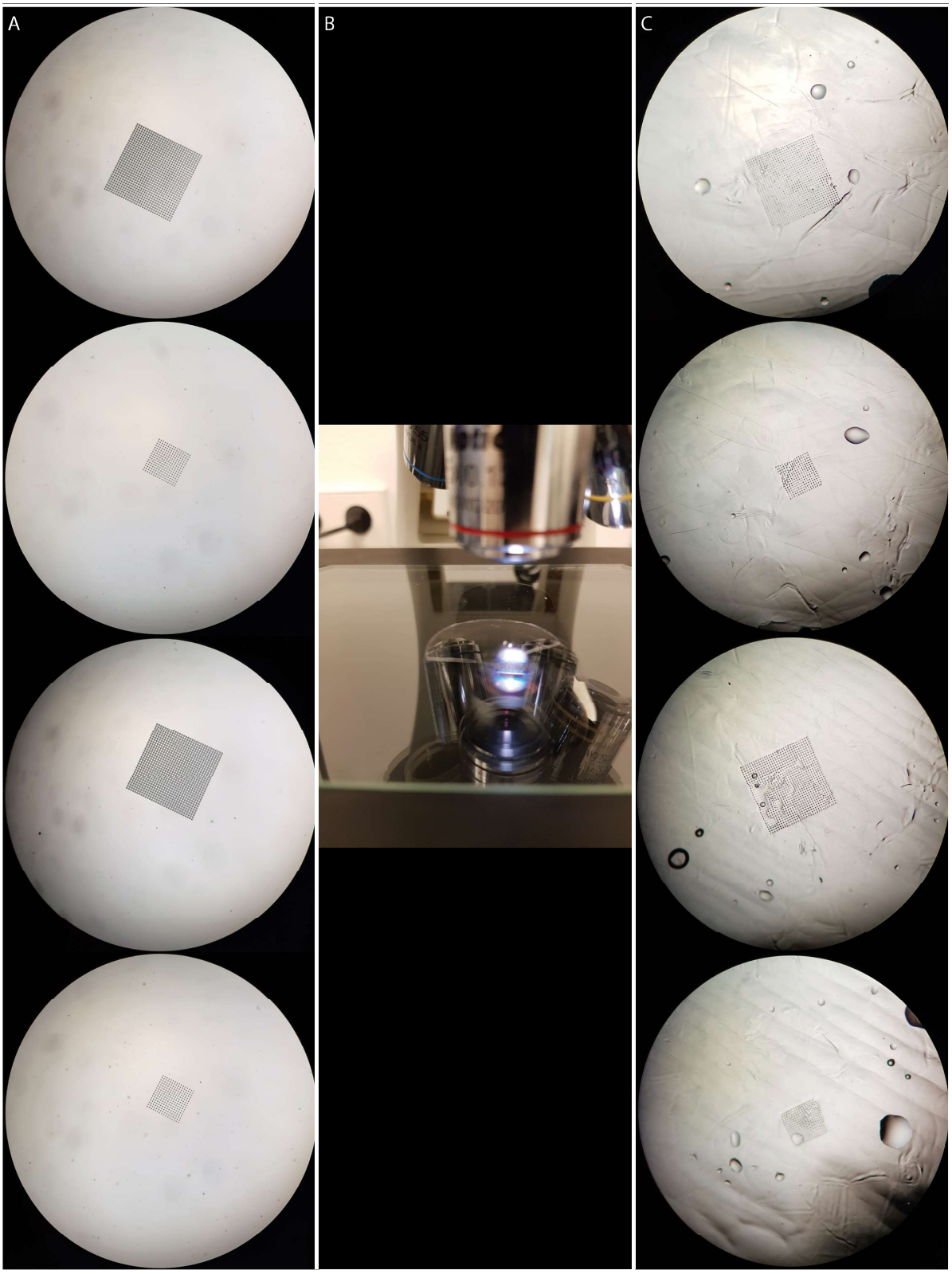

Figure D.69: Results of imprinting a multilayer substrate at 130 °C, 3000 N, with a holding time of 10 min. A: Mold after printing. B: Mold after imprinting. C: Substrate after imprinting and post treatment steps with EG.

0.5mm/1mm by 0.5mm/1mm membrane with optimal imprinted values, increased temperature
The substrate after imprinting and post treatment with EG is presented in figure D.70. There is a low number of transfered pillars.

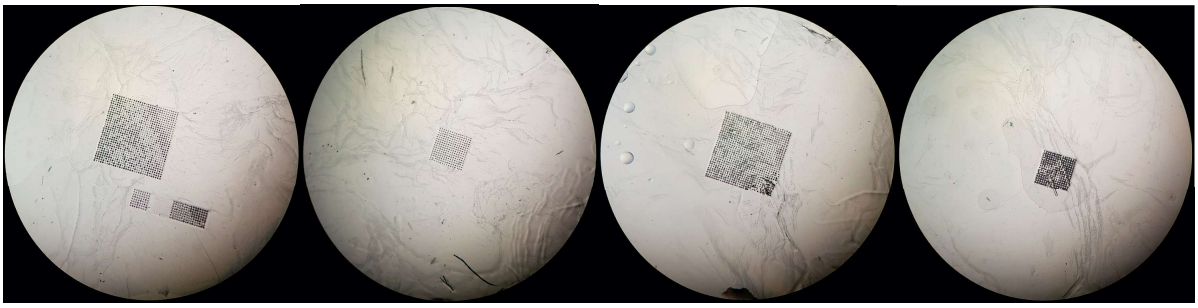

Figure D.70: Multilayer substrate after imprinting at 140 °C, 3000 N, with a holding time of 10 min and after post treatment with EG.

But after imaging the non conductive side of the membrane, no through-holes were created. The overview of the non conductive side of a manufactured 1 mm by 1 mm membrane is presented in figure D.71A and a close up of the same membrane is presented in figure D.71B. The increased imprinting temperature increased the mobility of the polymer which could have as effect that the substrate layer is harder puncture while the substrate layer flows easier around the pillars during the imprinting process.

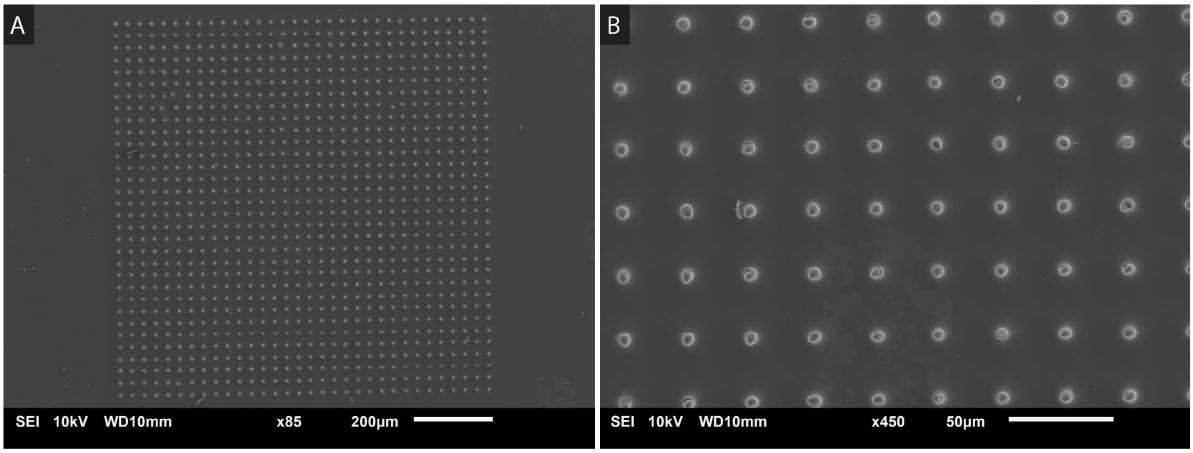

Figure D.71: SEM images of the membrane from the TOPAS side. A: Overview of the non conductive side of the membrane. B: Zoomed in SEM images of the imprinted multilayer substrate with a mold which contains a field of 1 mm by 1 mm pillars of 8 µm in diameter.

Influence of a tip angle of 85°
The mold before imprinting is presented in figure D.72A, the mold after imprinting in figure D.72B, the substrate after imprinting and immersing it overnight in EG in figure D.72C, and the substrate after placing it in EG in the US cleaner for 30 min in figure D.72D. The soft mold was broken during the imprinting step as shown in figure D.72B. This could have happened while there may be a height difference underneath the soft mold during the imprinting process like a small folded part of the Kapton foil. The results in figure D.72C looks promising, but after trying to peel off the membrane from the support layer it ripped. This happened because the pillars nailed the membrane to the substrate even after trying to remove those pillars by placing it in the US cleaner for 30 min. The same parameters are used to manufacture the 1 mm by 1 mm membranes as presented in figure D.69. The reason why it did work for the manufacturing of the membranes and did not work this time has to do with the layout of the soft mold. The soft mold used for this experiment contains all the pillars in the middle. During the imprinting process, before the pillars puncture through the first two layers, they press a flow of the sacrificial layer outward during the imprinting process. And, therefore, the pillars reached the support layer when they finally puncture through the first two layers of the multilayer substrate. In the case of the soft mold of the membranes, they were placed opposite to each other with a space in the middle. During the imprinting, the sacrificial layer starts to flow and is pressed outward and to the middle.

And, when the pillars puncture the conductive layer and the substrate layer, the sacrificial layer is still thick enough thanks to the flow of this layer to the middle.

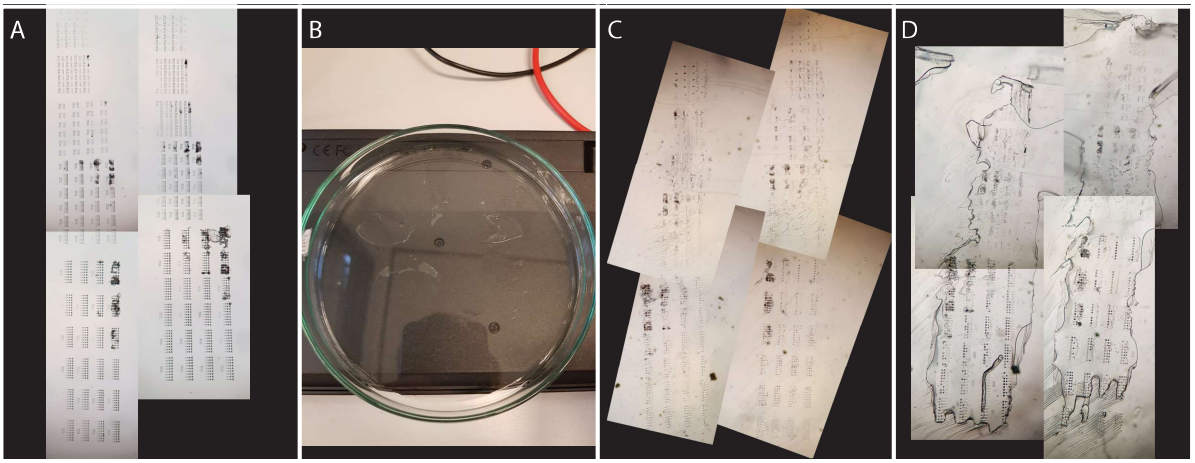

Figure D.72: Results of imprinting a multilayer substrateat 130 °C, 3000 N, with a holding time of 10 min to identify whether a tip angle of 85° improves the number of through-holes and/or improve the smallest through-hole diameter. A: Mold before imprinting. B: Mold after imprinting. C: Substrate after imprinting and immersion in EG overnight. D: Substrate after placing it in EG in the US cleaner for 30 min.

D.4. Conclusions

This appendix started with explaining the shift in the quality of the printed structures by the Photonic Professional GT which looked like less of the material was polymerized. This is depended of the laser power, scan speed, and the effectiveness of the photosensitivity of the photoresist. But all of these are ruled out as the cause of the problem. So, the only option left was to accept the shift in quality and redefine all the protocols to be able to manufacture membranes with an integrated porous electrode again. In the first part of this appendix, optimal values for printing the pillars of different diameters, base angles, tip angles, and different objectives are presented in table D.2 and in table D.3. The maximal laser power which can be used to print pillars, without boiling the resist, with different diameters and base angles is presented in table D.4. It is determined what the minimum required distance is of the pillars with a diameter of 0.4 µm per base angle and the height of the pillar to prevent them from falling over due to the capillary forces during the development of the mold. This is presented in figure D.40. Tuning all these printing parameters did not lead to working protocols. Also, cleaning the glass coverslip with oxygen plasma and chemically was tried as advised by Nanoscribe.[114] But this led to problems with finding the interface were to print the pillars by the Describe software. Therefore, this is not used. Subsequently, the imprinting protocol was redefined, summarized in figure 5.3B. The bending of the pillars and the collapsing of the pillars was solved by increasing the imprinting temperature to 130 °C. Which was also determined to be the optimal imprinting temperature. To lower the number of transfered pillars, the imprinting force had to be lowered from 4000 N to 3000 N. Still a lot of pillars got stuck into the substrate which is not caused by the layer conductive layer nor the substrate layer. It was shown that reducing the height of the pillars from 15 µm to 12.5 µm and adding an ASL layer to the mold decreased the number of transferred pillars. A new problem was observed, the nailing down of the membrane with integrated porous electrode to the support layer. This is partly solved by creating a new protocol to cast a thick layer of PAA on top of the support layer. This prevents the pillars from reaching the support layer and nailing down the membrane to this layer. But it could happen that too much of the sacrificial layer spreads outward during the imprinting process before the pillars puncture the conductive layer and the support layer. When the pillars finally puncture these two layers, the sacrificial layer at that moment is not thick enough anymore to prevent the pillars from reaching the substrate layer. It is tried to increase the adhesion between the printed pillars and the glass coverslip by decreasing the hatching distance which did help. And, it is shown that the US cleaner helps to remove pillars which were transferred from the mold to the multilayer substrate during the imprinting process. This led to the final protocols which were used to manufacture the polymeric membranes with integrated porous electrode with an effective surface area of 1 mm by 1 mm.

From the established protocols, a final manufacturing overview for manufacturing a membrane with integrated porous electrode is created. This overview schematically presented in figure D.73.

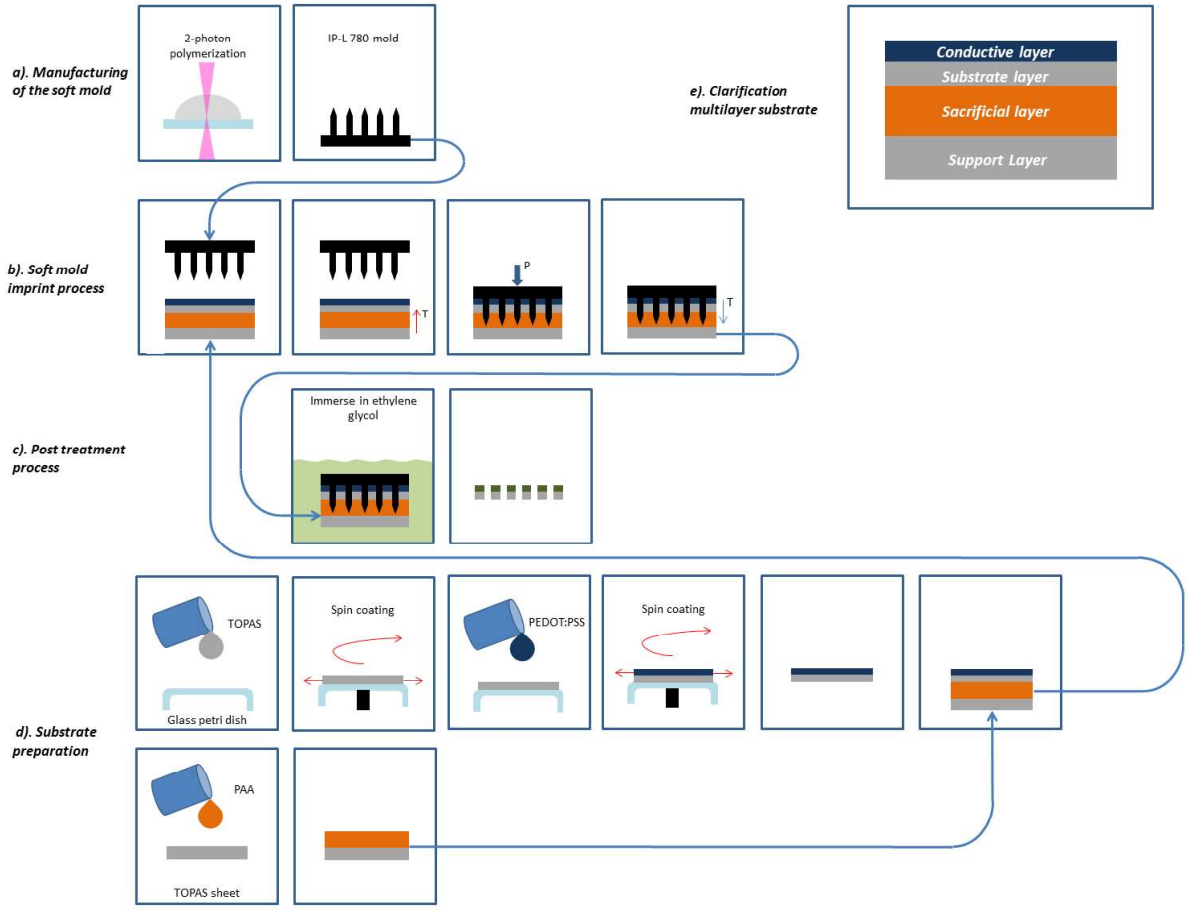

Figure D.73: Schematic overview of the final manufacturing process divided into four steps. A: The soft mold is manufactured with a two-photon polymerization process. D: The substrate consists of four polymeric layers, a conductive layer (PEDOT:PSS), a substrate layer (TOPAS), a sacrificial layers (PAA) and a support layer (TOPAS), which are spin coated (conductive layer and substrate layer) or casted (sacrificial layer) and placed on top of each other. B: The multilayer substrate is imprinted (soft NIL) to create the porous electrode and the through-holes. C: A post treatment step is performed to enhance the conductivity of the conductive layer, to decrease the water solubilty of the conductive layer and to dissolve the sacrificial layer which helps the demolding of the soft mold.

D.4.1. Manufacturing of the soft mold. (Figure C.73a)

A glass coverslip of 30 mm in diameter with a thickness of 0.17 mm +/- 0.01 mm is cleaned with acetone and followed by isopropanol. A drop of immersion oil is placed on the bottom of the coverslip and a drop of IPL-780 is placed on top of it. The coverslip is placed on a holder and placed in the Photonic Professional GT. A STL-file is created with Solidworks and converted into job-files with Describe and printed with the Photonic Professional GT. The minimum distance needed to prevent the pillars of 0.4 µm in diameter from falling over is presented in figure D.40. The optimal parameters for converting the STL files into job files and to the optimal parameters printing the pillars with the 63x objective in table D.2 and writing the pillars with the 25x objective in table D.3. When the print job is finished, the coverslip with the printed structure on top of it is developed for 25 min in PGMEA, followed by 5 min in 2-propanol.

D.4.2. Substrate preparation. (Figure C.73d)

Only the protocol for the manufacturing of the sacrificial layer was changed after the shift in the quality of the printed structures by the Photonic Professional GT. The others one remained the same but are repeated in this conclusion for completeness of the required protocols to manufacture a polymeric membrane with integrated porous electrode.

TOPAS

From the results, the following protocol is created to dissolve TOPAS granules into toluene.

1. Clean bottle with ethanol and let it evaporate for an hour

2. Weigh the correct amount of TOPAS granules
3. Fill the bottle with the correct amount of toluene
4. Add the TOPAS granules
5. Put the bottle in the ultrasonic cleaner for 15 min
6. Put the bottle on an orbital shaker at 2200 RPM for 10 min
7. Repeat last two steps until, when you tilt the bottle, the solution is viscous and fluidic

The final protocol for spin coating the TOPAS film with the desired thickness of 10 µm, will start with a cleaning procedure of the glass Petri dish. The Petri dish is cleaned with ethanol, followed by 2-propanol. The Petri dish is placed in the oven at 150 °C for 15 min to dehydrate. The Petri dish is placed in the fume hood to cool down. 1 mL of the TOPAS solution is spin coated, on the outside of the Petri dish, with a static dispense spin coating technique. The first step of the spin coat protocol has a spin time of 50 s, at 3900 RPM. Subsequently, the sample is spin coated for 30 s at 100 RPM. The acceleration for both steps is 250 RPM/s. The sample is left to dry overnight in the fumehood.

PEDOT:PSS
The final protocol for manufacturing the thin film of PEDOT:PSS is concluded to be as following, a glass Petri dish is treated for 5 min with oxygen plasma at 60 W. Two milliliters of PEDOT:PSS is dynamically dispended on the TOPAS film during the spin coating process. A spin speed of 1500 RPM, a spin coat time is 60 s, and an acceleration of 1000 RPM/s will be used. The sample is left to dry overnight in the fumehood.

PAA
A 100 wv% solution of PAA in DI water prepared by adding the correct amounts into a Falcon tube, and place it on an orbital shaker at 2200 RPM until the PAA is completely dissolved. Around 1 mL is dispensed on top of the TOPAS sheet and dried overnight in the fume hood.

Stacking layers
The two bilayers can be stacked, manually, on top of each other. The previously reported problem with air bubbles getting stuck between the sacrificial layer and the substrate layer is not happening anymore. So, they can just be placed on top of each other by hand.

D.4.3. Soft mold imprint process. (Figure C.73b)
The soft mold nano imprint lithography process is performed with an wafer bonder system. The mold and the multilayer substrate were placed between kapton foil with on top two graphene sheets. The multilayer substrate will be imprinted at 130 °C, at 3000 N and a holding time of 10 min. It was found that the optimal printing parameters which were selected by visually inspecting the pillars and selecting the ones which looked the closest to the designed ones in Solidworks are not necessarily the optimal ones for the imprinting process. The printing parameters which leads to successful through-holes are a laser power 22.5 mW and a scan speed of 10 000 µm s^{-1}. The pillars used are 8 µm in diameter, have a base angle of 40°, and a tip angle of 80°.

D.4.4. Post treatment process. (Figure C.73c)
The multilayer substrate is immersed in ethylene glycol until the sacrificial layer is completely dissolved which helps the demolding of the soft mold from the multilayer substrate. This is also done to increase the conductivity of the PEDOT:PSS layer and to decrease the water solubilty of the PEDOT:PSS layer. The resulting membrane is dried overnight in the fumehood.

E

Matlab code used to characterize the 1 mm by 1 mm membrane

Instead of determing which of the imprinted pores are actual through-holes and measuring all the relevant dimensions by hand, a Matlab algorithm is written to do this automatically. The algorithm generates a table which contains all the relevant morphological characteristic of the membrane. The work performed in this appendix is reflected on the roadmap to success, which is presented in figure E.1.

Figure E.1: Roadmap to success with symbols indicating which experiments are already furfilled and which are performed in this appendix.

E.1. Process flow of the image processing algorithm

A Matlab algorithm is written to characterize the morphology of the 1 mm by 1 mm membrane with integrated porous electrode. The image processing toolbox is used for this. The SEM image presented in figure 5.4D is processed by this algorithm. First, the SEM image was cropped to just the scalebar and just the image of the membrane with Paint version 1703. This is done to reduce the amount of excess information which can only influence the results in negative way. During the cropping, the SEM image which is a TIF file is converted to two PNG files. This process is visualized in figure E.2.

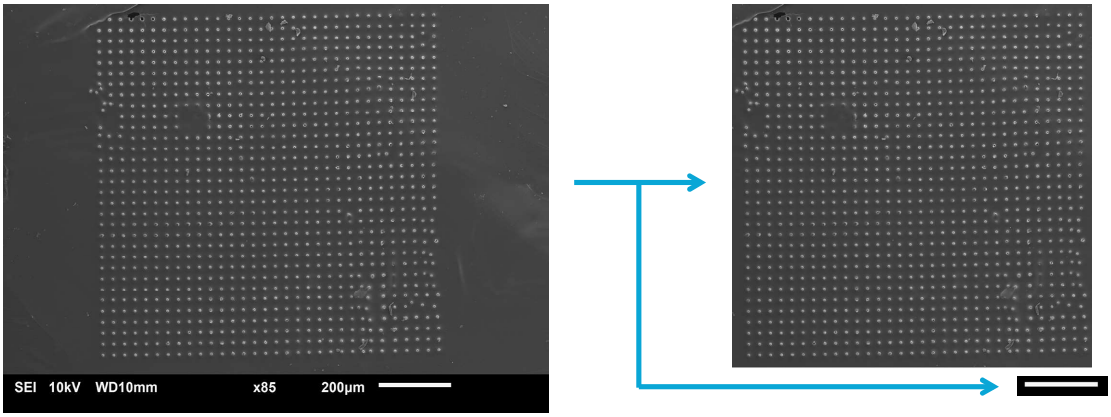

Figure E.2: Overview of the cropping and conversion of one SEM image to an image of just the scalebar and an image of just the nonconductive side of the membrane.

The scalebar was converted into coordinates by a technique called image segmentation. The cropped image of the scalebar is read by Matlab, figure E.3A. The change in contrast, which is calculated by the gradient of this picture with the Prewitt method, is used to detect the scalebar within the image. The result of this step is shown in figure E.3B. Finally, the scalebar is converted into coordinates, figure E.3C, of which the length of the scalebar can be used to determine the dimensions within the image of the membrane itself.

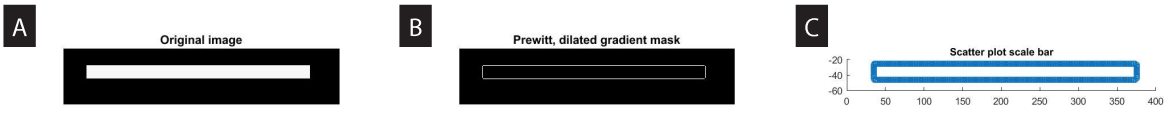

Figure E.3: Process flow of the segmentation of the scalebar. A: Image of the cropped scalebar. B: Image of the dilated gradient mask of the scalebar. C: The scalebar converted into coordinates.

The next step is to process the image of the membrane itself. The cropped version is shown in figure E.4A. A small white block is added manually to the top left corner while there is a small rip in the membrane. When the white block is not added, it causes the algorithm to find multiple incorrect pores within this rip. Looking closer at this image, the membrane is a grey color and the through-holes are black. To help the algorithm to locate the pores, the colors of the image are altered to enhance contrast between pores and not pores. So, there is looked at the RGB values of this image. While it only consists out of black and grey colors, only one of the three values of RGB has to be considered. A histogram of the image is made in which a big peak, at a value of 64, represents a large amount of grey color within the image, figure E.5A. Zooming in on the part which contains the black color, a small peak can be observed as well at a value of 27, figure E.5B. Within the algorithm, a boundary at 45.5 is selected which is in the middle of the two peaks. Everything above this value within the image of figure E.4A is converted into a light grey color at a value 200. And everything below the boundary is converted into a value of 10. This results in the altered image presented in figure E.4B. The black dots within this image are the pores of the membrane. Looking at the histogram of the altered image presented in figures E.5C and E.5D, it can be confirmed that the conversion was successful. Matlab is used to find the location and diameter of each of the black dots by using the imfindcircles function. This algorithm is based on circular Hough transform.[116] The altered image shown in figure E.4B improved the number

of correctly found pores drastically. The found circles are presented in figure E.4C. Overlapping circles are removed from the data while these are two circles in one pore. Subsequently, Delaunay triangulation is used to find all the closest neighbors of each pore.[117] These are indicated by the blue lines in figure E.4D.

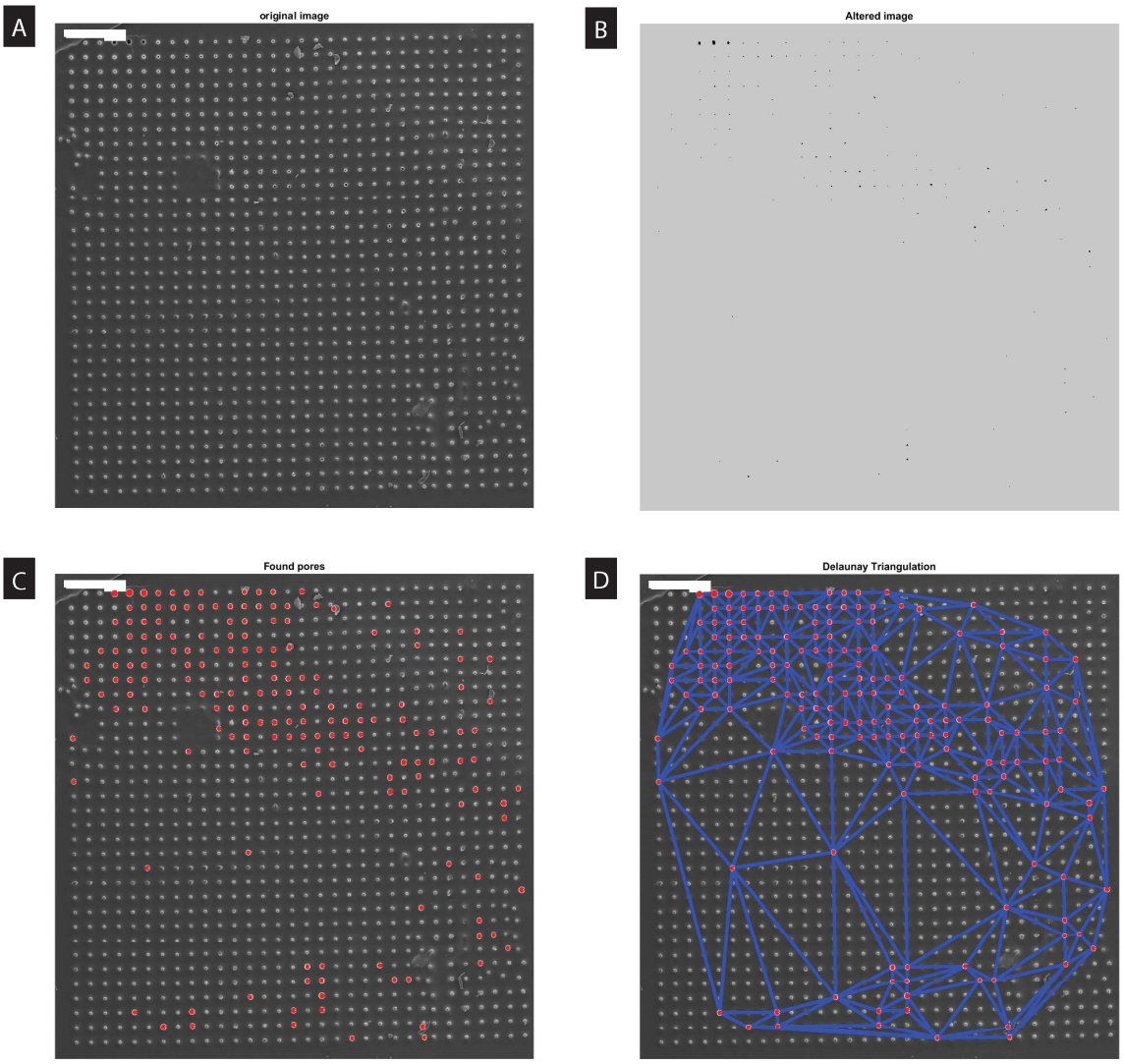

Figure E.4: Process flow of locating of the pores. A: Image of the cropped membrane with a small with block to prevent the alggorithm to find incorrect pores in the rip. B: Converted image to just a light grey color and a black color which indicates the through-holes. C: Visualization of the found pores by the imfindcircles function. D: Visualization of the created Delaunay triangulation to locate the neighbours of each pore.

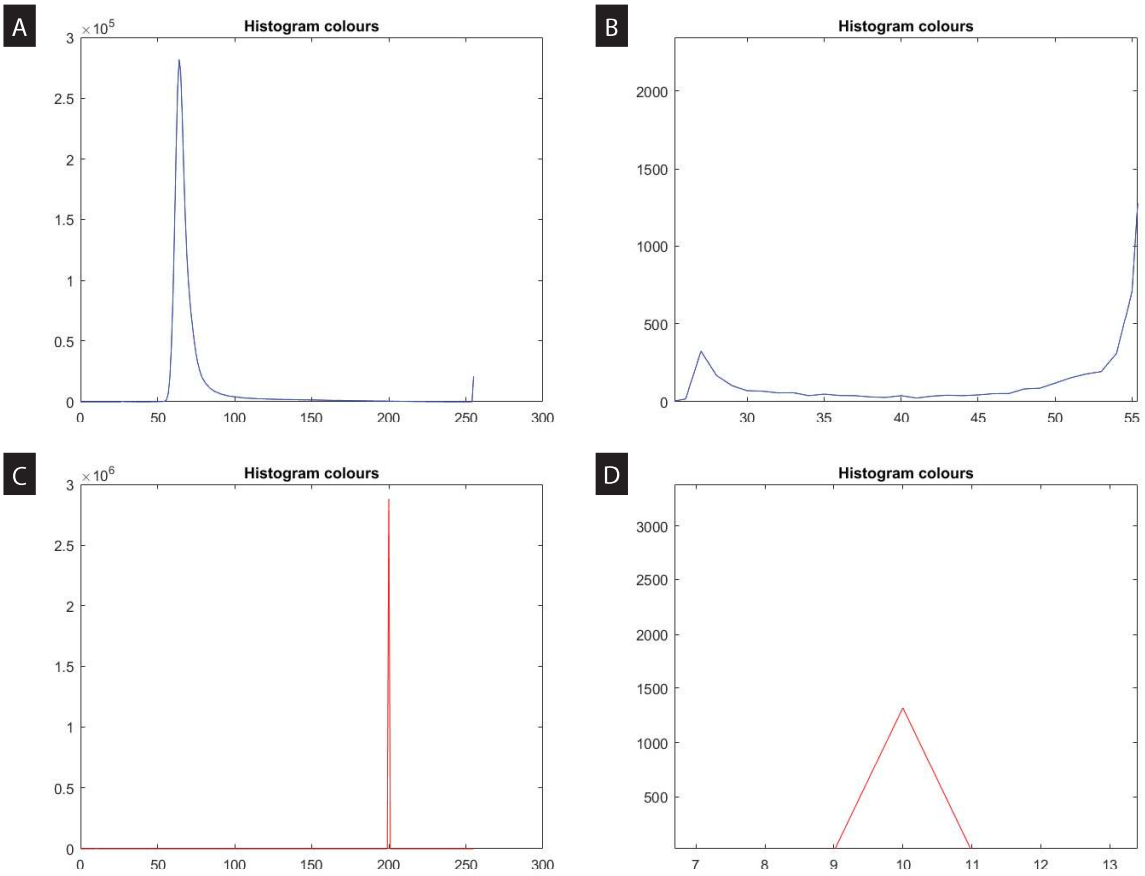

Figure E.5: Histograms of the RGB color values of the figures E.4A and E.4B. A: Histogram of the RGB color values of figure E.4A. B: Zoomed in part of the histrogram of figure E.4A. C: Histogram of the RGB color values of figure E.4B. D: Zoomed in part of the histrogram of figure E.4B.

There was aimed to manufacture a membrane of 1 mm by 1 mm. This surface area is added in the Matlab code as a constant. Combining this with the information required by analyzing the scalebar, the imfindcircles function of the membrane, and the Delaunay triangulation of the found circles, the membrane can finally be characterized. The scalebar provides the information needed to convert all the length related values to the actual lengths. The imfindcircles function found the number of pores and their diameter. This information is used to calculate the mean pore diameter, the smallest pore diameter, the largest pore diameter, the standard deviation of the pore diameter, the pore density, and the porosity. The Delaunay triangulation is used to measure the mean center to center distance of the pores and the standard deviation of the center to center distance. This is all done by the Matlab algorithm which produces a table containing all the relevant values, as shown in figure E.6.

	SEM image
Area [um^2]	1000000
Mean pore diameter [um]	2.7411
Min pore diameter [um]	2.3529
Max pore diameter [um]	6.6348
Standard deviation of the pore diameter [um]	0.5499
Number of pores	173
Pore density [pores/um^2]	1.7300e-04
Pore density [pores/cm^2]	17300
Porosity [%]	0.1062
Mean center to center distance [um]	70.8262
Standard deviation of the center to center [um]	51.9844

Figure E.6: Table generated by Matlab with parameters determined the characterization of SEM image of the 1 mm by 1 mm membrane.

E.2. Matlab Code of the image processing algorithm

```
clear all
close all
clc

%% Determine the length of the scalebar
% Load image
img_scalebar = imread('1mm_membrane_scalebar_200um.png');

% Display image in figure
figure, imshow(img_scalebar), title('Original image');

% Detect scalebar
[~, threshold] = edge(img_scalebar(:,:,1), 'prewitt');
BWs = edge(img_scalebar(:,:,1),'prewitt', threshold);

% Dilate image
se90 = strel('line', 1, 90);
se0 = strel('line', 1, 0);
BWsdil = imdilate(BWs, [se90 se0]);
figure, imshow(BWsdil), title('Prewitt, dilated gradient mask');

% Finding locations of the white dots
k = find(BWsdil==1);
lengthimage = size(img_scalebar(:,:,1));

for i = 1:length(k)
    number = k(i);
    location(i,1) = floor(number/lengthimage(1));
    while number > lengthimage(1)
      number = number -lengthimage(1);
    end
    location(i,2) = (-1)*number;

end

% Calculating factor to convert the distances in actual lengths
length_factor = (max(location(:,1))-min(location(:,1)))/200;
```

```
38
39 % Scatter plot of the scalebar
40 figure
41 scatter(location(:,1),location(:,2));
42 daspect([1 1 1])
43 title('Scatter plot scale bar')
44
45 %% Loading and filtering image
46 % Load image
47 img = imread('1mm_membrane_alt.png');
48
49 % Display image in figure
50 figure, imshow(img), title('original image');
51
52 % Split into RGB Channels
53 image = img;
54 Red = image(:,:,1);
55 Green = image(:,:,2);
56 Blue = image(:,:,3);
57
58 % Get histValues for each channel
59 [yRed, x] = imhist(Red);
60
61 % Plot the histValues together in one plot
62 figure
63 plot(x, yRed, 'Red');
64 title('Histogram colour of the original image');
65
66 % Alter the image from all black and grey colors to one black color and one
67 % grey color
68 for i = 1:length(img(:,1,1))
69
70     for j = 1:length(img(1,:,1))
71
72         if img(i,j,1) <= 45
73
74             img_alt(i,j,1) = 10;
75
76         else
77
78             img_alt(i,j,1) = 200;
79         end
80
81     end
82
83 end
84
85 img_alt = uint8(img_alt);
86
87 % Display altered image in figure
88 figure, imshow(img_alt), title('Altered image');
89
90 % Split into RGB Channels
91 Red = img_alt(:,:,1);
92
93 % Get histValues for the red values
```

```
94  [yRed, x] = imhist(Red);
95
96  % Plot of the histValues of the altered image
97  figure
98  plot(x, yRed, 'Red');
99  title('Histogram colour of the altered image');
100
101 %% Finding the circles, centers and radii
102 % Locating circles with the imfindcircles function
103 [centers, radii, metric] = imfindcircles(img_alt,[2 10],'ObjectPolarity','dark','
        Sensitivity',1,'EdgeThreshold',0.15);
104
105 % Remove overlapping circles
106 [centers,radii]=RemoveOverLap(centers,radii,1,2);
107
108 % Display found circles in figure
109 figure, imshow(img), title('Found Pores');
110 h = viscircles(centers,radii,'LineWidth',4);
111
112 % Performing the Delaunay triangulation
113 TRI = delaunayTriangulation(centers(:,1),centers(:,2));
114
115 % Display found circles in figure
116 figure, imshow(img), title('Delaunay Triangulation');
117 hold on
118 triplot(TRI,'LineWidth',4);
119 h = viscircles(centers,radii,'LineWidth',4);
120
121 % Determine mean center to center distance
122 figure
123 hold on
124 for i = 1:length(TRI.ConnectivityList(:,1))
125
126     X = TRI.Points(:,1);
127     Y = TRI.Points(:,2);
128
129     TRI_X(i,:) = [X(TRI.ConnectivityList(i,1)) X(TRI.ConnectivityList(i,2)) X(TRI.
            ConnectivityList(i,3)) X(TRI.ConnectivityList(i,1))];
130     TRI_Y(i,:) = [Y(TRI.ConnectivityList(i,1)) Y(TRI.ConnectivityList(i,2)) Y(TRI.
            ConnectivityList(i,3)) Y(TRI.ConnectivityList(i,1))];
131
132     plot(TRI_X(i,:),TRI_Y(i,:),'r--')
133
134     x = TRI_X(i,:);
135     y = TRI_Y(i,:);
136
137 dist(i) = (sum(sqrt(diff(x).^2+diff(y).^2))/length_factor)/3;
138 end
139
140 %% Characterizing the membrane
141 % Radii [um]
142 radii_um = radii/length_factor;
143 min_radii_um = min(radii_um*2);
144 max_radii_um = max(radii_um*2);
145 median_pore_um = mean(radii_um*2);
146 std_radii_um = std(radii_um*2);
```

```
147
148 % Number of pores
149 number_pores = length(radii);
150
151 % Area of the pores [um^2]
152 A_um = 1000000;
153
154 % Porosity [%]
155 A_pores_um = sum(pi*radii_um.^2);
156 porosity = (A_pores_um/A_um)*100;
157
158 % Pore density [pores/um^2]
159 pore_density_um2 = number_pores/A_um;
160 pore_density_cm2 = pore_density_um2*10^8;
161
162 % Center to center spacing [um]
163 dist_ave=sum(dist)/length(dist);
164 dist_std = std(dist);
165
166 % Generating the table
167 figure
168 T = table([A_um;median_pore_um;min_radii_um;max_radii_um;std_radii_um;number_pores;
      pore_density_um2;pore_density_cm2;porosity;dist_ave;dist_std],'RowNames',{'Area [
      um^2]';'Mean pore diameter [um]';'Min pore diameter [um]';'Max pore diameter [um]
      ';'Standard deviation of the pore diameter [um]';'Number of pores';'Pore density
      [pores/um^2]';'Pore density [pores/cm^2]';'Porosity [%]';'Mean center to center
      distance [um]';'Standard deviation of the center to center [um]'});
169 uitable('ColumnWidth',{64 400},'Data',T{:,:},'ColumnName','SEM image','RowName',T.
      Properties.RowNames,'Units', 'Normalized', 'Position',[0, 0, 1, 1]);
```

F

Permeability experiment

F.1. Introduction

A novel permeability experiment is designed and executed to verify the fluidic functionality of the polymeric membrane with integrated porous electrode. The work performed in this appendix is reflected on the roadmap to success, which is presented in figure F.1.

Figure F.1: Roadmap to success with symbols indicating which experiments are already furfilled and which are performed in this appendix.

F.2. Materials and methods

A manufactured membrane, with integrated porous electrode, with an effective surface area of 1 mm by 1 mm is attached to a holder which is 24 mm in diameter, as shown in figure F.2A. The membrane was attached

between two pieces of double sided tape with a small square cut into it. The microscopic image of the membrane between the double sided tape is presented in figure F.2B. The holder was supported above a balance (Scaltec SBC33) to the outside world which can be seen in figure F.2C. 5 mL of acetone was placed in the holder. The total weight of acetone which went through the pores of the membrane and fell onto the scale is written down every 10 s for 100 s.

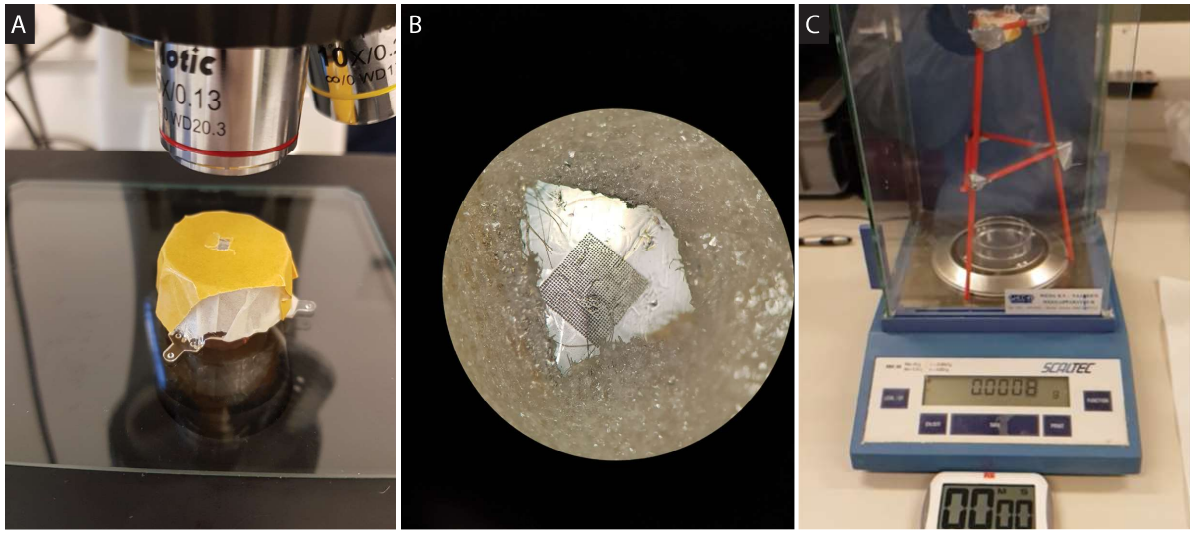

Figure F.2: Images of the experimental set up. A: Image of the holder with the membrane attached to it by double sided tape. B: Microscopic image of the membrane between the double sided tape. C: Overview of the set up placed above the scale.

F.3. Results and discussion

The manufactured membrane is presented in figure F.3. Normally, the non conductive side of the membrane would be characterized by the matlab code, which is shown in figure F.3D. Looking at a close up of the non-conductive side of the membrane, figure F.3E, small rips can be seen around the pillars which got stuck. This will cause the developed algorithm to find multiple small pores. Therefore, the conductive side of the membrane is characterized, presented in figure F.3B.

A total of 13 through-holes were found by the Matlab code of the 1024 pillars. This results in a pore density of 1.3×10^5 pores/cm^2 and a 1.3% success rate to manufacture through-holes of the intended pores. The resulting mean pore diameter is 4.61 µm (standard deviation = 0.93 µm, smallest pore diameter = 3.32 µm, largest pore diameter = 6.33 µm), the porosity is 0.02%, the mean center to center distance of the pores is 328.48 µm, and the standard deviation of the center to center distance is 197.24 µm.

The theoretical mass flow rate is calculated by determining the Poisseuille flow through one pore and including the hydrodynamic interactions between the pores, the distribution of the pores, wall slip, and inertial effects. All under the assumption of identical circular pores, incompressibility and low Reynolds numbers

$$\frac{\Delta p}{q} = \frac{3\mu}{a^3}[1 - G(\frac{a}{L})^3 + \frac{8}{3\pi}\frac{t}{a}(\frac{1}{1+4\kappa_n}) + f(\Re_e)].$$

Of which Δp = the pressure difference $[Pa]$, q = flow rate $[\frac{kg}{s}]$, μ = shear viscosity of the fluid $[Pas]$, a = pore radius $[m]$, G = geometric factor dependent on the pattern of the pores, L = center to center spacing of the pores $[m]$, t = thickness of the membrane $[m]$, κ_n = Knudsen number, and $\Re_e$ = Reynolds number.[118] To determine the mass flow rate through the membrane, the mass flow rate of one pore is multiplied with the number of open pores.

The pressure difference is caused by the 5 mL that is placed on top of the membrane in a holder with a surface area of 4.52×10^{-4} m^2. A shear viscosity of 3.01×10^{-4} Pas and density of 785 $\frac{m}{s^2}$ are used as characteristics of acetone.[119] The Knudsen number is 0.01 and the gravitational acceleration is 9.81 $\frac{m}{s^2}$. A thickness of 10 µm is used. The geometrical factor of 2.1 is selected which average of a square grid pattern and hexagonal pattern.[118] But the effect is in this case negligible while the change in mass flow through the membrane with and without a correction of the hydrodynamic interactions between the flow through different pores, results in a difference of $< 0.00001\%$. A mean mass flow rate of 2.6 mg s^{-1} is calculated. The total measured

mass of the acetone which went through the pores without wetting the pores beforehand over time is presented in figure F.4A. And the total measured mass of the acetone which went through the pores with wetting the pores beforehand over time is presented in figure F.4B. The fact that it is increasing over time shows that acetone is coming through the pores, verifying that the pores are indeed through-holes. The slope is lower in the beginning while it takes some time to get to the maximum flow rate through the pores due to the capillary forces experienced during the wetting of the pores and the bottom of the membrane. This is confirmed by the measurements which were done performed by wetting the membrane before placing the acetone on top of it.

Linear lines were fitted through the linear part of the experiments performed without wetting the pores. This is from 60 s to 100 s. From the experiments with the wetted pores, the same amount mass at the start and at the end is selected. This is from 30 s to 70 s. Not the complete range is selected while over a longer period of time the effect of the evaporation of the acetone can be observed. The fitted lines are plotted with a dotted line in figure F.4. The coefficient of determination, R^2, of these lines is 1.00 and 1.00. The slope of those fitted lines determines the mass flow rate of the experimental data. A mean mass flow rate of 19.3 mg s^{-1} was found with a standard deviation of 0.0006. The difference between the theoretical model and the measured mass can be explained while it looks like acetone could flow around the membrane, figures F.3A and F.3C.

F.4. Conclusion

Pores can be seen on both sides of the membrane which indicates that through-holes are created in the membrane. But because of the big difference in the theoretical mass flow rate and the measured mass flow rate, it is believed that acetone flowed around the membrane, and therefore the fluidic functionality can not be garantueed. But the set up it self gave consist results, proving this simple set up can be used to verify the fluidic functionality of a membrane.

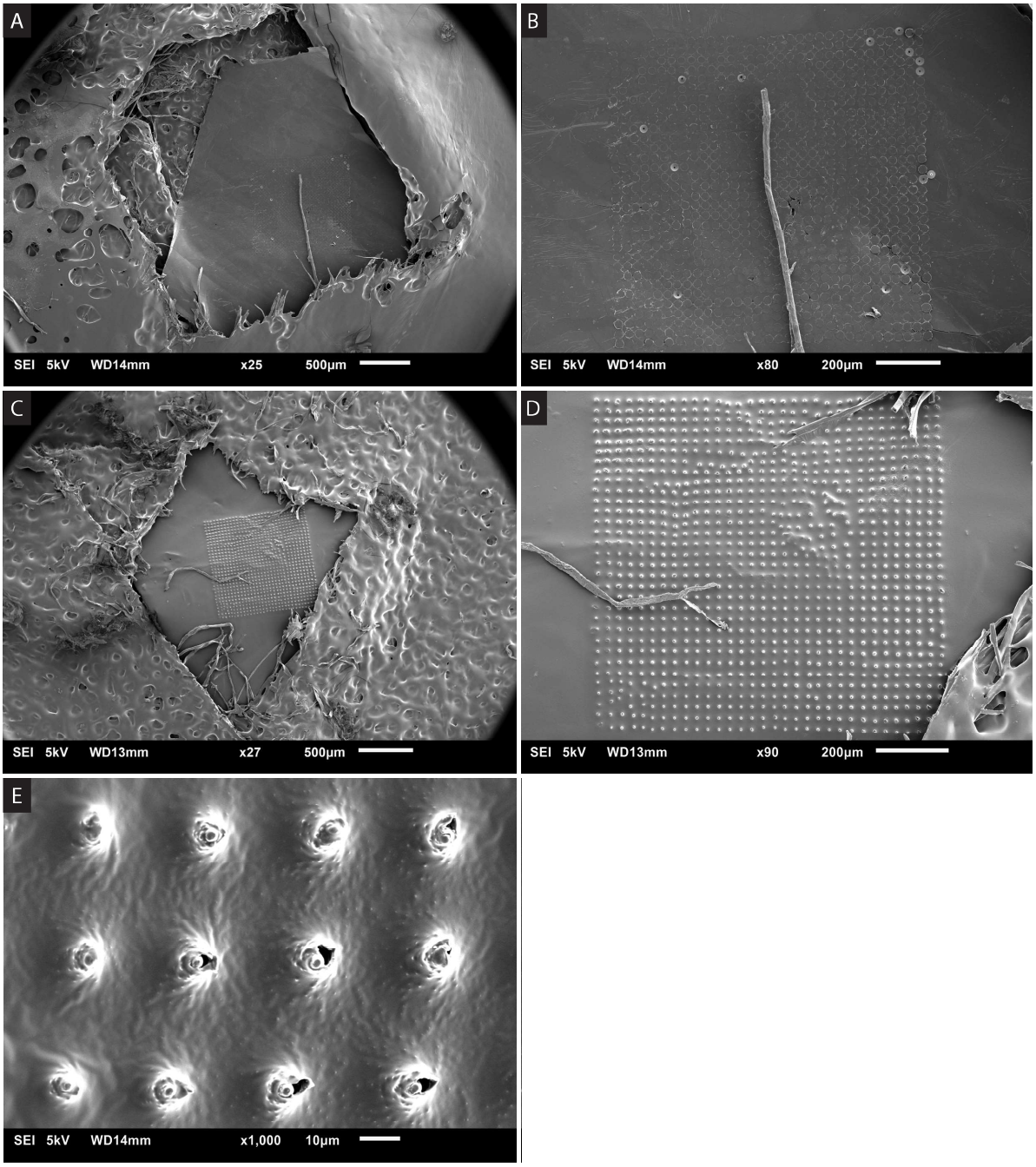

Figure F.3: SEM images of the membrane with integrated porous electrode used for the permeability experiments. A: Overview of the conductive side of the membrane between the double sided tape. B: Overview of the conductive side of the membrane. C: Overview of the nonconductive side of the membrane between the double sided tape. D: Overview of the nonconductive side of the membrane. E: Close up of the nonconductive side of the membrane.

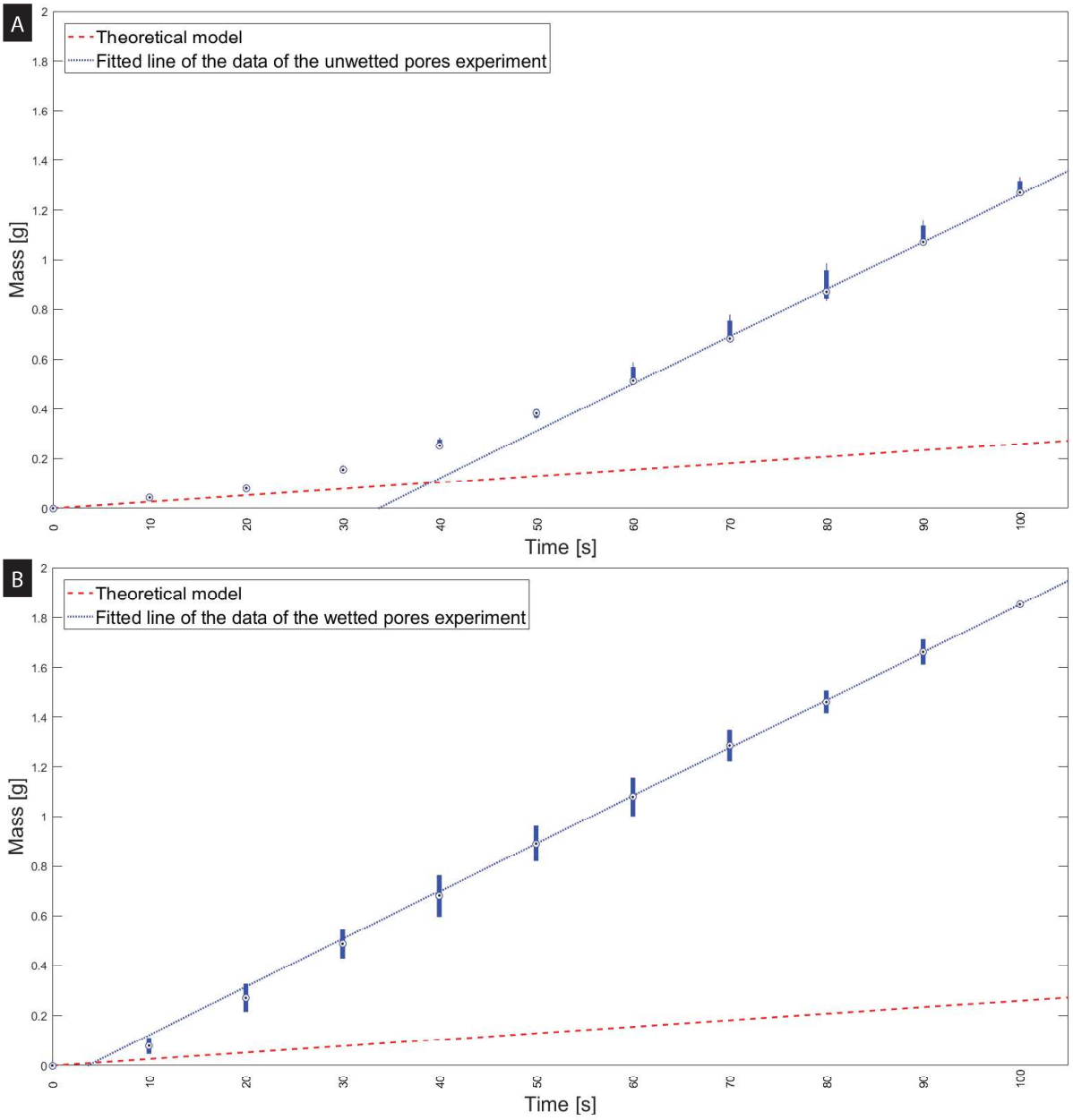

Figure F.4: Plots of the results of the permeability experiment. A: Boxplot (showing the median, 25th percentile, and 75th percentile) for the measuremed mass without wetting the pores beforehand. The red dashed line is the theoretical model and the blue dotted line is the fitted line. B: Boxplot (showing the median, 25th percentile, and 75th percentile) for the measuremed mass with wetting the pores beforehand. The red dashed line is the theoretical model and the blue dotted line is the fitted line.

Bibliography

[1] J. A. Dimasi, H. G. Grabowski, and R. W. Hansen, "Innovation in the pharmaceutical industry: New estimates of r&d costs," *Journal of Health Economics*, vol. 47, p. 20–33, Feb 2016.

[2] S. M. Paul, D. S. Mytelka, C. T. Dunwiddie, C. C. Persinger, B. H. Munos, S. R. Lindborg, and A. L. Schacht, "How to improve r&d productivity: the pharmaceutical industrys grand challenge," *Nature Reviews Drug Discovery*, vol. 9, pp. 203–214, Feb 2010.

[3] PhRMA, "Biopharmaceutical research & development:the process behind new medicines," Aug 2015.

[4] G. Hamilton, "Body parts on a chip," Jun 2013.

[5] BIO, Biomedtracker, and Amplion, "Clinical development success rates 2006-2015," p. 1–28, Jun 2016.

[6] K. Groff, E. Bachli, M. Lansdowne, and T. Capaldo, "Review of evidence of environmental impacts of animal research and testing," *Environments*, vol. 1, no. 1, pp. 14–30, 2014.

[7] H. Jo, H.-W. Jun, J. Shin, and S. Lee, *Biomedical engineering: frontier research and converging technologies*. Springer, 2016.

[8] N. S. Bhise, J. Ribas, V. Manoharan, Y. S. Zhang, A. Polini, S. Massa, M. R. Dokmeci, and A. Khademhosseini, "Organ-on-a-chip platforms for studying drug delivery systems," *Journal of Controlled Release*, vol. 190, p. 82–93, May 2014.

[9] F. Zheng, F. Fu, Y. Cheng, C. Wang, Y. Zhao, and Z. Gu, "Organ-on-a-chip systems: Microengineering to biomimic living systems," *Small*, vol. 12, p. 2253–2282, Feb 2016.

[10] A. Skardal, T. Shupe, and A. Atala, "Organoid-on-a-chip and body-on-a-chip systems for drug screening and disease modeling," *Drug Discovery Today*, vol. 21, p. 1399–1411, Sep 2016.

[11] S. Knowlton and S. Tasoglu, "A bioprinted liver-on-a-chip for drug screening applications," *Trends in Biotechnology*, vol. 34, p. 681–682, Sep 2016.

[12] B. M. Maoz, A. Herland, O. Y. F. Henry, W. D. Leineweber, M. Yadid, J. Doyle, R. Mannix, V. J. Kujala, E. A. Fitzgerald, K. K. Parker, and et al., "Organs-on-chips with combined multi-electrode array and transepithelial electrical resistance measurement capabilities," *Lab on a Chip*, vol. 17, pp. 2294–2302, Jun 2017.

[13] J. Yeste, M. García-Ramírez, X. Illa, A. Guimerà, C. Hernández, R. Simó, and R. Villa, "A compartmentalized microfluidic chip with crisscross microgrooves and electrophysiological electrodes for modeling the blood–retinal barrier," *Lab on a Chip*, vol. 18, pp. 95–105, Nov 2017.

[14] O. Y. F. Henry, R. Villenave, M. J. Cronce, W. D. Leineweber, M. A. Benz, and D. E. Ingber, "Organs-on-chips with integrated electrodes for trans-epithelial electrical resistance (teer) measurements of human epithelial barrier function," *Lab on a Chip*, vol. 17, pp. 2264–2271, May 2017.

[15] D. Caballero, S. Kaushik, V. Correlo, J. Oliveira, R. Reis, and S. Kundu, "Organ-on-chip models of cancer metastasis for future personalized medicine: From chip to the patient," *Biomaterials*, vol. 149, pp. 98–115, 2017.

[16] Y. Berdichevsky, K. J. Staley, and M. L. Yarmush, "Building and manipulating neural pathways with microfluidics," *Lab on a Chip*, vol. 10, pp. 999–1004, Jan 2010.

[17] Y. S. Zhang, J. Aleman, S. R. Shin, T. Kilic, D. Kim, S. A. M. Shaegh, S. Massa, R. Riahi, S. Chae, N. Hu, and et al., "Multisensor-integrated organs-on-chips platform for automated and continual in situ monitoring of organoid behaviors," *Proceedings of the National Academy of Sciences*, vol. 114, pp. E2293–E2302, Mar 2017.

[18] J. U. Lind, T. A. Busbee, A. D. Valentine, F. S. Pasqualini, H. Yuan, M. Yadid, S.-J. Park, A. Kotikian, A. P. Nesmith, P. H. Campbell, and et al., "Instrumented cardiac microphysiological devices via multimaterial three-dimensional printing," *Nature Materials*, vol. 16, p. 303–308, Oct 2016.

[19] P. Fanzio, A. Cagliani, K. G. Peterffy, and L. Sasso, "High throughput soft embossing process for micropatterning of pedot thin films," *Microelectronic Engineering*, vol. 176, p. 15–21, May 2017.

[20] Corning, "Transwell® permeable supports selection and use guide," 2013.

[21] R. W. Baker, *Membrane technology and applications.* John Wiley & Sons, 3 ed., 2012.

[22] Corning, "Permeable supports selection guide," 2016.

[23] G. Luka, A. Ahmadi, H. Najjaran, E. Alocilja, M. Derosa, K. Wolthers, A. Malki, H. Aziz, A. Althani, M. Hoorfar, and et al., "Microfluidics integrated biosensors: A leading technology towards lab-on-a-chip and sensing applications," *Sensors*, vol. 15, p. 30011–30031, Dec 2015.

[24] D. Grieshaber, R. Mackenzie, J. Vörös, and E. Reimhult, "Electrochemical biosensors - sensor principles and architectures," *Sensors*, vol. 8, p. 1400–1458, Mar 2008.

[25] S. Krabbe, D. Achatz, T. Nieradzik, C. Gerhardy, and W. Schomburg, "Ultrasonic welding of chemical optical sensors supporting o2, ph and co2 imaging in microfluidic systems," *Procedia Engineering*, vol. 120, p. 598–601, 2015.

[26] K. Sachsenheimer, L. Pires, M. Adamek, T. Schwartz, and B. E. Rapp, "Monitoring biofilm growth using a scalable multichannel impedimetric biosensor," *15th International Conference on Miniaturized Systems for Chemistry and Life Sciences (MicroTAS 2011)*, p. 1968–1970, Jan 2011.

[27] L. Pires, K. Sachsenheimer, T. Kleintschek, A. Waldbaur, T. Schwartz, and B. E. Rapp, "Online monitoring of biofilm growth and activity using a combined multi-channel impedimetric and amperometric sensor," *Biosensors and Bioelectronics*, vol. 47, p. 157–163, Mar 2013.

[28] L. Sasso, *Novel Materials for Cellular Nanosensors.* PhD thesis, Jun 2012.

[29] R. Pemberton, T. Cox, R. Tuffin, G. Drago, J. Griffiths, R. Pittson, G. Johnson, J. Xu, I. Sage, R. Davies, and et al., "Fabrication and evaluation of a micro(bio)sensor array chip for multiple parallel measurements of important cell biomarkers," *Sensors*, vol. 14, p. 20519–20532, Oct 2014.

[30] A. Wolf, D. O'Hare, and V. Muralidharan, "Is there a preferred size ratio between electrodes in a 3-electrode system?," May 2014.

[31] J. Wang, C. Wu, N. Hu, J. Zhou, L. Du, and P. Wang, "Microfabricated electrochemical cell-based biosensors for analysis of living cells in vitro," *Biosensors*, vol. 2, pp. 127–170, Apr 2012.

[32] M. A. B.V., "Electrochemical impedance spectroscopy (eis) part 2 – experimental setup," Jul 2011.

[33] L. Sasso, A. Heiskanen, F. Diazzi, M. Dimaki, J. Castillo-León, M. Vergani, E. Landini, R. Raiteri, G. Ferrari, M. Carminati, and et al., "Doped overoxidized polypyrrole microelectrodes as sensors for the detection of dopamine released from cell populations," *The Analyst*, vol. 138, pp. 3651–3659, Jul 2013.

[34] G. Kaur, R. Adhikari, P. Cass, M. Bown, and P. Gunatillake, "Electrically conductive polymers and composites for biomedical applications," *RSC Adv.*, vol. 5, p. 37553–37567, Apr 2015.

[35] G. Kaur, R. Adhikari, P. Cass, M. Bown, and P. Gunatillake, "Electrically conductive polymers and composites for biomedical applications," *RSC Advances*, vol. 5, p. 37553–37567, Apr 2015.

[36] H.-Q. Liang, K.-J. Ji, L.-Y. Zha, W.-B. Hu, Y. Ou, and Z.-K. Xu, "Polymer membranes with vertically oriented pores constructed by 2d freezing at ambient temperature," *ACS Applied Materials & Interfaces*, vol. 8, pp. 14174–14181, May 2016.

[37] N. Y. Shim, D. A. Bernards, D. J. Macaya, J. A. Defranco, M. Nikolou, R. M. Owens, and G. G. Malliaras, "All-plastic electrochemical transistor for glucose sensing using a ferrocene mediator," *Sensors*, vol. 9, pp. 9896–9902, Dec 2009.

[38] D. A. Bernards, D. J. Macaya, M. Nikolou, J. A. DeFranco, S. Takamatsu, and G. G. Malliaras, "Enzymatic sensing with organic electrochemical transistors," *J. Mater. Chem.*, vol. 18, pp. 116–120, 2008.

[39] D. Nilsson, T. Kugler, P.-O. Svensson, and M. Berggren, "An all-organic sensor–transistor based on a novel electrochemical transducer concept printed electrochemical sensors on paper," *Sensors and Actuators B: Chemical*, vol. 86, pp. 193–197, Sep 2002.

[40] S. Y. Yang, B. N. Kim, A. A. Zakhidov, P. G. Taylor, J.-K. Lee, C. K. Ober, M. Lindau, and G. G. Malliaras, "Detection of transmitter release from single living cells using conducting polymer microelectrodes," *Advanced Materials*, vol. 23, p. 1–10, Mar 2011.

[41] M. Borghetti, M. Serpelloni, E. Sardini, and S. Pandini, "Mechanical behavior of strain sensors based on pedot:pss and silver nanoparticles inks deposited on polymer substrate by inkjet printing," *Sensors and Actuators A: Physical*, vol. 243, pp. 71–80, Jun 2016.

[42] P. Fanzio, C.-t. Chang, M. Skolimowski, S. Tanzi, and L. Sasso, "Microfluidic polymeric device with integrated conductive polymer electrodes for wearable ph sensing application," May 2017.

[43] C. M. Palumbiny, C. Heller, C. J. Schaffer, V. Körstgens, G. Santoro, S. V. Roth, and P. Müller-Buschbaum, "Molecular reorientation and structural changes in cosolvent-treated highly conductive pedot:pss electrodes for flexible indium tin oxide-free organic electronics," *The Journal of Physical Chemistry C*, vol. 118, pp. 13598–13606, Jun 2014.

[44] B. S. Lalia, V. Kochkodan, R. Hashaikeh, and N. Hilal, "A review on membrane fabrication: Structure, properties and performance relationship," *Desalination*, vol. 326, p. 77–95, Aug 2013.

[45] A. Dobos and A. Filimon, *Polymeric membranes: From basic concepts and separation mechanisms to their impact on daily life*, vol. 1, p. 429–440. Formatex Research Center, 2016.

[46] A. Yamaguchi, F. Uejo, T. Yoda, T. Uchida, Y. Tanamura, T. Yamashita, and N. Teramae, "Self-assembly of a silica–surfactant nanocomposite in a porous alumina membrane," *Nature Materials*, vol. 3, p. 337–341, Apr 2004.

[47] Y. Luo and R. N. Zare, "Perforated membrane method for fabricating three-dimensional polydimethylsiloxane microfluidic devices," *Lab on a Chip*, vol. 8, p. 1688–1694, Aug 2008.

[48] Z.-X. Low, Y. T. Chua, B. M. Ray, D. Mattia, I. S. Metcalfe, and D. A. Patterson, "Perspective on 3d printing of separation membranes and comparison to related unconventional fabrication techniques," *Journal of Membrane Science*, vol. 523, p. 596–613, Feb 2017.

[49] M. Worgull, *Replication Processes*, pp. 13–55. William Andrew, 2009.

[50] R. Jena, C. Yue, Y. Lam, P. Tang, and A. Gupta, "Comparison of different molds (epoxy, polymer and silicon) for microfabrication by hot embossing technique," *Sensors and Actuators B: Chemical*, vol. 163, p. 233–241, Mar 2012.

[51] M. Worgull, *Elementary Process Variations*, p. 149–162. William Andrew, 2009.

[52] E. W. K. Young, E. Berthier, D. J. Guckenberger, E. Sackmann, C. Lamers, I. Meyvantsson, A. Huttenlocher, and D. J. Beebe, "Rapid prototyping of arrayed microfluidic systems in polystyrene for cell-based assays," *Analytical Chemistry*, vol. 83, p. 1408–1417, Jan 2011.

[53] A. D. Printz, E. Chan, C. Liong, R. S. Martinez, and D. J. Lipomi, "Photoresist-free patterning by mechanical abrasion of water-soluble lift-off resists and bare substrates: Toward green fabrication of transparent electrodes," *PLoS ONE*, vol. 8, p. 1–10, Dec 2013.

[54] J. Choi, A. Roychowdhury, N. Kim, D. E. Nikitopoulos, W. Lee, H. Han, and S. Park, "A microfluidic platform with a free-standing perforated polymer membrane," *Journal of Micromechanics and Microengineering*, vol. 20, Jul 2010.

[55] H. Schift, S. Bellini, and J. Gobrecht, "Perforated polymer membranes fabricated by nanoimprint," *Microelectronic Engineering*, vol. 83, p. 873–875, Jan 2006.

[56] J. S. Kuo and D. T. Chiu, "Disposable microfluidic substrates: Transitioning from the research laboratory into the clinic," *Lab on a Chip*, vol. 11, p. 2656–2665, Jul 2011.

[57] P. S. Nunes, P. D. Ohlsson, O. Ordeig, and J. P. Kutter, "Cyclic olefin polymers: emerging materials for lab-on-a-chip applications," *Microfluidics and Nanofluidics*, vol. 9, p. 145–161, Apr 2010.

[58] V. Doushkina and E. Fleming, "Optical and mechanical design advantages using polymer optics," *Advances in Optomechanics*, vol. 7424, pp. 74240Q–3–74240Q–12, Sep 2009.

[59] TOPAS, "Cyclic olefin copolymer (coc): Topas," 2011.

[60] ZEONEX, "Cyclo olefin polymer (cop): Zeonex," 2016.

[61] V. Linder, B. Gates, D. Ryan, B. Parviz, and G. Whitesides, "Water-soluble sacrificial layers for surface micromachining," *Small*, vol. 1, p. 730–736, Jul 2005.

[62] U. Lang, P. Rust, and J. Dual, "Towards fully polymeric mems: Fabrication and testing of pedot/pss strain gauges," *Microelectronic Engineering*, vol. 85, p. 1050–1053, May 2008.

[63] F. C. Krebs, "Fabrication and processing of polymer solar cells: A review of printing and coating techniques," *Solar Energy Materials and Solar Cells*, vol. 93, p. 394–412, Apr 2009.

[64] F. Zabihi, Y. Xie, S. Gao, and M. Eslamian, "Morphology, conductivity, and wetting characteristics of pedot:pss thin films deposited by spin and spray coating," *Applied Surface Science*, vol. 338, p. 163–177, May 2015.

[65] M. Leester-Schädel, T. Lorenz, F. Jürgens, and C. Richter, *Fabrication of Microfluidic Devices*, p. 23–57. Springer International Publishing, 2016.

[66] M. Vaezi, H. Seitz, and S. Yang, "A review on 3d micro-additive manufacturing technologies," *The International Journal of Advanced Manufacturing Technology*, vol. 67, p. 1721–1754, Nov 2012.

[67] Y. Qin, *Micromanufacturing engineering and technology*. William Andrew, 2nd ed., May 2015.

[68] K. Hon, L. Li, and I. Hutchings, "Direct writing technology—advances and developments," *CIRP Annals - Manufacturing Technology*, vol. 57, p. 601–620, Oct 2008.

[69] G. Ozaydin-Ince, A. M. Coclite, and K. K. Gleason, "Cvd of polymeric thin films: applications in sensors, biotechnology, microelectronics/organic electronics, microfluidics, mems, composites and membranes," *Reports on Progress in Physics*, vol. 75, p. 1–40, Dec 2011.

[70] J. Li, X. L. Zhao, and H. Yan, "Highly conductive and transparent pedot/pss thin films with large area prepared by bar-coating method," *Materials Science Forum*, vol. 852, p. 1123–1131, Mar 2016.

[71] H. Okuzaki, S. Takagi, F. Hishiki, and R. Tanigawa, "Ionic liquid/polyurethane/pedot:pss composites for electro-active polymer actuators," *Sensors and Actuators B: Chemical*, vol. 194, p. 59–63, Mar 2014.

[72] J. Dong, J. Liu, G. Kang, J. Xie, and Y. Wang, "Pushing the resolution of photolithography down to 15nm by surface plasmon interference," *Scientific Reports*, vol. 4, p. 1–6, Jul 2014.

[73] Y. Wang, T. Deng, and Z. Liu, "Fabrication of nanopore and nanopore arrays in si substrate by wet etching method at wafer scale," *2016 China Semiconductor Technology International Conference (CSTIC)*, May 2016.

[74] N. Roy, A. Yuksel, and M. Cullinan, "Design and modeling of a microscale selective laser sintering system," *Joint MSEC-NAMRC Symposia*, vol. 3, Jun 2016.

[75] K. S. Worthington, L. A. Wiley, E. E. Kaalberg, M. M. Collins, R. F. Mullins, E. M. Stone, and B. A. Tucker, "Two-photon polymerization for production of human ipsc-derived retinal cell grafts," *Acta Biomaterialia*, vol. 55, p. 385–395, Mar 2017.

[76] R. D. Farahani, K. Chizari, and D. Therriault, "Three-dimensional printing of freeform helical microstructures: a review," *Nanoscale*, vol. 6, p. 10470–10485, Jun 2014.

[77] S. Juodkazis, V. Mizeikis, K. K. Seet, M. Miwa, and H. Misawa, "Two-photon lithography of nanorods in su-8 photoresist," *Nanotechnology*, vol. 16, p. 846–849, Apr 2005.

[78] Nanoscribe GmbH, "Photonic professional gt," 2018.

[79] Nanoscribe GmbH, "True 3d laser lithography," 2012.

[80] Nanoscribe GmbH, "Ip photoresists," 2018.

[81] E. D. Lemma, F. Rizzi, T. Dattoma, B. Spagnolo, L. Sileo, A. Qualtieri, M. D. Vittorio, and F. Pisanello, "Mechanical properties tunability of three-dimensional polymeric structures in two-photon lithography," *IEEE Transactions on Nanotechnology*, vol. 16, p. 23–31, Jan 2017.

[82] M. Molitch-Hou, "The best and most unique 3d printer materials: Photopolymer edition," Jul 2016.

[83] S. P. Davis, B. J. Landis, Z. H. Adams, M. G. Allen, and M. R. Prausnitz, "Insertion of microneedles into skin: measurement and prediction of insertion force and needle fracture force," *Journal of Biomechanics*, vol. 37, p. 1155–1163, Aug 2004.

[84] Y. Temiz, R. D. Lovchik, G. V. Kaigala, and E. Delamarche, "Lab-on-a-chip devices: How to close and plug the lab?," *Microelectronic Engineering*, vol. 132, p. 156–175, Jan 2015.

[85] D. F. Stamatialis, B. J. Papenburg, M. Gironés, S. Saiful, S. N. Bettahalli, S. Schmitmeier, and M. Wessling, "Medical applications of membranes: Drug delivery, artificial organs and tissue engineering," *Journal of Membrane Science*, vol. 308, no. 1, pp. 1–34, 2008.

[86] S. M. Casillo, A. P. Peredo, S. J. Perry, H. H. Chung, and T. R. Gaborski, "Membrane pore spacing can modulate endothelial cell–substrate and cell–cell interactions," *ACS Biomaterials Science & Engineering*, vol. 3, pp. 243–248, Feb 2017.

[87] R. N. Carter, S. M. Casillo, A. R. Mazzocchi, J.-P. S. Desormeaux, J. A. Roussie, and T. R. Gaborski, "Ultrathin transparent membranes for cellular barrier and co-culture models," *Biofabrication*, vol. 9, pp. 1–13, Feb 2017.

[88] J.-H. Lee, E. T. K. Peterson, G. Dagani, and I. Papautsky, "Rapid prototyping of plastic microfluidic devices in cyclic olefin copolymer (coc)," *Microfluidics, BioMEMS, and Medical Microsystems III*, p. 82–91, Jan 2005.

[89] G. Bandlamudi, *Systematic Characterization of Ht Pemfcs Containing Pbi/H_3po_4systems: Thermodynamic Analysis and Experimental Investigations*. Logos Verlag Berlin, 2011.

[90] S. J. Cooper, A. Bertei, D. P. Finegan, and N. P. Brandon, "Simulated impedance of diffusion in porous media," *Electrochimica Acta*, vol. 251, pp. 681–689, Oct 2017.

[91] F. M. Smits, "Measurement of sheet resistivities with the four-point probe," *The Bell System Technical Journal*, vol. 37, pp. 711–718, May 1958.

[92] S. Smit, "Conducting polymer microfluidic valve," 2017.

[93] C. Chang, "Micromanufacturing of conductive polymer electrodes for sensing microsystems," Mar 2017.

[94] A. Finn, B. Lu, R. Kirchner, X. Thrun, K. Richter, and W.-J. Fischer, "High aspect ratio pattern collapse of polymeric uv-nano-imprint molds due to cleaning," *Microelectronic Engineering*, vol. 110, p. 112–118, Oct 2013.

[95] M. Heckele and W. K. Schomburg, "Review on micro molding of thermoplastic polymers," *Journal of Micromechanics and Microengineering*, vol. 14, p. R1–R14, Dec 2003.

[96] D. Lipomi, R. Martinez, L. Cademartiri, and G. Whitesides, *Soft Lithographic Approaches to Nanofabrication*, vol. 7, p. 211–231. Elsevier, Dec 2012.

[97] H. Lan, "Soft uv nanoimprint lithography and its applications," *Updates in Advanced Lithography*, p. 169–195, Jul 2013.

[98] S. E. A. Gratton, S. S. Williams, M. E. Napier, P. D. Pohlhaus, Z. Zhou, K. B. Wiles, B. W. Maynor, C. Shen, T. Olafsen, E. T. Samulski, and et al., "The pursuit of a scalable nanofabrication platform for use in material and life science applications," *Accounts of Chemical Research*, vol. 41, p. 1685–1695, Aug 2008.

[99] M. Pla-Roca, J. G. Fernandez, C. A. Mills, E. Martínez, and J. Samitier, "Micro/nanopatterning of proteins via contact printing using high aspect ratio pmma stamps and nanoimprint apparatus," *Langmuir*, vol. 23, p. 8614–8618, Jul 2007.

[100] S. S. Williams, S. Retterer, R. Lopez, R. Ruiz, E. T. Samulski, and J. M. Desimone, "High-resolution pfpe-based molding techniques for nanofabrication of high-pattern density, sub-20 nm features: A fundamental materials approach," *Nano Letters*, vol. 10, p. 1421–1428, Feb 2010.

[101] F. Zhang and H. Y. Low, "Transfer printing of 3d hierarchical gold structures using a sequentially imprinted polymer stamp," *Nanotechnology*, vol. 19, pp. 1–5, Sep 2008.

[102] T. Gorter and A. Reinders, "A comparison of 15 polymers for application in photovoltaic modules in pv-powered boats," *Applied Energy*, vol. 92, p. 286–297, Apr 2012.

[103] The Chemours Company FC, "Shop teflon™ fluoroplastic resins," Feb 2016.

[104] The Chemours Company FC, "Teflon af amorphous fluoroplastic resins," 2016.

[105] D. M. Patil, G. A. Phalak, and S. T. Mhaske, "Design and synthesis of bio-based uv curable pu acrylate resin from itaconic acid for coating applications," *Designed Monomers and Polymers*, vol. 20, p. 269–282, Oct 2016.

[106] S. Belligundu and P. S. Shiakolas, "Study on two-stage hot embossing microreplication: silicon to polymer to polymer," *Journal of Micro/Nanolithography, MEMS, and MOEMS*, vol. 5, pp. 021103–1–021103–8, Apr 2006.

[107] M. T. Koesdjojo, Y. H. Tennico, J. T. Rundel, and V. T. Remcho, "Two-stage polymer embossing of coplanar microfluidic features for microfluidic devices," *Sensors and Actuators B: Chemical*, vol. 131, p. 692–697, May 2008.

[108] D. Johansen, "Investigation of topas® for use in optical components," 2005.

[109] J. M. Stormonth-Darling, R. H. Pedersen, and N. Gadegaard, "Polymer replication techniques," *Design of Polymeric Platforms for Selective Biorecognition*, p. 123–155, Jan 2015.

[110] Nanoscribe GmbH, "Photonic professional (gt) user manual."

[111] M. Tyona, "A theoritical study on spin coating technique," *Advances in materials Research*, vol. 2, p. 195–208, Dec 2013.

[112] C. Nguyen, T. Vu-Khanh, and J. Lara, "Puncture characterization of rubber membranes," *Theoretical and Applied Fracture Mechanics*, vol. 42, p. 25–33, Sep 2004.

[113] Z. Wei, T. M. Schneider, J. Kim, H.-Y. Kim, J. Aizenberg, and L. Mahadevan, "Elastocapillary coalescence of plates and pillars," *Proceedings of the Royal Society A: Mathematical, Physical and Engineering Sciences*, vol. 471, p. 1–17, Jan 2015.

[114] Nanoscribe GmbH, "Adhesion to the substrate," Sep 2014.

[115] B. Overes, "Imprint lithography using nanocrystalline cvd diamond molds," 2018.

[116] R. van Dommelen, "Surface self-assembled colloidal crystals for the use in pattern replication by hot embossing," Sep 2017.

[117] MathWorks, "Delaunay triangulation," 2017.

[118] K. H. Jensen, A. X. C. N. Valente, and H. A. Stone, "Flow rate through microfilters: Influence of the pore size distribution, hydrodynamic interactions, wall slip, and inertia," *Physics of Fluids*, vol. 26, pp. 052004–1–052004–13, May 2014.

[119] A. Navrotsky, "The interface between mineral physics and materials science," *Physics and chemistry of Earth materials*, pp. 408–414, Dec 2010.